When Cardiac Biophysics Meets Groupwise Statistics: Complementary Modelling Approaches for Patient-Specific Medicine

Maxime Sermesant

Université de Nice – Sophia Antipolis

École Doctorale STIC

When Cardiac Biophysics Meets Groupwise Statistics

Complementary Modelling Approaches for Patient-Specific Medicine

Mémoire présenté pour l'obtention de

L'HABILITATION À DIRIGER DES RECHERCHES

Par

Maxime Sermesant

Le 9 Juin 2016

Devant le jury :

Pr Michael Brady	Oxford University	*Rapporteur*
Pr Yves Coudière	Bordeaux University	*Rapporteur*
Pr Daniel Rueckert	Imperial College London	*Rapporteur*
Pr Nicholas Ayache	Inria	*Examinateur*
Pr Michel Haïssaguerre	Liryc Institute	*Examinateur*
Pr Reza Razavi	King's College London	*Président*

Dedicated to K&C&T.

Contents

Acknowledgements

I would like to first thank my committee. It was a real honour to have such a prestigious and pleasant committee, with great reviews and discussions. Research is standing on the shoulders of giants, and I have been very lucky to be able to learn directly from some of these giants.

Then I would like to thank the Epidaure / Asclepios team where I did most of the presented research. It has been a very productive and friendly environment, which is the best combination one could expect. At a scientific level, I would like to acknowledge Nicholas Ayache for his vision which always kept the team in challenging and motivating research areas. I want to deeply thank Hervé Delingette and Xavier Pennec for everything I learned from them in Computational Physiology and Computational Anatomy, through always fruitful and lively discussions. It allowed me to do exciting research at the frontier between both.

I am deeply grateful to all the students and collaborators who worked with me, most of the content of this manuscript is from them. You should always hire people more clever than you, and I was lucky to be able to do so (who said it was easy? ;)

I would like to also thank the Division of Imaging Sciences, King's College London, which hosted me for almost three years at Guy's Hospital, and where I learned hugely on the clinical environment and day to day interactions with clinicians. It was also in a very friendly and productive environment and this is in particular due to the impressive skills of Reza Razavi in motivating and supporting people while always exploring new research paths.

Big thank you also to the IHU Liryc (in particular to Hubert Cochet and Pierre Jaïs) for the day-to-day interactions and the possibility to apply parts of this research directly to patient care.

Finally, lots of love to Karine, Corentin and Timaël, who make me happy to wake up everyday (which is a huge achievement in itself, for those who know me... :)

– Maxime Sermesant, 24/06/2016

Overview of the Presented Research

Research Topics since my PhD

This manuscript presents excerpts of the research work I performed and supervised over the last decade combining cardiac modelling and clinical data in order to help diagnosis and therapy planning. This is by nature a very collaborative and multi-disciplinary work, achieved at the intersection of academic, clinical and industrial environments. There is also an important underlying software work in order to reach a clinical impact, which will not be detailed here but is visible in the most recent clinical publications and the start-up projects.

During my PhD, I developed an electromechanical model of the heart that was usable as prior knowledge in image processing tasks. It was a generic model that could provide some physiological constraints but its parameters were not adjusted to the specific patient analysed. Since my PhD, my research was articulated around two main axes. First I developed methods to personalise such an electromechanical model of the heart to the clinical data of a patient, in order to help therapy planning by simulations. Second, I integrated biophysical and statistical methods in order to be able to model the cardiac function at a group level. This is required in order to assist clinical decision, as any clinical tool needs to be evaluated in a statistical manner.

A Combined Modelling Approach

All along these years, my research has gone back and forth between modelling and imaging, and the most recent work was in combining computational physiology and computational anatomy. This is a very exciting area that integrates two different ways of targeting patient-specific medicine. On one hand, computational physiology tries to build a computer model of the patient based on biophysical models of the human body, from the cell to the organ. On the other hand, computational anatomy aims at statistical learning from healthy and pathological groupwise data, in order to evaluate a specific patient against a template of the population / patient-group (see Fig. 1).

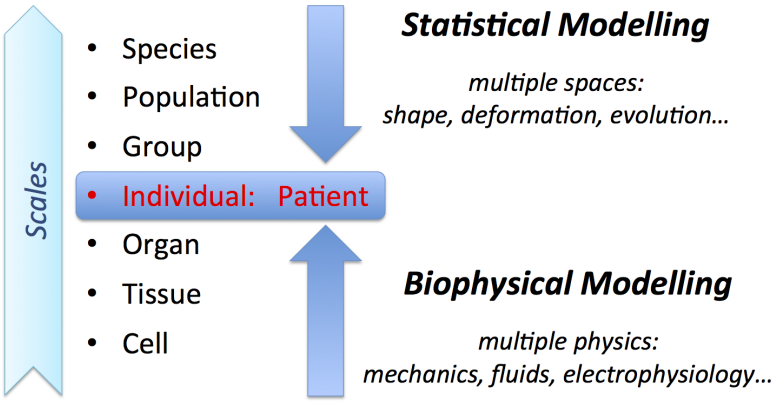

Figure 1: Biophysical and statistical approaches for patient-specific medicine: two sides of the same coin.

These two research areas have undergone tremendous progress over the last decade, which can be clearly seen by the number of dedicated publications and conferences. Milestones were achieved in developing new methods for adjusting generic models to patient data (personalisation) and for computing statistics on complex objects like shapes and deformations. The parallel development of computational power and numerical strategies now opens new avenues for the application and integration of these results.

I really see the biophysical and statistical approaches as complementary, because I think that used independently they lack important features. For the biophysical approach, without a statistical analysis of the studied population it is often impossible to know which are the dominant phenomena to model among the numerous multi-scale and multi-physics features of the cardiac function. On the other hand, once computed, a statistical model is very hard to interpret without some mechanistic insights on the phenomena observed, and biophysical models are a great tool to explore such mechanisms.

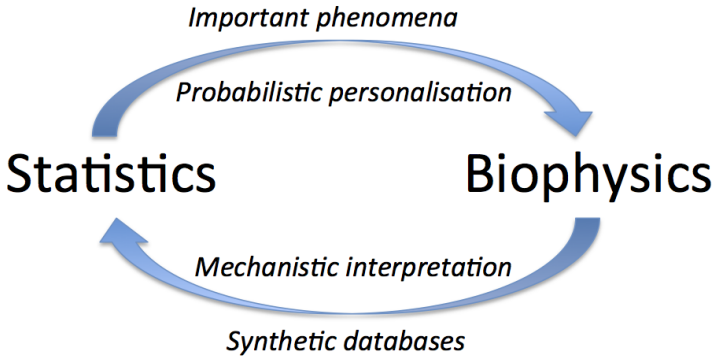

Figure 2: Statistics and biophysics complement each other, and therefore reinforce the findings.

I will present in this manuscript contributions illustrating these two aspects and potential approaches on how to combine them.

Results and Contributions

This manuscript is organised in three parts. The first part is presenting contributions in methods to obtain patient-specific cardiac models, and how it was applied to different clinical questions. The second part presents statistical models of cardiac structure and function for the groupwise analysis of the heart and its remodelling. The third part presents contributions combining the two previous approaches of biophysical and statistical models.

This introduction is presenting the different chapters and contributions, while details and references are in the attached publications.

Part I: Patient-Specific Biophysical Models of the Heart

> *"The notion of a single and ultimate (cardiac) model is as useful as the idea of a universal mechanical tool for all possible repairs and servicing requirements in daily life. The ideal model will be as simple as possible and as complex as necessary for the particular question raised."*
>
> – A. Garny, D. Noble, P. Kohl, *Dimensionality in cardiac modelling, Progress in Biophysics and Molecular Biology, 87-1, 2005.*

As clearly expressed in this quote, one of the main challenges in modelling is to select the right model for a given application. There is now a wide range of cardiac models available in the literature, and when trying to answer a particular question it is important to weigh the pros and cons of each model in order to be sure that the chosen one will represent adequately the phenomena of interest.

Once the model equations are there, the next challenge is to design a personalisation process that will adjust the model parameters so that the simulated observations match the measured ones. To achieve this, we follow a causality process, starting from the anatomy, then the electrophysiology and finally the mechanics. In our approach at Inria, we currently neglect the feedback loops, for instance the influence of the mechanical deformation on the electrophysiological conduction velocity, or on the anatomical remodelling. These are important phenomena, but we believe that the available data is still sparse to be able to adjust more complex models including these effects. Moreover the most adequate model equations to represent them are still unclear.

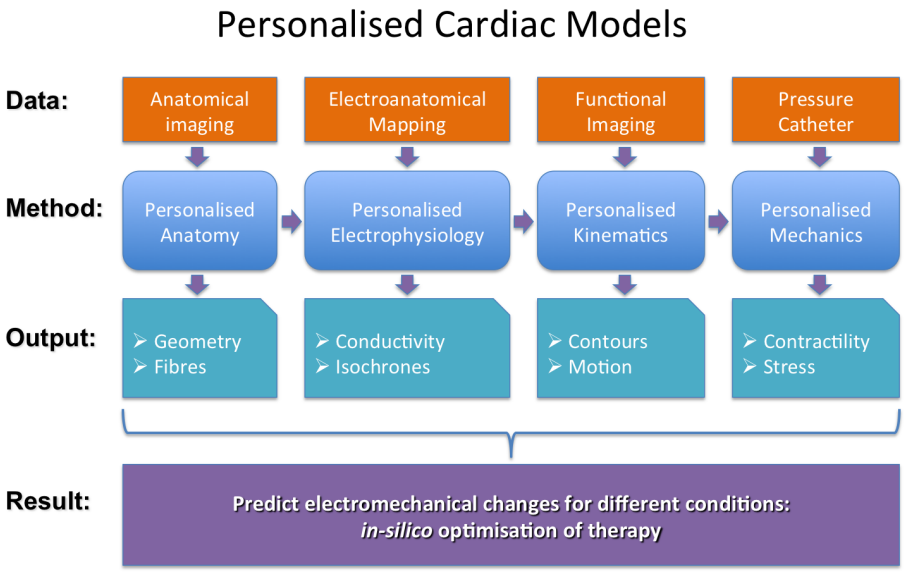

Figure 3: General scheme of the patient-specific models of this manuscript.

In the following chapters we will present the methodologies we developed to obtain patient-specific fibre orientations, electrophysiological and mechanical models. Each of these three aspects will be illustrated in its application to a specific clinical question.

Chapter 1: in vivo Human Cardiac Fibre Architecture Estimation

– This chapter is based on [Toussaint et al., 2013]: Toussaint, N., Stoeck, C. T., Schaeffter, T., Kozerke, S., Sermesant, M., and Batchelor, P. G. In vivo human cardiac fibre architecture estimation using shape-based diffusion tensor processing. *Medical Image Analysis*, 17(8):1243 – 1255, 2013.

When modelling cardiac electromechanical activity, one of the first steps is to define the anatomical structure of the model, which includes the shape of the myocardium and the local muscle fibre orientation. While the anatomy of the heart can now be obtained automatically from 3D medical imaging thanks to the important progress in cardiac image segmentation, the cardiac fibre structure is still a challenge to acquire. The complex 3D muscle fibre architecture of the heart makes it difficult to measure, even by dissection. This is the reason why most cardiac simulations use fibre orientations from a rule-based model. The use of diffusion tensor magnetic resonance imaging (DT-MRI) opened up possibilities for non destructive 3D measurement of the fibre orientations. However the acquisition time is still not compatible with 3D in vivo imaging.

I co-supervised a PhD student (Nicolas Toussaint, King's College London) in order to take advantage of the mathematical modelling of the cardiac shape to reconstruct a dense map of 3D fibre architecture from a few DT-MRI slices acquired in vivo. Through the adapted coordinates, this framework also enabled to compute statistics over a small group of volunteers and to generate a dense 3D atlas of healthy cardiac fibre architecture in vivo.

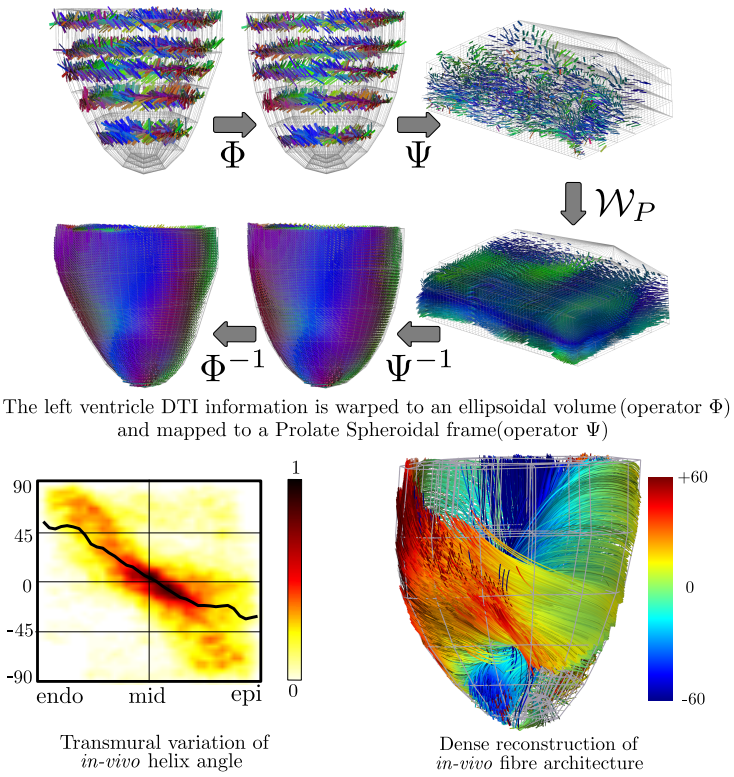

Figure 4: Shape-based interpolation of sparse in vivo DT-MRI of the heart

This work achieved an significant step forward in measuring cardiac fibres in 3D as the existing literature was only acquiring one 2D slice of data. The development of tools to integrate and manipulate several 2D slices in order to reconstruct a full dense 3D fibre architecture was a significant contribution, and the resulting paper [Toussaint et al., 2013] is well cited. The MICCAI 2010 paper we published on this topic was among the seven finalists being considered for the Young Scientist Publication Impact Award at MICCAI 2015.

Chapter 2: Patient-Specific Cardiac Electrophysiology: Application to Ventricular Tachycardia

– This chapter is based on [Chen et al., 2016]: Chen, Z., Cabrera-lozoya, R., Relan, J., Sohal, M., Shetty, A., Karim, R., Delingette, H., Gill, J., Rhode, K., Ayache, N., Taggart, P., Rinaldi, C., Sermesant, M., and Razavi, R. Biophysical modelling predicts ventricular tachycardia inducibility and circuit morphology: A combined clinical validation and computer modelling approach. *Journal of Cardiovascular Electrophysiology*, 2016 (in press).

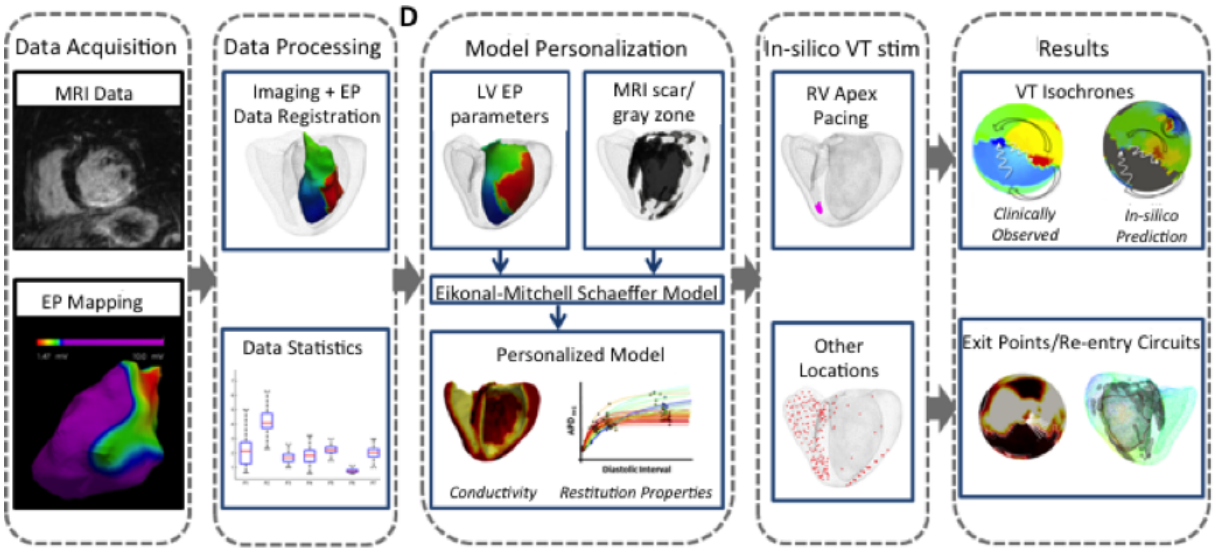

Figure 5: Patient-specific modelling of cardiac electrophysiology for ventricular tachycardia prediction.

Models of cardiac electrophysiology have been developed for decades, however there was still no real adaptation of such models to spatial patient data in order to validate them and utilise them in a clinical application.

We proposed a principled approach to go from electroanatomical mapping clinical data to personalised parameters of a cardiac electrophysiology model. This approach is original as it couples two different models, as they have different computational complexity and represent two different aspects of cardiac electrophysiology. We first use an Eikonal model in order to estimate the electrical conductivity by matching the measured conduction velocity. Then we use the Mitchell-Schaeffer reaction-diffusion model in order to estimate the restitution parameters of the model from data recorded at different pacing frequencies. This coupling enabled to reach a total personalisation time compatible with clinical time constraints.

This work was evaluated with experimental data [Relan et al., 2011b] and applied to retrospective clinical data [Relan et al., 2011a]. Then, through a European project (euHeart) with an expert clinical centre (St Thomas' Hospital, London), we acquired 3D mapping of the heart during a whole pacing procedure in order to evaluate the predictive power of the personalised models. This unique dataset made it possible to demonstrate for the first time on clinical data that such personalised models where able to accurately predict the re-entry circuits [Chen et al., 2016]. This could open up possibilities in model-based planning of cardiac ablation procedures.

Chapter 3: Patient-Specific Cardiac Electromechanics: Application to Cardiac Resynchronisation Therapy

– This chapter is based on [Sermesant et al., 2012]: Sermesant, M., Chabiniok, R., Chinchapatnam, P., Mansi, T., Billet, F., Moireau, P., Peyrat, J., Wong, K., Relan, J., Rhode, K., Ginks, M., Lambiase, P., Delingette, H., Sorine, M., Rinaldi, C., Chapelle, D., Razavi, R., and Ayache, N. Patient-specific electromechanical models of the heart for the prediction of pacing acute effects in CRT: A preliminary clinical validation. *Medical Image Analysis*, 16(1):201–215, 2012.

Numerous mechanical constitutive laws were proposed to model the myocardium in the literature, mostly fitted to tissue-level experimental data. However there was still a gap between what can be estimated from invasive experimental data and clinical data. We therefore proposed an approach in order to estimate the mechanical parameters and the boundary conditions of an electromechanical model of the heart from imaging data. If available, we also used invasive pressure measurements. We based this approach on a multi-scale model previously developed at Inria which includes few parameters and has a physiological behaviour.

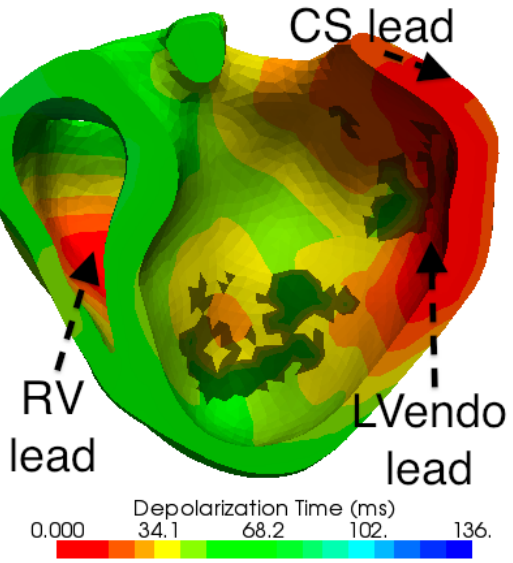

Figure 6: Patient-specific model for the prediction of pacing in heart failure.

We ran this personalisation strategy in order to estimate the parameters of two heart failure patients. We used the sinus rhythm data as baseline to estimate all the electrophysiological and mechanical parameters. We then simulated different pacing conditions on this patient-specific model. We demonstrated that the personalised models were able to predict accurately the changes in pressure curves with pacing.

This was the first mechanical personalisation pipeline applied to clinical data and including a quantitative evaluation of the model predictive power. It required the coordination of experts in various fields and many different contributions in order to perform this complex pipeline, but the results obtained are worth the effort, as it is a milestone for personalised cardiac models. We further developed the automatic mechanical personalisation in [Marchesseau et al., 2013], which MICCAI version received the Young Scientist Award in 2012. Moreover the on-going VP2HF European project is extending this pipeline to fully non-invasive data.

Finally, collaborators at Siemens developed a personalised model approach for Cardiac Resynchronisation Therapy planning based on these ideas and results, which is now evaluated at a large scale.

Part II: Groupwise Statistics on Cardiac Shape and Function

"It is not certain that everything is uncertain."

– Blaise Pascal, *"Pensées", 1670*

The personalised models achieved very promising results, but only on very few cases. Therefore it is still difficult to be certain of their validity, there is a need to reach a larger statistical power to convince the clinical community. This would also allow to quantify the uncertainty on the given predictions. But additional methods are needed to be able to process all this data at a groupwise level, which is the topic of this part.

Over the last decades, medical imaging generated a vast amount of high dimensional data. Due to its 3D nature, with also potential temporal components, it is therefore an ideal environment to analyse distributions of complex objects like shapes, deformations, tensors... however tools are lacking to perform this.

It therefore opened new avenues of research to compute quantitative statistics on such data. Important methodological works have been achieved in this area which was coined "Computational Anatomy" [Miller and Qiu, 2009]. In this part, I will present how I collaborated with researchers in Computational Anatomy in order to propose contributions in the analysis of the cardiac structure, function and remodelling.

Chapter 4: Statistical Model of Cardiac Shape and Remodelling

– This chapter is based on [McLeod et al., 2013]: McLeod, K., Mansi, T., Sermesant, M., Pongiglione, G., and Pennec, X. Statistical shape analysis of surfaces in medical images applied to the tetralogy of fallot heart. In Modeling in Computational Biology and Biomedicine, Lectures Notes in Mathematical and Computational Biology, pages 165–191. Springer, 2013. ISBN 978-3-642-31207-6.

My research on this topic was to collaborate with experts in computational anatomy in order to design a statistical model of the cardiac shape that could represent its evolution with age. We proposed a statistical model of the LV and RV remodelling in repaired Tetralogy of Fallot in order to correlate features of the shape and its evolution with clinical knowledge. As it is very difficult to obtain a longitudinal study on such a long time (10+ years), we used a cross-sectional approach on a dataset from a European project (Health-e-Child) established with experts in paediatric cardiology.

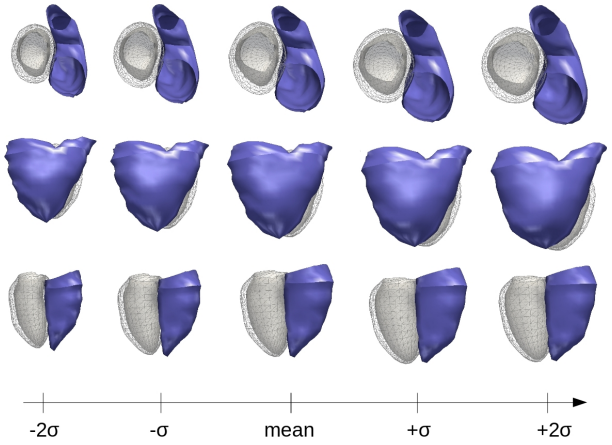

Figure 7: Statistical model of cardiac shape remodelling in repaired Tetralogy of Fallot.

This was the first time that the quantitative evolution of the heart shape with growth and remodelling could be computed due to the difficulty of jointly representing spatial and longitudinal information. There were some sparse clinical indexes related to shape that were known to be impacted by the RV remodelling in this pathology, but no 3D quantitative estimation of this evolution. Through this cross-sectional analysis of a patient group and by leveraging on both the mathematical currents representation of surfaces and diffeomorphic deformations, we could analyse the variability of the shape in this group. We then estimated the variations of shape that correlate most with age to obtain this statistical model of remodelling.

The findings were relevant as they could be interpreted by our clinical collaborators, through known features of this pathology. It opens up new possibilities in estimating how much a patient's trajectory differs from the average behaviour in Tetralogy of Fallot. It could therefore help in the difficult question of the optimal timing of valve replacement in these patients.

Chapter 5: Statistical Model of Cardiac Motion

– This chapter is based on [McLeod et al., 2015]: McLeod, K., Sermesant, M., Beerbaum, P., and Pennec, X. Spatio-temporal tensor decomposition of a polyaffine motion model for a better analysis of pathological left ventricular dynamics. *IEEE Transactions on Medical Imaging*, 34(7):1562–1575, July 2015. ISSN 0278-0062.

My aim on this topic is to define a reduced model of cardiac motion which is rich enough to correctly represent the particularities of normal and pathological hearts but simple enough so that meaningful statistics can be computed on it.

We proposed a poly-affine representation of the cardiac motion, with specific adjustments to the heart (smoothness, incompressibility). By parametrising cardiac function through local affine transformations, we directly work on parameters related to strain, which is a very relevant clinical index of cardiac function, directly related to the local viability of the myocardium and its working conditions. By reducing the number of parameters we are also more robust to noise.

This compact representation opened the way to a statistical analysis of cardiac motion. We can easily reorient these transformation in standard coordinates (prolate spheroidal coordinates) for groupwise analysis. This was achieved by tensor decomposition.

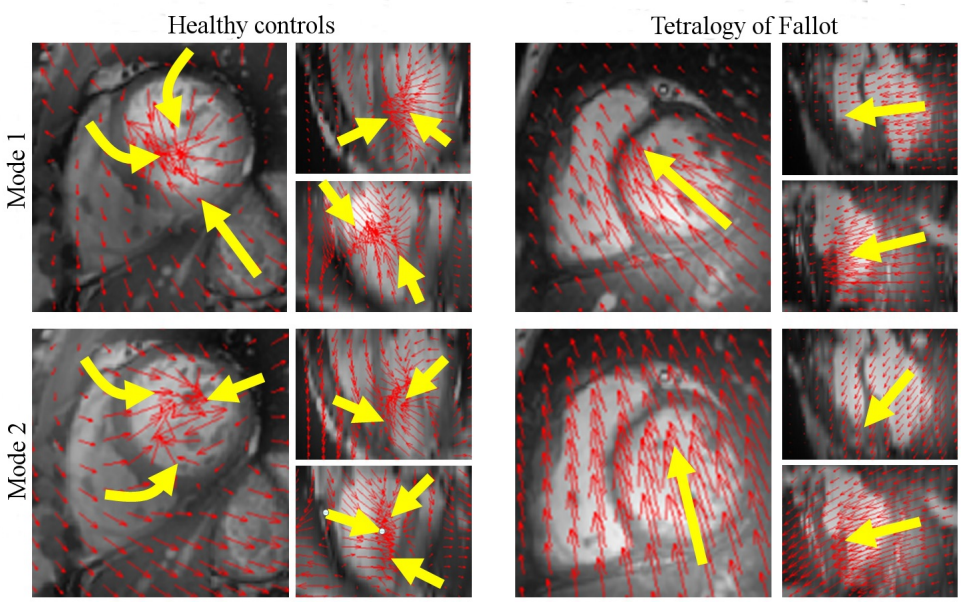

Figure 8: Statistical analysis of cardiac motion for healthy volunteers and Tetralogy of Fallot patients.

By using such a compact representation many applications can be derived on the statistical analysis of motion. Moreover it is a generative model as we can inject any derived poly-affine parameters within a given cardiac shape and orientation. This allows to visualise the resulting mean models (see Figure above) and the variations around them.

There are still many derivations to develop on this topic, both in terms of better image analysis tools and better groupwise statistics. Its coupling with the 3D electromechanical model is also very promising, as it could be a basis to represent the motion in the direct model.

Part III: When Biophysics Meets Statistics

"Uncertainty is an uncomfortable position. But certainty is an absurd one."

– Voltaire

"As far as the laws of mathematics refer to reality, they are not certain; and as far as they are certain, they do not refer to reality."

– Albert Einstein, *"Geometry and Experience", January 27, 1921*

This part presents the different research works where I tried to combine the previous two parts on modelling and statistics. It enables in particular to introduce uncertainty in biophysical modelling, and to generate larger datasets in statistical learning.

Chapter 6: Statistical Learning from Model-based Synthetic Images

– This chapter is based on [Prakosa et al., 2014]: Prakosa, A., Sermesant, M., Allain, P., Villain, N., Rinaldi, C. A., Rhode, K. S., Razavi, R., Delingette, H., and Ayache, N. Cardiac electrophysiological activation pattern estimation from images using a patient-specific database of synthetic image sequences. *IEEE Transactions on Biomedical Engineering*, 61(2):235–245, 2014.

Machine learning achieved very impressive results in many areas. But one particular difficulty in clinical applications is that it is very difficult to obtain ground truth data and a large enough database in order to train learning algorithms on such complex phenomena. The approach we proposed was to use biophysical modelling in order to generate additional synthetic data. It opens up possibilities to generate large databases on which algorithms can be trained and tested.

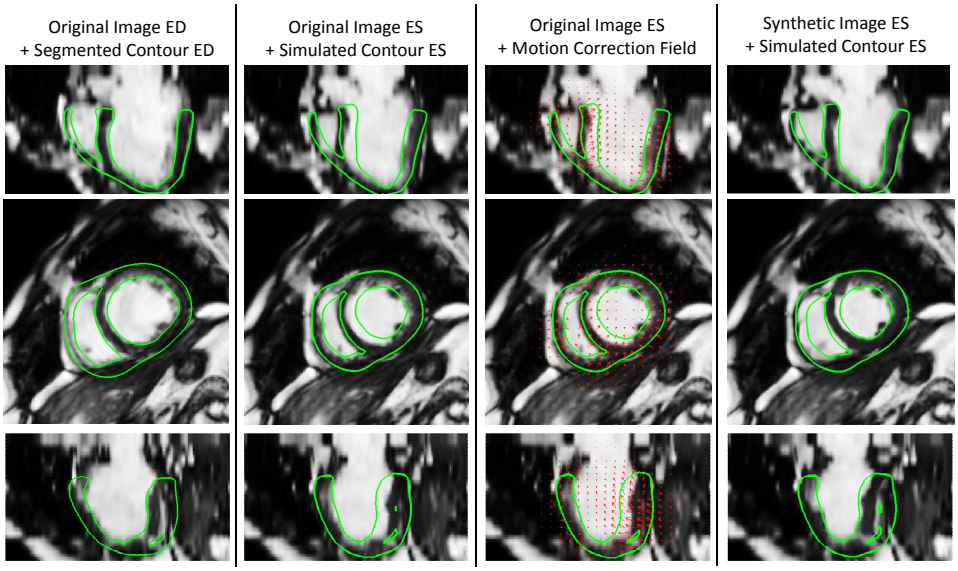

Figure 9: Model-based synthetic images for machine learning from patient-specific database.

However, an additional difficulty of clinical applications is that every patient is different, so generalisation is often challenging. The novel idea of a "Patient-Specific Database" made it possible to train machine learning algorithms on a database which was very close to the patient condition.

As any statistical approach requires a large amount of data, the generative aspect of biophysical modelling is very useful in this context. We tested how such data could be used to develop machine-learning algorithms on a phenomenon which is very difficult to observe clinically (the local electromechanical coupling) and tested how much this could be further applied to real data.

This work was further extended within the STRAUS projet with Philips to develop synthetic image databases for benchmarking image processing tools, and within the ERC MedYMA project.

Chapter 7: Probabilistic Personalisation of Cardiac Electrophysiology

– This chapter is based on [Konukoglu et al., 2011]: Konukoglu, E., Relan, J., Cilingir, U., Menze, B., Chinchapatnam, P., Jadidi, A., Cochet, H., Hocini, M., Delingette, H., Jaïs, P., Haïssaguerre, M., Ayache, N., and Sermesant, M. Efficient probabilistic model personalization integrating uncertainty on data and parameters: Application to Eikonal-diffusion models in cardiac electrophysiology. *Progress in Biophysics and Molecular Biology*, 107 (1):134–146, 2011.

One of the most intrinsic ways to integrate both statistical and biophysical modelling is to formulate the uncertainty directly within the biophysical models, and therefore achieve their personalisation directly in a statistical framework. This was the contribution of this chapter. We used a simpler electrophysiological model (the Eikonal model) and combined two recent methodologies in uncertainty quantification and signal processing: polynomial chaos expansion and compressed sensing. This allowed to explicit a surrogate model for a stochastic version of the Eikonal model, as well as to personalise this model from synthetic and real data in a very efficient manner.

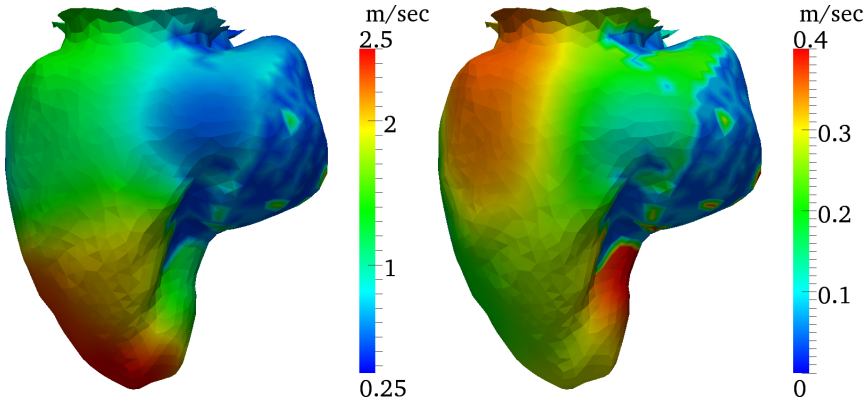

Figure 10: Probabilistic personalisation of a cardiac electrophysiology model, with a mean (left) and standard deviation (right) of the local conductivity.

The idea is to decompose the prior probability distribution of the parameters on a orthonormal basis of polynomials, and express the output of the model as a combination of the same polynomials. The coefficients on this basis being sparse, they can be efficiently estimated through compressed sensing. The for a given set of measurements, the posterior probability distribution of the parameters can be estimated through Monte Carlo sampling on this fast surrogate model.

We chose to use this framework to shed light on a long standing question in cardiac electrophysiology personalisation, which is to evaluate the relative importance of endocardial versus epicardial clinical data for such personalisation. This has important consequences, as it enables to evaluate how much non-invasive body surface potential mapping could replace invasive catheter mapping. The results were very interesting because we could show quantitatively that even if epicardial data knows less about the onset of activation (which happens on the endocardium), it still provides a more reliable estimation of the overall conductivity.

To my knowledge this was among the very first papers to combine polynomial chaos and compressed sensing, and definitely the first on such non linear PDE.

Chapter 8: Coupling Statistics on Shapes with a Reduced Model of Cardiac Flow

– This chapter is based on [Guibert et al., 2013]: Guibert, R., Mcleod, K., Caiazzo, A., Mansi, T., Fernández, M. A., Sermesant, M., Pennec, X., Vignon-Clementel, I., Boudjemline, Y., and Gerbeau, J.-F. Group-wise construction of reduced models for understanding and characterization of pulmonary blood flows from medical images. *Medical Image Analysis*, 18(1):63–82, Oct. 2013.

This article explored a very interesting aspect of combining statistics and biophysics, which is to directly couple the statistics on shapes to the statistics on simulations. It emerged from a collaboration I set up between the Necker paediatric hospital, the Inria REO team and the Inria Asclepios team. The original idea was to see if Computational Fluid Dynamics (CFD) could help in optimising a device to reduce the diameter of the right ventricular outflow tract, in order to be able to subsequently implant a prosthetic valve.

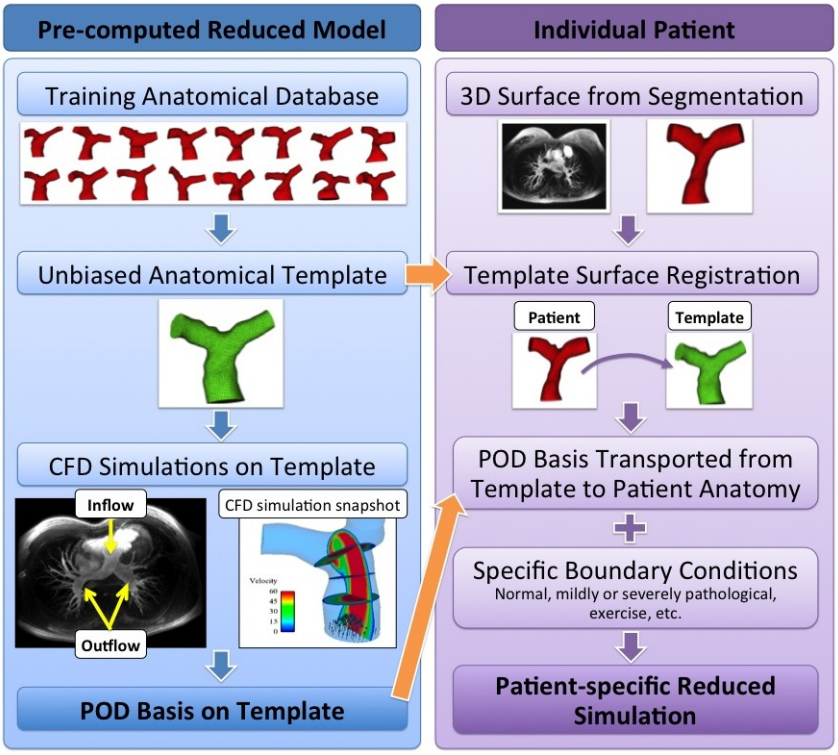

Figure 11: Computation of a reduced model on an atlas (left) and transport to a new patient for simulation (right).

As this has to be done over a patient population, the novel idea presented in this chapter was to run simulations over an average shape, to then compute a reduced model on this anatomy, and finally to transport this reduced model to a new anatomy. By using such an approach, the idea is that the important features of this pathology will be captured by the reduced model, which is simulated on a relevant geometry captured by the template.

It required to integrate two very different areas of mathematics. The two most interesting findings were first the computation of an average CFD simulation on an average shape, which corresponds to a "Shape and CFD" template. Second, we develop a strategy to transport the different modes of the reduced model from the template shape to a patient-specific shape. This transport has to be done carefully, for instance to preserve the divergence-free property of the flow velocity basis.

Chapter 9: Combined Learning and Modelling Approach for Ablation Target Prediction

– This chapter is based on [Cabrera Lozoya, 2015]: Cabrera Lozoya, R. Radiofrequency ablation planning for cardiac arrhythmia treatment using modeling and machine learning approaches. PhD thesis, *Université Nice Sophia Antipolis*, Sept. 2015.

In this chapter we explored another way to integrate statistics (machine learning) and biophysical simulations. This novel approach enriches the features extracted from medical imaging with features derived from personalised biophysical simulations. We demonstrated that such simulation-based features improved the efficacy of machine learning by revealing other aspects of the clinical data for a given patient.

This was applied to the non-invasive pre-intervention generation of a target map for the ablation of ventricular tachycardia. Care was also given to be able to provide a confidence measure in this generated map.

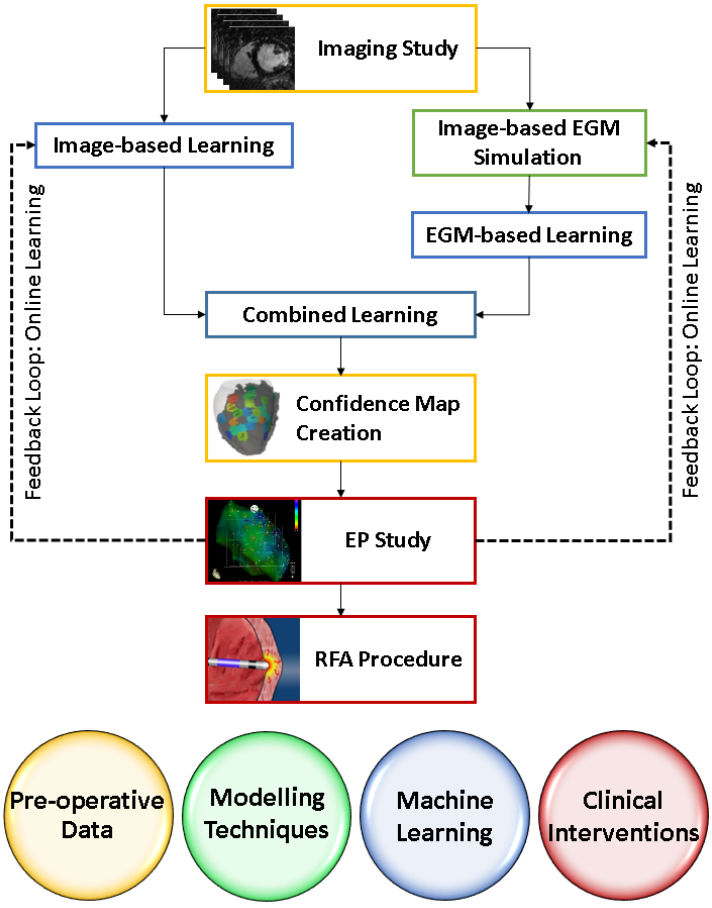

Figure 12: Pipeline presenting how the combination of biophysical modelling and machine learning could be applied to the non-invasive predication of ablation targets.

Different ways of integrating imaging and modelling features were tested. Extensions could include online learning with invasive measurements in order to improve the target map.

This worked opened a new avenue of research which is now a consequential part of my active collaboration with the cardiology, radiology and modelling teams of the IHU Liryc, Bordeaux.

Supervision, Responsibilities & Other Research Activities

Research is really a team work, and these results are definitely a group effort. Over these years I had the chance to supervise great people including 11 PhD students (T. Mansi, J. Relan, K. McLeod, N. Toussaint, D. Lepiller, F. Billet, A. Prakosa, S. Giffard-Roisin, R. Cabrera Lozoya, M.-M. Rohé, R. Molléro), 3 post-docs (P. Chinchapatnam, K. Wong, N. Duchateau) and 7 software engineers (B. Bleuzé, F. Vichot, F. Arslan, L. Cadour, H. Fadil, M. Buckingham, E. Pernod). This has been instrumental in being able to achieve such research.

Collaborations are also crucial outside the team, and I have been lucky to meet great academic, clinical and industrial partners, with whom I have long-standing and fruitful collaborations. Our numerous discussions always helped me in focussing my research on topics that matter, and I learned a lot from them, I cannot list them all here but they appear as co-authors in my publications. These productive interactions resulted in 60 journal articles and 80 conference publications, which are well cited (3600+ citations, h-index: 32, from Google scholar, April 2016). A detailed list of publications can be found in my web page:
https://team.inria.fr/asclepios/team/maxime-sermesant/

This has also led me to be involved in the writing and organisation of several European projects (euHeart, Health-e-Child, VPH NoE, MedYMA, MD-Paedigree, VP2HF) which enabled very fruitful collaborations.

I co-organised several events (FIMH 2009, MICCAI 2012, STACOM workshop since 2010) and it is always a pleasure to contribute in this way to the fertile interactions in the research community of medical imaging and cardiac modelling.

Thanks to the multidisciplinary aspect of my research, I had the pleasure to be invited to give talks in several topics including Mathematics (Domain Decomposition, SIAM Uncertainty Quantification), Radiology (European Society of Cardiovascular Radiology), Cardiology (European Society of Cardiology, Cardiostim), Cardiac Modelling (Cardiac Physiome).

On the technology transfer side, in addition to the industrial collaborations, I participated in two start-up projects: Therapixel for touchless image interaction (http://www.therapixel.com) and inHeart for cardiac interventional guidance (in the process to be created, demonstrated to the French president at the IHUs day: http://ihumeeting.com/home/). It is always very rewarding to see new technology developed in academic research actually helping clinicians in their daily activity.

Conclusion

I present in this manuscript several contributions in supervising research at the interface between biophysical and statistical modelling. Statistical and biophysical approaches have a huge potential in enriching each other and opening new avenues of research. This is an opportunity to create virtuous circles between two very different but complementary approaches. By combining the power of these two visions, we can aim for more robust and realistic combined models able to tackle the challenges of clinical applications.

The remaining of the manuscript is based on published articles that are cited at the beginning of each chapter.

Part I

Patient-Specific Biophysical Models of the Heart

Chapter 1

in vivo Human Cardiac Fibre Architecture Estimation

– This chapter is based on [Toussaint et al., 2013]: Toussaint, N., Stoeck, C. T., Schaeffter, T., Kozerke, S., Sermesant, M., and Batchelor, P. G. In vivo human cardiac fibre architecture estimation using shape-based diffusion tensor processing. *Medical Image Analysis*, 17(8):1243 – 1255, 2013.

1.1 Introduction

Cardiac fibre architecture is fundamental to cardiac function, as it influences the myocardial electrophysiological and mechanical properties. For instance, the electrical propagation is three times faster along the fibre direction than along its orthogonal plane [Kanai and Salama, 1995]. Moreover, cardiac contraction is mainly explained by the arrangement of fibres [Bovendeerd et al., 1992; Anderson et al., 2008]. For these reasons its study can have an important impact on clinical decisions, as several cardiac pathologies – such as myocardial infarction, cardiomyopathy, hypertension or valvular heart diseases – involve a rearrangement of myocardial fibres [Sutton and Sharpe, 2000; Helm et al., 2006].

Diffusion Tensor MRI (DTI) can image non-invasively the fibre orientation distribution of the myocardium [Hsu et al., 1998; Basser et al., 2000; Scollan et al., 2000; Holmes et al., 2000]. Moreover, the intrinsic laminar sheet structure can also be revealed by taking into account the full information given by the tensors [Helm et al., 2005; Peyrat et al., 2007; Lombaert et al., 2011b]. However, translating these techniques to *in vivo* setting is extremely challenging [Sosnovik et al., 2009]. Indeed, the displacements due to diffusion measured in DTI are three orders of magnitude smaller than the bulk motion of the heart, resulting in inaccurate diffusion signal. To tackle this problem, [Reese et al., 1995] introduced a method based on stimulated echo acquisition (STE) where the diffusion signal is integrated over the entire heart beat. Later improved by [Tseng et al., 1999], this approach has been applied in 2D and proven useful for the depiction of clinically relevant information in several scenarios [Dou et al., 2003; Wu et al., 2009; Nielles-Vallespin et al., 2011; Sosnovik et al., 2009]. Alternatively, [Gamper et al., 2007] proposed a method that uses a standard spin echo (SE) technique in order to improve the Signal to Noise Ratio (SNR) efficiency. By means of bipolar gradient lobes, this technique only remains sensitive to acceleration and higher order motion, and enables the acquisition of 2D diffusion images. These techniques remain challenging to apply in practice. Due to time constraints, the amount of slices acquired is very limited and the SNR performances can be poor. It is therefore of interest to investigate and adapt the analysis and post-processing procedures to such specific situation.

In this chapter, we propose to use a coordinate system known as Prolate Spheroidal in order to generate a curvilinear scheme for data analysis and dense approximation of the fibre architecture of the Left Ventricle (LV).

The contributions of this work are two-fold: first a conformal mapping method that allow the description of acquired tensor data in the LV wall into a normalised Prolate Spheroidal (PS) frame is introduced, using non-linear registration and coordinate change. Second, a dense approximation scheme in this PS frame is proposed, using a trivariate kernel regression in order to approximate tensors at all locations in the LV from sparsely acquired data. It is demonstrated that using PS coordinates allows meaningful interpretation of data in the LV, in particular the orientation of the underlying fibres. Moreover, it is shown that changing the coordinate system from Cartesian to PS leads to better overall approximation of the global tensor field. These techniques are tested on a high resolution *ex vivo* DTI dataset, and applied to a set of *in vivo* data acquired on 5 healthy volunteers.

1.2 Material and Methods

1.2.1 *Ex Vivo* High Resolution Cardiac DTI Dataset

A DTI dataset of a healthy human myocardium was downloaded from the John Hopkins University website[1]. It was provided by Prof. Patrick A. Helm and Raimond L. Winslow at the Center for Cardiovascular Bioinformatics and Modeling and Prof. Elliot McVeigh at the National Institute of Health. Data was acquired in a 1.5T GE CV/I MRI Scanner (General Electrics Medical System), with a spatial resolution of $0.4297 \times 0.4297 \times 1.0$ mm^3.

1.2.2 *In Vivo* Cardiac DTI Acquisition

Cardiac DTI was performed on 5 healthy subjects (2 males, 3 females) on a 1.5T clinical MR scanner (Philips Healthcare, Best, The Netherlands) equipped with a gradient system with maximal strength of 80mT/m and a slew rate of 100mT/m/ms per axis. A 32 channel cardiac coil array was used for signal reception. The imaging protocol consisted of a B0 map for image based shimming [Schär et al., 2004], a trigger delay scout sequence for estimation of optimal trigger points during systolic contraction [Stoeck et al., 2011], the actual DTI acquisition and a single breath hold 3D T2 contrast enhanced whole heart acquisition. All sequences were ECG-triggered, and Diffusion Weighted Images (DWIs) were acquired during free breathing using a respiratory navigator, with a gating window of 5mm, placed on the right hemidiaphragm. DTI acquisition was planned in short axis view of the heart and 4-6 parallel slices were acquired along the long axis of the LV. Imaging was performed using a diffusion weighted spin echo sequence with single shot echo planar imaging (EPI) readout (see Fig. 1.1). Imaging parameters were as follows: Echo Time (TE)/Repetition Time (TR) 59ms / 2R-R intervals, Field Of View (FOV): 230×102 mm^2, in-plane resolution: 2×2 mm^2, slice thickness: 5 mm. The Diffusion Weighted MR sequence is illustrated in Fig. 1.1.

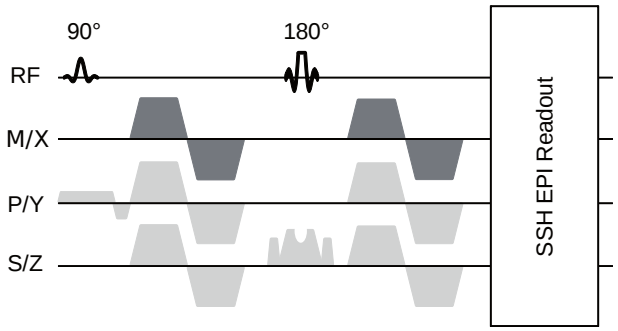

Figure 1.1: DTI spin echo pulse sequence with single shot EPI readout. Diffusion encoding is established with a pair of velocity compensating bipolar gradients. For local look imaging, the excitation pulse is applied in phase encoding direction, while the echo pulse remains in slice-select direction. The echo pulse duration is shortened using VERSE.

[1] http://www.ccbm.jhu.edu/research/DTMRIDS.php

In order to operate with a single DTI acquisition protocol in all volunteers, a TR of two R-R intervals was chosen to assure a sufficiently high SNR of each single shot DWI. Readout and echo time was shortened by using a rectangular FOV (local-look), applying the excitation pulse in phase encoding direction and the refocusing pulse in slice-select direction [Gamper et al., 2007]. Furthermore a partial Fourier coefficient of 0.63 was used and the echo pulse duration was further shortened by applying the variable rate selective excitation (VERSE) technique [Hargreaves et al., 2004]. Diffusion encoding was achieved by two bipolar gradients [Dou et al., 2003] applied in 18 directions distributed on the unit sphere, creating a b-value of $500 s/mm^2$. Ten averages were acquired for each diffusion encoding direction. The total scan time was 10 to 15 minutes per DTI slice, depending on navigator efficiency.

Diffusion imaging was followed by a 3D whole heart acquisition using a T2 contrast prepared multi-shot gradient echo sequence with a resolution of $2 \times 2 \times 4$ mm^3. The trigger delay of the whole heart acquisition was set identical to the trigger delay of the diffusion weighted imaging.

Despite the respiratory navigation, residual misalignments, of the order of 2-3 mm, can occur between DWIs. This is corrected prior to averaging per direction using an approach very similar to the one detailed in [Oubel et al., 2012]: each DWI S_i is rigidly registered to an arbitrary chosen reference image S_r^k, using the Mutual Information similarity metric, resulting in a rigid transformation A_i^k. The mean diffusion image between all transformed S_i is computed and serves as a reference S_r^{k+1} for the following registration iteration. In this $(k+1)$ iteration, the transformations A_i^k are used as initialisation for the registration algorithm, therefore avoiding successive resampling of the initial DWIs S_i. The operation is repeated until the mean square error (MSE) between two consecutive iterations is lower than a small threshold ϵ: $MSE(S_r^{k+1}, S_r^k) < \epsilon$. In practice five iterations were sufficient for convergence.

Tensors were reconstructed in each voxel by solving the Stejskal-Tanner's diffusion equation system [Stejskal and Tanner, 1965] using linear regression as described in [Basser et al., 1994]. Only tensors lying within the LV compact myocardium were considered for further processing. Illustrations of the acquisitions are presented in Fig. 1.2.

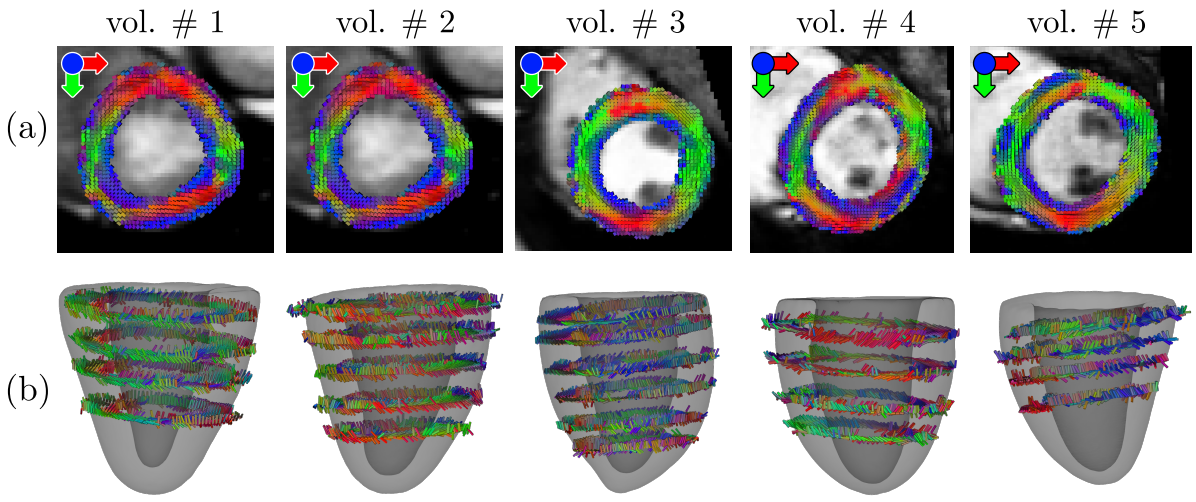

Figure 1.2: Acquired volunteer data. (a) One slice of Diffusion Tensors. Tensors are colour-coded according to the direction of their main eigenvector, i.e. red: horizontal / green: vertical / blue: through-plane. (b) Distribution of the slices for each volunteer, super-imposed onto the Left Ventricle (LV) segmentation.

1.2.3 Conformal Mapping of Left Ventricular Data

In this section we describe a method to represent DTI information contained in the LV wall into a common reference frame. This is achieved with the use of the PS curvilinear coordinate system. It involves a non-linear registration of the LV wall onto a truncated ellipsoid, and a change of coordinate.

Prolate Spheroidal Coordinates

The LV wall is a relatively thin and non-convex structure with a shape close to an ellipsoid. The PS coordinates are well adapted to such an object, and have the advantage to be physiologically meaningful with respect to the ventricular shape and fibre architecture [Nielsen et al., 1991; Costa et al., 1996; LeGrice et al., 2001; Rohmer and Gullberg, 2006].

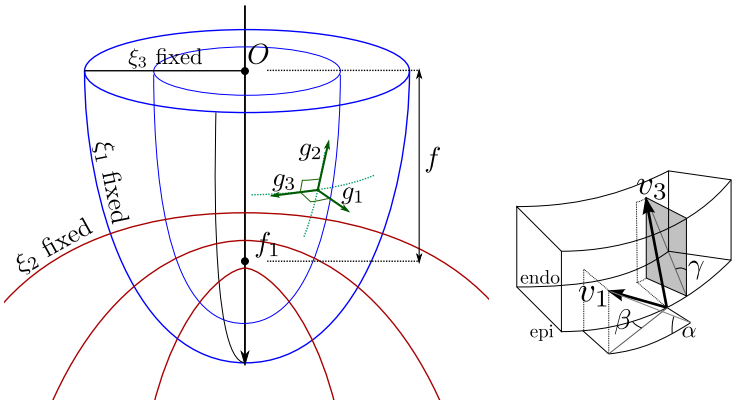

Figure 1.3: Left: PS coordinate system depends on an arbitrary ellipsoid centre and semi-foci distance. The iso-lines of constant coordinates are drawn to illustrate its relevance for the ventricular shape. Right: definition of helix (α), transverse (β) and sheet (γ) angles with respect to the tensor's first (v_1) and third (v_3) eigenvectors.

The transformation operator from Cartesian coordinates $x = (x_1, x_2, x_3)^T$ to PS coordinates $\xi = (\xi_1, \xi_2, \xi_3)^T$ is denoted $\Psi : x \to \xi = \Psi(x)$. However, it is more commonly given in its inverse form Ψ^{-1}:

$$\begin{cases} x_1 &= f \sinh(\xi_1) \sin(\xi_2) \cos(\xi_3) \\ x_2 &= f \sinh(\xi_1) \sin(\xi_2) \sin(\xi_3) \\ x_3 &= f \cosh(\xi_1) \cos(\xi_2) \end{cases} \tag{1.1}$$

where f is the semi-foci distance.

The first coordinate ξ_1 is strictly positive and can be interpreted as the transmural depth, ξ_2 as the long axis abscissa going from 0 at the apex to $\sim \pi/2$ at base level, and ξ_3 as a circumferential abscissa from 0 to 2π. In the common Cartesian system, the contravariant basis is stationary in $\mathbb{R}^3$. The PS equivalent, here denoted $\mathcal{G} = (g_1, g_2, g_3)$ (where $g_i = \frac{\partial x}{\partial \xi_i}$) varies in space, following the natural shape of the ventricle (see 1.B for explicit expression of contravariant vectors).

PS coordinates have the advantage of describing the highly non-convex volume of the ventricle walls as a parallelogram, as shown in Fig. 1.4. In the PS frame, the shortest path from two distinct points of the ventricle remains in the ventricle. Therefore, a metric defined in this frame becomes *geodesically convex*.

Diffeomorphic Registration

In order to ensure that the curvilinear coordinate system follows the shape of the anatomical LV, the imaged ventricle has to be registered to a perfectly shaped truncated ellipsoid volume. The source and target images S and T of this registration step are respectively the binary mask of the segmented LV and the binary mask of a corresponding approximated truncated ellipsoid volume. Fig. 1.5 shows a superposition of delineations of the masks S and T onto the anatomical image. S is obtained by manual segmentation of the myocardium using the 3D anatomical image. The volumetric truncated ellipsoid T was computed as the closest to the segmentation S, using the centre of mass and main axis of symmetry of S.

The non-linear algorithm used to register S to T is the symmetric version of the log-domain diffeomorphic demons [Dru and Vercauteren, 2009]. This algorithm has the crucial characteristic to provide invertible displacement fields, needed to produce forward and backward transformation

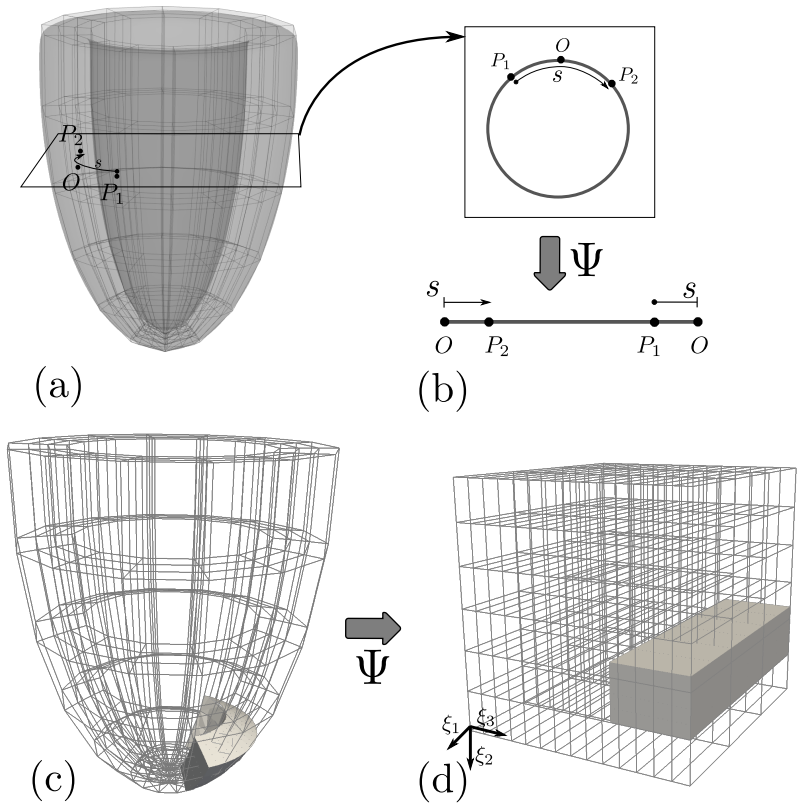

Figure 1.4: (a,b): A short axis circle drawn in the Cartesian space (a) is represented as a segment in the Prolate Spheroidal (PS) frame (b). ξ_3 being defined with a modulo, the segment is reproduced at infinity on both sides, and the barycentre of P1 and P2 remains O. (c,d): A left ventricle volume is non convex in a Cartesian frame (c) whereas the same volume expressed in a PS frame becomes a convex box (d).

between the subject's anatomy and the volumetric truncated ellipsoid. Transformations are respectively denoted Φ and Φ^{-1}. Additionally, the displacement was constrained to be elastic (but yet compressible) as described in [Mansi et al., 2011a], in order to obtain a smooth displacement of the middle-wall area, where no texture is present in the masks to guide registration. This technique provides forward and backward transformations between the volunteer's anatomy and a volumetric truncated ellipsoid.

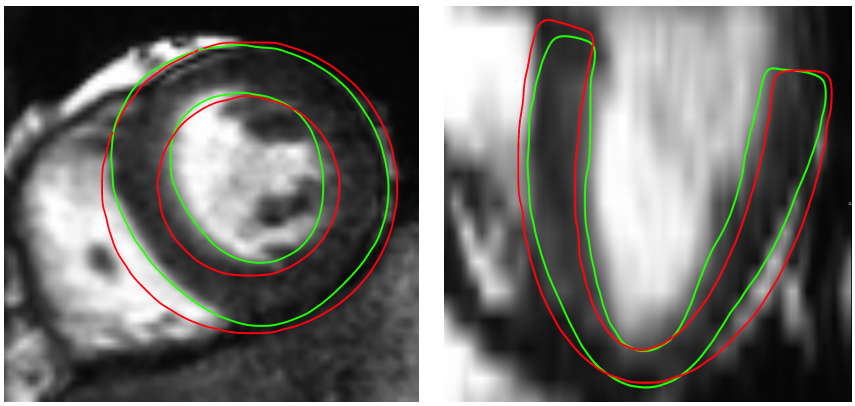

Figure 1.5: Binary mask S of the acquired left ventricle (in green) obtained by manual segmentation. From the centre of mass and main axis of revolution of S is derived the closest volumetric truncated ellipsoid mask T (in red).

Transformation Workflow

Once the LV of the subject is transformed onto the perfectly shaped truncated ellipsoid volume T using transformation Φ, the operator Ψ can be used to express this information in PS coordinates. Transformation from Cartesian to PS coordinates is defined by inverting the system in Eq. 1.1. Details of the inversion are given in 1.A. The overall transformation process towards a common PS frame can be summarised as follows:

$$\xi = \Psi \circ \Phi(x) \tag{1.2}$$

The operators Φ and Ψ are fully invertible, apart from the singularity segment (see 1.A). As a consequence, it is possible to transform any LV input data into the PS frame, process it in a well adapted coordinate system, and transform it back to the anatomical referential.

The global transformation process of this conformal mapping is illustrated in Fig. 1.6. The anatomical left ventricular wall volume Ω is transformed to the convex box Ω'' that is the PS frame. A natural path lying within the LV wall (dotted lines in Ω) becomes a straight line in Ω''. Therefore, any process, such as interpolation or geodesic distance definition, described in PS frame will follow the natural shape of the LV.

Extension to Tensors In our work, the type of data under consideration is not scalar but consists of tensors. Adjustments to the transformation operators Φ and Ψ are needed in order to account for that increased data dimensionality. Let us denote $\tilde{\Phi}$ the *induced* transformation from Φ on tensors. Transforming the diffusion tensors implies a reorientation scheme using the Jacobian $\mathcal{J}_{\Phi^{-1}}$ (in our case directly available from Φ^{-1}). In [Peyrat et al., 2007], two different reorientation strategies are compared: The Finite Strain (FS) method separates the deformation in a rigid rotation and a pure deformation one, and only applies the rotation $\hat{\mathcal{J}}_{\Phi^{-1}}$ to the tensor. The Preservation of Principal Direction (PPD) method takes the full Jacobian to reorient the tensor. The study concludes that FS is best suited for preserving the geometrical properties of diffusion tensors in this context. The FS strategy was chosen for this reason and its computational efficiency.

Similarly, extending the change of coordinate to tensors requires the *induced* transformation of the operator Ψ. The Jacobian of Ψ corresponds to the contravariant basis $\mathcal{G}$ (Eq. 1.11). This matrix is orthogonal by definition (PS coordinates is an orthogonal coordinate system), but not orthonormal. The norm of the contravariant vectors correspond to the scale factors of the coordinate system, which are the local derivatives $h_i = \partial x / \partial \xi_i$ (see 1.B). In our setting, the domain of definition is a volumetric ellipsoid Ω', and factors h_i vary spatially within the domain. In particular, they decrease with the distance to the long-axis. Therefore, taking the full Jacobian of Ψ to reorient the tensors and performing interpolation in the PS frame would privilege tensors of endocardial regions against epicardial ones, which is not desirable. For this reason, only the rotational component of $\tilde{\Psi}$ is used: let us denote $\hat{\mathcal{G}}$ the matrix constructed from the normalised column vectors of $\mathcal{G}$, using the scale factors h_i. Recalling that $\mathcal{G}$ is direct and orthogonal, $\hat{\mathcal{G}}$ has therefore by construction a determinant equal to 1. Equation 1.2 is rewritten with the induced transformations on tensors:

$$\begin{gathered} \xi = \Psi \circ \Phi(x) \text{ and } D_\xi = \tilde{\Psi} \circ \tilde{\Phi}(D_x) \\ \text{with : } \begin{cases} \tilde{\Phi} : D \to \tilde{\Phi}(D) = \hat{\mathcal{J}}^T_{\Phi^{-1}}.D.\hat{\mathcal{J}}_{\Phi^{-1}} \\ \tilde{\Psi} : D \to \tilde{\Psi}(D) = \hat{\mathcal{G}}^T.D.\hat{\mathcal{G}} \end{cases} \end{gathered} \tag{1.3}$$

The induced transformations $\tilde{\Phi}$ and $\tilde{\Psi}$ both represent the finite strain transformations of tensors under Φ and Ψ.

Normalisation of the PS frame For any PS position ξ, the third component ξ_3 is defined between 0 and 2π. The 0 position is imposed to be the intersection between the anterior wall and the Right Ventricle (RV). Similarly, the second component ξ_2 is normalised by construction between 0 at the apex and ξ_2^{base} at the basal region. The value ξ_2^{base} depends on where the base was in the manual segmentation S. The first component ξ_1, on the other hand, is not naturally normalised as it varies as a hyperbolic cosine. The upper and lower limit values of ξ_1 depend on both the radius of the LV and its thickness.

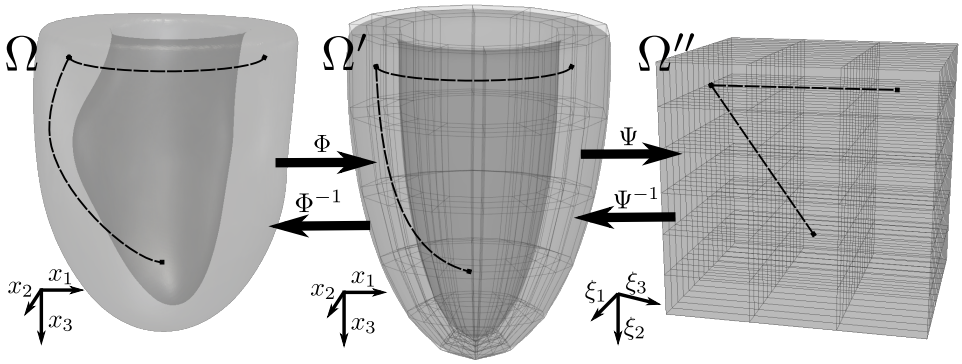

Figure 1.6: Data transformation throughout the procedure. The anatomical LV (Ω) is registered onto a truncated volumetric semi-ellipsoid (Ω') with the displacement field Φ. The change of coordinate system from Cartesian to PS is performed with the operator Ψ, which results in a convex representation of the ventricular volume (Ω'').

Data Accumulation The transformation scheme presented in Eq. 1.3 can be applied to DTI datasets of several subjects. All resulting sets of data are then described in a singular normalised PS frame, and can be combined in order to perform comprehensive groupwise analysis. This combination of data sets will further be referred to as $\mathcal{A}$. As DTI tensors are expressed in the PS contravariant basis $\mathcal{G}$, it becomes straightforward to derive meaningful information such as a measure of deviation of their main eigenvector from circumferential direction (projection on g_3). Circumferential, transmural and apico-basal variations of any information also become straightforward to express given the definition of the coordinate system.

1.2.4 Kernel-Based DTI Dense Approximation from Sparse Data

In this section the approximation of a dense 3D tensor field from a set of sparse DTI measurements distributed across the ventricle is considered. Considering an input set P of M measured positions (or centres) and tensors $P = (X_i, D_{X_i})_{i \in M}$, the approximation operator $\mathcal{W}_P$ is defined over a domain Σ (e.g. covering the ventricular wall volume), that describes how to recover data at position X from noisy and scattered input data:

$$\forall X \in \Sigma,\ D_X := \mathcal{W}_P(X) \tag{1.4}$$

where Σ refers to the spatial target domain where samples are needed. It can be of lower or higher cardinality than P and may not be necessarily defined on a regular grid nor constrained within the convex hull of P. Solutions to approximate missing data and data fitting have been explored in the past. For instance, in [Fillard et al., 2005], the authors used Radial Basis Functions (RBFs) in order to find a smooth solution for $\mathcal{W}_P$ that satisfies the interpolant constraint. However, because input data can be corrupted by significant noise, we intentionally chose not to satisfy the interpolation condition. That is, the *approximation* operator (or quasi-interpolant) was considered rather than a rigorous *interpolation* operator. An interpolation operator gives back the input data at measure points (i.e. $\mathcal{W}_P(X_i) = D_{X_i}$), whereas a quasi-interpolant can approximate results ($\mathcal{W}_P(X_i) \neq D_{X_i}$). Methods to regularise noise corrupted tensor fields have been proposed in the literature [Fillard et al., 2007; Frindel et al., 2009]. In the present method the regularisation is integrated into the approximation operator: the operator $\mathcal{W}_P$ consists of taking a weighted mean of surrounding tensors as an estimate. To avoid swelling effect on tensors and to address the fact that the spatial density of P can be low in the practical case, the mean in the log-Euclidean sense [Arsigny et al., 2006] was used. Other metrics meeting those requirements could be used, such as in [Yang et al., 2012] for instance, where a tensor is described by its eigenvalues and orientation features. The approximation operator is therefore

written as follows:

$$\mathcal{W}_P : X \to \mathcal{W}_P(X) = \exp\left(\frac{\sum_{i=1}^{N} K(X - X_i)\log(D_{X_i})}{\sum_{i=1}^{N} K(X - X_i)}\right) \tag{1.5}$$

K is a vector to scalar kernel ($\mathbb{R}^3 \to \mathbb{R}$). In our setting, K is trivariate and not necessarily isotropic:

$$K_H : dX \to K_H(dX) = \det(H)^{-1} k\left(\sqrt{dX^T H^{-2} dX}\right)$$

where H is a 3×3 diagonal matrix that needs to be optimised [Härdle and Marron, 1985]. The function k is a given univariate kernel function. In this work, the Normal Gaussian function was chosen for k: $k(s) = (2\pi)^{-1/2} \exp(-s^2/2)$. Diagonal values of H therefore control the smoothness of the resulting approximation in the considered coordinate frame.

The approximation operator in Eq. 1.5 is applied on the set of acquired data centres $P'' = (\xi, D_\xi)$ in the PS frame, therefore enforcing spacial coherence independently in each of the main directions of the heart anatomy (e.g. radial, longitudinal and circumferential in PS coordinates). It is important to note that $\Psi \circ \Phi$ also needs to be applied to each position x of the target domain Ω where estimates are needed. Each resulting estimate $\mathcal{W}_P(\xi)$ is eventually transformed back to Cartesian coordinates and warped back to the initial geometry using inverse transformation operators Ψ^{-1} and Φ^{-1}. The global transformation process is summarised in Fig. 1.7, and the approximation operator can be written as:

$$\mathcal{W}_P(x) = \Phi^{-1} \circ \Psi^{-1} \circ \mathcal{W}_P(\xi) \tag{1.6}$$

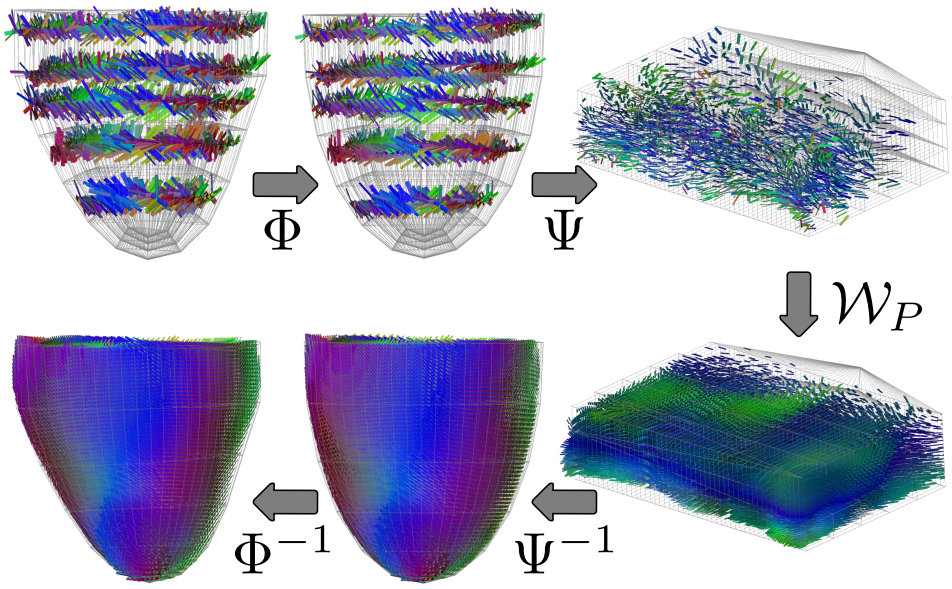

Figure 1.7: This chart illustrates the global workflow, for one dataset, from a set of DTI slices towards the full ventricular approximated tensor field. All operators are fully invertible and diffeomorphic, apart from $\mathcal{W}_P$.

1.3 Experiments and Results

1.3.1 *In-Vivo* Group-wise Analysis

In this experiment the conformal mapping as detailed in Sec. 1.2.3 was applied to the set of *in-vivo* DTI data obtained healthy volunteers (see Sec. 1.2.2) in order to extract meaningful fibre

orientation information. Transformations in Eq. 1.3 were applied to each of the subject datasets. The log-demons registration parameters were as follows: the velocity field diffusion-like regularisation σ was 2.5 mm, the Poisson ratio κ controlling the degree of global elasticity was $\kappa = 0.8$ (Eq. 9 in [Mansi et al., 2011a]), and the number of iterations in the multi-resolution scheme was $15 \times 10 \times 5$. Transformations resulted in a combined dataset $\mathcal{A}$ containing 18350 data centres expressed in the PS frame. Coherency between ellipsoids was ensured by imposing that the plane $(\xi_3 = 0)$ coincides with the junction between the LV and the RV at the anterior wall region. Boundaries of the first component ξ_1 were measured in each dataset, obtaining the following limits: $[0.35 \pm 0.02 \sim 0.55 \pm 0.03]$. The basal upper bound of ξ_2 was also measured (ξ_2^{base}), obtaining a value of $107\,\mathrm{deg} \pm 4$. A normalisation of the first and second components ξ_1 was therefore applied to $\mathcal{A}$, with a target range corresponding to the mean of the measured limits. Figure 1.8 presents the accumulated dataset $\mathcal{A}$. As $\mathcal{A}$ is expressed in PS coordinates, it is not convenient to visualise in this form. The operator Ψ^{-1} was therefore applied in order to transform $\mathcal{A}$ back to Cartesian coordinates, where it is then contained in the truncated ellipsoid Ω'. This figure shows an overall good coverage of the ventricle. As predicted, the area close to the apex is poorly populated due to the challenge of the acquisition in this part of the LV. The non-linear motion involved in this region makes the acquisitions not representative of the actual anatomical fibre structure.

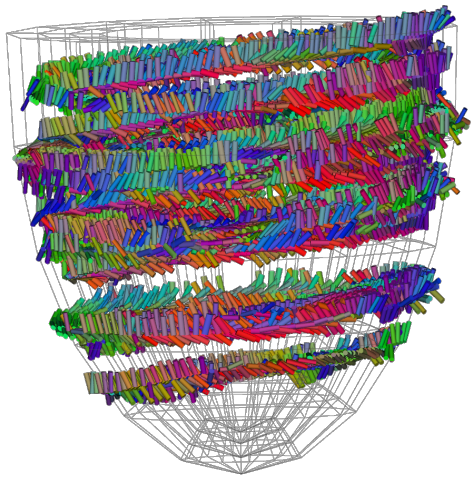

Figure 1.8: All volunteers data was registered and mapped to a common PS frame. This illustration shows the accumulation of the datasets (denoted $\mathcal{A}$) in the template truncated ellipsoid volume. Tensors are shown as segments pointing to their first eigenvectors. The total amount of slices was 23 and the total amount of data centres was 18350.

Three different angles of interest were then extracted from the acquired *in vivo* tensors of $\mathcal{A}$. As described in Fig. 1.3, the helix angle, denoted α, is the signed angle between the tensor's main eigenvector v_1 and the transmural short axis plane (g_1, g_3). Its variation with respect to the transmural depth (ξ_1) is of particular interest as it follows a recognisable pattern on healthy subjects as depicted *ex vivo* [Scollan et al., 2000; Lombaert et al., 2011a]. The transmural angle β is the signed angle between v_1 and the wall surface (g_2, g_3). The laminar structure of the myocardial fibres can also be described by the DTI information [Helm et al., 2005]. The plane defined by the vectors v_1 and v_2 is believed to be parallel to the underlying laminar sheet [Kung et al., 2011b]. The sheet angle γ is defined as the signed angle between v_3 and the wall surface (g_2, g_3). A high absolute value of γ implies that the local laminar sheet is close to be parallel to the wall surface. These projections were directly available as the tensors D_ξ are already expressed with respect to the PS contravariant basis $\mathcal{G}$. Using the PS expression of the diffusion tensors, these angles are mathematically defined as follows:

$$\begin{cases} \alpha = \arcsin(v_1, g_2) \\ \beta = \arcsin(v_1, g_1) \\ \gamma = \arcsin(v_3, g_1) \end{cases} \tag{1.7}$$

Joint histograms of the helix, transverse and sheet angles of population gathered in $\mathcal{A}$ with respect to the transmural depth ξ_1 are presented in Fig. 1.9. The helix angle α was found to vary between $+55\,\mathrm{deg}$ at the endocardium to $-30\,\mathrm{deg}$ at the epicardium, with a correlation coefficient of 0.581. The transverse angle β was found stable along the transmural depth with a mean equal to 0, and has a consequently low correlation coefficient of 0.260. The sheet angle γ was poorly correlated with the transmural depth, with a coefficient of 0.012.

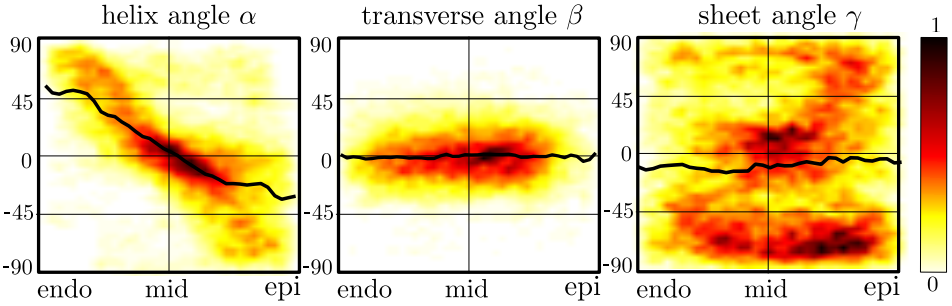

Figure 1.9: Joint histograms of respectively the helix α, transverse β, and sheet γ angles with respect to the transmural depth. Angles were derived from the projections of the tensors D_ξ onto the Prolate contravariant basis. The helix angle shows a variation between $+55\,\mathrm{deg}$ at the endocardium to $-30\,\mathrm{deg}$ at the epicardium.

1.3.2 Dense Approximation: Parameters Estimation

In this experiment the dense approximation scheme detailed in Sec. 1.2.4 was evaluated on an high resolution *ex vivo* human DTI dataset (see Sec. 1.2.1. The approximation operator depends on a 3×3 diagonal matrix H that describes the shape of the trivariate kernel K_H used in the approximation operator $\mathcal{W}_P$. This experiment aims at finding the optimal kernel width H_{opt} to use depending on two acquisition parameters: the density of slices and the amount of noise in the data. This optimisation was achieved by minimising the discrepancy between measured tensor data D_{X_i} and corresponding estimate $\mathcal{W}_P(X_i)$, while keeping a certain degree of smoothness.

In order to simulate a sparse distribution of acquired slices, it was hypothesised that a typical *in vivo* cardiac DTI acquisition would consist of a limited amount of short axis (SA) slices with a certain degree of noise. Furthermore, these slices are usually constrained to the equatorial part of the ventricle as motion pattern and partial volume effects around the apex hamper acquisition of images with sufficient quality. In consequence, N SA equatorial slices from the *ex vivo* dataset were extracted while avoiding the apex and base boundaries, as shown in Fig. 1.10.

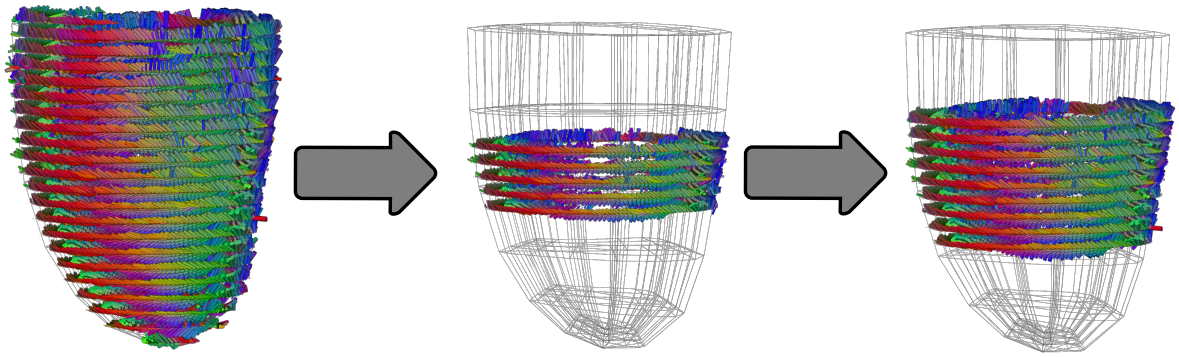

Figure 1.10: Reference tensor field was down-sampled and reoriented to obtain a voxel size of $2\times2\times4mm$ in a short axis slice orientation (left). The number of slices N was varied to simulate different *in vivo* acquisition situations.

In order to simulate noise in the data, each of the N slices was then transformed to a series of 6 DWIs, using the L_2 norm over the tensors as a baseline image and 6 non-collinear gradient

orientations uniformly distributed on the sphere. Complex Rician noise [Gudbjartsson and Patz, 2005] of variance V was added to the DWIs, before tensor re-estimation.

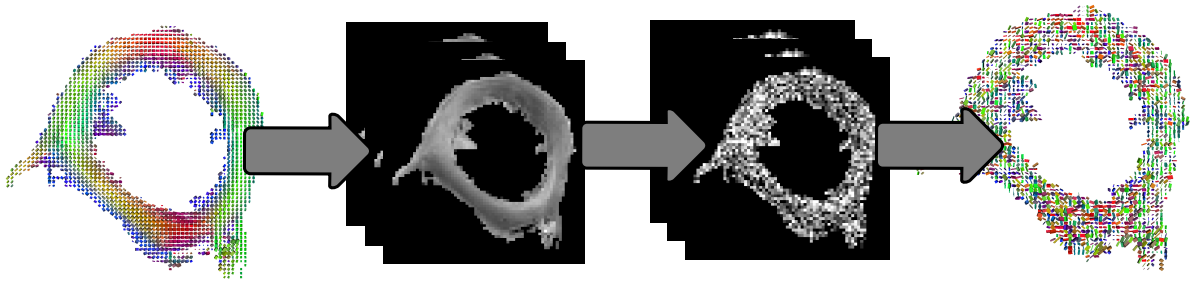

Figure 1.11: 6 Diffusion Weighted Images (DWIs) were artificially computed from the reference tensor field. Each DWI was corrupted by additive Rician noise, and the tensor field was then estimated. The variance of the added Rician noise in this example was $V = 0.04$ for each DWI, which results in an SNR of 10.0.

The resulting noisy DTI slices were then used as input data for the approximation scheme detailed in Sec. 1.2.4 and the full ventricular tensor field was computed. The output was compared to the true tensor field in a voxel-wise manner. A similarity measure was used to optimise matrix H_{opt}, as a trade-off over the entire ventricle domain Ω between a Least Square (LS) term that describes the data fit and a smoothness term (Reg):

$$H_{opt} = \underset{H \in Diag(3)}{\operatorname{argmin}} \; LS(H) + \lambda \cdot Reg(H),$$
$$\text{with} \begin{cases} LS(H) & = \sum_* dist\left(D_*, \mathcal{W}_P(*)\right)^2 \\ Reg(H) & = \sum_* \parallel \partial \mathcal{W}_P(*) \parallel^2 \end{cases} \tag{1.8}$$

where $*$ refers to $x \in \Omega$ in Cartesian coordinates or $\xi \in \Omega''$ in PS coordinates, and λ to the scalar controlling the influence of the regularisation. Among different existing similarity measures between tensors (named $dist$ in the formula), the Log-Euclidean metric distance [Arsigny et al., 2006] was chosen. That is, the Frobenius norm of the matrix-log difference: $dist(A, B) = \parallel \log(A) - \log(B) \parallel$. The smoothness term (or regularisation term) can be seen as an equivalent of the total variation of the tensor field, i.e. the squared norm of the tensor field gradient in the log domain: $\partial \mathcal{W}_P(*) = \nabla \log(\mathcal{W}_P(*))$. The parameter space of this minimisation problem therefore only consists of the three diagonal elements of the bandwidth matrix H. The minimisation of Eq. 1.8 was performed using a gradient-free multivariate optimisation scheme [Powell, 2008].

The regularisation parameter λ controls the influence of the tensor field smoothness in the estimation of the optimal matrix H_{opt}. A common technique used to choose its value is the L-curve method as described in [Hansen, 1992]. The L-curve was computed, as well as its curvature for the set of variables ($N = 7$, $SNR = 10$) in order to find a suitable value for λ. The curvature of the L-curve was found almost constant. However, it indicated an inflexion point at $\lambda \sim 0.05 - 0.1$. The constant curvature might be explained by the fact that the system we try to solve is non-linear and does not correspond to a Tikhonov regularisation problem, as opposed to the system described in [Hansen, 1992].A value of $\lambda = 0.1$ was therefore used for all optimisation results described in this experiment.

For a better comprehension of the noise levels, the Signal to Noise Ratio (SNR) of the noisy DWIs was computed. A region of interest R was drawn in the exterior wall of one of the DWIs. Then the SNR was calculated as follows: $\text{SNR} = mean(R)/std(R)$. For instance, the reference *ex vivo* dataset used as a ground truth has a value of $\text{SNR}_0 = 36$.

The optimisation of the diagonal matrix H was performed for different case scenarios of values of N and values of SNR_V. The remaining residual error between the reference tensor field and the approximated one was computed. The error corresponds to the angle difference between main eigenvectors of the reference and the approximated tensor, denoted ε, in a voxel-wise manner. If ε is considered as a random variable, then it can be seen as the combination of two independent random

variables that are the polar angular errors ε_1 and ε_2. To be calculated, those polar angular errors need the definition of two arbitrary planes going through the reference tensor's first eigenvector v_{1_r}, then ε_1 and ε_2 are the respective (signed) projections of the approximated tensor's first eigenvector v_{1_a} onto each of the planes, as shown in Fig. 1.12. Spherical trigonometry therefore infers that ε follows the distribution of $\arccos(\cos\varepsilon_1 \cdot \cos\varepsilon_2)$. An example of such distribution is simulated in Fig. 1.12. In this simulation ε_1 and ε_2 are chosen to have a zero-mean Gaussian distribution. The distribution of ε was calculated (shown in red in Fig. 1.12), it has a strongly skewed shape. The value of the mode (or peak) is therefore a good indicator of the most probable angular error, and of the performance of the approximation scheme.

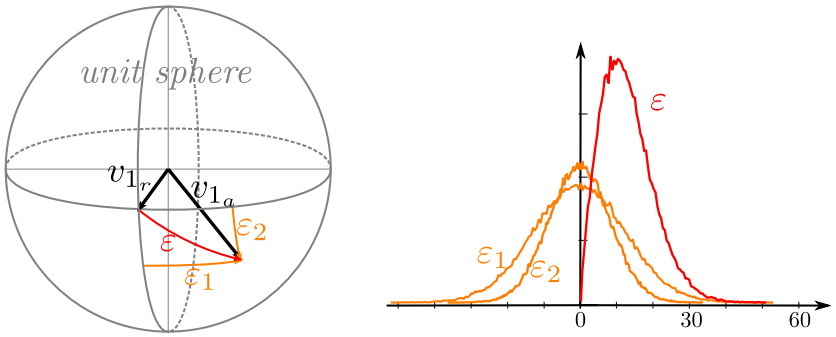

(a) Angular error ε as a combination of polar angles

(b) Corresponding statistical distributions

Figure 1.12: (a) Residual error ε due to the approximation scheme on the angle between the approximated tensor's first eigenvector v_{1_a} and that of the reference tensor v_{1_r}. ε can be seen as a combination of two independent polar signed angles ε_1 and ε_2. (b) If ε_1 and ε_2 have a zero-mean Gaussian distribution, then the distribution of ε is strongly skewed, and depends on the standard deviations of the polar angle errors.

Mode value of the residual error ε are reported in Fig. 1.13(a). The two graphs show this mode value as a function of both the number of slices N and the SNR of the DWIs, when using Cartesian coordinates (left) and PS coordinates (right) for the approximation scheme. For instance, for the case scenario (N=7, SNR=10), mode values of $11.5\,\mathrm{deg}$ and $8.3\,\mathrm{deg}$ were found (grey and black dots in the figure). The corresponding values for the bandwidth matrix were $H_{opt}^{cart} = \mathrm{diag}(3.3, 3.3, 5.9)$ (in mm) and $H_{opt}^{prol} = \mathrm{diag}(0.009,\ 0.20,\ 0.31)$.

To visually evaluate the spatial distribution of the residual approximation error, we present in Fig. 1.13(b) the local distributions of ε along the ventricle for the specific case of (N=7, SNR=10). The grey rectangles represent the location of the 7 input noisy DTI slices.

Additionally, fibre tractography was performed using the approximated dense tensor fields resulting from Cartesian and PS coordinates approaches in order to visually assess the impact of using the PS frame for interpolation. Fibres were tracked in a voxel-wise manner using a propagation term as described in [Fillard and Gerig, 2003], using an advection-diffusion propagation term derived from [Weinstein et al., 1999]. Fibre tractography results are presented in Fig. 1.14. For comparison, tractography was also applied to the initial fully sampled tensor field.

1.3.3 *In-Vivo* Fibre Tractography Results

In this section, the dense approximation scheme was applied to each 5 individual *in vivo* datasets separately, and to the accumulated dataset $\mathcal{A}$, using optimal parameters H_{opt} as found in Sec. 1.3.2, in order to visually assess the resulting dense fibre orientations.

In order to choose adequate optimal bandwidth matrix for the dense approximation, the SNR and the ventricle coverage of the *in vivo* acquisitions were measured. The mean SNR was 10 and the mean ventricle coverage was of 40%. These measures were reported on the graphs in Fig. 1.13(a) (grey and black dots) and the corresponding diagonal values of H_{opt} were chosen for the dense approximation. The approximation scheme was then applied to each of the subject's datasets

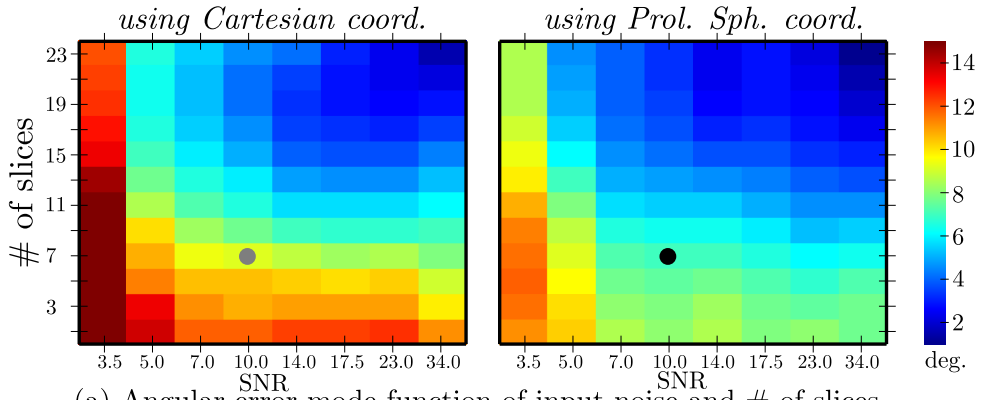

(a) Angular error mode function of input noise and # of slices

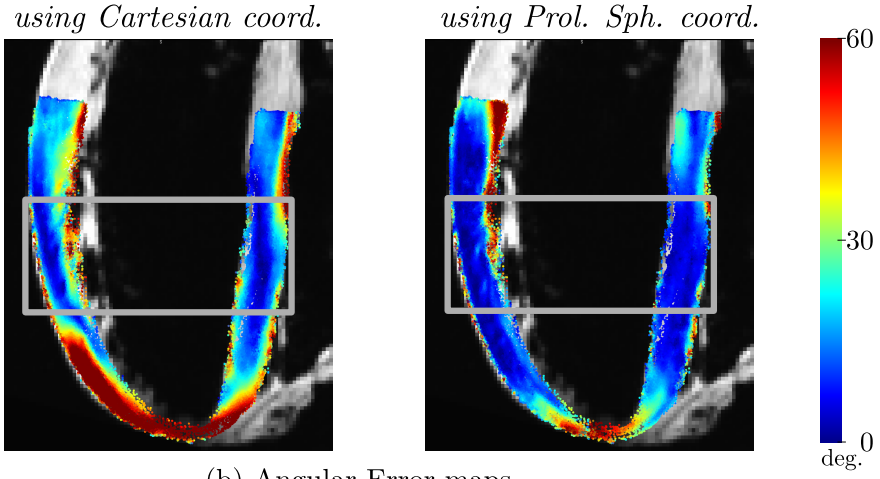

(b) Angular Error maps

Figure 1.13: (a) Mode of the residual angular error ε of the approximation process showed as a function of both the number of slices N and the SNR of the DWIs. (b) Maps of the angular error for the case N=7 and SNR=10. Results are presented for both Cartesian (left) and Prolate Spheroidal (right) coordinates. Grey rectangle: region covered by the 7 slices.

separately, as well as to the combined dataset $\mathcal{A}$, using PS coordinates. Resulting dense tensor fields were transformed back into Cartesian coordinates and to their respective anatomical geometry using operators Ψ^{-1} and Φ^{-1}. The resulting dense tensor fields are presented in Fig. 1.15(a) in a mid-ventricular short axis section. All obtained dense tensor fields were eventually used for fibre tractography for qualitative assessment of the resulting fibre orientations. Fibre tractography results for each subject are presented in Fig. 1.15(b). For the special case of $\mathcal{A}$, there does not exist any corresponding anatomical geometry, i.e. there exists no anatomical template in our workflow. The resulting dense tensor field from $\mathcal{A}$ was therefore warped onto the geometry of volunteer # 3, and fibre tractography was performed. The result is presented in Fig. 1.15(c), where the fibres are colour-coded with the local helix angle α.

1.3.4 Implementation

The segmentation of the ventricles was performed using the CardioViz3D software [Toussaint et al., 2008]. The registration between the segmented LV and the truncated ellipsoid was done with the implementation available in [Dru and Vercauteren, 2009], with the addition of the elasticity constraint as detailed in [Mansi et al., 2011a]. The tensor estimation as well as the tractography results were obtained using the Tensor ToolKit library[2], which implements methods described in [Fillard et al., 2007]. Visualisation of tensor fields and fibre fields were obtained using the vtkINRIA3D software [Toussaint et al., 2007]. All algorithms concerning the conformal mapping and the dense

[2]https://gforge.inria.fr/projects/ttk

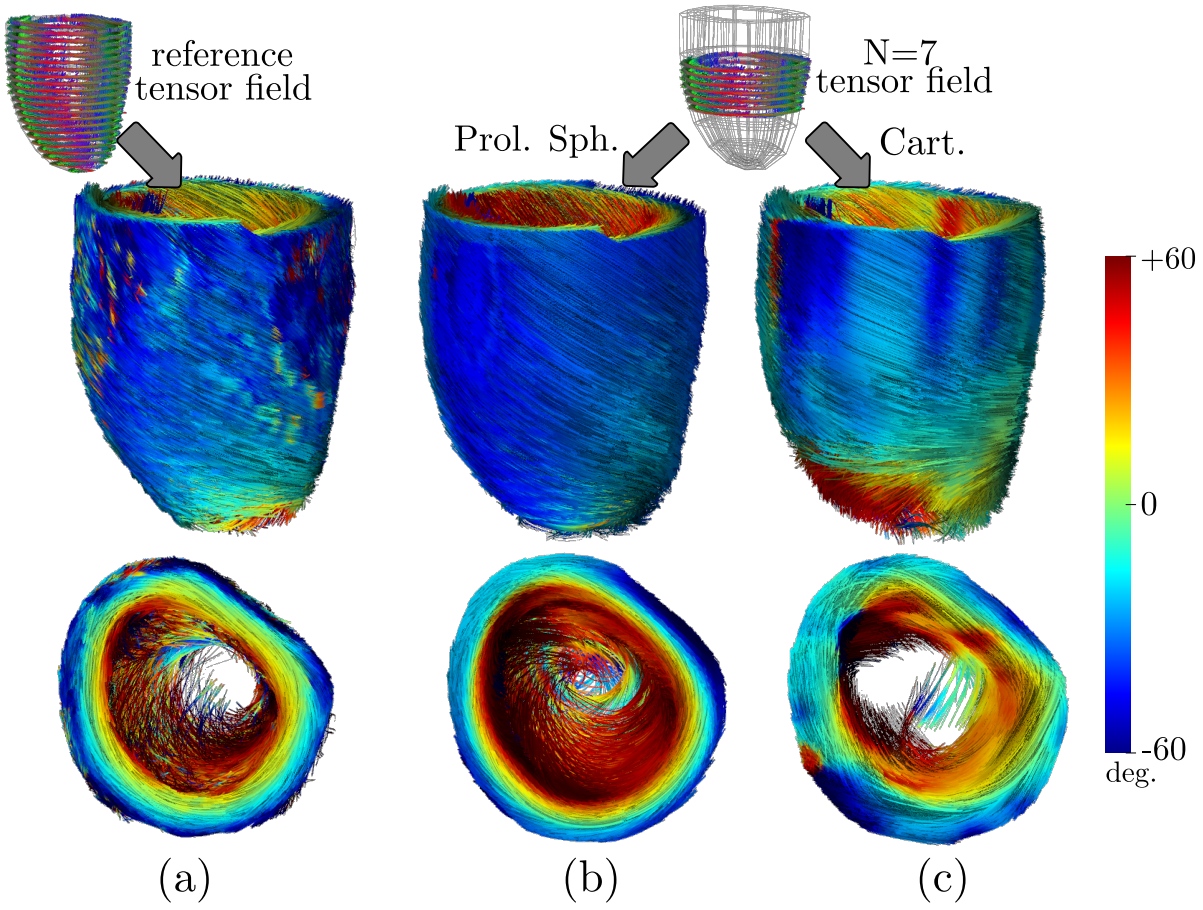

Figure 1.14: (a) Tractography result from the reference fully sampled tensor field. (b) and (c) Tractography results from approximated tensor fields when using the noisy set of tensors (N=7, SNR=10), and respectively the PS approach (b) and Cartesian approach (c).

approximation were developed in a C++ ITK-VTK based framework, and have been made available as an open-source library, the Cardiac Prolate Spheroidal ToolKit [3]

1.4 Discussion

1.4.1 Group-Wise Study

The PS conformal mapping methodology described in this chapter constructs a normalised referential for the LV from which DTI information can be analysed in a straightforward manner. Its application to an *in vivo* database of healthy subjects allowed to observe the global distribution of fibre orientation throughout the ventricle. As the accumulated dataset $\mathcal{A}$ is expressed in the PS frame, simple projections of the tensors D_ξ main eigenvectors on the contravariant basis $\mathcal{G}$ allowed for the extraction of local fibre orientation. A strong and linear negative correlation between the helix angle and the transmural depth was observed, confirming previous *ex-vivo* studies. The reported range of $+55 \sim -30\,\mathrm{deg}$ (Fig. 1.9) is in relative agreement with values reported in the literature for *ex vivo* canine and human hearts [Streeter and Hanna, 1973; Scollan et al., 2000; Anderson et al., 2008]. The value at the endocardium is strongly influenced by the limit of the segmentation. Accordingly, one has to be careful not to include the papillary muscles of the LV in the segmentation as they tend to bias the elevation angle's endocardial limit by introducing vertical tensors in the computation. This consideration might partly explain the asymmetry of the ranges reported both in this experiment and in the literature. The transverse angle shows a stable mean value of zero along the transmural depth. This indicates that fibres are mostly oriented parallel to the wall surface, as also observed

[3] https://github.com/ntoussaint

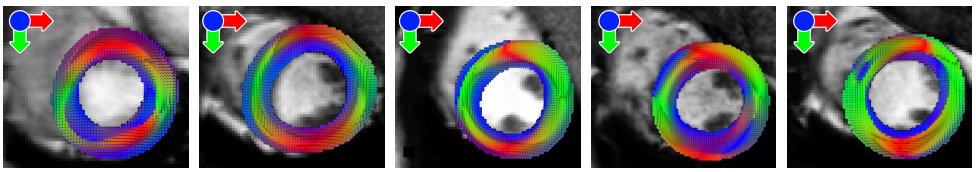

(a) short axis slice of the approximated tensor field for each volunteer

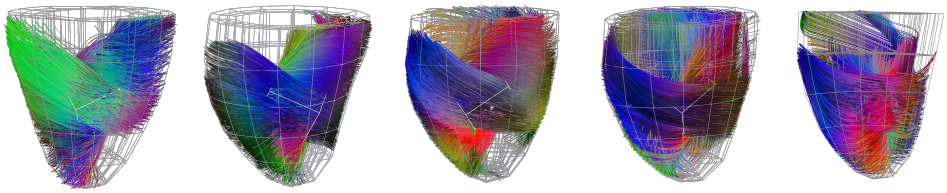

(b) Fibre reconstruction from the approximated tensor field for each volunteer

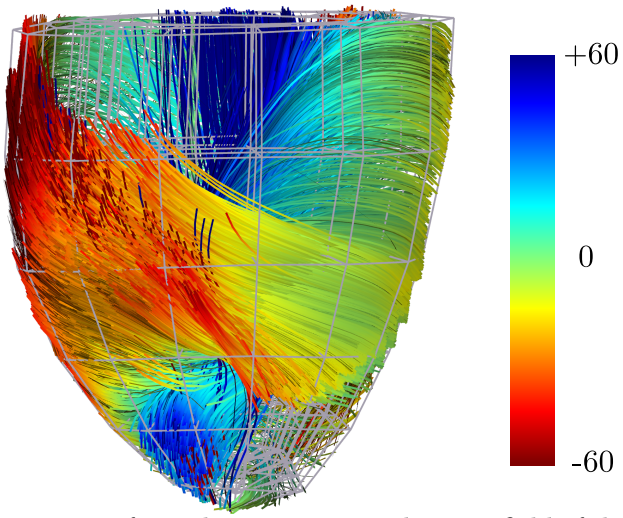

(c) Fibre reconstruction from the approximated tensor field of the cumulation of all datasets ($\mathcal{A}$), color coded with the helix angle α

Figure 1.15: (a) Slice of approximated tensor field for each volunteer. (b) Part of the resulting fibre tracking illustrating the transmural helix angle variation. (c) Fibre tracking result on the accumulated dataset. Fibres are colour-coded with the helix angle α.

ex vivo in [Lombaert et al., 2011a]. On the other hand, the sheet angle does not seem to have a significant correlation with the transmural depth. Similar results were obtained e.g. in [Lombaert et al., 2011b]. A low correlation with the transmural depth does not necessarily mean the absence of features: a primary cluster can be seen at the high negative values all along the transmural depth, and a secondary cluster is situated close to zero at the mid-wall region. These clusters indicate that a majority of laminar sheets seem to be oriented parallel to the wall surface, and that some laminar sheets parallel to the short axis can be seen at mid-wall depth. Further investigation is needed to study the local laminar sheet structure rather than study its global variation along one axis.

1.4.2 Dense Approximation and Fibre Tracking

The dense approximation scheme presented in this work takes advantage of the PS frame mapping in order to infer spatial coherency of the approximation along the natural shape of the ventricle. As demonstrated in Fig. 1.13 and 1.14, This approach shows better approximation accuracy when compared to the common Cartesian approach. The tensor fields and fibre architecture approximated from *in vivo* data (Fig. 1.15(a,b)) demonstrate a variation of fibre orientation from endocardium to epicardium that is in agreement with the expected structure as reported in the literature for *ex vivo* hearts [Scollan et al., 2000; Peyrat et al., 2007]. The double helix pattern is observed on all datasets. Accumulating the datasets in $\mathcal{A}$ allowed us to appreciate the average fibre orientation

structure among the population of this study (Fig. 1.15(c)), where the helical pattern of the fibres is clearly represented.

1.4.3 Sensitivity to Parameters

Segmentation The anatomical shape of the ventricle was extracted using manual segmentation, and the closest truncated ellipsoidal volume was then computed from this segmentation. Segmentation errors might thus bias the study by including or excluding tensor information at the boundaries of the LV. As shown in Fig. 1.2, the endocardial boundary of the segmentation was carefully monitored to avoid the papillary muscles. The axis of rotation of the truncated ellipsoid is defined as the main axis of mass of the segmented LV. A variation of this axis will slightly impact the resulting statistical study. For instance, its effect on the graphs presented in Fig. 1.9 would be an increase/decrease of the vertical standard deviations of the angles α, β, and γ with no impact on the mean values. However, since a misevaluation of this axis by only $10\,\mathrm{deg}.$ at the base would already deviate the apex location by 1cm, the error would be straightforward to pick during the process. In this case a manual adjustment of the axis becomes necessary to ensure a good overlap of the ellipsoid and the LV walls throughout the volume.

Registration Additionally, errors could potentially be introduced by the diffeomorphic registration between the segmented ventricle and the truncated ellipsoid. Measure points and DTI information are transported to this ellipsoid simply for statistical analysis and interpolation purposes. Since tensors are reoriented according to the Jacobian of the transformation Φ, it can safely be said that only the rotation components of Φ can potentially bias the accuracy of the statistical results. It is therefore important that the segmentation is smooth to prevent for strong rotation components of the transformation Φ that would cause an anatomically incorrect extra rotation of the tensor information. In our experiments the displacement fields were found to be smooth with displacement vectors of the order of 1.28 ± 0.77 mm and Jacobian determinants of the order of 0.96 ± 0.06 (mean $\pm$ std).

Noise The evolution of the error ε with respect to the addition of slices (each column of the error maps in Fig. 1.13(a)) seems to be significantly robust to noise. That is, the pattern was almost constant until reaching a SNR ≤ 5. This is again explained by the relatively strong smoothness of the fibre orientation structure in a healthy left ventricle such as the one used as reference in this sensitivity analysis.

Smoothing In the experiments shown in this work, a global kernel width matrix was used throughout the ventricle. Local variations in the acquired tensor dataset can be smoothed by this process. In the case of healthy subjects, this property might be desirable under the reasonable hypothesis that the fibre structure is relatively smooth. On the other hand, in clinical cases such as infarct subjects, the fibre architecture is suspected to be disoriented in the scar region. In this situation some more local approach would be necessary. For instance, one could consider using smaller kernel parameters in such regions in order to depict the fibre structure in more details. Tensor shape indices, such as the Fractional Anisotropy (FA) or the Spherical Coefficient (SC), could potentially be used as a detector of such regions in order to adjust the kernel parameters accordingly. As suggested in [Yang et al., 2012], a metric on tensor which avoid FA collapse should be preferred in this situation.

1.5 Conclusion

This work demonstrates that human *in vivo* cardiac DTI is feasible in a reasonable acquisition time. The acquisition protocol that allowed such acquisition was described and applied to a set of 5 healthy volunteers. The methodological contributions of this work are two-fold. First, a conformal mapping workflow was proposed for the analysis of cardiac DTI data in the left ventricular myocardium, that combines the use of the PS curvilinear coordinate system and a non-linear registration to a truncated

ellipsoid. This workflow was applied *in vivo* to analyse the fibre orientation structure of the group of subjects. Results showed a structure in good agreement with those reported in the literature for *ex vivo* specimens. Second, an approximation scheme was presented to compute a 3D approximation of a dense tensor field from sparsely acquired DTI data. The performance of this scheme was demonstrated using a gold standard *ex vivo* dataset. It was then applied to the group of healthy volunteers. Resulting reconstructed dense fibre structure presents a visible double helical pattern in agreement with the cardiac anatomical knowledge.

The main advantage of this approach is the integration of the curvilinearity of the object of interest in the groupwise study and in the approximation process. This is particularly interesting when the data is sparsely distributed across the ventricle. The Riemannian metric induced by redefining the problem in PS coordinates becomes *geodesically convex*, which is a very desirable property in such processes.

Future developments of the techniques introduced in this chapter involve a local approach to the dense approximation scheme, where the kernel sizes would be adapted to the local coherence of the tensors. Such improvement could be used to depict and localise fibre disarray involved in scar patients, and potentially improve therapy planning in these cases.

1.A Inversion of Prolate Spheroidal Coordinates

Recalling the trigonometric and hyperbolic identities:

$$\cos^2 + \sin^2 = 1, \text{ and } \cosh^2 - \sinh^2 = 1$$

If the following notations is taken for Eq. 1.1:

$$A = f^2 \qquad B = {x_1}^2 + {x_2}^2$$
$$C = {x_3}^2 \qquad \alpha = \sin^2(\xi_2)$$

then, using first and second definitions from Eq. 1.1, and the trigonometric identity, we obtain:

$$B = A \sinh^2(\xi_1)\alpha \tag{1.9}$$

$\sinh^2(\xi_1)$ is a function of α, A, and C using the third definition from Eq. 1.1 and the hyperbolic identity, which eventually gives a polynomial in α:

$$A\alpha^2 + (-A + B + C)\alpha - B = 0 \tag{1.10}$$

Of the two roots of this polynomial, only one is positive. Noting that $\alpha = \sin^2(\xi_2)$ is positive by definition, only one root corresponds to the solution:

$$\sin^2(\xi_2) = \frac{(A - B - C) + \sqrt{(A - B - C)^2 + 4AB}}{2A}$$

Recalling that ξ_2 is an angle from 0 to π, $\sin(\xi_2)$ is always positive, and ξ_2 can then be extracted. ξ_1 is also a positive number by definition, and can therefore be extracted from Eq. 1.9 when $\sin^2(\xi_2) \neq 0$ (everywhere but on the axis of revolution). When $\sin^2(\xi_2) = 0$, one can use $\sinh^2(\xi_1) = C/A - 1$, which holds true everywhere on the axis apart between foci, where PS coordinates are undefined. Note that this singularity can be noticed directly from the third line of Eq. 1.1 and by recalling that $\cosh(*) \geq 1$. Indeed we then have $|x_3| > f$ required on the axis. In practice this singularity is never reached as it is always outside the ventricle wall. We can nevertheless extend the definition domain by its limit close to the axis of revolution, i.e. imposing $\xi_1 = 0$ in the segment between foci, rendering the singularity "removable".

Finally, ξ_3 is simply obtained by dividing second with first line of Eq. 1.1: $\xi_3 = \arctan(x_2/x_1)$, which holds true everywhere except at the axis of revolution. If the point is on the axis of revolution, ξ_3 can take any value between 0 and 2π. We use $\xi_3 = 0$ by convention.

1.B Contravariant Basis vectors

The PS contravariant basis $\mathcal{G} = (g_1, g_2, g_3)$, defines the differential vectors for each of the coordinates: $g_i = f\partial x/\partial \xi_i$.

$$
\begin{aligned}
g_1 &= f \begin{pmatrix} \cosh(\xi_1)\sin(\xi_2)\cos(\xi_3) \\ \cosh(\xi_1)\sin(\xi_2)\sin(\xi_3) \\ \sinh(\xi_1)\cos(\xi_2) \end{pmatrix} \\
g_2 &= f \begin{pmatrix} \sinh(\xi_1)\cos(\xi_2)\cos(\xi_3) \\ \sinh(\xi_1)\cos(\xi_2)\sin(\xi_3) \\ -\cosh(\xi_1)\sin(\xi_2) \end{pmatrix} \\
g_3 &= f \begin{pmatrix} -\sinh(\xi_1)\sin(\xi_2)\sin(\xi_3) \\ \sinh(\xi_1)\sin(\xi_2)\cos(\xi_3) \\ 0 \end{pmatrix}
\end{aligned} \tag{1.11}
$$

The basis $\mathcal{G}$ is direct and orthogonal, but not orthonormal. The norm of each column vector is the inverse of the corresponding scale factor: $\|g_i\| = 1/h_i$.

The calculation of the scaling factors and the contravariant basis is involved in the "Finite Strain" reorientation for the induced transformation $\tilde{\Psi}$, and the normalised basis is written $\hat{\mathcal{G}} = \text{diag}(h_i)\ \mathcal{G}$.

Chapter 2

Patient-Specific Electrophysiology: Application to Ventricular Tachycardia

– This chapter is based on [Chen et al., 2016]: Chen, Z., Cabrera-lozoya, R., Relan, J., Sohal, M., Shetty, A., Karim, R., Delingette, H., Gill, J., Rhode, K., Ayache, N., Taggart, P., Rinaldi, C., Sermesant, M., and Razavi, R. Biophysical modelling predicts ventricular tachycardia inducibility and circuit morphology: A combined clinical validation and computer modelling approach. *Journal of Cardiovascular Electrophysiology*, 2016 (in press).

2.1 Introduction

Current risk stratification in patients who are at risk of potentially fatal ventricular arrhythmias but without a prior history of sustained arrhythmia relies on determination of left ventricular (LV) function, the presence of myocardial scar and arrhythmia inducibility during electrophysiological testing [Moss et al., 1996; Nat, 2006]. In patients with ventricular arrhythmias, especially those with ischaemic cardiomyopathy (ICM), radiofrequency ablation (RFA) is increasingly used to treat ventricular tachycardia (VT) in order to reduce implantable cardioverter defibrillator (ICD) discharges, improve patient quality of life and reduce mortality due to ICD shocks. The current risk stratification strategy is imperfect with not all high-risk patients receiving an ICD and those receiving one never experiencing appropriate therapies. Similarly, ablation of VT is technically challenging with a recurrence rate of up to 40% with a lack of clinical consensus on the optimal ablation strategy Aliot et al. [2009]. Better risk stratification and higher ablation success rates would potentially improve patient outcomes. There is therefore a need to identify individuals at high risk of developing ventricular arrhythmia and the arrhythmia substrate amenable to RFA in order to guide the optimal ablation strategy.

Computational modelling of cardiac arrhythmogenesis and arrhythmia maintenance have made a significant contribution to the understanding of the underlying mechanisms of arrhythmia [Cherry and Fenton, 2004; Courtemanche and Winfree, 1991; Panfilov and Keener, 1995; Jalife and Gray, 1996; Watanabe et al., 2001]. Studies have identified multiple factors involved in the onset of arrhythmia, including wave fragmentation, spiral wave breakups, heterogeneity of repolarization, action potential duration (APD) restitution and conduction velocity (CV) [Trayanova and Tice, 2009; Killeen et al., 2008; Pueyo et al., 2011; Yue et al., 2005; Arevalo et al., 2007; Banville and Gray, 2002]. In particular, the heterogeneity in APD restitution, the adaptation of APD as a function of the cardiac cycle length, has a crucial role in arrhythmogenesis [Cherry and Fenton, 2004; Clayton et al., 2011a; Nash et al., 2006]. Image-based computational models have incorporated cardiac structural information into such simulations [Ashikaga et al., 2013; Relan et al., 2011a]. However the integration of both personalized structural and functional data has not previously been performed.

We hypothesized that using electrophysiological mapping data and structural anatomical data acquired respectively from invasive electrophysiology studies and high-resolution cardiac magnetic resonance imaging (MRI), we could develop a patient-specific biophysical model to evaluate how

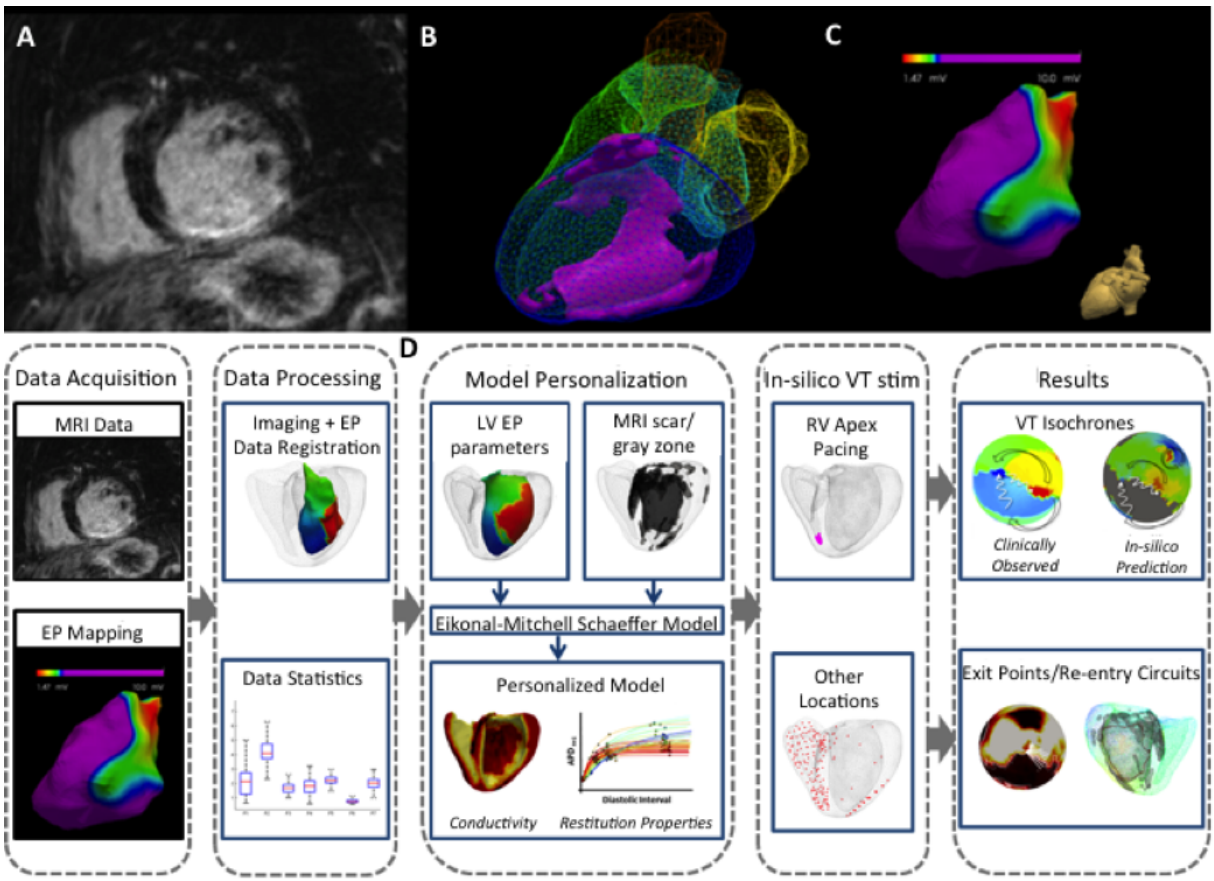

Figure 2.1: Personalized computer modelling process. Upper panel: (A) high-resolution contrast-enhanced MRI scar images; (B) whole heart model segmented from 3D steady-state free precession (SSFP) MRI with scar (core and gray zone) in violet; (C) low voltage areas from electroanatomical mapping. Lower panel: (D) model personalization and in silico VT stimulation study procedure workflow.

these properties were involved in the induction of VT. We compared *in silico* VT stimulation studies against clinical VT stimulation studies conducted in the cardiac catheterization laboratory to predict both VT inducibility and the characteristics of the induced VT circuits.

2.2 Materials and Methods

2.2.1 Patients

All patients were prospectively invited to participate in the study following local research ethics committee approval and all patients gave written consent prior to study inclusion. We studied 3 patients with ischaemic cardiomyopathy (ICM) defined in accordance with the criteria of the World Health Organisation/International Society and Federation of Cardiology [Richardson et al., 1996]. All patients were being considered for ICD implant for primary prevention on the basis of their LV function. Patients underwent MRI with delayed enhancement (DE) for scar assessment prior to their electrophysiology study to acquire cardiac anatomical and functional information. All patients underwent a clinically indicated VT stimulation study. Table 2.1 summarizes patient characteristics and MRI findings.

2.2.2 MRI Acquisition and Image Processing

All 3 patients completed MRI morphological and volumetric assessment as well as scar characterization by DE-MRI. Imaging was performed on a Philips Achieva 1.5T scanner using a 32 channel cardiac

Table 2.1: Baseline patient characteristics and MRI findings.

Patient	1	2	3
Condition	ICM	ICM	ICM
Gender	M	M	M
Age	73	69	64
LVEF, %	27	35	35
Scar on MRI	Yes	Yes	Yes

LVEF:ejection fraction; ICM: ischaemic cardiomyopathy.

coil. A high-resolution three-dimensional (3D) whole heart balanced steady-state free precession (B-SSFP) free-breathing scan with (acquired) isotropic resolution of 1.8 mm^3 was performed using respiratory navigator motion correction for the purpose of cardiac structure segmentation. LV volumetric assessment was performed using a standard stack of short-axis B-SSFP slices. High-resolution scar imaging was acquired using a free-breathing respiratory navigated inversion-recovery sequence 20 minutes post intravenous injection of a gadolinium contrast agent (Gadobutrol 0.2mmol/kg), with an acquired voxel size 1.3×1.3×2.6mm^3, field of view approximately 300×300×100mm, repetition time/echo time of 5.4/2.6ms and flip angle 25 degrees. Patient-specific inversion time for the sequences was selected individually based on a preceding Look-Locker scan to ensure the optimal nulling of the myocardium.

The 3D B-SSFP structure images were processed to obtain a structural model of the four chambers of the heart using software developed within an open source frame-work GIMIAS [Peters et al., 2007; Larrabide et al., 2009]. The LV myocardial scar distribution was segmented using signal intensity (SI) based analysis from the high-resolution DE-MR images. Using the full width-half-maximum (FWHM) method, all voxels with SI values above the half of the maximum SI were automatically characterized as scar core. The standard deviation of a manually selected remote region of presumed non-infarct myocardium was computed. Pixels with SI higher than twice this standard deviation (2SD) but lower than that identified as scar core were automatically assigned as gray zone (an admixture of scar and healthy myocardium scar, often in the region of scar border zone) [Kim et al., 2009]. Finally, a personalized 3D model of the ventricles was derived from the MRI images: a tetrahedral mesh was generated from the binary mask of the ventricles using the CGAL software (`http://www.cgal.org`). Each element of the mesh was labelled (healthy / scar core / gray zone) according to the segmentation of the myocardium performed in the previous step.

2.2.3 Electroanatomical Mapping and Signal Processing

LV non-contact electroanatomic mapping (EAM) was performed using a multi-electrode array catheter (EnSite Velocity System, St Jude Medical, MN, USA) passed via the femoral artery retrogradely across the aortic valve into the LV cavity in all patients. The EnSite system uses the inverse solution method to reconstruct endocardial electrical potentials within the LV cavity [Schilling et al., 1998]. The chamber geometry was reconstructed using locator signals from a steerable electrophysiological catheter. The patients underwent a simultaneous VT stimulation study according to the Wellens protocol with pacing from the RV apex during the mapping study [Wellens et al., 1985] as part of the clinical work-up for risk stratification to determine if an ICD should be implanted as per National guidelines [Nat, 2006].

Unipolar electrograms (UEG) derived from non-contact mapping were filtered from an electrophysiology recorder (EnSite Velocity System) with a band-pass filter. In order to optimize QRS complex and T wave detections, the high-pass and low-pass filter cut-off frequencies were set respectively at 10Hz/300Hz and 0.5Hz/30Hz. The data were then exported for offline analysis. The depolarization times were detected within the QRS window and derived from the zero crossings of the laplacian of the measured UEGs [Coronel et al., 2000]. The repolarization times were detected within the ST window for the signals and derived using the alternative method [Yue et al., 2004].

The alternative method has repolarization times derived from $-dV/dt_{max}$ for the negative T-wave, at the dV/dt_{min} for the positive T-wave, and the mean time between $-dV/dt_{max}$ and dV/dt_{min} for the biphasic T-waves.

The relationship between the diastolic interval (DI) of one cardiac cycle and the APD of the subsequent cardiac cycle is described by the APD restitution curve (APD-RC). The difference between the depolarization time and repolarization time was used to estimate the activation recovery time (ARI), which is a surrogate marker for APD. The APD-RC was estimated during steady state RV pacing (600ms, 500ms and 400ms) with sensed extras at different coupling intervals. The APD-RC was represented by a non-linear equation using a least-squares fit to the mono-exponential function as previously detailed on experimental and clinical data [Relan et al., 2011a,b].

2.2.4 Cardiac Electrophysiology Models

The present study used a coupled personalization framework that was previously evaluated in details [Relan et al., 2011a,b]. It combines the benefits of two different kinds of mathematical models while keeping the computational complexity tractable. The Eikonal (EK) model was used to estimate the conductivity parameters over the ventricle derived from non-contact mapping of the ventricular endocardial surface potential, which were then used to set the parameters for the Mitchell-Schaeffer (MS) model. Additionally, the MS model is able to hold the memory of one preceding cycle and has restitution properties, thus is able to simulate arrhythmias macroscopically. Both models are computed on the whole 3D myocardium. This personalization framework has already been detailed in a previous publication and the predictive power of such personalized model was evaluated on experimental data [Relan et al., 2011a,b]. The process of building the models from the MRI and EAM data is illustrated in Figure 2.1 and a summary on the used models and their personalization are included in the following sections.

Eikonal (EK) Model The EK model simulates the propagation of the depolarization wave in cardiac tissue by computing the local activation time. It is governed by the Eikonal-diffusion equation and solved using the fast marching method. It can be written as:

$$c_o\sqrt{d_{EK}}(\sqrt{\nabla T(x)^t M \nabla T(x)} - \nabla \cdot (d_{EK} M \nabla T(x))) = \tau(x) \tag{2.1}$$

Where :

c_o is a dimensionless constant (=2.5)

$\tau(x)$ is the cell membrane time constant (=0.003s)

d_{EK} is the square of the tissue space constant along the fiber and is related to the specific conductivity of the tissue in the fiber direction, it has units of m^2

$M = diag(1, \rho, \rho)$ is a diffusion tensor that incorporates the tissue anisotropy into the model

$\rho = {}^1/_{2.5^2}$ is the anisotropy ratio between longitudinal and transverse diffusion. This value is given to have a conduction velocity (CV) 2.5 times faster in the fiber direction

Details for solving the previous non-linear equation are explained in a prior publication [Sermesant et al., 2005].

Mitchell Schaeffer (MS) Model The MS model is a simplified biophysical model derived from the Fenton Karma ionic model [Mitchell and Schaeffer, 2003; Fenton and Karma, 1998]. It models the transmembrane potential as the sum of a passive diffusive current and several active reactive currents including combination of all inward and outward phenomenological ionic currents. This is described in the MS model by a system of partial differential equations:

$$\begin{cases} \partial_t u = div(D\nabla u) + \frac{zu^2(1-u)}{\tau_{in}} - \frac{u}{\tau_{out}} + J_{stim}(t) \\ \partial_t z = \begin{cases} \frac{(1-z)}{\tau_{open}} & \text{if} \quad u < u_{gate} \\ \frac{-z}{\tau_{close}} & \text{if} \quad u > u_{gate} \end{cases} \end{cases} \tag{2.2}$$

Where:

u is a normalized transmembrane potential variable

z is a gating variable which depicts the depolarization and repolarization phases by opening and closing the currents gate

$J_{in} = \frac{zu^2(1-u)}{\tau_{in}}$ represents the inward currents (primarily Na^+ and Ca^2+) which raise the action potential voltage

$J_{out} = \frac{u}{\tau_{out}}$ represents the outward currents that decrease the action potential voltage (mainly K^+), describing repolarization

J_{stim} is the stimulation current at the pacing location

$\tau_{in}, \tau_{out}, \tau_{open}, \tau_{close}$ have units of seconds

M is a diffusion tensor that controls the diffusion term in the model

This model incorporates both APD and CV restitution effects, and the restitution curves can be written in an analytical formulation, which can be used to estimate restitution parameters.

2.2.5 Model Personalization

Apparent Conductivity Parameter Estimation. The apparent conductivity (AC) of tissue can be measured by the parameter d_{EK} in the EK model. It is initially estimated on the endocardial surface as a global value using a bisection method that matches the average conduction velocity of the measured depolarization time (DT) isochrones to the simulated ones. It is used as an initial estimate in an adaptive multi-level domain decomposition algorithm, which minimizes the mean-squared difference of the simulated and measured DT isochrones [Chinchapatnam et al., 2008]. One particular aim of this step is to estimate areas with high conduction velocity, which can represent parts of the Purkinje network.

Extrapolation of myocardial volumetric parameters from endocardial data, imaging and body surface ECG In order to propagate the estimated parameters to the whole myocardium, the present approach uses a diffusion-like process that smoothly extrapolates the estimated endocardial parameters. This estimation is based on the model using the anatomical 3D information from the MRI scar images and the global electrical information (ECG). The transmural AC value is estimated in order to fit the measured QRS duration, by a one-dimensional minimization of the following cost function: (mean-squared difference of simulated and measured isochrones at endocardium + squared difference of simulated and measured QRS duration). The simulated QRS duration is calculated as the difference between the maximum and the minimum depolarization times in the biventricular mesh and the measured QRS duration is estimated from the surface ECG. The AC values for RV endocardium and RV myocardial mass are set at 5 mm^2 and 0.64 mm^2 as previously described [Keener and Sneyd, 1998]. Such estimation method has been validated by experimental data [Relan et al., 2011b]. Due to the absence of transmural electrical propagation information, no variation is assumed across the healthy left ventricular myocardium, excluding the LV endocardium which was personalized as described in the previous paragraphs and the scar personalized from imaging.

Coupling of EK and MS Model Parameters The AC parameter for d_{EK} model is a scale for the diffusion speed of the depolarization wave front in the tissue. In 3D, the model Conduction Velocity (CV) is related to d_{EK} as :

$$c_{EK} = \alpha_{EK}\sqrt{d_{EK}} + \beta_{EK} \tag{2.3}$$

where the constants α_{EK} and β_{EK} are introduced to take into account the discretization errors (in particular of the curvature) in 3D.

The corresponding conductivity parameter for MS model, d_{MS} is also a scale for the wave diffusion speed in the tissue. The model CV here is related to d_{MS} as:

$$c_{MS} = \alpha_{MS}\sqrt{d_{MS}} + \beta_{MS} \tag{2.4}$$

where the constants α_{MS} and β_{MS} are introduced for the same reasons as of EK model, while τ_{in} is kept as a constant. The estimated AC parameter d_{EK} can then be used to estimate the parameter d_{MS} as previously described [Relan et al., 2011a].

To represent the volumetric heterogeneity of the border zone, the intensity values derived from the 3D DE-MRI images were used to modulate the spatial variation in the AC values of scar border zone (the higher the signal intensity seen on DE-MRI images, the lower the tissue conductivity). AC values were assigned to zero in the scar core, to reflect the paucity of viable cardiac myocytes.

APD Restitution Curves. APD restitution is an electrophysiological property of the cardiac tissue and defines the adaptation of APD as a function of the heart rate. Its slope has a heterogeneous spatial distribution. The APD restitution curve (APD-RC) defines the relationship between the diastolic interval (DI) of one cardiac cycle and the APD of the subsequent cardiac cycle. The slope of these RCs is controlled by a model parameter τ_{open} of the MS model and depicts the APD heterogeneity present at multiple heart rates. APD-RC for MS model is explicitly derived as:

$$APD_{n+1} = f(DI_n) = \tau_{close} ln(\frac{1-(1-h_{min})e^{\frac{-DI_n}{\tau_{open}}}}{h_{min}}) \tag{2.5}$$

where $h_{min} = 4(\tau_{in}/\tau_{out})$ and n is the cycle number. The maximum value of APD is also explicitly derived as $APD_{max} = \tau_{close} ln(1/h_{min})$.

2.2.6 in silico VT Stimulation Study

In all patients, clinical VT stimulation studies were carried out at the same time as EAM. The personalized model was used to simulate a clinical VT stimulation study *in silico* in order to predict the initiation and maintenance of ventricular arrhythmia. The simulated study was performed in accordance with the clinical study protocols that were carried out in these patients: the pacing stimuli were applied from the RV apex following the Wellens protocol. If a sustained VT was initiated *in silico*, the VT cycle isochrones were computed to locate the site of the earliest activation corresponding to the exit point of the re-entrant VT circuit. These results were compared with the observed results from the clinical VT stimulation studies. Each stage for the VT stimulation *in silico* was simulated in parallel on a cluster of computers. The personalization plus VT simulation study for a mesh of >230,000 tetrahedra runs in approximately 12 hours.

In order to test *in silico* the inducibility of VT from other pacing sites, the VT stimulation study was also simulated from alternate pacing sites in the RV and LV that encompassed the basal and apical freewall/lateral/septum/anterior and inferior walls. This allowed identification of all the potential VT circuits and exit points of induced sustained monomorphic VT from the simulated study. The exit points identified during the clinical VT stimulation studies as well as the exit points identified during the *in silico* simulations were characterized in terms of the spatial heterogeneities of the AC, APD restitution properties, scar and gray zone at their locations.

VT simulation with solely image-based personalized parameters. A sensitivity analysis where the performance of a model constructed using non-personalized empirical electrical parameters was compared to that using personalized patient-specific electrical data. For all cases, patient anatomy and scar geometry was preserved. The VT simulation procedure was performed as described in the previous sections.

The personalized mesh was divided into three different types of tissue, guided by the delayed enhanced MR imaging information: healthy myocardium, grey zone and scar core. Nodes within the scar core tissue were set to have zero apparent conductivity values. Conduction and restitution

parameters in the healthy myocardium tissue were set to the average value computed from the personalized models across patients. This yielded values of 4 m^2s^2 for the apparent conductivity and τ_{close} = 180ms, τ_{in} = 0.3ms, τ_{out} = 6ms, τ_{open} = 160 ms for the restitution model parameters.

According to the described values of conduction velocity and restitution parameters in the literature, model parameters were modified in the grey zone areas [Yao et al., 2003; Decker and Rudy, 2010]. Conduction velocity parameters were reduced by 90% with respect to those in the healthy myocardium. Restitution parameter values in the grey zone regions were set to have a 25% longer action potential duration (increase in τ_{close} parameter) and a 31% smaller upstroke velocity (increase in the τ_{in} parameter) than those in the healthy myocardium.

2.3 Results

During the clinical VT stimulation studies, patients 1 and 2 developed sustained monomorphic VT, while patient 3 was non-inducible. All were implanted with an ICD for primary prevention based on guidelines following clinical assessment. During a follow-up, Patient 2 received appropriate ICD therapy for sustained VT.

2.3.1 VT Induction and Clinically Observed Exit Points

Patient 1 had induced sustained monomorphic VT with a cycle length (CL) of 275ms at Stage 11 of the Wellens protocol (S1 500ms, with S2, S3 and S4 at 250ms, 240 and 360ms respectively). Patient 2 had induced SMVT with a cycle length of 245ms at Stage 4 of the Wellens protocol (S1 600ms, with S2 at 400 and S3 at 360ms). In Patient 1, the endocardial activation recorded from EAM showed the re-entrant VT circuit initiating from the LV lateral wall, spreading anteriorly and then posteriorly before returning to the lateral wall. In Patient 2, the re-entrant VT circuit exited from the LV infero-lateral wall, spreading antero-laterally and then towards the septum, before returning to the infero-lateral wall. The patterns of activation for both re-entrant VT circuits are illustrated in Figure 2.2.

2.3.2 Model Personalization, Parameters

A qualitative assessment of spatial heterogeneities of the LV myocardium in terms of apparent conductivity and APD restitution properties for each patient are illustrated on polar plots in Figure 2.3. There appeared to be a broad spatial heterogeneity in AC in all the study patients, as is shown on the boxplots on the lower part of Figure 2.3. However, patients 1 and 2 showed higher spatial heterogeneity of APD-RC properties. The VT exit points that were observed during the clinical VT stimulation studies in Patients 1 and 2 were in the scar border zone/gray zone as determined by the DE-MRI scans.

2.3.3 Model-Predicted Induced VT

The VT stimulation studies performed on all patients were simulated *in silico* using the personalized computer model. Sustained monomorphic VT was induced at Stage 7 of the virtual Wellens protocol for Patient 1 (drive-train S1 at 400ms, first coupled extra stimulus S2 at 220ms) and stage 5 for Patient 2 (drive-train S1 at 500ms, and coupled S2 at 220ms). LV polar plots of the clinical and virtual VT isochrones are illustrated in Figure 2.4 for comparison. Sustained VT was not inducible *in silico* for Patient 3.

The personalized model of Patient 1 predicted a sustained re-entrant VT (induced with drive-train S1 at 400ms, S2 at 200ms and S3 at 200ms) circuit with a cycle length of 260ms compared with the clinically observed cycle length of 275ms with a macroscopically similar activation pattern and a predicted exit point that matched with the observed clinical one. The personalized model of Patient 2 also predicted a positive VT (induced with drive-train S1 at 500ms, S2 at 200ms) stimulation study with a cycle length of 250ms compared with 245ms for the clinical VT. The induced VT was sustained and the re-entrant pathway stable. Notably the direction of the activation pattern during

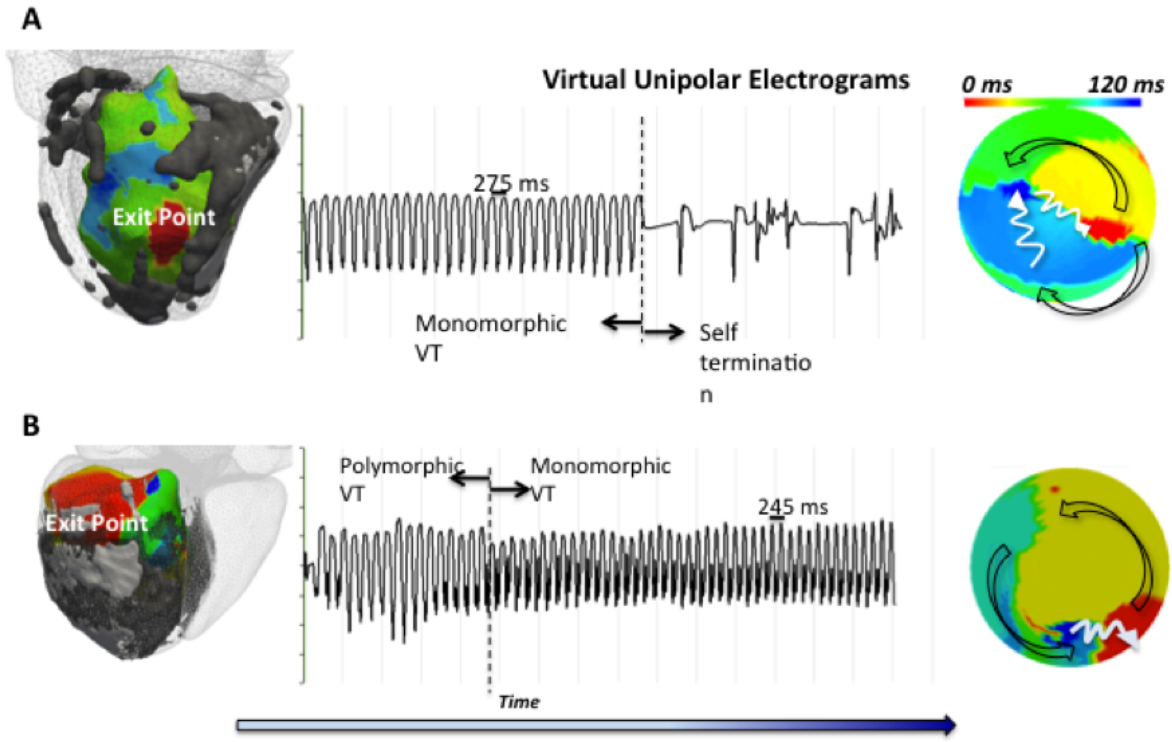

Figure 2.2: Isochrones mapping during re-entrant VT. (A) Patient 1 with VT cycle length 275ms and (B) Patient 2 with VT cycle length 245ms. In Patient 1, the sustained VT self terminated after attempts of pace termination given due to patient's favorable hemodynamic response. In Patient 2, the sustained VT required DC-cardioversion due to patient's unfavorable hemodynamic response. The 3D VT isochrones with exit points (red) in relation with scar core (white) and gray zone (gray) are shown in the left panels. Unipolar electrograms recording during VT are shown in the middle panels. LV polar plots of VT isochrones illustrating the direction of activation pattern are shown in the right panels.

the predicted re-entrant VT was reversed from that observed clinically; however, the predicted exit point correlated with the clinically observed one.

We performed additional quantitative analysis on the patients' 3D anatomies to make a comparison of clinically observed and predicted exits points in terms of anatomic location. We defined the exit region compassing anatomical points with an activation time within 10ms of the earliest activation. The distance between the clinically observed and simulated exit points was defined as the 3D Euclidean distance between the centres of both exit regions. A difference of 7mm and 8mm were found, respectively, for patients 1 and 2. The personalized model of Patient 3 could not induce VT using the virtual Wellens protocol, but induced frequent monomorphic ventricular ectopic in agreement with the clinical study.

2.3.4 *in silico* VT Stimulation from Additional Sites

VT stimulation study was also performed *in silico* by pacing from other sites than the RV apex used during the clinical study for Patients 1 and 2. Different VT circuits with three additional exit points were observed in both patients. The exit points were located on the boundary of scar in the region of the gray zones from the DE-MRI images. The composite of different exit points are plotted in Figure 2.5 in terms of their APD restitution properties and AC.

2.3.5 Three-Dimensional VT Circuit Visualization

The computer model enabled the prediction of a 3D VT circuit, as opposed to the 2D VT activation pattern observed by the non-contact EAM, by taking into account the 3D geometric information

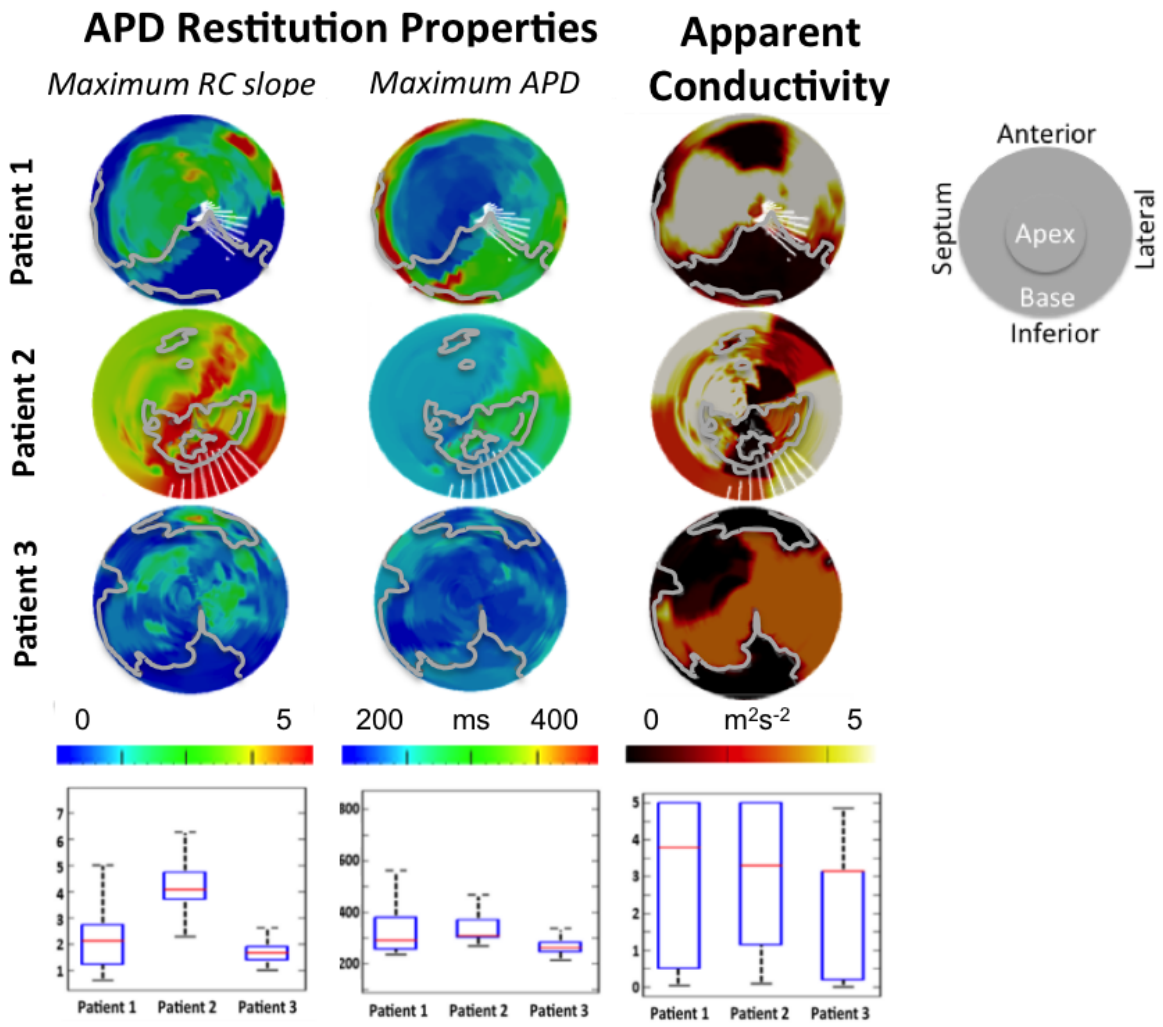

Figure 2.3: (Top) LV polar plot representation of the spatial distribution of the maximum slope for APD-RCs, maximum asymptotic APD and AC. Scars identified by DE-MRI with its border zone (highlighted by gray contours) and clinically observed exit points (highlighted by white contours) during re-entrant VT are overlaid to the polar plots. (Bottom) Box-whiskers plots of spatial heterogeneity of the personalized parameters.

from MRI including the transmurality of scar core and gray zone across the LV wall. This allowed additional insights on the wave propagation within the myocardium through computer simulation. For Patient 2, the main VT circuit in the myocardium computed from the geodesic path of the predicted VT isochrones is shown in red in Figure 2.6. Between the entry (the latest activated region) and the exit (the earliest activated region) points, the activation wave front of the re-entrant VT propagates in the region of the gray zone. The estimated wave front path surrounds the scar core and lies within the scar border zone, entering from the endocardial surface, meandering within the ventricular wall, and exiting via the epicardial surface.

2.3.6 Results for solely image-based personalized parameters.

We performed additional sensitivity analysis using solely image-based personalized electrical parameters instead of personalized patient-specific electrical data in the two patients with positive clinical VT stimulation studies and found that using combined personalized electrical and image data can potentially improve the accuracy of VT inducibility and predictions regarding the location of exit zones predictions.

Using non-personalised empirical electrical parameters VT was not inducible in Patient 1. It also induced a different macroscopic VT circuit morphology from the one seen during the clinical study

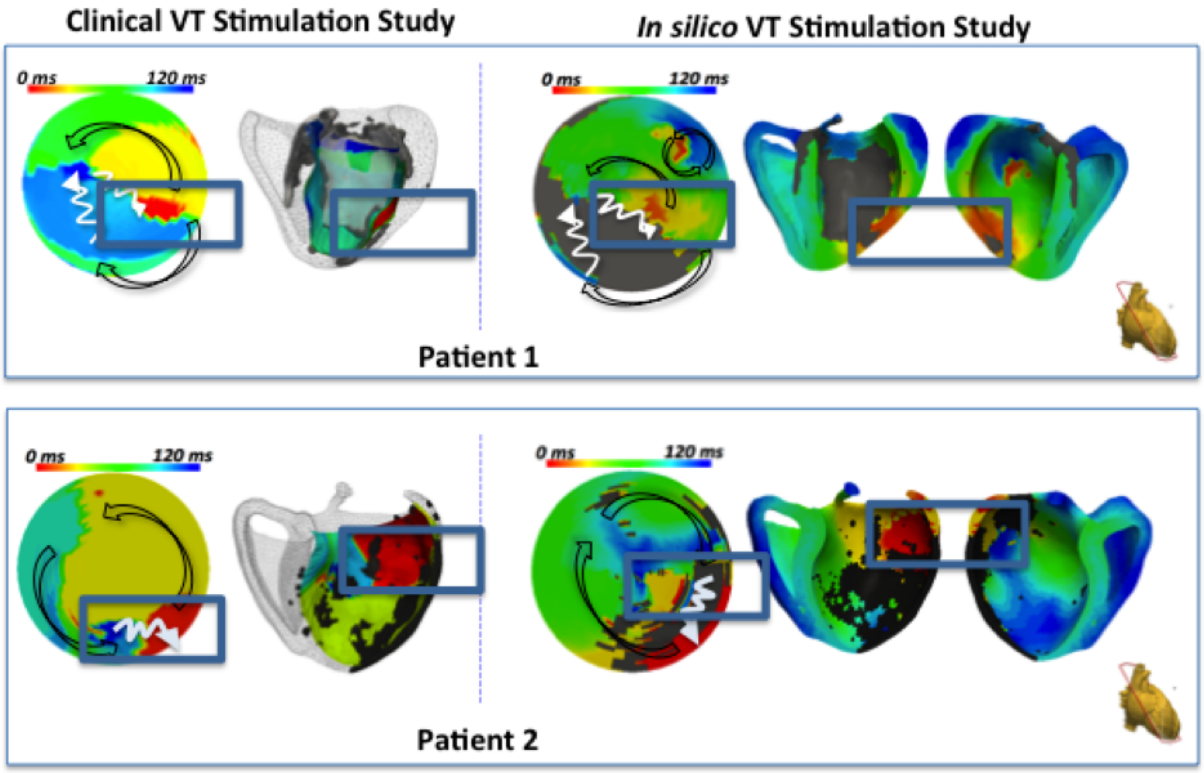

Figure 2.4: VT isochrones of induced re-entrant VT during clinical VT stimulation study (left panel) and during in silico VT stimulation study (right panel). The arrows point towards the directions of propagation. Scars (core and gray zone) are superimposed to the LV shell shown in darkened regions.

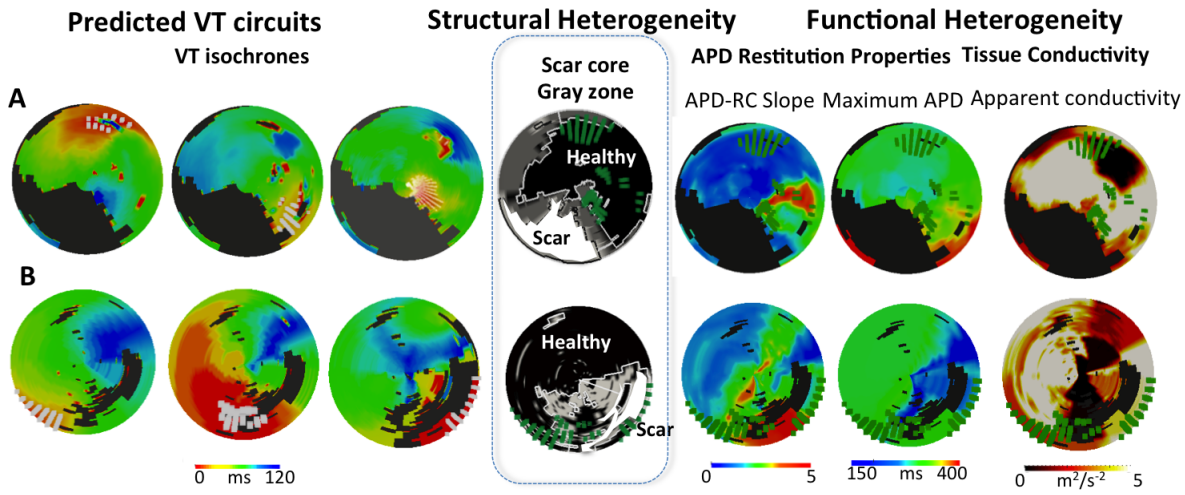

Figure 2.5: Correlation of predicted exits points with structural heterogeneity and functional heterogeneity. A = Patient 1. B = Patient 2. The left panel shows the isochrones for the three predicted VT circuits with fangs of white lines denoting the exit points. The middle panel demonstrates the LV scar distribution with black region denoting healthy myocardium, white region denoting the scar core and the gray region denoting the gray zone/scar boarder zone with overlying composite exit points (fanged green lines). The right panel demonstrates the electrical properties with overlying composite exit points (fanged green lines).

in Patient 2. The Euclidean distance between the centre of the clinical exit region and that predicted using non-personalized electrical parameters was 37mm, and with using personalized electrical parameters it was 8mm.

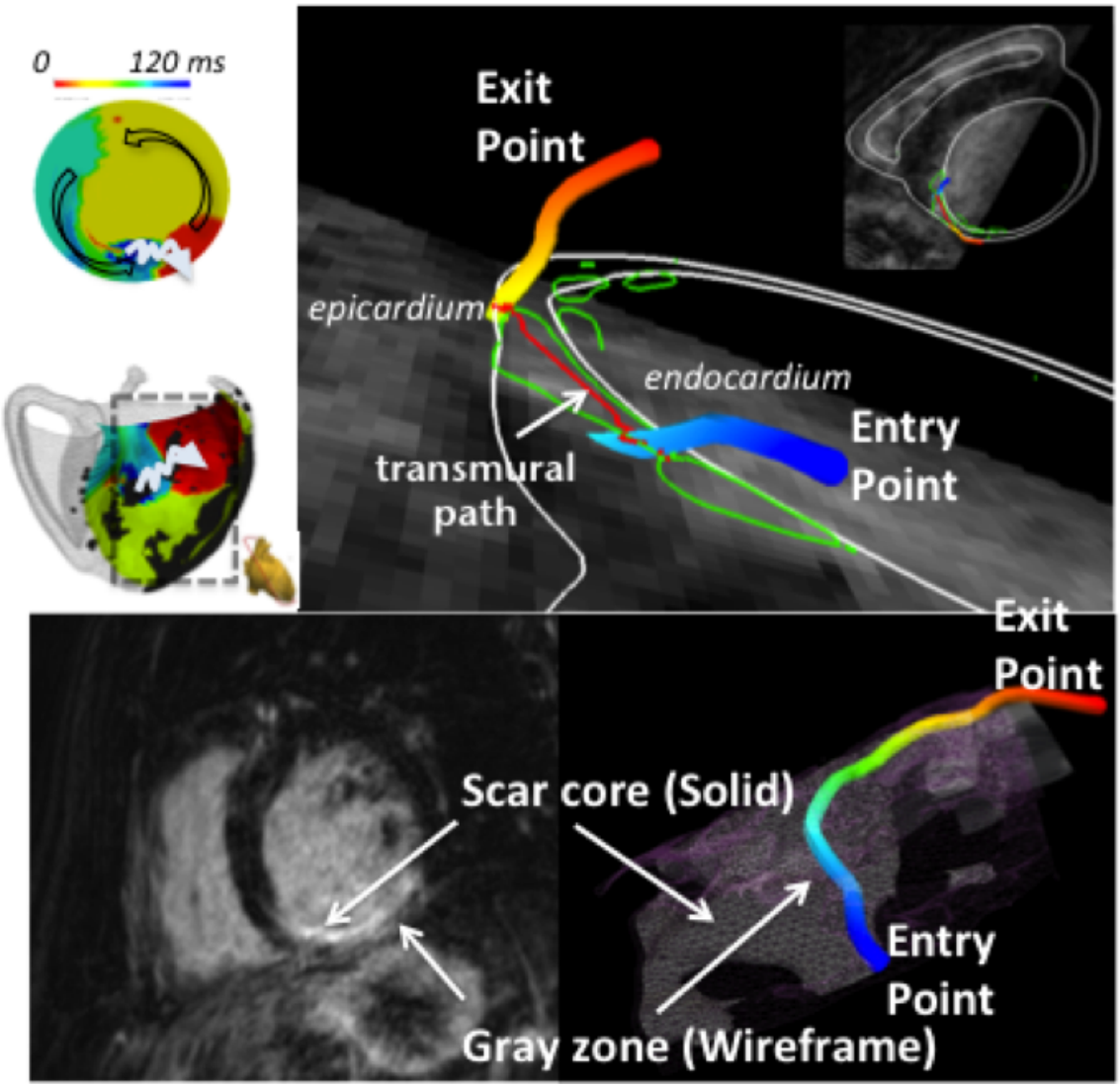

Figure 2.6: Estimation of the intra-myocardial path between the entry and exit points during re-entrant VT. Estimated endocardial 2D geodesic path between the entry and exit points from electroanatomical study during clinical VT stimulation study is demonstrated by the isochrones map. Estimated intra-myocardial 3D geodesic path (red line) takes into account of the scar heterogeneity from the high-resolution MR images. The entry and exit points are illustrated by the graded colours on the 3D path with blue denoting late activation and red denoting early activation. The activation wave path is shown traveling within the region of scar border zone (purple wire mesh), between the scar core and the gray zone.

2.4 Discussion

The present study provides new insights into the prediction of VT circuits using a biophysical model. The principal findings of our study are as follows:

1. *In silico* VT stimulation studies were able to predict inducibility of VT in patients at risk of ventricular arrhythmia.

2. The characteristics of the modeled VT circuits correlated well with the clinically observed circuits in terms of cycle length, macroscopic activation patterns and VT exit sites.

Encouragingly, the personalized cardiac models encompassing both anatomical and electrical properties in the present study were able to predict not only the inducibility of re-entrant VT, but also the re-entrant VT circuit properties and anatomical locations of the substrate. Whilst cardiac

modelling has been an active research area for decades, personalized cardiac modelling using patient-specific clinical data is in its infancy. Recently, Ashikaga et al. presented a retrospective study that compared the actual target VT ablation sites with that predicted from an image based cardiac model and found a good correlation between the predicted ablation sites located mostly at the scar border zone and the actual ablation sites [Ashikaga et al., 2013]. In keeping with our data, they highlighted an advantage of incorporating 3D geometric information gained from MRI, which allowed the prediction of the potential critical isthmus on the epicardial surface. This is important, as conventional mapping techniques used during ablative therapy are limited especially when the substrate of the VT circuit lies on the opposite side of the mapping surface. Our study is unique in that as well as anatomical and scar information, we incorporated functional data including APD-RC properties and tissue conductivity and their spatial heterogeneity into our patient-specific models. Previously, Arevalo H et al. suggested that VT dynamics were primarily governed by the geometric parameters of the scar-core and border zone using image-based computational VT modeling work with scar data acquired from high-resolution MRI of *ex vivo* canine heart (reconstructed voxel size $200\mu m^3$) and empirical ionic cell parameters [Arevalo et al., 2013]. Whilst we realize that contrast-enhanced MRI provides important scar geometry that governs the substrate of re-entrant VT, we also recognize that the resolution of the current standard clinical MR imaging technique is limited (common voxel size $2\times2\times8\ mm^3$) in providing the level of spatial geometry details that we would like to see at the border zone. Thus the term "gray zone" reflecting the spectrum of intermediate signal intensity seen on MRI scar images at the scar border zone was originated. We believe that additional knowledge and understanding of patient-specific heterogeneity in local electrical parameters would assist in predicting the likely culprit conduction channels/isthmus, and not the bystanders, that is critical to the clinical VT. This by confirmed by the results of our simulations on the solely image-based personalization of the electrical parameters in the model. We found that using combined personalized electrical and image data can potentially improve the accuracy of VT inducibility and predictions regarding the location of exit zones predictions.

2.4.1 Clinical application

The current personalization and *in silico* stimulation framework has potential for VT circuit prediction which could aid in ablation guidance. Successful VT termination through ablation may be achieved when the critical isthmus is successfully interrupted with ablation lesions. Predicted VT exit points could be potential targets for ablation. *In silico* personalized models may offer significant clinical benefit in predicting the risk of ventricular arrhythmia in patients and guiding treatments including ICD implantation and VT ablation. If VT exit points can be predicted with biophysical models then this information may be used to guide ablation in patients. Such models also offer additional flexibility as the model can simulate any combination of paced stimuli from different locations with varying pacing cycle lengths, which may not be feasible in clinical practice. We have indeed demonstrated that additional potential exit points, which still lay at the scar border zone/gray zone, can be induced from in silico VT stimulation studies.

2.4.2 Study Limitations

The study is limited by the small number of patients included, however the invasive nature of the study precludes analysis of a large number of patients. The electro-anatomical data are derived from non-contact mapping with the inherent limitations of this type of mapping [Schilling et al., 1998]. Non-contact mapping was chosen for its ability to provide 'beat-to-beat' mapping in the setting of rapid and unstable VT circuits, which could not be mapped with contact mapping techniques.

On the modelling side, the personalisation required high-resolution MRI data. In patients with pre-existing ICDs such imaging may not always be feasible. The cardiac model also made several simplifications in particular for the Purkinje network and pathological changes of cardiac fibre orientations. Though lacking detailed representation of such microscopic parameters, the model exhibited the main macroscopic properties of the tissue such as conductivity, APD and APD restitution. As with any personalization of computational physiology model, there is a degree of uncertainty due

to the limitations in acquired temporal and spatial resolution clinical data, as well as in the model. Computational methods were developed to incorporate a simpler model in an efficient Bayesian inference method that can take into account the uncertainties on the data and model parameters in the personalization [Konukoglu et al., 2011]. Extending such methods to the model used in the study could account the uncertainties in the application of the model.

2.5 Conclusion

We demonstrated in this manuscript that our personalized biophysical model was able to predict macroscopic VT circuits and exit point locations in agreement with clinically observed datasets. Our results suggest that patient-specific cardiac models may offer incremental clinical benefit in terms of ventricular arrhythmia risk stratification and in the planning and delivery of ablation strategies for re-entrant ventricular arrhythmias.

Non-invasive body surface mapping may be explored to obtain non-invasively such personalised cardiac model in order to facilitate the translation of the biophysical cardiac model processing pipeline to clinical practice [Rudy, 2013; Zettinig et al., 2014].

Chapter 3

Patient-Specific Mechanics: Application to Resynchronisation Therapy

– This chapter is based on [Sermesant et al., 2012]: Sermesant, M., Chabiniok, R., Chinchapatnam, P., Mansi, T., Billet, F., Moireau, P., Peyrat, J., Wong, K., Relan, J., Rhode, K., Ginks, M., Lambiase, P., Delingette, H., Sorine, M., Rinaldi, C., Chapelle, D., Razavi, R., and Ayache, N. Patient-specific electromechanical models of the heart for the prediction of pacing acute effects in CRT: A preliminary clinical validation. *Medical Image Analysis*, 16(1):201–215, 2012.

3.1 Introduction

Cardiovascular diseases (CVD) remain a major cause of morbidity and mortality in the Western World[1]. Within CVD, congestive heart failure (CHF) has an increasing prevalence mainly caused by the steadily increasing number of survivors following myocardial infarction. This leads to progressive derangements in myocardial function arising from scar formation post infraction. CHF has an extremely poor prognosis with a 50% mortality in the first three years after diagnosis. Many patients with heart failure also have significant conduction disease with a broad QRS on ECG often manifested as left bundle branch block. This results in electrical and mechanical dysynchrony and declining myocardial pump function. Cardiac resynchronisation therapy (CRT) consists of implanting pacing leads to improve the synchronisation of cardiac contraction [Cazeau et al., 2001]. Recent large randomised controlled clinical trials have shown that CRT induces significant reductions in morbidity and mortality [Cleland et al., 2005]. However, clinical trials have also demonstrated that up to 30% of patients are non-responders to the therapy [Ismail and Makaryus, 2010]. There is still significant controversy surrounding patient selection and optimisation of CRT (e.g. lead positioning, pacemaker settings). Current guidelines for selection for CRT rely on symptomatic, echocardiographic and electrocardiographic criteria. A broad QRS ($> 130\,ms$) is generally required to merit CRT implant. For instance, recent studies in patient selection showed that patients with heart failure and narrow QRS intervals do not currently benefit from CRT (RethinQ, [Beshai et al., 2007]) and that no single echocardiographic measure of dyssynchrony may be recommended to improve patient selection (PROSPECT, [Chung et al., 2008]). While image-based methods may give some insights into who might respond to therapy [Aggarwal et al., 2009], with e.g. detailed strain analysis from Magnetic Resonance Imaging (MRI) [Kirn et al., 2008], the precise prediction of the therapeutic effects and and how best to optimise pacing parameters remain out of reach. Therefore, new approaches are needed in order to provide a more accurate characterisation of ventricular electromechanical function to facilitate improved planning and delivery of the therapy.

In parallel, the last decades have seen major progress in medical imaging, cardiac modelling and computational power facilitating personalised simulations (i.e. using models with patient-specific parameters) of cardiac activity. While the scientific importance and enormous clinical potential of

[1] see for instance http://www.americanheart.org/statistics/ and http://www.heartstats.org/

this approach have been acknowledged [Crampin et al., 2004; Hunter and Nielsen, 2005; Kerckhoffs et al., 2008c], its translation into clinical applications has yet to be achieved. We aim to build on the major scientific advances in cardiac modelling that have already been made, in order to proceed to the next level and individualise such models to each specific patient using state-of-the-art multi-modal imaging. This approach has the potential to have a major impact on clinical practice. Indeed, patient management may be improved by allowing the clinical response at specific pacing sites to be predicted and fine-tuned in each patient.

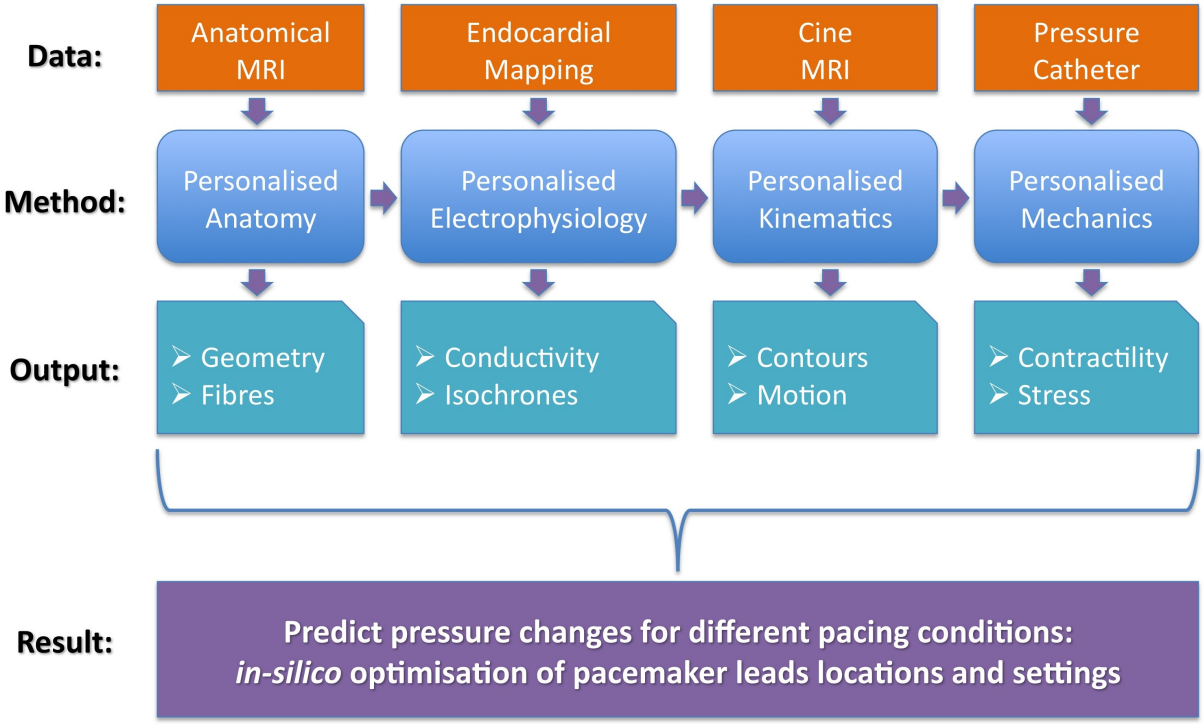

Figure 3.1: Global scheme of the clinical data used for the personalised models, the generated output maps and parameters, and the resulting predictions.

In this chapter, we demonstrate proof of concept of the personalisation of an electromechanical model of the heart to predict the responses in cardiac function due to effects of pacing the left ventricle at different endo and epicardial sites (see Fig. 3.1). Such predictions may be used to quantify the improvement in cardiac function that can be expected from CRT. Such a model may also be able to predict the optimal location of the pacemaker leads (stimulation electrodes) and allow optimal programming of timing of the electrical stimulation to ensure a maximal haemodynamic benefit. In this work we have only focused on the acute haemodynamic effects of CRT. The prediction of chronic reverse remodelling of the heart with CRT [Sutton and Keane, 2007] is out of the scope of the presented work.

There is an important body of literature on the functional imaging of the heart, for instance: measurements of electrical activity, deformation, flows, fibre orientation, and on the modelling of the electrical and mechanical activity of the heart. Many of these models are *direct* computational models, designed to simulate in a realistic manner the cardiac action in a realistic manner, often requiring high computational costs and the manual tuning of a very large number of parameters.

Mechanical modelling was used in order to constrain and regularise [Yan et al., 2007] or better interpret deformation from imaging data [Liu and Shi, 2007] with simultaneous parameter estimation [Hu et al., 2003], but without any prediction of changes with therapy.

Recently, computational models have been used to simulate CRT on a generic anatomy in computer studies [Kerckhoffs et al., 2010] or in comparison with animal experiments [Kerckhoffs et al., 2008a,b] and have provided important insights on the pathophysiology of dyssynchrony. In order to translate such models into the clinical arena and impact patient management and therapeutic planning, the models need to be individualised to each specific patient, which remains a challenging

task especially due to the dimensionality of the problem and the parameter observability.

The proposed approach involves models whose complexity is directly related to the phenomena observed in clinical data. This is the reason why these models are often simplified compared to those published in the literature. The observability of patient parameters parameters (electrophysiological, mechanical and haemodynamic) was crucial in the personalisation step. Utilising a limited number of pre-specified parameters allowed their identification from clinical measurements on a specific patient by solving a tractable *inverse* problem (see Fig. 3.1). While some steps of this method were interactive, the chosen models have the correct theoretical properties to make an automated adjustment possible.

A preliminary section details the clinical context, the data acquisition, and the data fusion into the same spatio-temporal reference frame. We then present the four sections describing the personalisation of the model anatomy, electrophysiology, kinematics and mechanics. Finally we demonstrate the predictions of acute haemodynamics in comparison to direct interventional measurements for multiple pacing conditions in two clinical cases.

3.2 Clinical Context, Data Acquisition and Fusion

The construction, testing and personalisation of biophysical models rely on the ability to fuse data from an array of sources. For cardiac modelling, the fusion of anatomical, mechanical, and electrophysiological data is of primary importance. This fusion must be both in the spatial and temporal domains. The sources of data used in the presented work are Magnetic Resonance Imaging (MRI), electrophysiology catheters, pressure catheter and X-ray fluoroscopy.

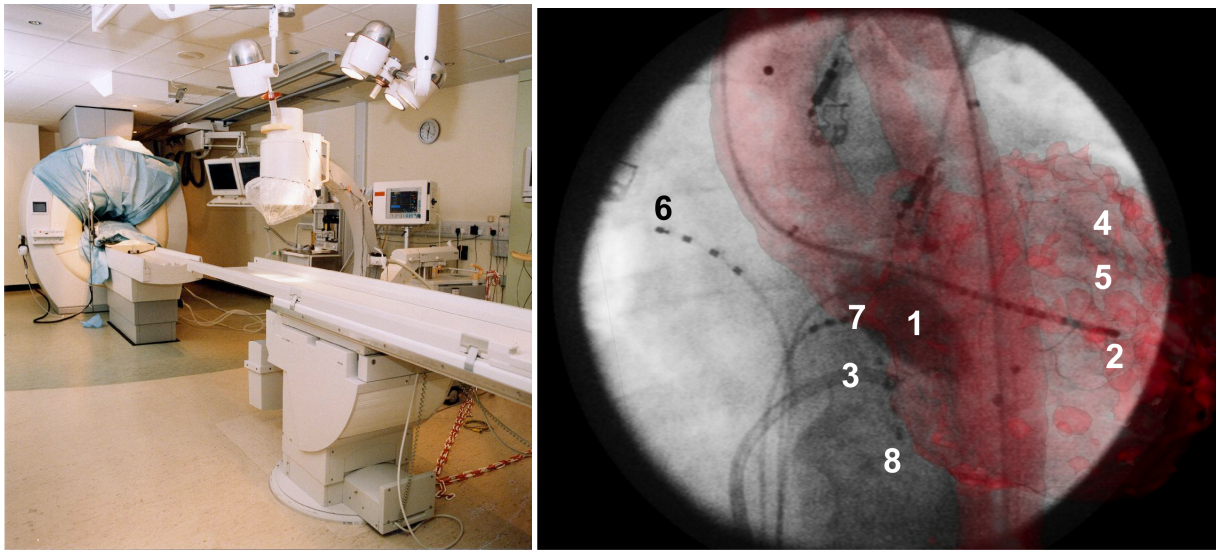

(a) XMR Suite (b) X-ray/MR fusion

Figure 3.2: (a) XMR suite with the MR scanner and the X-ray C-arm. (b) Real-time overlay of MRI-derived left ventricular (LV) surface model (red) onto live X-ray fluoroscopy image (grey scale) to guide the placement of catheters: (1) St. Jude Ensite balloon, (2) LV roving, (3) coronary sinus sheath, (4) coronary venous/epicardial, (5) pressure, (6) high right atrium, (7) His bundle, (8) right ventricle.

High quality cardiac anatomical and functional data can be obtained from MRI, such as myocardial shape, wall motion, blood flow and infarct sites, with a spatial resolution of approximately $1.5 \times 1.5 \times 7\,mm^3$ and a temporal resolution of around $30\,ms$. Electro-anatomical data can be obtained from catheter-based measurements that are guided using X-ray fluoroscopy with a spatial resolution of less than a centimetre and a temporal resolution close to a millisecond. Acute haemodynamic data is acquired using a high fidelity (200 Hz) pressure sensor to measure left ventricular pressure.

Spatial fusion of electrical and anatomical data requires an effective image registration strategy.

Our solution has focused on the use of an X-ray/MR (XMR) hybrid imaging system that allows the seamless collection of both MRI and X-ray-based data (see Fig. 3.2). We have developed a real-time registration solution [Rhode et al., 2005] that allows the spatial integration of MRI-based anatomical and functional data with X-ray-based catheter data, such as intracardiac electrophysiological and pressure signals. For the temporal integration, the electrocardiogram provides the information on the heart rhythm to enable the synchronisation of the datasets.

We present data based on two clinical cases scheduled to receive CRT. The first patient was a sixty year old woman with heart failure and NYHA class III symptoms[2]. The aetiology of heart failure was non ischaemic dilated cardiomyopathy with no flow-limiting disease on coronary angiography although cardiac MRI did show subendocardial postero-lateral scar in the left ventricle. The left ventricular ejection fraction was 25% on maximal tolerated heart failure medication. The surface ECG demonstrated significant conduction disease with left bundle branch block (LBBB) QRS duration of 154 ms (normal QRS is less than 120 ms). Echocardiography, including Tissue Doppler, confirmed significant mechanical dysynchrony in keeping with the ECG findings.

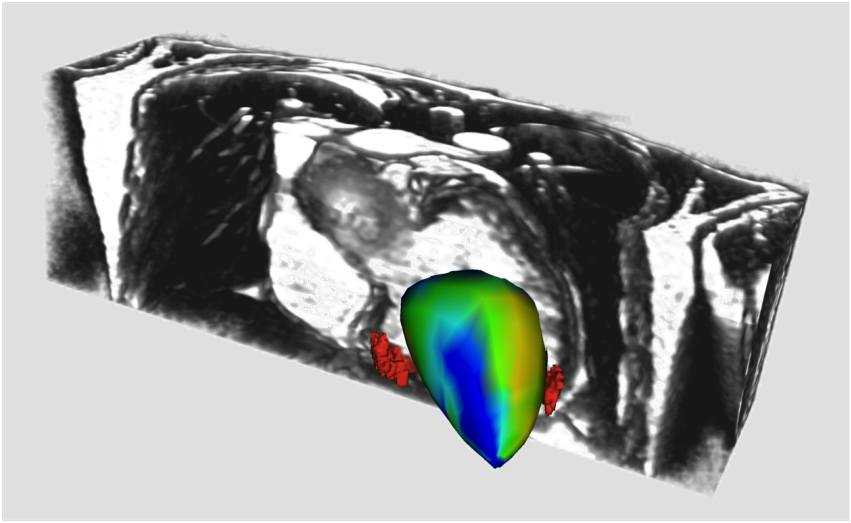

Figure 3.3: Fusion of late-enhancement derived scars (red surfaces), anatomical MR (volume rendering) and Ensite isochronal map (colored surface).

The second patient was a seventy seven year old woman with a much more developed dilated cardiomyopathy. She was in NYHA class III heart failure with a LV ejection fraction of 18% and left bundle branch block QRS duration of 200ms. There was no late gadolinium enhancement but functional conduction block was observed in the electrophysiological mapping.

For both cases, the clinical data used to set up the patient-specific models consisted of a cine-MRI[3] for the estimation of ventricular function and volumes and late enhancement images with gadolinium contrast agent for scar anatomy (in case of scars). A non-contact mapping study was performed using the Ensite 3000 multi-electrode array catheter system (St Jude, Sylmar, CA). This consists of a 64 laser-etched wire braid mounted on an 8mm balloon. The array records intracavity far-field potentials that are sampled at 1.2 kHz and digitally filtered at 0.1-300Hz. The resulting signals allow the reconstruction of over 3000 virtual unipolar electrograms superimposed on a computerised model of the left ventricle created using a locator signal on a roving endocardial catheter. We can then obtain both isopotential and isochronal maps. While non-contact mapping can suffer from motion and distance artefacts, it is well suited to create biophysical models as it can map several different pacing conditions from a single heart beat (while contact mapping would require a relatively large number of cycles for each pacing mode). The XMR fusion provides the location of the Ensite mapping with respect to the MR-derived information (see Fig. 3.3). We will illustrate the whole

[2]NYHA classes stand for the stages of heart failure according to the New York Heart Association. Patients with NYHA III are comfortable at rest but any other activity causes fatigue, palpitation, or dyspnea.

[3]cine-MRI usually cover the ventricles by a set of 2D dynamic sequences for which the image data are acquired with a temporal resolution of 20-40ms.

method with the data from Patient 1, but the same process was applied to the data from Patient2.

3.3 Personalised Anatomy

3.3.1 Model Specification

The anatomical model used is the compact (i.e. without trabeculae) ventricular myocardium. As we did not simulate the valves, we did not integrate the papillary muscles into the segmentation. This anatomical model is represented with a tetrahedral mesh which resolution is around 2 mm (mean edge length). This is to be compatible with the resolution of the data and the computational time of the models. We label the different tetrahedra of the mesh for regional parameter adjustment. The labels used include the AHA segments and the scars. Endocardial and epicardial surfaces were labelled as well. The complex cardiac fibre architecture has an important role in the electrical and mechanical function of the heart: electrical propagation and mechanical contraction are mainly along the fibre direction. The introduction of the fibre orientation in cardiac electromechanical modelling is thus essential for accurately simulating cardiac function. We use a synthetic model built with analytical laws describing general trends of fibre orientations observed in different studies [Streeter, 1979]. We assign a fibre orientation to each vertex of the mesh.

3.3.2 Model Personalisation

There is an extensive literature on the segmentation of the heart from medical images(see for instance [Ecabert et al., 2008; Zheng et al., 2008a; Peters et al., 2010] and references therein). However, to cope with extreme and variable anatomies due to pathologies, we developed a simple yet efficient semi-automatic method which combines specific image processing tools to extract the biventricular myocardium from cine-MRI. We segmented in the mid-diastolic volume of the cardiac sequence: the left ventricle (LV) endocardium (Fig. 3.4, red contour), the right ventricle (RV) endocardium (Fig. 3.4, blue contour) and the epicardium (Fig. 3.4, green contour). To this aim, we

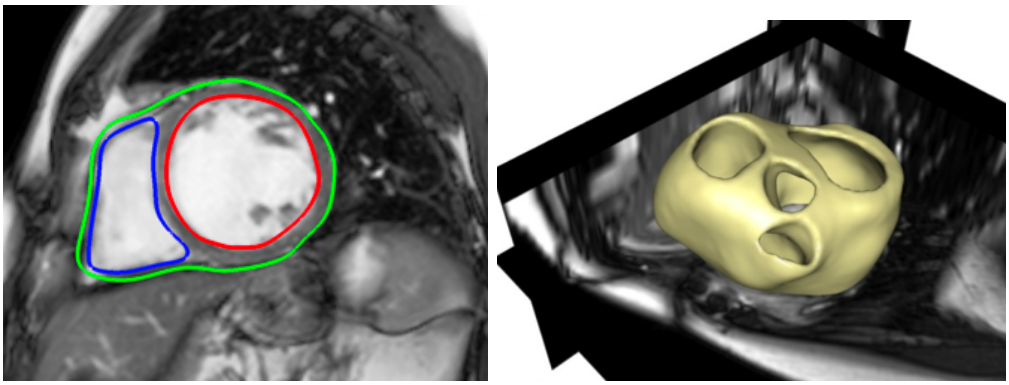

Figure 3.4: Personalised anatomy using image segmentation. Left: Three surfaces were defined during the segmentation, the left ventricular endocardium (in red), the right ventricular endocardium (in blue) and the epicardium (in green). Right: 3D visualization of the obtained anatomical model.

developed an interactive tool based on variational implicit functions [Turk and O'Brien, 1999]. This tool[4] allows the user to intuitively model any 3D surface in the 3D scene by placing, moving or deleting control points inside, on and outside the desired surface [Toussaint et al., 2008]. Then it computes in real-time the implicit function that interpolates those points and extracts its zero-level set surface. Union and intersection operations using these surfaces enables to generate a binary mask of the patient myocardium muscle.

[4] http://www-sop.inria.fr/asclepios/software/CardioViz3D/

Then the CGAL[5] and GHS3D[6] software were used to respectively extract the surface mesh from the volumetric binary mask and build the volumetric tetrahedral anatomical model from the surface mesh. Each tetrahedron was automatically labelled according to the anatomical region it belonged to (LV, RV or scar tissue, see Fig. 3.5). The scar label was based on the expert manual delineation on late enhancement MRI. Also, for regional parameter estimation, subdivision of the left ventricle according to the American Heart Association 17 segments was performed, see Fig. 3.5.

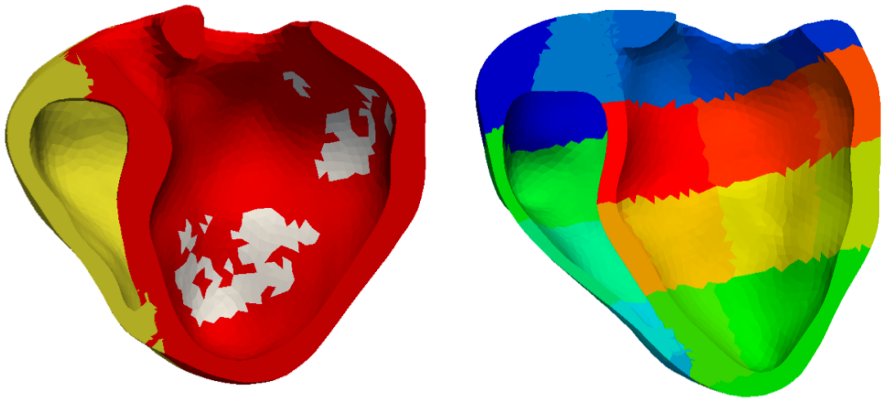

Figure 3.5: Labelled volumetric mesh. Three main areas are defined: left ventricle *(in red)*, right ventricle *(in yellow)* and scar *(in white)*. Additional AHA segments subdivision is also performed for regional personalisation

We generate the personalised fibre orientations by setting the parameters of the analytical model according to the angles observed in a statistical atlas [Peyrat et al., 2007], mapped into the geometry of the patient's heart (see Fig. 3.6). We only used here transverse anisotropy, neglecting the effect of the myocyte layers [Caldwell et al., 2009].

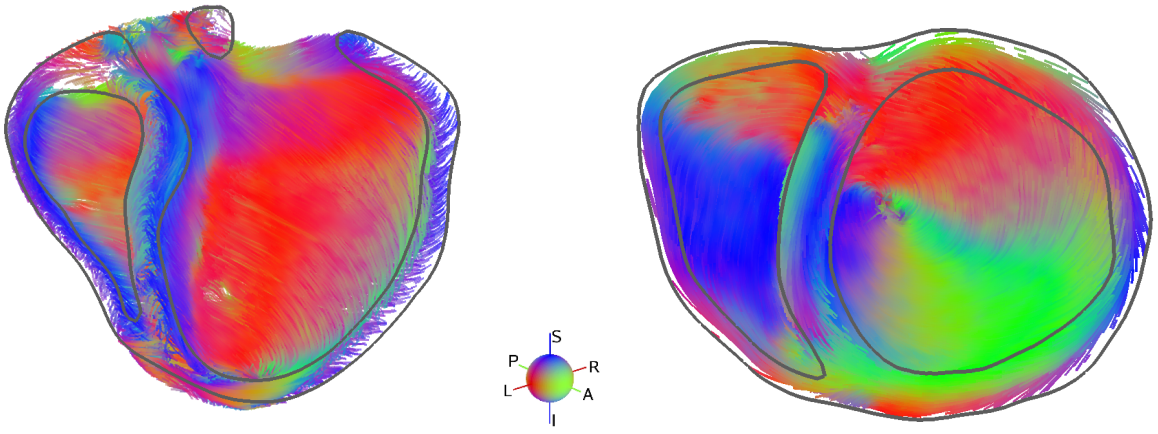

Figure 3.6: Long axis and short axis cut of the fibre orientations generated on the patient anatomy according to the statistical atlas information. Colour encodes direction.

3.3.3 Error Analysis

From visual inspection, the manual segmentation error is close to the image resolution. We can add more control points to refine the mesh, but the uncertainty on the data due to the large slice thickness and differences in breathing position make it unnecessary.

[5]http://www.cgal.org/
[6]http://www-roc.inria.fr/gamma/gamma/ghs3d/

There is definitely error in the personalised fibres as we do not have patient data to guide this personalisation and we do not model the influence of the pathology on these.

3.4 Personalised Electrophysiology

3.4.1 Model Specification

Modelling cellular electrophysiology (EP) is a very active research area [Hodgkin and Huxley, 1952; Noble, 1962; Beeler and Reuter, 1977; Luo and Rudy, 1991; Noble et al., 1998; Ten Tusscher et al., 2004]. At the organ level, it involves a cell membrane model embedded into a set of partial differential equations (PDEs) representing a continuum. Solving the dynamic PDEs is computationally very demanding, due to the space scale of the electrical propagation front being much smaller than the size of the ventricles, and the stability issues related to the dynamic nature of the equations. Moreover, the currently available clinical electrophysiological data only reliably measures the depolarisation times, and not the extracellular or transmembrane potentials. The advantage of the Eikonal equation [Keener and Sneyd, 1998; Colli Franzone et al., 1990] is that the front can be observed at a larger scale, resulting in much faster computations. Furthermore this equation can be solved very efficiently by using an anisotropic multi-front fast marching method [Sermesant et al., 2007]. For these reasons, we based our model on the Eikonal diffusion (ED) equation. The static ED equation for the depolarisation time (T_d) in the myocardium is given by

$$c_0\sqrt{\nabla T_d^t D \nabla T_d} - \nabla \cdot (D \nabla T_d) = \tau \tag{3.1}$$

where c_0 is a dimensionless constant related to the cell membrane, τ is the cell membrane time constant, ∇ the gradient operator and $\nabla\cdot$ the divergence operator. The tensor quantity relating to the fibre directions is given by $D = dA\bar{D}A^t$, where d is the square of the membrane space constant and thus related to the volumetric electrical conductivity of the tissue, A is the matrix defining the fibre directions in the global coordinates system and $\bar{D} = \mathrm{diag}(1, \lambda^2, \lambda^2)$. The parameter λ is the anisotropic ratio of membrane space constants along and transverse to the fibre direction f and is of the order 0.4 in human myocardium (see [Tomlinson, 2000] for more details on the ED equation and its parameters). $CV = c_0\sqrt{d}/\tau$ is homogeneous to a conduction velocity thus we present this parameter in the parameter map (Fig. 3.7) for easier interpretation.

3.4.2 Model Personalisation

To personalise the electrophysiological model, there were two important adjustments to perform: the onset of the electrical propagation, and the local conduction velocity. From the Ensite map of the left ventricular endocardium, we could see where the right ventricle excitation traverses the septum into the left ventricle (it corresponds to the isochrone 0 in the mapping data). We thus estimated the right ventricle Purkinje extremities as the symmetric through the septum of the zero-isochrone in the left ventricle Ensite data. We then used the ECG to compute the QRS duration in order to estimate a mean conduction velocity. We finally estimated the cardiac cell parameter d in the Eikonal model which corresponds to an apparent conductivity (AC). We estimated the AC by matching the simulated propagation times of the model to the clinically measured propagation times of the patient.

Several methods for the automatic adjustment of the AC were already proposed for surfaces [Moreau-Villéger et al., 2006; Chinchapatnam et al., 2008]. Such approaches were extended to volumetric models, by using a coupled error criterion both on endocardial depolarisation times (Fig. 3.7.a) and QRS duration. The multidimensional iterative minimisation is done using the NEWUOA algorithm [Powell, 2006].

The AC estimation was divided into two parts, first the endocardium and then the myocardial wall. This adjustment has the following steps:

1. Location of the electrical onset from the mapping data

2. Estimation of the endocardial regional AC by minimising the regional mean error between measured and simulated depolarisation times on the endocardial surface, with adaptive domain decomposition (at each iteration, we subdivide the region with the highest error, see [Chinchapatnam et al., 2008] for details)

3. Coupled estimation of the myocardial AC. The LV myocardium is divided into four regions: Septal, Anterior, Lateral, Posterior. For each region, a single AC value is used for the whole myocardial wall thickness (except the endocardium). We compute this estimation by minimising a cost function J composed of both the endocardial error with mapping and the QRS duration error with ECG:

$$J = \sum_{j=1}^{\mathrm{n_e}} \frac{1}{\mathrm{n_e}} (T_d^s - T_d^m)^2 + (T_{\mathrm{onset}}^s - T_{\mathrm{onset}}^m)^2 + (\mathrm{QRSd}^s - \mathrm{QRSd}^m)^2$$

where T_d^s and T_d^m are the simulated and measured endocardial depolarisation times on the n_e endocardial points, T_{onset}^s and T_{onset}^m are the simulated and measured onset depolarisation times on LV endo, and QRSd^s and QRSd^m the simulated and measured QRS durations.

3.4.3 Error Analysis

We applied this method to the baseline measurements and obtained a good fit to the data (Fig. 3.7.b), with a final mean error between simulated and measured isochrones of $9.1\,ms$. Fig. 3.7.c shows the CV map from the estimated AC. The scar locations were obtained from the segmentation of the late enhancement MR images. The resulting AC map provides information on some potential Purkinje network (high values) as well.

In the second patient case, a site of functional block was identified in the mapping data isochrones, and automatically estimated when fitting the isochrones. We defined it as transmural, as simulations without fully transmural block were not producing results in accordance with the endocardial data. We ran the personalisation algorithm and obtained a $8.0\,ms$ final mean error.

For Patient 1, the final number of endocardial regions was 56, with the smallest region having an area of around 23 mm^2. For Patient 2, the final number of endocardial regions was 37, with the smallest region having an area of around 75 mm^2.

This personalisation provides results with less than 10% error on the endocardium and a realistic extrapolation to the whole myocardium. The detailed figures of the errors for the different pacing conditions are presented in Tables 3.1 and 3.2. These errors are low after each personalisation, however we only have a very partial view of the propagation from baseline data (only the left ventricle endocardium, and for one condition), thus the accurate prediction of the isochrones for different pacings is still work in progress.

In the following two sections we discuss how a simplified model was used to estimate the cardiac motion (kinematics), and then how a more complex model was used to simulate the cardiac forces (mechanics).

3.5 Personalised Kinematics

3.5.1 Model Specification

In this subsection, we extract the cardiac motion from the cine-MRI. There are numerous methods proposed in the literature for this task, but we want here to take advantage of the entire patient data already integrated through the previous two sections. Thus we use a 3D proactive deformable model approach to estimate the motion of the heart from cine-MRI volumes. It enables to input the prior knowledge on the anatomy and electrophysiology in the motion estimation, while other methods from the literature cannot benefit from such knowledge.

The 3D model used here was a simplified electromechanical model designed for cardiac image analysis and simulation [Sermesant et al., 2006a], derived from a multi-scale modelling of the myocardium [Bestel et al., 2001]. The complexity of the model was designed to match the relatively sparse

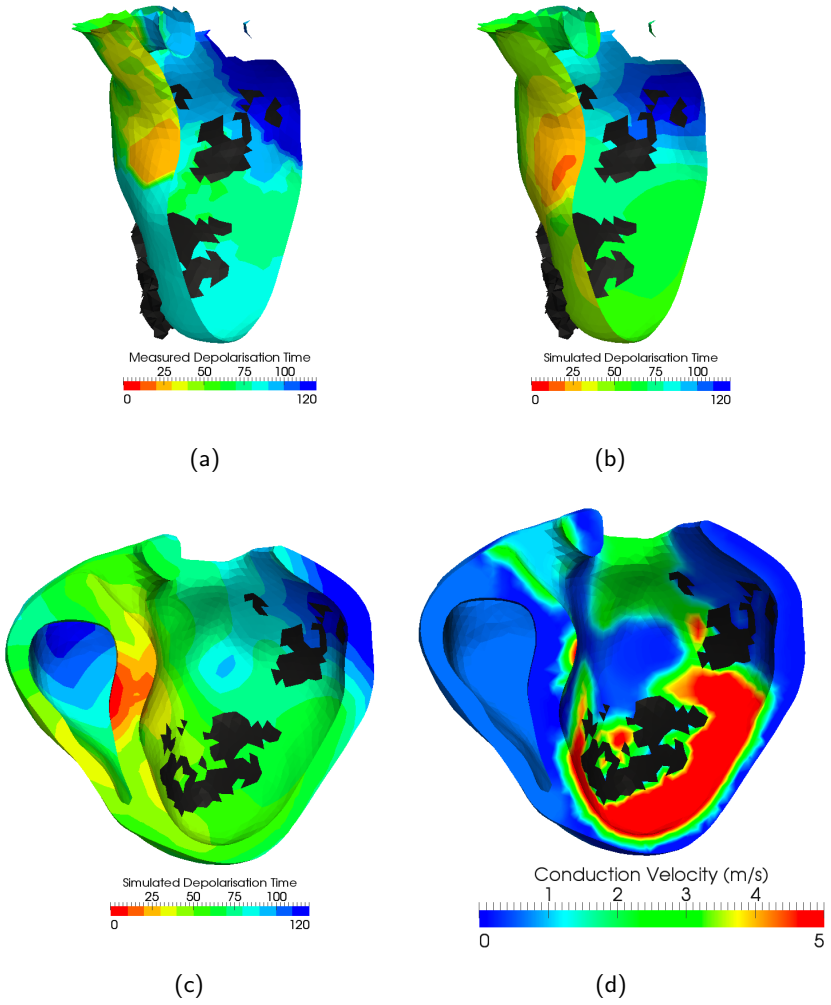

Figure 3.7: (a) Long axis cut of the measured isochrones projected on the MR-derived endocardium (septum is in front). (b) Simulated endocardial isochrones with the personalised model, and (c) within the whole myocardium. (d) Conduction velocity (CV) parameter map from the automatically estimated AC. High CV areas (in red) represent probable areas of Purkinje extremities. Black regions are scar locations from MRI.

measurements. It is composed of two elements in parallel: one anisotropic linear visco-elastic to represent the passive properties of the tissue and one active contractile element controlled by the command u. This command was set to a constant k_{ATP} (the contraction rate) when depolarisation occurs at time T_d and to a constant $-k_{RS}$ (the relaxation rate) when repolarisation occurs at repolarisation time $T_r = T_d + APD$, with APD a given Action Potential Duration. For one tetrahedral element, the active stress σ_c was controlled by u through the ordinary differential equation (a reduced version of the more detailed stress model used for personalised mechanics in next Section 3.6):

$$\dot{\sigma}_c + |u|\sigma_c = |u|_+\sigma_0$$

where σ_0 is the peak stress parameter and $|u|_+$ represents the positive part of the command u (u is positive during contraction and negative during relaxation). Then, the integral of the divergence of the active stress over a tetrahedron results in a 3D force vector $\vec{f_C} = \sigma_c \int_S \left(\vec{f}.\vec{n}\right) \vec{f} dS$ with f the fibre direction, $\vec{n}$ the surface normal and dS the element surface of the tetrahedron. The simplified dynamics law is then:

$$M\ddot{Y} + C\dot{Y} + KY = F_P + F_C + F_B \tag{3.2}$$

with Y the position vector, $\dot{Y} = dY/dt$ the velocity, $\ddot{Y} = d^2Y/dt^2$ the acceleration, K the stiffness matrix for the transverse anisotropic elastic part (parallel element), M a diagonal mass matrix, C

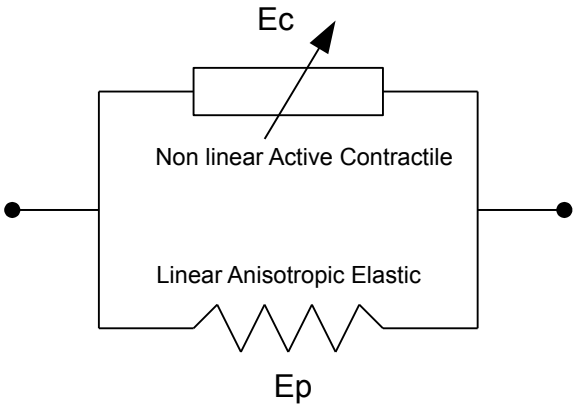

Figure 3.8: Simplified model constitutive law with a linear anisotropic elastic element (E_c) and a non linear active contractile element (E_c).

the Rayleigh damping matrix (internal viscosity component), F_C the assembled contraction force, F_P the developed pressure forces in the ventricles and F_B a force vector corresponding to the other boundary conditions. Furthermore, we simulated the four cardiac phases (filling, isovolumetric contraction, ejection and isovolumetric relaxation) as detailed in [Sermesant et al., 2006a]. Finally, the arterial pressures were computed using a Windkessel model [Stergiopulos et al., 1999].

3.5.2 Model Personalisation

We estimated the motion of the heart by coupling this electromechanical model with cine-MRI, based on the proactive deformable model described in [Sermesant et al., 2006a; Billet et al., 2009]. We have shown in [Billet et al., 2008] that this method is related to the data assimilation approach described in [Moireau et al., 2008]. Numerous studies on the adjustment of a geometrical model of the heart to time series of medical images are based on the concept of deformable models [Park et al., 1996; McInerney and Terzopoulos, 1996; Montagnat and Delingette, 2005]. In this framework, a mesh is fitted to the apparent boundaries of the myocardium by minimising the sum of two energies: a data attachment term and a regularisation term. In our case, this regularisation term consisted in the energy of the dynamical system of the simplified electromechanical model of the heart.

We aimed to minimise the difference between the simulated motion of the myocardium and the apparent motion in the images. To this end, we defined an image force F_I which attracts each surface vertex Y_i towards its corresponding voxel Y_i^{img} in the image. This corresponding voxel is searched for both with a gradient approach [Montagnat and Delingette, 2005] (looking for high gradient voxels along the mesh normal direction) and with a block-matching algorithm [Ourselin et al., 2000] associated with each surface vertex of the mesh. This combination allowed to correct the block-matching tracking, when the initial position was not exactly on the endocardium. The new law of dynamics with these additional image forces F_I is then given by this equation:

$$M\ddot{\hat{Y}} + C\dot{\hat{Y}} + K\hat{Y} = F_P + F_C + F_B + F_I \tag{3.3}$$

where $\hat{Y}$ is the estimated position of the heart nodes.

From global parameters like the ejection fraction we could calibrate the mechanical parameters of the contractile element (k_{ATP}, k_{RS} and σ_0).

3.5.3 Error Analysis

Fig. 3.9 shows the MR images at end-diastole and at end-systole of the cardiac cycle. The superimposed lines represent the intersection of the endocardial and epicardial surfaces of the mesh with the images.

We can observe that despite the limited quality of routine clinical images, the estimation of the myocardium contours is good, especially for the left ventricle (see Fig. 3.9 for a comparison with

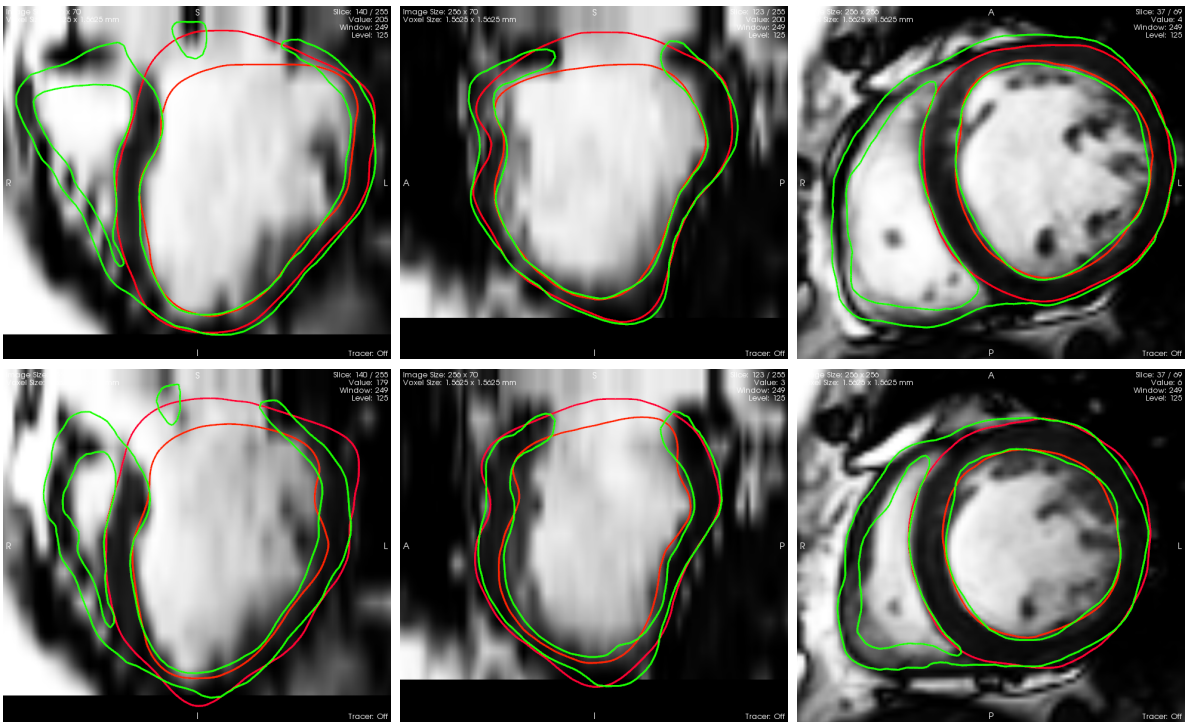

Figure 3.9: Results of the motion tracking: manual delineation of LV blood pool and LV epicardium (without valves, red line) estimated myocardial mesh (green line) superimposed with cine-MRI at (top) end-diastole and (bottom) end-systole.

an independant manual delineation, we focus here on the compact myocardium, not on papillary muscles and trabeculae). Due to the lack of contrast on the epicardium and the thinness of the right ventricle, achieving a good tracking of the RV wall is still challenging.

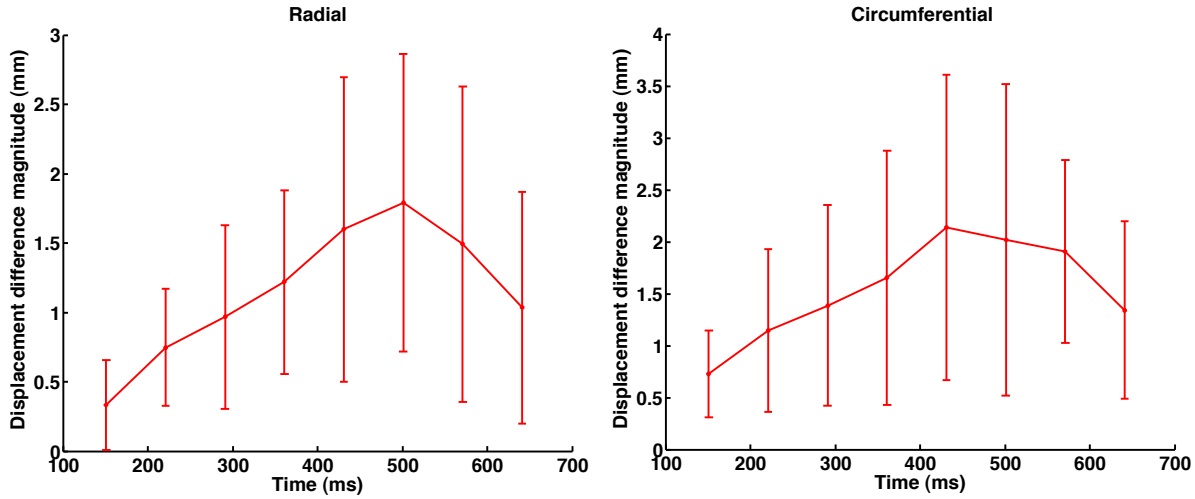

Figure 3.10: Mean radial (left) and circumferential (right) displacement error between the estimated motion and the manually measured one in 7 short axis tagged MRI slices (in-plane image resolution is $1.6mm^2$).

This approach allowed to recover a realistic motion of the heart, including a twisting component captured by the model even if the images provide information mostly in the direction orthogonal to the endocardium. This was actually validated with additional tagged-MRI acquired on the first patient, where the circumferential motion estimated with this method from cine-MRI was in good agreement (up to the image resolution) with the one measured from the tags by manually tracking tag intersections in seven short axis slices (see Fig. 3.10). A more detailed validation and sensitivity

analysis of this method can be found in [Wong et al., 2010].

3.6 Personalised Mechanics

We then adjust a more detailed mechanical model in order to personalise the simulated pressure curve.

3.6.1 Model Specification

The myocardium constitutive law has to model the active, non-linear, anisotropic, incompressible and visco-elastic properties of the cardiac tissue. Numerous formulations have been proposed in the literature, see e.g. [Humphrey et al., 1990; Nash, 1998; Hunter et al., 1997; Caillerie et al., 2003; Hunter et al., 1998; Smith et al., 2000; Humphrey, 2002; Sachse, 2004] and references therein. The particularity of the model used in this study is that it was designed to have a complexity compatible with the clinical data used for the personalisation. As apparent motion and left ventricular pressure are the main components of the observations, we relied on models with limited parameters representing the passive and active parts of the constitutive law.

Most of the components of the mechanical model discussed in this section are quite classically used in heart models. However, the specificity of our model are its consistency with essential thermomechanical requirements and the physiological interpretation of its components. Moreover, its global integration preserves these requirements from the continuous dynamical equations to the discrete versions (see details in [Sainte-Marie et al., 2006]).

Denoting by σ_c the active stress and by e_c the strain along the sarcomere, the myofibre active constitutive law relates σ_c and e_c as follows [Bestel et al., 2001]:

$$\left\{\begin{array}{ll} \dot{\tau}_c = k_c\dot{e}_c - (\alpha|\dot{e}_c| + |u|)\tau_c + \sigma_0|u|_+ & \tau_c(0) = 0 \\ \dot{k}_c = -(\alpha|\dot{e}_c| + |u|)k_c + k_0|u|_+ & k_c(0) = 0 \\ \sigma_c = \tau_c + \mu\dot{e}_c + k_c\xi_0 & \end{array}\right. \tag{3.4}$$

where u still models the electrical input from the action potential ($u > 0$ contraction, $u \leq 0$ relaxation). As the previous simplified model was derived from this one, identically named variables and parameters are related but here the active component is more detailed. Parameters k_0 and σ_0 characterise muscular contractility and respectively correspond to the maximum value for the active stiffness k_c and for the stress τ_c in the sarcomere, while μ is a viscosity parameter.

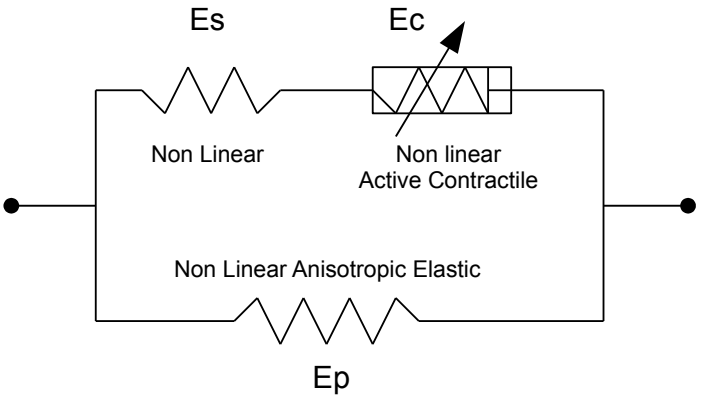

Figure 3.11: Complex model constitutive law with a non linear hyperelastic element (E_p), a non linear active contractile element (E_c), and a non linear series element (E_s.

The above active constitutive law was used within a rheological model of Hill-Maxwell type [Chapelle et al., 2001]. This rheological model is compatible with large displacements and strains and led to a continuum mechanics description of the cardiac tissue [Sainte-Marie et al., 2006]. In the parallel

branch of the Hill-Maxwell model we considered a viscoelastic behaviour, with a hyperelastic potential given by the Ciarlet-Geymonat volumic energy [Le Tallec, 1994]:

$$W = \kappa_1(J_1 - 3) + \kappa_2(J_2 - 3) + \kappa(J - 1) - \kappa \ln J,$$

where (J_1, J_2, J) denote the reduced invariants of the Cauchy-Green strain tensor, and $(\kappa_1, \kappa_2, \kappa)$ are material parameters.

Then the pressure within the ventricle represents the main loading which balances the tissue stresses in the dynamics equilibrium equation, also called principle of virtual work when written in a weak form, see [Sainte-Marie et al., 2006] for the detailed expression in the heart model considered. During the ejection phase, the ventricle pressure also equilibrates the Windkessel pressure. Globally, the model equations are closed, and we can see the ventricle pressure as an output of the system, while the electrical activation u is the input.

3.6.2 Model Personalisation

We input into the model the depolarisation and repolarisation times estimated in Section 3.4, and now adjust the mechanical material parameters. Some valuable information on the spatial distribution of these may be obtained from clinical measurements such as late enhancement MRI, but the actual values of the perturbed parameters cannot be directly measured. The completely automated estimation of these parameters is still a scientific challenge, but we demonstrate here that an interactive calibration of the parameters based on global physiological indicators and cardiac motion can provide already satisfactory predictability in the direct simulation of the cardiac function.

For this simulation, image information was no longer used to constrain the motion, thus boundary conditions are especially important to achieve realistic motion. As can be seen in the cine-MRI sequences, there is an epicardium area near the apex on the inferior wall with small displacements, probably in relation with the attachment of the pericardium to the diaphragm. We modelled this physiological feature by prescribing some stiff viscoelastic support as boundary conditions in this area. Furthermore, we used soft viscoelastic support conditions on the valve annuli to model the truncated anatomy. The corresponding viscoelastic coefficients also required proper calibration with respect to the motion observed in image sequences.

The constitutive parameters have then been manually calibrated using the pressure-volume loop and the cine-MRI by means of the local motion pattern of the ventricles. In a nutshell, the hyperelastic constitutive parameters were calibrated using the data (ventricle pressure and volume) corresponding to the atrial contraction. Next, the tissue contractility was globally adjusted to obtain an adequate ejection fraction when maintaining a fixed value for the arterial pressure, namely, the measured end-systolic pressure. In order to represent the less contractile areas, the corresponding contractility parameters were weighted by a factor $1/5$ with respect to their global value, as substantiated in [Chabiniok et al., 2009]. Finally, the Windkessel parameters (proximal capacitance C_p, resistance R_p, distal capacitance C_d and resistance R_d) were calibrated so as to obtain an adequate arterial pressure curve over the whole cycle.

3.6.3 Error Analysis

With these personalised parameters, we obtain a simulated motion relatively close to the one estimated from the personalised kinematics. We compared the simulated motion with the personalised mechanical parameters to the motion extracted from the images with the personalised kinematic model and we obtained differences close to the in-plane voxel size (see Fig. 3.12).

We output the simulated ventricular pressure and compared it with the measurements, see Fig 3.13. This personalised mechanical model simulated a ventricular pressure curve in very good agreement with the catheter measurement (see Fig. 3.13).

From this interactive adjustment, it was observed that for these two patients, the global contractility was a key parameter in the pressure personalisation, and the local adjustments were mostly correcting the differences in local motion, without much impact on the global indices.

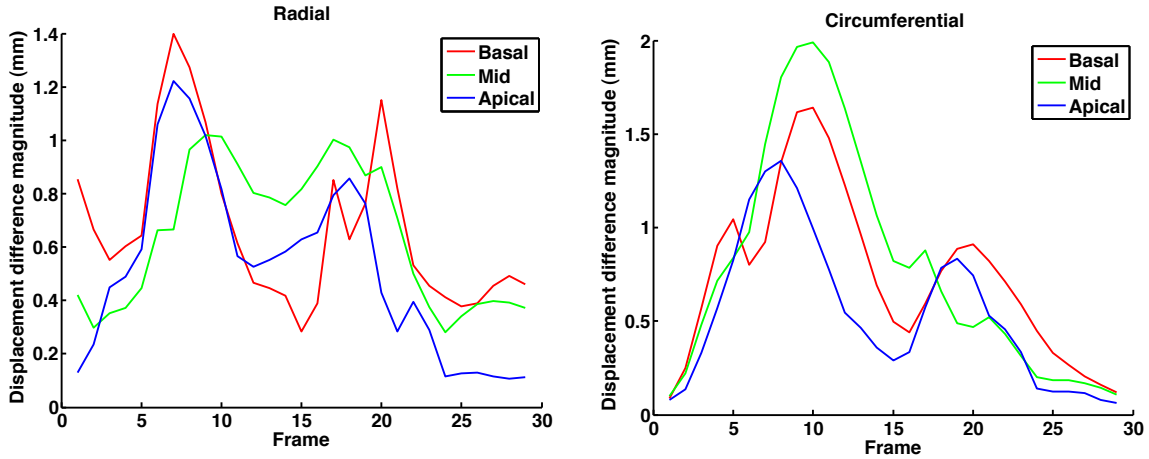

(a) (b)

Figure 3.12: Comparison between the motion from the personalised mechanical model and the personalised kinematic model in radial (left) and circumferential (right) directions, for three (basal, mid and apical) ventricular regions.

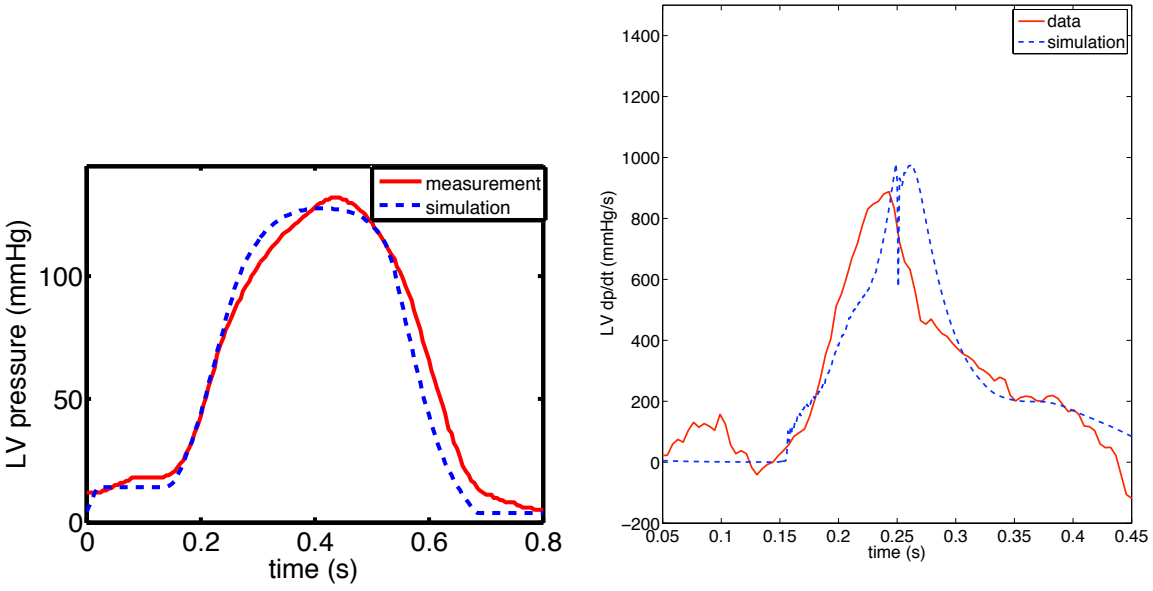

(a) (b)

Figure 3.13: Measured (solid red) and simulated (dashed blue) (a) pressure curves and (b) dP/dt curves in sinus rhythm.

Note that the slope of the simulated pressure curve (dP/dt) is less accurate in the diastolic phase as the repolarisation time measurement from non-contact mapping data is more difficult due to the small size of the T wave and far-field effects, but CRT mostly focus on the contraction phase.

3.7 Prediction of the Acute Effects of Pacing

During the acute electrophysiological study preceding device implantation, different pacing configurations were tested to evaluate the effect of different lead locations and delays. We measured the acute haemodynamic response to different pacing parameters and lead locations. This was assessed using a pressure wire in the LV cavity from which we were able to measure dP/dt. This also provides

the opportunity to estimate what could be the expected haemodynamic benefit from the pacemaker implant.

In this section, we tested the ability of our personalised electromechanical model of the myocardium to predict the changes in the heart function due to a new pacing condition. The different pacing protocols tested here were atrial pacing (atrial), right ventricular pacing (RV), left ventricular endocardial pacing (LVendo), biventricular pacing (BiVsim), and biventricular pacing with simultaneous endocardial left ventricular pacing (TriV). We first estimated the volumetric depolarisation isochrones using the method of Section 3.4 and then input these isochrones into the already personalised model of section 3.6 to simulate the new pressure curve.

For each of the pacing modes, we used the personalisation strategy of Section 3.4 to obtain the volumetric depolarisation isochrones from the endocardial mapping data. The obtained endocardial

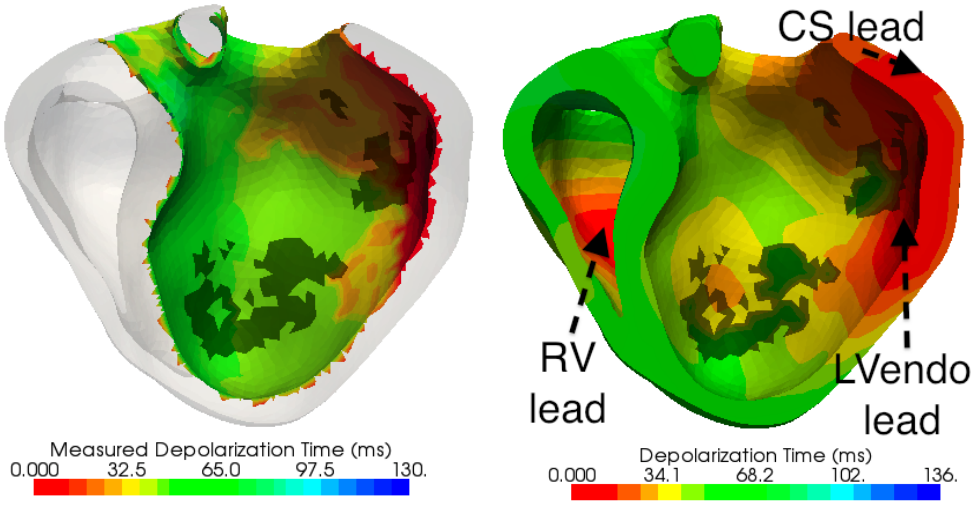

(a) (b)

Figure 3.14: (a) Measured isochrones for TriV pacing, projected on the MR endocardium. The onsets on the LV free wall from the coronary sinus (CS) and endocardial (LVendo) pacing catheters are clearly visible. (b) Predicted volumetric isochrones using the AC map estimation from the known onset locations in LV and RV and the endocardial activation.

isochrones are in good agreement with the data (see for instance Fig. 3.14.b).

Over all the different pacing modes and regions, we obtained an average AC of 1.68±0.29 for Patient 1 and 2.74±0.61 for Patient 2. Each pacing configuration was producing AC maps with the same global characteristics, but local modifications fitting the local specificities of each pacing helped in achieving a good accuracy in all the cases.

For the mechanical simulation, we used the model personalised in section 3.6 on baseline in sinus rhythm, without changing any parameter. We only input the new electrical command corresponding to the different pacing conditions. Hence, the model parameters were not changed, except for the electrical activation input.

3.7.1 Model Predictions

The resulting simulated pressure curves (see Fig. 3.15) obtained are in very good agreement with the measured. These curves allowed to test in particular the predictions on the slope changes of this pressure, which is sought to be optimised by CRT. One important index of the effectiveness of the contraction is the maximum of the pressure time-derivative, $(dP/dt)_{max}$. It describes how the pressure builds up during the isovolumetric contraction. We present in Fig. 3.16 and Fig. 3.17 the results on the predictions of $(dP/dt)_{max}$ for the two patients (numerical figures can be found in Table 3.4 and Table 3.5).

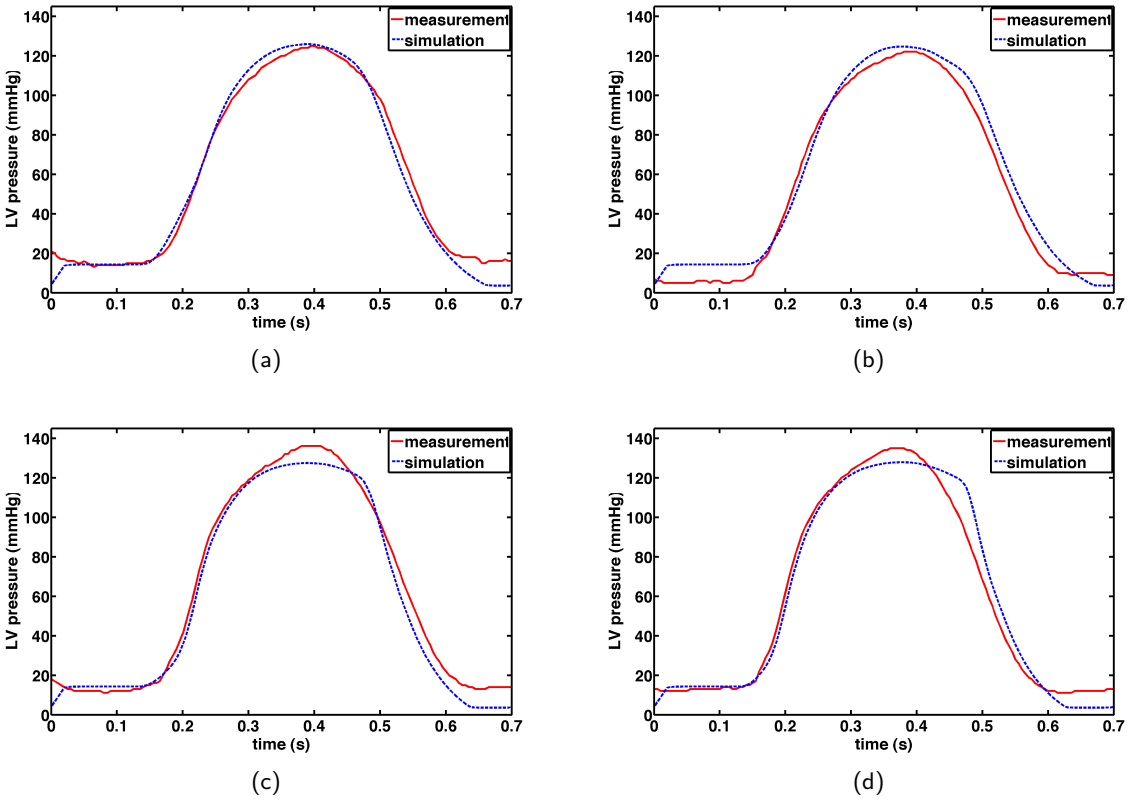

Figure 3.15: Measured (solid red) and predicted (dashed blue) pressure curves for (a) atrial, (b) RV, (c) LVendo, and (d) TriV pacing modes.

3.7.2 Error Analysis

For this first patient, the different simulated pacing modes with the model personalised from baseline measurements achieved a very good agreement of the predicted pressure curve with the recorded data from the pressure catheter (see Fig. 3.15.a). The improvement of the cardiac function brought by the pacing in Patient 1 was very reliably predicted by the *in silico* simulations. Such accuracy was achieved for all the different pacing modes (see Fig. 3.16).

We applied exactly the same methodology on Patient 2, with a more pronounced dilated cardiomyopathy (DCM) and without any myocardial scar. A functional conduction block was visible from the electrophysiological mapping data, which was reproduced in the personalised model. For the mechanical personalisation, in order to achieve a good adjustment to the measured motion and pressure, the passive tissue stiffness was increased (see Table 3.3). This could be explained by a fibrotic remodelling in a highly developed DCM. The adjustment on baseline and the predictions of $(dP/dt)_{max}$ for atrial, BiV, and TriV pacing are presented in Fig. 3.17.

For this second patient, the predictions were still in agreement with the measurements, however with a slightly larger error. This is probably due to the influence of functional block in viable tissue and therefore a binary definition of block and healthy tissue may be too simplistic since the conduction properties are more heterogeneous than the current modelling parameters allow. Moreover, the transmurality of such block is harder to evaluate as it does not appear in images. The adjustment of the electrophysiology model was more difficult, which can explain the loss in accuracy of the resulting mechanical simulations.

Overall, in these two patients we obtained a mean error on simulated dP/dt_{max} of $47.5 \pm 35\ mmHg.s^{-}1$, which is less than 5% error. This is a very low error, given the different potential sources of error in this whole personalisation.

The accuracy of the predictions in the different pacing modes relies heavily on the accuracy of the volumetric isochrones provided to the mechanical model. This is why for this first validation we used all the available mapping data to test the mechanical predictions.

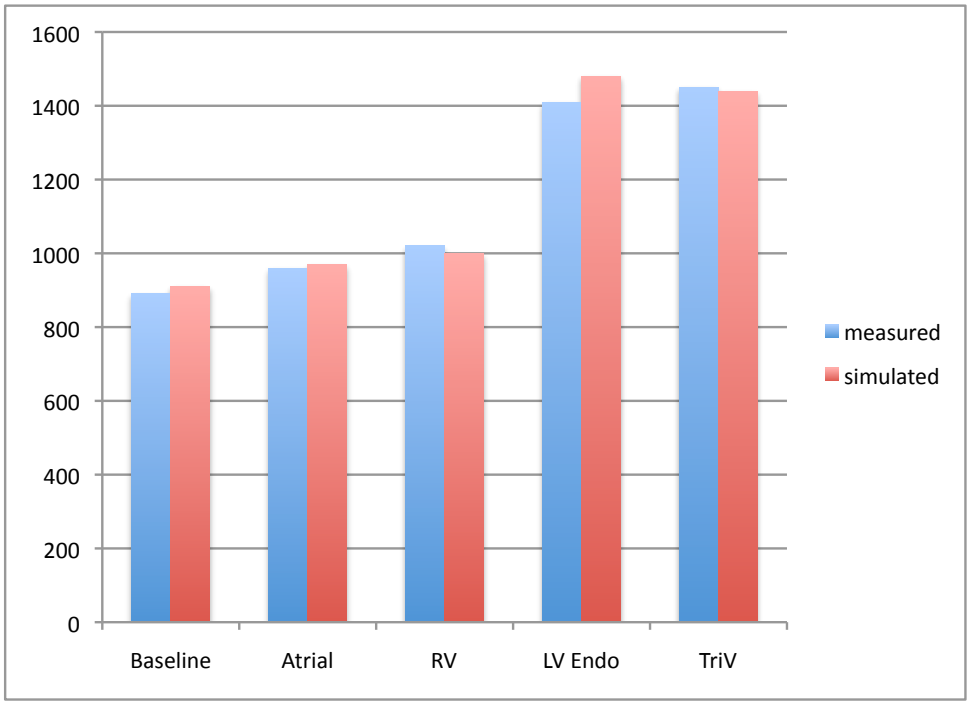

Figure 3.16: Patient 1: Measured (blue) and simulated (red) $(dP/dt)_{max}$ for different pacing conditions. Parameters were estimated on baseline and then kept constant.

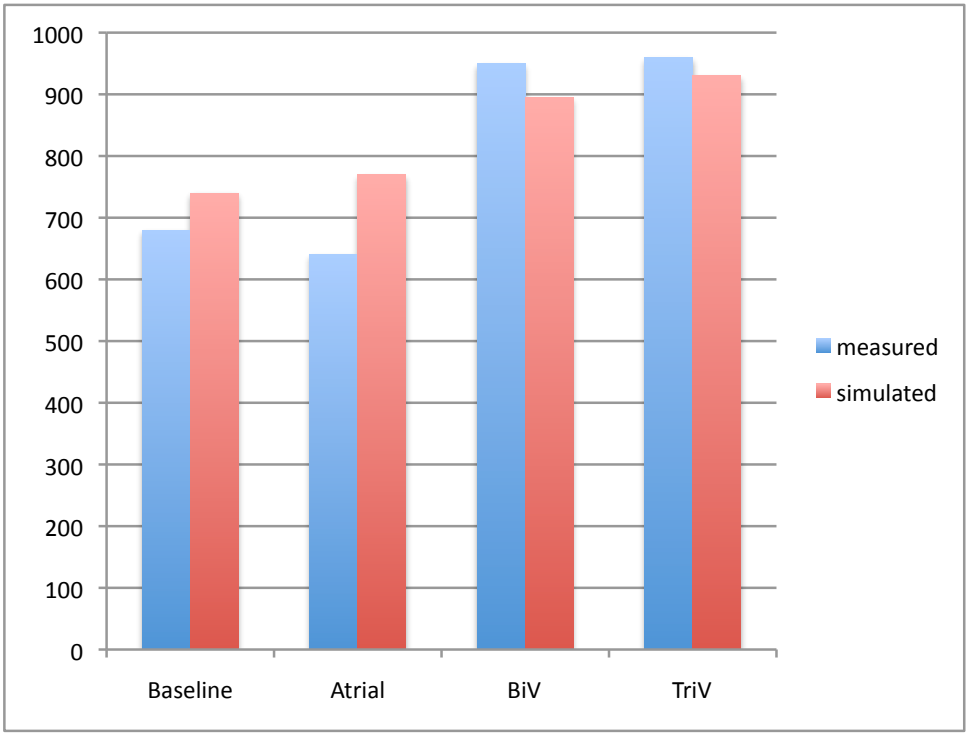

Figure 3.17: Patient 2: Measured (blue) and simulated (red) $(dP/dt)_{max}$ for different pacing conditions. Parameters were estimated on baseline and then kept constants.

3.8 Conclusion

We have developed and demonstrated a personalised electromechanical modelling technique to determine patient-specific estimates of myocardial conductivity and contractility parameters using cardiac MRI, LV endocardial electrophysiological mapping and pressure recordings. We then used this model to predict the acute haemodynamic effects of different left ventricular pacing configurations in

two subjects with heart failure. The behaviour of the model in sinus rhythm as well as the predictions of the model under different pacing conditions compare well with the measured data for these two clinical cases, which makes such an approach very promising.

This case study demonstrated how electromechanical models of the heart can be adjusted to be patient-specific and is a proof of concept of how this approach may be useful for therapy planning. By integrating information about the anatomy, the electrophysiology, the kinematics and the mechanics, we can explore the correlation between these different aspects for a given patient in order to provide an integrated view of the patient's cardiac function and simulate and evaluate different therapies before their actual application.

This method is still a relatively complex pipeline, however there are interesting perspectives in order to automate many steps and simplify its application. At the anatomical level, the automatic extraction of the different structures of the heart from medical images is becoming available [Ecabert et al., 2008; Zheng et al., 2008a; Peters et al., 2010]. Regarding the fibre orientation, it is known that scarring affects local fibre organisation [Zimmerman et al., 2000], but this is not incorporated into in our anatomical model at present. As conductivity and contractility are reduced within the scars in the simulations, the impact of these organisational changes may be limited. Recent progress with *in vivo* cardiac DTI are very encouraging for patient-specific fibre architecture measurement [Wu et al., 2009; Toussaint et al., 2010] and could be used instead of the currently prescribed directions. However, data on the myocyte layers will be significantly harder to measure, thus the effects of the orthotropic anisotropy would only come from prior knowledge [Caldwell et al., 2009].

For the electrophysiology, the isochrones could also have been predicted using the baseline parameters, but the detailed validation of the predictive power of the electrophysiological model is not the focus of this manuscript, we used the mapping data for each pacing mode and demonstrate firstly the predictions achieved on the mechanical side. Moreover, the pacing modes give additional information on the myocardium wall conductivity, through the QRS duration, so we use all the available data to improve the personalisation. However, the validation of the electrophysiological predictions is needed in order to be able to test *in silico* a large range of pacing conditions. Finally, such model-based approach would be most beneficial if it could be based purely on non-invasive data, using for instance the important work on the inverse problem of electrocardiography (see e.g. [Pfeifer et al., 2008]).

For the mechanics, while several steps still require interactive adjustment, the methodology for automatic parameter estimation is becoming available [Sermesant et al., 2006b; Moireau et al., 2008; Wang et al., 2009; Moireau et al., 2009]. Any available motion information (for instance from tagged-MRI) can be directly used within such frameworks. A robust method for automatic mechanical parameter estimation from patient data would make the translation of such methods into clinical practice achievable.

To conclude, in the case of CRT, such predictions could help optimise *in silico* the positioning of pacemaker leads and device settings to improve the clinical response to CRT in individual patients. This will be the purpose of future work.

3.A Numerical Values of Errors and Parameters

3.A.1 Final Error in Personalised Electrophysiology

We present in Tables 3.1 and 3.2 the mean and standard deviation of the depolarisation time error on the LV endocardium and the error on the QRS duration.

3.A.2 Adjusted Parameters in Personalised Mechanis

We summarised in Table 3.3 the adjusted values of the mechanical parameters. We can observe the increased stiffness and decreasd contractility of the scars in Patient 1 and the generally increased stiffness and decreased contractility in Patient 2, that may be due to the importance of the cardiomyopathy.

Pacing Mode	Mean Error ± Std Dev (ms)	QRS Error (ms)
Baseline	9.1 ±7.3	1.3
Atrial	7.3 ±6.9	1.6
RV	7.3 ±6.5	0.1
LV Endo	6.0 ±5.5	0.4
TriV	9.1 ±6.5	5.2

Table 3.1: Patient 1 final error values obtained after electrophysiology model personalisation.

Pacing Mode	Mean Error ± Std Dev (ms)	QRS Error (ms)
Baseline	8.0±7.1	0.065
Atrial	7.5±7.0	0.054
RV	8.7±8.1	0.11
BiV	11.6±10.3	2.8
TriV	8.1±8.5	2.4

Table 3.2: Patient 2 final error values obtained after electrophysiology model personalisation.

Parameter	Patient 1	Patient 2
κ_1 (in Pa)	Healthy: 10^4	1.5×10^4
	Scar: 10^5	
κ_2 (in Pa)	Healthy: 80	120
	Scar: 800	
κ (in Pa)	Healthy: 10^5	1.5×10^6
	Scar: 10^6	
σ_0 (in Pa)	LV: 3.4×10^5	3.0×10^5
	RV: 1.7×10^5	1.5×10^5
	Scar: 4.6×10^4	
C_p (in m^3/Pa)	2.3×10^{-10}	7.0×10^{-10}
R_p (in $Pa.s/m^3$)	2.1×10^7	7.2×10^6
C_d (in m^3/Pa)	7.2×10^{-9}	2.7×10^{-8}
R_d (in $Pa.s/m^3$)	2.0×10^8	8.0×10^7

Table 3.3: Mechanical parameter values used in the two cases after personalisation.

3.A.3 Comparison between Measured and Simulated dP/dt_{max}

We sum up in Tables 3.4 and 3.5 the simulated and measured dP/dt_{max} values for the two patients.

Pacing	Measured	Simulated
Baseline	890	930
Atrial	960	970
RV	1020	1000
LV Endo	1410	1440
TriV	1450	1420

Table 3.4: Patient 1 measured and simulated dP/dt_{max} in $mmHg.s^{-1}$.

Pacing	Measured	Simulated
Baseline	680	740
Atrial	640	770
BiV	950	895
TriV	960	930

Table 3.5: Patient 2 measured and simulated dP/dt_{max} in $mmHg.s^{-1}$.

Part II

Groupwise Statistics on Cardiac Shape and Function

Chapter 4

Statistical Model of Cardiac Shape and Remodelling

– This chapter is based on [McLeod et al., 2013]:
McLeod, K., Mansi, T., Sermesant, M., Pongiglione, G., and Pennec, X. Statistical shape analysis of surfaces in medical images applied to the tetralogy of fallot heart. In Modeling in Computational Biology and Biomedicine, Lectures Notes in Mathematical and Computational Biology, pages 165–191. Springer, 2013. ISBN 978-3-642-31207-6.

4.1 Introduction

During the past ten years, the biophysical modelling of the human body has been a topic of increasing interest in the field of biomedical image analysis. New treatments, therapy plans and surgical techniques are continually being developed and enhanced to improve the outcome for patients, The aim of such modelling is to formulate personalised medicine, where a digital model of an organ can be adjusted to a patient using personal clinical data as input to the given model. This virtual organ would enable to estimate parameters which are difficult to quantify in clinical routine and to test therapies in silico as well as to predict the evolution of the organ over time and with therapy. These methods can be interesting for example in predicting the long-term outcome of a newly developed treatment in which longitudinal patient data is not yet available, or for testing the outcome of a number of different treatment methods virtually to predict the best plan for a given patient. This notion is largely driven by the fact that testing individual treatments to determine the best choice for a given patient is neither ethical, nor in fact possible and can bridge the gap between clinical population testing by combining this with personalised patient-specific models.

When the biological mechanisms involved are too complex, robust statistical approaches could be used to produce generative models from data. Such statistical analyses can both provide a predictive model and guide the biophysical approach. However, computing statistics on dynamic 3D shapes is very challenging. Traditional methods rely on point based parameterisations of the shapes, where the point-to-point correspondences can be an important limiting factor for the usability of the method since the correspondences must be correct and consistent over all the shapes. New approaches were recently developed to compute such statistics without this limitation [Durrleman et al., 2009c, 2008b, 2009b; Durrleman, 2010; Mansi et al., 2009; Mansi, 2010; Mansi et al., 2011b; Hufnagel, 2010]. Here, the statistical shape analysis tools are based on currents, a non-parametric representation of shapes (here, the term 'shape' is used to refer to geometric data such as curves and surfaces). These tools have a wide range of applications, and provide a well-posed framework for statistical shape analysis of groups. Due to the fact that the methods do not assume point correspondences between structures (and in fact assigning landmarks to structures such as the heart are arbitrary), a wider range of data can be used. For example, one can use surfaces to model organs such as the heart, brain, and lungs, curves to model sulcal lines on the brain cortex, and sets of curves to represent fibre bundles from diffusion MRI in the brain. The goal of this chapter is to give an overview of this methodology in

the context of a specific clinical problem: the prediction of the cardiac shape remodelling in repaired tetralogy of Fallot due to chronic regurgitation.

4.1.1 Repaired Tetralogy of Fallot

Tetralogy of Fallot (ToF) is a congenital heart defect that affects approximately four out of every 10,000 babies [Hoffman and Kaplan, 2002]. The primary defect associated with this condition is a ventricular-septal opening which allows blood to flow freely between the ventricles. Secondary is stenosis in the pulmonary artery which restricts the blood flow from the right ventricle to the lungs. Due to a misalignment of the aorta over the ventricular-septal defect, the aorta is fed by both the left and right ventricle rather than just the left ventricle. Patients may also have hypertrophy in the right ventricle that causes a boot-like shape of the ventricle which is characteristic of this condition.

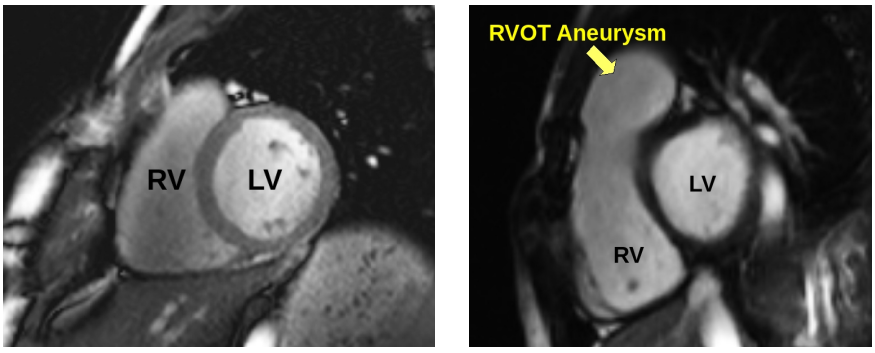

Figure 4.1: Comparison of a normal heart with a Tetralogy of Fallot heart.

These abnormalities require open heart surgical repair early in infancy. As part of this surgery, the stenosis in the pulmonary artery is cleared to allow blood to flow more freely through the artery. As a consequence, the pulmonary valves which control one way blood flow from the right ventricle to the pulmonary artery can be destroyed completely or damaged, causing blood to leak back to the right ventricle. The long-term outcome of this condition is right ventricular remodelling caused by the regurgitated blood (see Fig. 4.1). Nowadays, patients undergo follow up operations to reduce this post-operative sequelae. In particular, the valves are replaced with an artificial device to reduce the regurgitation. A clinical challenge for these patients is determining the optimal time for intervention. On the one hand, it is preferable to wait as long as possible before performing such operations since the artificial devices have a limited life-span resulting in the need for repeat follow-up operations. Either open heart surgery or percutaneous valve replacement may be required, depending on the diameter of the pulmonary annulus. These therapies carry some danger, so minimising the frequency and total number of surgeries is crucial for these patients. On the other hand, the heart undergoes remodelling due to the regurgitated blood producing volume overload in the right ventricle and if left long enough this damage can be irreversible. Determining the optimal time for intervention is a trade-off between maximising the time between operations and minimising damage to the heart.

Therefore, the clinical application for this condition is to better understand how the heart evolves over a large period of time, often decades, with and without surgery, with the main goal to be able to predict the optimal time for intervention. However, due to the large variability of shape, the optimal time, placement and size of the artificial device can be difficult to determine. Furthermore, the complexity of the biological mechanisms involved in heart growth hinders the development of direct model of cardiac remodelling. Statistical shape analysis can therefore be employed to aid in further understanding the pathology to assist cardiologists with diagnosis, therapy planning, and long term prognosis. More particularly, we are interested in determining quantitative measures of the shape that correlate with the cardiac function and the severity of the disease in these patients (bio-markers of the disease). Such bio-markers could be used to assess the severity of the disease

when regurgitation cannot be assessed or to provide structural information that may appear before deterioration of the blood dynamics.

4.1.2 Chapter Organisation

In the following sections, we will first review in Section 4.2 statistical shape analysis methods with a particular focus on the statistical analysis of surfaces. We will introduce the formalism of deformations which is at the centre of most of the current works in computational anatomy [Thompson et al., 2004]. Then, we will detail the framework of currents to represent surfaces, and show how this can be turned into an effective shape analysis technique. Section 4.3 will apply this methodology to the shape of the heart of 13 patients with repaired tetralogy of Fallot. Correlating the shape with clinical variables will illustrate how we can extract some insight about the relationship between morphology and physiology. Last but not least, we will exemplify how the lack of longitudinal measurements can be bypassed by building a statistical generative growth model from cross-sectional data which summarises the heart shape remodelling at the population level.

4.2 Statistical Shape Analysis

4.2.1 Shapes, Forms and Deformations

There is generally no physical model that can faithfully relate the shape of organs in different patients. Thus, to analyse their variability in a population, one usually extracts some anatomically representative landmarks (or more generally geometric features), and models their statistical distribution across the population, via a mean shape and covariance structure analysis after a group-wise matching for instance. One of the earliest methods [Bookstein, 1978, 1986] consists in studying the variability of anatomical landmark positions among a population: after a global pose (position and orientation) normalisation and the consistent identification of landmarks within all patients (see Fig. 4.2), a principle component analysis (PCA) is performed to extract the main modes of variation of the shape.

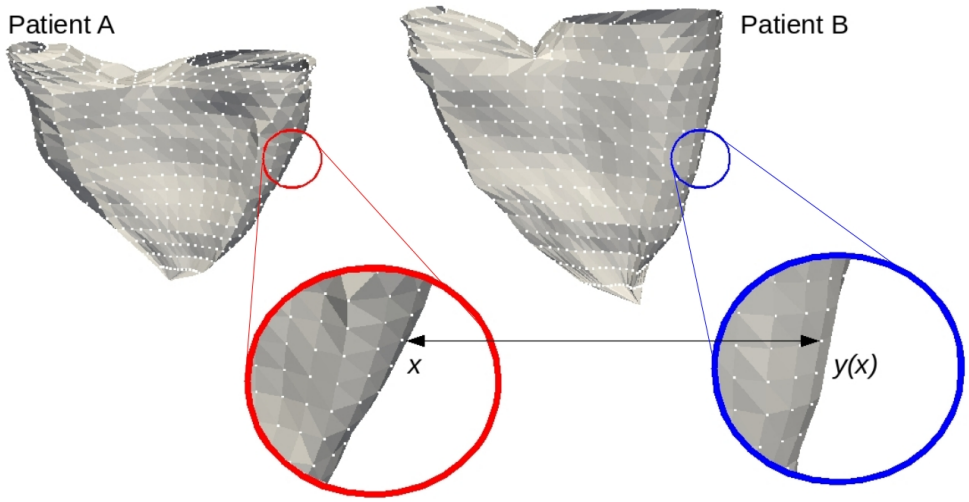

Figure 4.2: Using landmark-based methods to register one surface mesh to another surface mesh, for each point x in patient A, we require the corresponding point $y(x)$ in patient B. This requires a full parameterisation of the patient surface meshes. This is illustrated on the right ventricle of two patients with rToF.

Shapes

In such a process, the global pose of our objects is often considered as a nuisance factor related to the arbitrary coordinate system of the acquisition device: generally speaking the shape of an object is

understood as the geometric information that is invariant under translation, rotations and rescaling. Thus, one is often interested only in the *shape*, i.e. what remains if we quotient out the object space by a group action, usually rigid body, similarity or affine transformations. For instance, when we consider the equivalent classes of sets of N (labeled or unlabelled) points under the action of a global similarity (resp. rigid body) transformation, we obtain the celebrated shape (resp. size and shape) spaces of Kendall at al [Kendall, 1989; Dryden and Mardia, 1991; Le and Kendall, 1993; Small, 1996]. One can define similarly the shape spaces of curves by removing the effect of re-parameterisations and the global pose of the curve Joshi et al. [2006]; Mio et al. [2007]; Joshi et al. [2007b,a]. However, in medical image analysis, the natural coordinate system of an organ is its position and orientation with respect to surrounding tissues and organs in the image. Thus, once images are normalised by aligning them to a reference anatomy, the pose of organs is a variable of interest and should be kept for analysis.

Deformations

An alternative modelling of shapes was proposed by D'Arcy Thompson in 1917 [D'Arcy Thompson, 1917]. The idea is to assume that there is an atlas object, which represents the reference shape (this can be seen as an atlas or an equivalent of the mean shape). Then, the variability of the shape is analysed through the deformations of this reference object towards the actual observations: a shape difference is encoded by the transformation that deforms one onto the other. As the deformation of a smooth object should be a smooth object, we have to work with diffeomorphisms (invertible, one-to-one mappings with smooth inverses). This formalism was promoted to a generic shape analysis tool by Grenander and Miller [Grenander, 1993; Miller and Younes, 2001] based on advanced mathematical tools to compute on infinite dimensional groups of diffeomorphisms [Trouvé, 1998]. One key feature of this lift of the shape characteristics from the object space to the transformation space is that it allows to apply the typical deformations to other objects than the ones analysed in the first place (provided that they also live in the coordinate system of the atlas). For instance, [Durrleman et al., 2008b] analysed the variability of sulcal curves on the surface of the brain cortex to extract the main deformation modes. These modes could then be used to deform accordingly the surface of the cortex or the full 3D volume of the brain.

However, the problem is even more complex than previously as we want here to perform statistics on large deformations, which are known to belong to a non-linear and infinite dimensional manifold. The Riemannian setting is one of the most powerful structures to generalise simple statistics to non-linear spaces: it provides a definition of the distance between points of our manifold and a notion of shortest path / straight lines using geodesics [Pennec, 2006, 2008]. The main difficulty is that the mean value cannot be defined through an integral or a sum as in Euclidean spaces. Instead, one must look for points in the manifold that minimise the dispersion of the other points around it, which is commonly measured by the variance (the mean squared distance). This is what is called the Fréchet or Karcher mean. Then, one can compute the covariance matrix (the directional dispersion around the mean) by developing the manifold onto its tangent space at the mean point. Basically, this amounts to representing each data point by the momentum (initial speed vector) needed to shoot a geodesic to it from the mean (we use the term "geodesic shooting" to define the integration of the Euler-Lagrange equations, which plays the role of the exponential map in Riemannian geometry).

This generalisation of statistics has to be slightly modified to fit the atlas deformation model: the 'distance' between the atlas and a shape is given here by the length of the shortest path in the space of deformations. The atlas is called unbiased if it is centred, i.e. if it minimises (among all possible atlases) the sum of squared distances to the shapes [Joshi et al., 2004]. In this sense, this is the Fréchet mean of the shapes. Then, each shape is represented by the momentum of the deformation that allows to regenerate the shape by deforming the atlas. These momentum all belong to the tangent space[1] of the diffeomorphisms at the identity, which is a vector space in which we can perform a PCA [Vaillant et al., 2004]: shooting in the space of deformations along the first eigenvectors of the covariance matrix of the momentum give deformation modes that represent the

[1] More precisely to the cotangent space

main shape variability when applied to the atlas.

4.2.2 From Points to Surfaces: the Formalism of Currents

Landmarks can be encoded by the probability of their location in space (typically a Gaussian around their expected value). When the noise is going to zero, then this pdf becomes singular. However, we can continue to deal with these types of singularities by considering distributions (generalised functions) instead of functions, which include Diracs. Mathematically, a Dirac is not a function, but an object which can be characterised by the result of its integration against any function of a sufficiently smooth functional space: $\forall f \in W, \int \delta_x(y).f(y).dy = f(x)$. This is actually an element of the linear functionals over the space W. In that framework, a set of N points x_k can be represented by the 'pdf' $p(x) = 1/N \sum_i \delta_{x_k}(x)$, and its evaluation on a function $f(x)$ results in the mean of the values of f at the points x_k.

When we move to curves and surfaces, we are dealing with the locally singular locus of points in certain directions only: curves and surfaces are continuous along their tangent. The extension of the notion of distributions that allows to take that information into account is the geometric integration theory. The basic idea is to integrate differential forms, but for objects like smooth surfaces in 3D, we shall simply define currents by their action on vector fields, similarly to the way distributions are defined by their action on scalar functions.

Currents for Surfaces

Let W be a Hilbert space of vector fields (a possibly infinite complete vector space provided with a scalar product). For a given surface S, we can measure the flux of any vector field $\omega \in W$ through this surface:

$$\mathcal{S}(\omega) = \int_{x \in S} \langle\, \omega(x) \mid n(x) \,\rangle\, d\sigma(x),$$

where $n(x)$ is the normal to the smooth surface at point $x \in S$ and $d\sigma(x)$ the surface element around point x. The shape of the surface S is characterised by the variation of the flux as the test vector field ω varies in W. Thus, the surface actually defines a continuous linear form on W which can be identified to an element of the dual space W^*, which is the space of linear functionals from W to $\mathbb{R}$ (currents). The nice property of currents is that it is a vector space: we can add or subtract current from each others, or multiply them by a scalar. However, we should keep in mind that the space of currents is larger than the space of smooth surfaces: one can for instance add many pieces of surfaces together in a non continuous way to create a non-continuous object.

Now that we have identified surfaces to currents, we need to define more carefully what is the space W that we consider. The core element proposed by [Glaunès, 2005] is to consider a Kernel metric (typically the Gaussian kernel $K_W(x,y) = \exp(-\|x-y\|^2/\lambda_W^2)$) in order to turn W into a Reproducible Kernel Hilbert Space (RKHS). The reproducibility property implies that W is the dense span of basis vector fields of the form $\omega_x^\alpha(y) = K_W(x,y)\alpha$. This means that any vector field of W can be written as an infinite linear combination of such basis vectors. The kernel induces a scalar product which is easily computed on two basis vectors: $\left\langle \omega_x^\alpha \,\middle|\, \omega_y^\beta \right\rangle_W = \alpha^\mathsf{T} K_W(x,y)\beta$. The kernel can be seen as a low pass filter which weights more heavily the high spatial frequencies of the vector field ω than the low frequencies.

Since W is a Hilbert space, by the Rietz representation theorem, there exists an isometric linear mapping $\mathcal{L}_W$ from W to W^* which maps to each $\omega \in W$ the linear form that reproduces the scalar product: $(\mathcal{L}_W(\omega))(\omega') = \langle\, \omega \mid \omega' \,\rangle_W$. This canonical isomorphism allows to define the dual of an element, or conversely to map to each surface the vector field that optimises the flux. For instance, the dual of the above basis vectors are the Dirac delta currents $\delta_x^\alpha = \mathcal{L}_W(\omega_x^\alpha)$ as we have $\langle\, \omega_x^\alpha \mid \omega \,\rangle_W = \alpha^\mathsf{T}\omega(x)$. These can be seen as vector fields whose spatial support is concentrated at one point only. The space of currents W^* is the dense span of these basis elements. For instance, the surface S is represented by the current $\mathcal{S} = \int_{x \in S} \delta_x^{n(x)} d\sigma(x)$. The usual way to define a norm on the dual space is to take the operator norm: $\|\mathcal{S}\|_{W^*} = \sup_{\omega \in W, \|\omega\|=1} |\mathcal{S}(\omega)|$. The distance induced

by this norm might seem difficult to use, but thanks to the RKHS properties, we have a closed form for basis vectors:

$$\left\langle \delta_x^\alpha \,\middle|\, \delta_y^\beta \right\rangle_{W^*} = \alpha^\mathsf{T} K(x,y)\beta 2 \left\langle \delta_x^\alpha \,\middle|\, \delta_y^\beta \right\rangle_{W} \alpha^\mathsf{T}\beta$$

It is interesting to notice that this distance can be approximated by

$$\|\delta_x^\alpha - \delta_y^\beta\|^2_{W^*} = \|\alpha-\beta\|^2 + 2\|x-y\|^2/\lambda_W^2 \alpha^\mathsf{T}\beta + O\left(\|x-y\|^4/{\lambda_W}^4\right),$$

when the points x and y are within a fraction of λ_W, while the distance is essentially constant (and equal to $\|\alpha\|^2_{L_2} + \|\beta\|^2_{L_2}$) when the points x and y are more than a few λ_W apart. This behaviour is typical of a robust distance in statistics, meaning that outliers (over a few λ_W in distance) will have (almost) no effect on the optimisation of the distance between the surfaces as it is an almost constant penalty.

In practice, surfaces are often represented by discrete triangulated meshes. Assuming that each face has a support which is smaller than ε times the scale λ_W, we can approximate the surface by the current $\mathcal{S} = \sum_k \delta_{x_k}^{\alpha_k}$, where x_k is the barycentre and α_k the normal weighted by the area of the face. From the above Taylor expansion of the distance, we can see that the approximation error is less than ε^2 for each face in the W^* norm.

The scalar product between two discrete currents is obtained by linearity:

$$\left\langle \sum_k \delta_{x_k}^{\alpha_k} \,\middle|\, \sum_j \delta_{y_j}^{\beta_j} \right\rangle_{W^*} = \sum_{k,j} \alpha_k^\mathsf{T} K_W(x_k,y_j)\beta_j$$

and the distance between two discrete surfaces is simply $\text{dist}^2(S,S') = \|\mathcal{S}-\mathcal{S}'\|^2_{W^*}$.

Sparse Representation of Currents using Matching Pursuit Algorithm

Representing shapes using currents gives a nice theoretical framework that allows us to compute simple statistics such as mean and principal modes. However, the complexity of the distance computation is quadratic in the number of Dirac delta currents used to represent the shape. This number can be quite high if we take highly detailed surface meshes, even though it adds nothing for the comparison of surfaces at a given scale λ_W. Therefore, in order to remain computationally as efficient as possible, we require a sparse representation of currents that retains the information needed for the scale of the analysis. This is the essence of the matching pursuit algorithm as described in [Durrleman et al., 2009b].

In brief, the matching pursuit algorithm is a greedy approach for finding an approximation of the current T that solves $\mathcal{L}_W^{-1}(T) = \gamma$, for a given vector field $\gamma \in W$. This amounts to finding N points (x_k) and vectors (α_k) such that the current $Pk(T) = \sum_{k=1}^N \delta_{x_k}^{\alpha_k}$ is as close as possible to T. If the points are known, then $\Pi(T)$ is the orthogonal projection of T onto $Span(\delta_{x_k}^{\epsilon_q}; q=1,2,3, k=1...N)$, where ϵ_q is the canonical basis of $\mathbb{R}^3$. The orthogonality condition: $\langle T, \delta_{x_k}^{\epsilon_q}\rangle_{W^*} = \langle \Pi(T), \delta_{x_k}^{\epsilon_q}\rangle_{W^*}$ leads to a linear set of $3N$ equations

$$\sum_{p=1}^{N} (K(x_i,x_p)\alpha_p)_k = \gamma(x_i)_k \tag{4.1}$$

which can be solved iteratively over the continuous space of Dirac delta currents to find the point positions (x_k) as well as their associated momenta and the residual vector field. Additionally, we can also sample the vector field on a grid Λ. Applying the matching pursuit in the discrete case constrains the estimated momenta to lie on the nodes of the grid which forces the estimated current to belong to a discrete set of currents W_Λ^*. This simplifies the problem in both complexity as well as computation time. Figure 4.3 shows a sparse representation of the right ventricle.

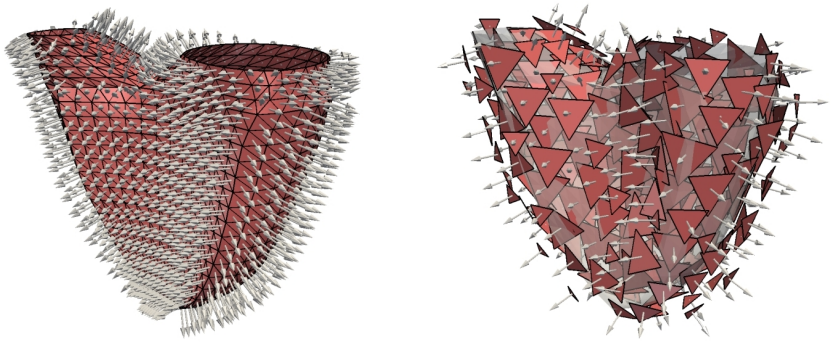

Figure 4.3: The Dirac delta currents of a triangulated mesh are the normal vectors of every face, centred at the face barycentre. A greedy algorithm reduces the amount of delta currents needed to represent the shape while preserving the accuracy of the representation.

4.2.3 An Algorithm for Surface Registration using Currents

Having defined a non-parametric representation of surfaces, we now require an algorithm to register one surface to another. Here, the term registration is meant to define the action of transforming two objects into the same co-ordinate system. Since we are comparing topologically similar shapes, the transformations are restricted to those which preserve the topology of the object and give a smooth one-to-one (invertible) transformation (i.e. a diffeomorphism). The space of diffeomorphisms give non-linear deformations that allow local smooth variations to be captured in the registration. However, diffeomorphic transformations have an infinite degree of freedom, therefore optimising over the whole group of diffeomorphisms may not be possible. So, we use a smaller infinite group of diffeomorphisms to allow computations with discrete parameterisations using the Large Deformation Diffeomorphic Metric Mapping (LDDMM) method described in [Beg et al., 2005; Miller et al., 2003] for images.

The LDDMM framework uses a group of diffeomorphisms constructed through integration of time-varying vector fields that belong to a RKHS. This gives a geodesic flow of diffeomorphisms ϕ_t for a continuous parameter t within the interval $[0, 1]$. At time $t = 0$, we have the identity mapping ϕ_0. The mapping at time 1 gives the desired transformation ϕ_1 which is required for mapping one image to the other. The path of any point x is defined by $\phi_t(x)$ and leads to the final position $\phi(x) = \phi_1(x)$. By following the reverse path, we can compute the inverse deformation.

The basic idea of the LDDMM framework is to minimise the distance between objects after transformation (this is the similarity energy or data attachment term) with a penalisation for the length of the deformation trajectory (which is the regularisation energy). A time t, the speed at point $y = \phi_t(x)$ is $v_t(y) = d\phi_t(y)/dt$. This suggests to define the energy of a velocity field at deformation ϕ_t using a right-invariant metric:

$$\|v_t\|^2_{\phi_t} = \left\|v_t \circ \phi_t^{-1}\right\|^2_W$$

where $\|.\|_W$ is the norm of the RKHS of the velocity fields at the identity transformation. The energy of the deformation trajectory is thus $E(\phi_t) = \int_0^1 \left\|v_t \circ \phi_t^{-1}\right\|^2_W dt$ and the optimal curves joining $\phi_0 = Id$ to ϕ_1 are geodesics in the space of diffeomorphisms. Since optimal transformations are geodesics, we know that they are completely determined by their initial value, here the velocity field $v_0(x)$ (or more specially the initial momentum $K_W^{-1}v_0$). Denoting ϕS the action of the transformation ϕ on the source object S, the registration criterion to the target object T is thus:

$$C(\phi) = \mathsf{dist}(\phi_1 S, T)^2 + \int_0^1 \left\|v_t \circ \phi_t^{-1}\right\|^2_W dt$$

For our surface registration problem, the objects are surfaces represented by their associated currents $\mathcal{S}$ and $\mathcal{T}$ and the distance is taken in the space of currents W^*. Since our currents have a finite point-wise support, we can show that the optimal initial momentum of the deformation has the same

point-wise support (if $\mathcal{S} = \sum_i \delta_{x_k}^{\alpha_k}$, then $v_0(x) = \sum_i K_W(x, x_k)\beta_k$ for some set of vectors β_k), which means that we are left with a finite dimensional optimisation problem [Vaillant and Glaunes, 2005; Glaunès, 2005].

4.2.4 Building an Unbiased Atlas

For building the optimally centred atlas, we took the *forward* strategy that models the set of surfaces as the deformation of an unknown *ideal* atlas plus some residuals [Durrleman et al., 2009b]. This can be expressed as:

$$T_i = \phi_i \hat{T} + \varepsilon_i. \tag{4.2}$$

for i patients, where $\hat{T}$ is the atlas we are estimating, ϕ is the deformation that maps the atlas to the surfaces T, and ε represents the residuals (shape features not captured by the atlas such as changes in topology etc.). The mean shape information is described in the atlas $\hat{T}$ while the shape variability is encoded in the transformation ϕ_k.

The atlas is first initialised by taking the mean of the patient meshes. This initial atlas is then registered to each of the patients individually. A new atlas $\hat{T}$ that minimises the error

$$\Lambda(\hat{T}) = \left\| T_i - \phi_i(\hat{T}) \right\|_{W^*}^2 \tag{4.3}$$

is computed. We then register the updated atlas to the individuals, recompute the atlas and loop until convergence (see Algorithm 1).

Algorithm 1 Atlas Estimation

Require: N segmented patient images (surface meshes).

1: Rigidly align meshes to a reference patient using rotations and translations.
2: Create initial atlas $\hat{T}_0$ as the mean of the patient meshes.
3: **loop** {*over* N *until convergence*}
4: Estimate the transformations ϕ_k that register the atlas $\hat{T}_{N-1}$ to the individual T_k.
5: Update the atlas by minimising the error in 4.3 using the estimated transformations ϕ_k and the atlas $\hat{T}_{N-1}$
6: **end loop**
7: **return** Final atlas $\hat{T}_N$ and the related transformations ϕ_k^N.

4.3 Application on ToF Data

To demonstrate the usefulness of our statistical shape analysis in a clinical context, we consider a population of patients with repaired tetralogy of Fallot.

As mentioned in the introduction, the clinical problem in rToF patients is in better understanding the shape remodelling over time to aid in determining the optimal time for surgical intervention. In view of this problem, we are first interested in identifying the clinically relevant shape patterns by investigating the relationship between shape and given clinical indices. The assumption here is that changes in heart morphology may reveal structural and functional dysfunctions due to the chronic regurgitation. In particular, we aim to establish which shape patterns are related to the pathology in order to give further insights into the condition. We can then go beyond the identification of pathological shape patterns, to estimate a predictive growth model of the heart to give an indication of how the heart will grow and re-model in time for this pathology.

Making use of currents to represent shapes, and an atlas to give an average representation of the population, we can apply statistical methods to address key questions for diagnosis, prognosis and prediction.

4.3.1 The Analysis Pipeline

Patient Data We consider a data-set of thirteen patients (10 males, mean age $\pm$ SD $= 19 \pm 9$) with repaired tetralogy of Fallot. Steady-state Free Precision cine MRI were acquired using a 1.5T scanner (Avanto, Siemens AG, Erlangen) in the short axis view covering entirely both ventricles (10-15 slices; isotropic in-plane resolution: $1.1 \times 1.1\, mm^2$ to $1.7 \times 1.7\, mm^2$; slice thickness: 5mm to 10mm; 25-40 phases).

Surface Mesh Delineation In the case of ToF patients, we are interested in studying the shape of the left and right ventricles of the heart. Using the statistical shape analysis methods described in the previous section, we can consider the ventricles as surfaces represented by triangulated meshes. The surface meshes of the right and left ventricle endocardium (inner layer of heart tissue), and left ventricle epicardium (outer layer of heart tissue) are defined using image segmentation by delineating the boundaries of each ventricle at end-diastole using the methods proposed by Zheng et al. [Zheng et al., 2008b] (see Fig. 4.4). This method defines the delineated boundaries using an anatomical model and thus establishes a point correspondence between meshes. Therefore, in this instance we used a standard least-squares method to first rigidly align the surface meshes to reduce the effect of patient positioning.

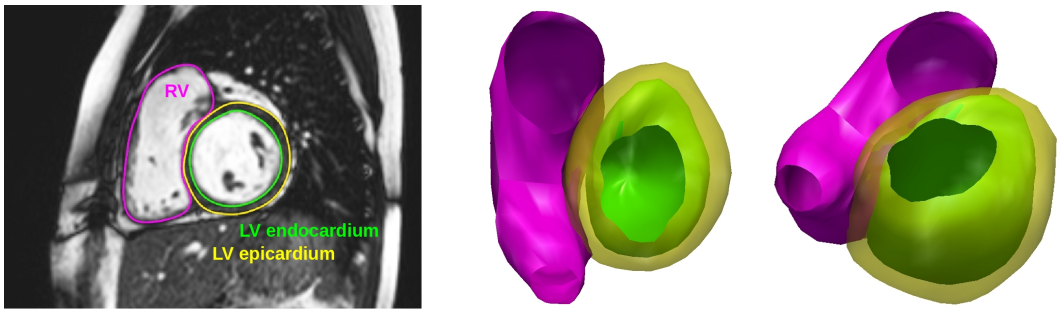

Figure 4.4: Delineated boundaries of the right ventricle (pink), left ventricle endocardium (green) and left ventricle epicardium (yellow) shown on one image slice (left) and the 3D reconstruction (center and right).

Mean Atlas Construction Using the algorithm for computing a mean shape with the currents method described in Section 4.2, we estimated an atlas for the ToF data, see Fig. 4.5. Eleven iterations of the alternate minimisation for the shape atlas (Algorithm 1) were needed to reach convergence. The resulting atlas $\hat{T}$ was well centred (mean over standard deviation of the deformations was 0.36946). Atlas-to-patient registration is implemented in parallel on a cluster of computers, which means that the atlas creation time is minimally dependent of the number of patients used to create it.

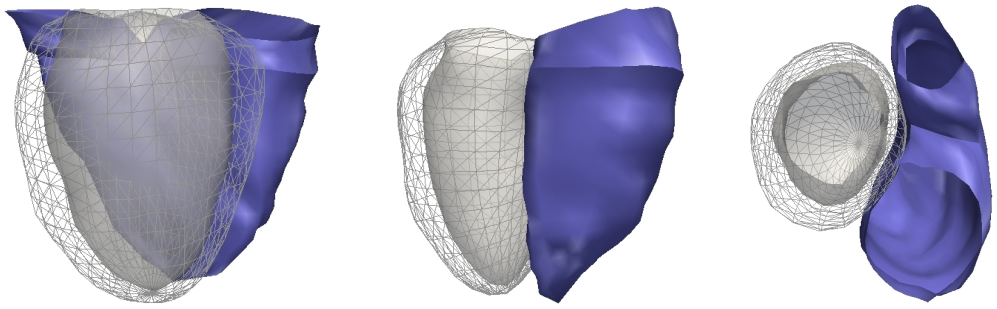

Figure 4.5: Three views of the mean atlas estimated from 13 patients with repaired ToF with the right ventricle in blue, left ventricle endocardium in white and left ventricle epicardium in wire-frame.

4.3.2 Diagnosis Parameters

A key topic in computational shape analysis is identifying pathologically specific shape features in populations of diseased patients compared to controls (see [Cates et al., 2008] and references therein for instance). Beyond simply identifying the pathological shape features, we would like to also quantify the degree to which the shape is altered due to the pathology. One way in which this can be done is by correlating the shapes with clinical features to determine the severity of the disease, which requires a consistent representation of the patient shapes. For this we use firstly principal component analysis (PCA) to extract the main modes of shape variation followed by standard statistical design to exhibit those that are correlated to the pathology (see Fig. 4.6 top row).

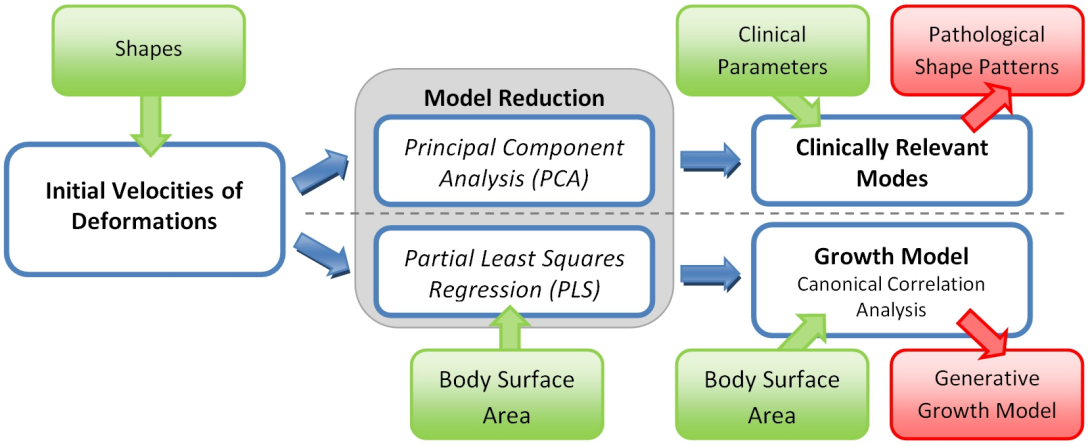

Figure 4.6: Shape analysis pipeline with both clinically relevant model reduction and growth model generation. Using PCA modes and standard correlation analysis, the pathological shape patterns can be identified. Using a combination of PLS regression and CCA a statistical generative growth model can be derived.

Model Reduction using Principal Component Analysis

Since statistical shape analysis is a high dimensional problem with a large number of parameters and variables to solve for (despite the matching pursuit reduction, a shape can still be represented by hundreds of moments), we first reduce the dimension of the problem by applying principal component analysis (PCA). This gives the modes of deformation that describe the amount of variation of shape observed in the population.

PCA is applied on the initial velocity fields $v_0^{(i)}$ to extract the main deformation modes observed in the population. PCA finds basis vectors, the modes, of the space of variables (here the initial velocities) that best explain their variance. The modes p are calculated by solving the eigenvalue problem $\Sigma p = \mu p$, where the elements σ_{ij} of the covariance matrix Σ are calculated in the kernel space W. Assuming that the deformation from the atlas to patient i is parameterised by the initial vector field $v_0^{(i)}(x) = \sum_k K_W(x, x_k)\beta_k^{(i)}$, where the x_k are the point positions of the delta Dirac currents of the atlas, and $\beta_k^{(i)}$ the moment vector at x_k, then the mean initial vector field is $\bar{v}_0(x) = \sum_k K_W(x, x_k)\bar{\beta}_k$ and the covariance is

$$\sigma_{ij} =< v_0^i - \bar{v}_0, v_0^j - \bar{v}_0 >_V = \sum_{k,l} (\beta_k^{(i)} - \bar{\beta}_k) K_W(x_k, x_l)(\beta_l^{(j)} - \bar{\beta}_l) \tag{4.4}$$

The principal components are obtained by computing the spectral decomposition $\Sigma = PMP^T$. M is the diagonal matrix of the eigenvalues σ_m, or variances, sorted in decreasing order and P is the orthonormal matrix (in the L_2 -norm sense) of the eigenvectors p^m. The m^{th} loading l^m of the PCA decomposition is given by the formula:

$$l^m = \sum_i p^m[i]\beta^{(i)} \tag{4.5}$$

In this equation, $p^m[i]$ is the i^{th} element of the m^{th} eigenvector of Σ, $\beta^{(i)} = (\beta_1^{(i)} - \bar{\beta}_1, ...\beta_n^{(i)} - \bar{\beta}_n)^T$ is the $n \times 3$ matrix that gathers the n centred moment of patient i. As a result, the initial velocity field of the m^{th} mode is $v_{0_{lm}}(x) = \sum_k K_W(x, x_k) l^m$. The variability captured by this m^{th} deformation mode between $[-\eta\sigma^m; +\eta\sigma^m]$ is visualised by deforming the atlas T with the deformations ϕ^{-m} and ϕ^{+m} parameterised by the moments $\bar{\beta} - \eta l^m$ and $\bar{\beta} + \eta l^m$ respectively. Selecting the first p modes only among the $N-1$ possible modes (where N is the number of patients) allows to explain a percentage $\sum_{m=1}^{p} \sigma^m / \text{trace}(\Sigma)$ of the total variance.

The orthogonal projection of each patient's initial velocity field onto the selected PCA subspace gives a unique shape vector. This simply corresponds to the coordinates of the projection in the basis constituted by the chosen eigen-modes:

$$s^{i,m} =< v_0^{(i)} - \bar{v_0}, v_{0_{lm}} >_W = \sum_{j,k} [\beta_j^{(i)} - \bar{\beta}] K_W(x_j, x_k) l_k^m \tag{4.6}$$

Using PCA we have reduced the amount of data needed to represent the shape of a patient by two or more orders of magnitude. The precision of the representation is controlled by the number of components of the PCA subspace. However, it has to be observed that modes with low variances may still be relevant to external clinical parameters. For instance, a mode that captures a local bulging is probably more related to the pathology than a global scaling of the shape although this bulging is not very visible in the population and could be considered as noise in the model. Consequently, we are fairly conservative in the selection of the PCA subspace and select the modes based on their relationship with the clinical parameters of interest and not their variance, as described in the following sections.

Identifying Factors Between Shape and Clinical Features

The $s^{i,m}$'s quantify the amount of variability along the m^{th} mode present in patient deformation. We can thus investigate the heart shape by relating these shape vectors to clinical parameters that quantify the pathology. Ordinal clinical parameters are investigated using non-parametric rank-based statistics. Kruskal-Wallis analysis of variance is applied to find effects between the investigated parameters and shape [Team, 2009]. If an effect is found, post-hoc two-sample Wilcoxon test is used to determine which levels differ [Team, 2009]. Continuous clinical parameters are investigated using linear regression and Akaike Information Criterion (AIC) model reduction Akaike [1974] to detect relevant modes and the direction of correlation.

To illustrate this method, in [Mansi et al., 2011b] we showed that these methods enable one to identify shape features related to the severity of the regurgitation for a data-set of 49 repaired ToF patients. The relationship between RV shape and pulmonary regurgitation were investigated by relating the PCA shape vectors with tricuspid regurgitation, trans-pulmonary valve regurgitation and pulmonary regurgitation volume indices taken from colour doppler ultrasound and phase-contract magnetic resonance images (PC-MRI). 90% of the spectral energy was explained by 18 PCA modes.

4.3.3 Building an Evolution Model

As explained beforehand, understanding and quantifying heart remodelling in these patients is crucial for planning pulmonary valve replacement. Given that there is a lack of longitudinal data available for these patients, we make use of the atlas as the mean of the population and cross-sectional statistics to formulate a generative growth model. Such a model could be used as reference, from which the pathology evolution of one patient could be quantitatively compared. In cross-sectional statistical design, one does not propagate the evolution over time for a single patient but rather considers each patient as an instance in the growth evolution. In this way we can model the growth of the population given these instances using regression analysis (see Fig. 4.7). By making use of the initial velocities v_0^i that parametrize the deformations ϕ^i computed using the methods described in the previous sections, we can regress the velocities against an index of patient growth using standard statistical techniques.

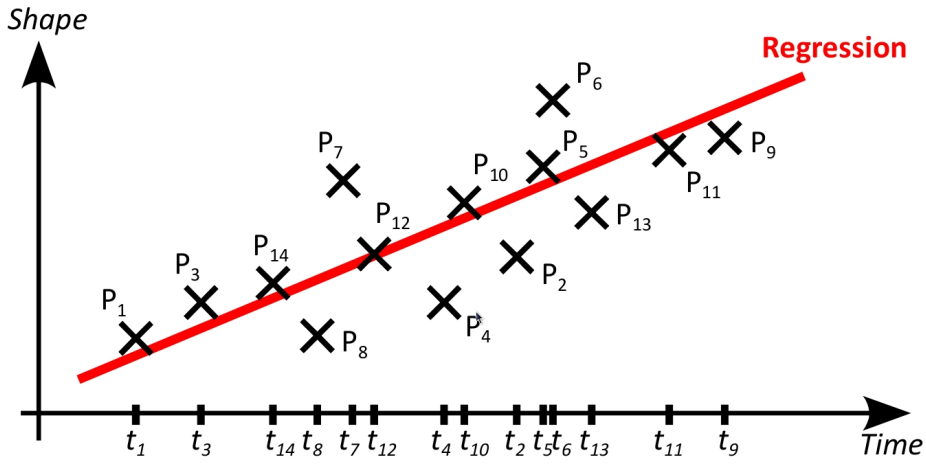

Figure 4.7: Cross-sectional regression of shapes. Each patient is associated to a point in time (patient age for instance). A regression model is derived from the temporal data.

In order to obtain statistically significant results, we first need to reduce the dimensionality of the problem to consider just the factors related to patient growth, while also removing any co-linearity between factors. In the previous section the model reduction was performed using PCA. In this case we chose instead to use partial least squares (PLS) regression since it has the added advantage of computing the components that are most related to a given external parameter (i.e. patient growth). Using PLS allows us to compute the components that best describe the variance of both the matrix of predictors (X) and the matrix of responses (Y), as well as the covariance between X and Y, in a manner such that the regression $Y = f(X)$ is optimal.

In the case of ToF patients, we would ideally like to model the atlas deformation of a patient as a function of growth (i.e. $deformation = f(growth)$, however solving this problem is not possible due to the large number of deformation parameters that would need to be predicted with a single, one-dimensional, parameter (growth). Rather, we revert the problem to be a function of the deformations: $growth = f(deformations)$ which has a much lower number of parameters to predict. The outputted values are then projected onto the reduced PLS subspace and from that we can revert the problem to the desired form as a function of the shape using canonical correlation analysis (CCA) to give a generative growth model of the heart.

For this example we use body surface area (BSA) as the index of growth rather than patient age to better represent the growth given the variable age at which children enter puberty. We use the Dubois formula [DuBois and DuBois, 1915] to compute the BSA for each patient:

$$BSA(m^2) = 0.007184 \times weight(kg)^{0.425} \times height(cm)^{0.725} \tag{4.7}$$

The pipeline we have just described for computing a generative growth model is shown in Fig. 4.6 (bottom row).

Model Reduction using Partial Least Squares Regression

As introduced in the previous section, regression using the partial least squares regression (PLS) method is based on finding an optimal basis of the predictor variables X that maximizes the variances of X and Y as well as their covariances. The method can be considered as the optimal estimation of two weight vectors r and s that satisfy

$$\max_{|r|=|s|=1} cov(Xr, Ys) = \max_{|r|=|s|=1} var(Xr)corr(Xr, Ys)^2 var(Ys) \tag{4.8}$$

under the constraint that the regression between X and Y is optimal. Mathematically, the centred variables $X_c = X - \bar{X}$ and $Y_c = Y - \bar{Y}$ are modelled by

$$X_c = TP^T + E$$
$$Y_c = UQ^T + F$$

where T and U are the matrices of the PLS modes, P and Q are the loading matrices which describe the weight of each variable in X and Y respectively and E and F are the residual terms which are the same size as X_c and Y_c respectively. Additionally the following regression condition is imposed for the PLS modes:

$$U = TD + G \tag{4.9}$$

where D is a diagonal matrix of weights and G a matrix of residuals. Due to this added condition, the PLS loadings P and Q are not necessarily orthogonal as is the case for PCA modes.

Algorithm 2 Partial Least Squares Regression (PLS)

Require: Variables X and Y, number of components $p \leq N-1$.

1: $X_c^0 = X - \bar{X}$, $Y_c^0 = Y - \bar{Y}$
2: **for** $n = 1$ *to p* **do**
2: $r^n \leftarrow$ first eigenvector of $X_c^{nT} Y_c^n Y_c^{nT} X_c^n$
2: $t^n \leftarrow X_c^n r^n / \parallel r^n \parallel n^{th}$ *PLS component of X*
2: $s^n \leftarrow Y_c^n t^n / t^{nT} t^n$
2: $u^n \leftarrow Y_c^n s^n / \parallel s^n \parallel n^{th}$ *PLS component of Y*
2: $p^n \leftarrow X_c^n t^n / t^{nT} t^n \; n^{th}$ *loading of X*
2: $q^n \leftarrow Y_c^n u^n / u^{nT} u^n \; n^{th}$ *loading of Y*
2: $X_c^{n+1} \leftarrow X_c^n - t^n p^{nT}$ *deflation of* X_c
2: $Y_c^{n+1} \leftarrow Y_c^n - t^n [t^{nT} Y_c^n / t^{nT} t^n$ *deflation of* X_c
3: **end for**
4: **return** $T = (t^n)_{n=1...p}$, $P = (p^n)_{n=1...p}$, $U = (u^n)_{n=1...p}$, $Q = (q^n)_{n=1...p}$

Several algorithms have been proposed to compute the PLS modes. In this work, we use the PLS1 method, an efficient iterative algorithm that does not require matrix inversion as summarised in Algorithm 2. X is the matrix of the initial velocity field moments for all patients and Y is the vector of the BSA values for all patients. The first five PLS modes are shown in Figure 4.8 and the explained variance and correlation of modes is shown in Figure 4.9. These modes account for 99% of the covariance between shape and BSA in the population and 61% of the shape variability and are oriented along increasing BSA. Visually we can see that Modes 1 and 3 display an overall dilation in both the left and right ventricles. The second mode shows a narrowing in the right ventricular outflow tract with a noticeable dilation in the left ventricle which can be seen in the top view of the mode. Modes 4 and 5 show an elongation at the right ventricular outflow tract. Mode 5 also shows an aneurysm in the right ventricle outflow tract which is characteristic of rToF patients, although it is still not clear if this is due to pulmonary regurgitations (although both are correlated) or the initial surgical patch.

Generating a Growth Model using Canonical Correlation Analysis

Using PLS as described above allows us to predict BSA given the shape, however what we would like is to estimate the shape given BSA. To reverse the relationship we use canonical correlation analysis (CCA) on the PLS shape vectors (the $t_i's$ of Algorithm 2). CCA computes the vectors r and s that maximise the correlation between the two sets X and Y:

$$\max_{|r|=|s|=1} corr(Xr, Ys)^2 \tag{4.10}$$

where Y is the vector of BSA values and $X = [t_1, \ldots t_N]^\intercal$ is the matrix of shape descriptors.

If we define the covariance matrices $V_{UZ} = \frac{1}{N-1} U^\intercal Z$, then the matrix $\Gamma = V_{XX}^{-1/2} V_{XY} V_{YY}^{-1/2}$ can be seen as a multi-variate generalisation of the uni-dimensional correlation coefficient $r = \sigma_{XY} / \sqrt{\sigma_{XX} \sigma_{YY}}$. The sought correlations are obtained by SVD decomposition of Γ:

$$\Gamma = ASB^T \tag{4.11}$$

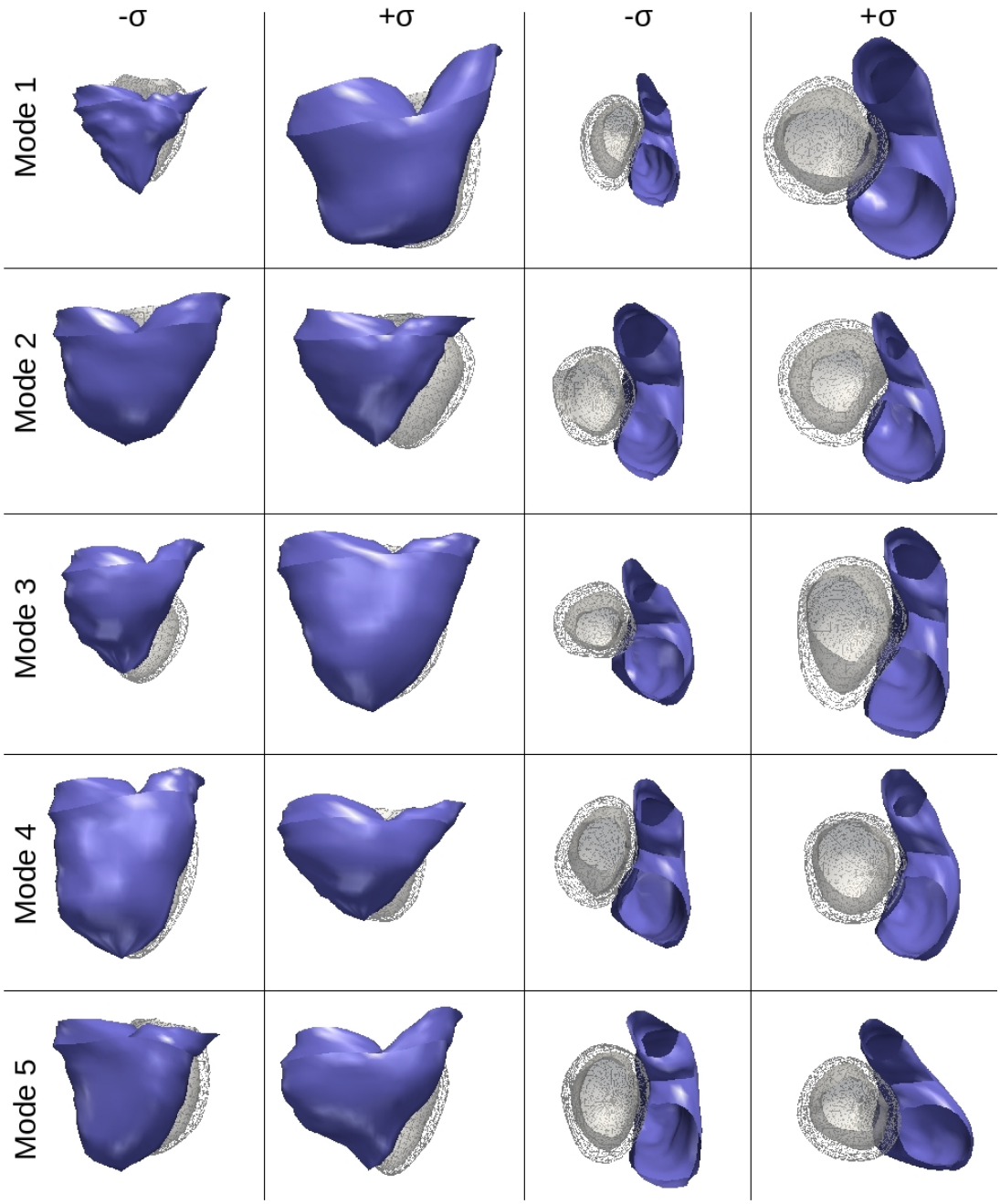

Figure 4.8: The first five PLS modes of variation that describe 99% of the observed BSA variability and 61% of the observed shape variability in the population.

S is the diagonal matrix of the correlation coefficients between correlation vectors and A and B are rotation matrices of correlation vectors, i.e. $A^T A = B^T B = Id$. In our application, Y is a one-column matrix. Hence, S has only one non-null coefficient R, which is the overall correlation between the PLS shape vectors X and BSA. B is a scalar equal to ± 1 that determines the direction of BSA correlation. The elements of the first correlation vector of A, denoted by ρ, relate to the amplitude and direction of correlations of each predictor, namely each PLS mode, when Y varies along the direction defined by the sign of B. In other words, when BSA varies by 1, the k^{th} predictor varies by $BR\rho[k]$. We can therefore compute a generative average model of heart growth by artificially increasing BSA and deforming the atlas T with the growth deformation Φ parametrized by the moments $\mu = B.R.\Sigma_k \rho[k] p^k$, where p^k is the k^{th} PLS loading.

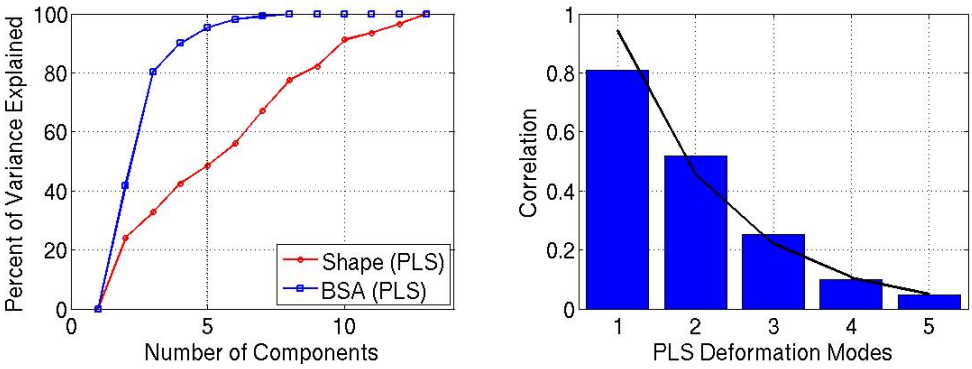

Figure 4.9: Cumulative variance of PLS modes with respect to shape and BSA (left panel) and CCA correlation coefficients between BSA and PLS modes with exponential fitted curve in black (right panel).

Interpretation

The growth model computed on the ToF data-set is shown in Fig. 4.10. This model shows an expected overall growth of both ventricles as body surface area increases. We can also see the caving of the septum into the right ventricle as time passes and the elongation of the right ventricular outflow tract which is observed in these patients over time.

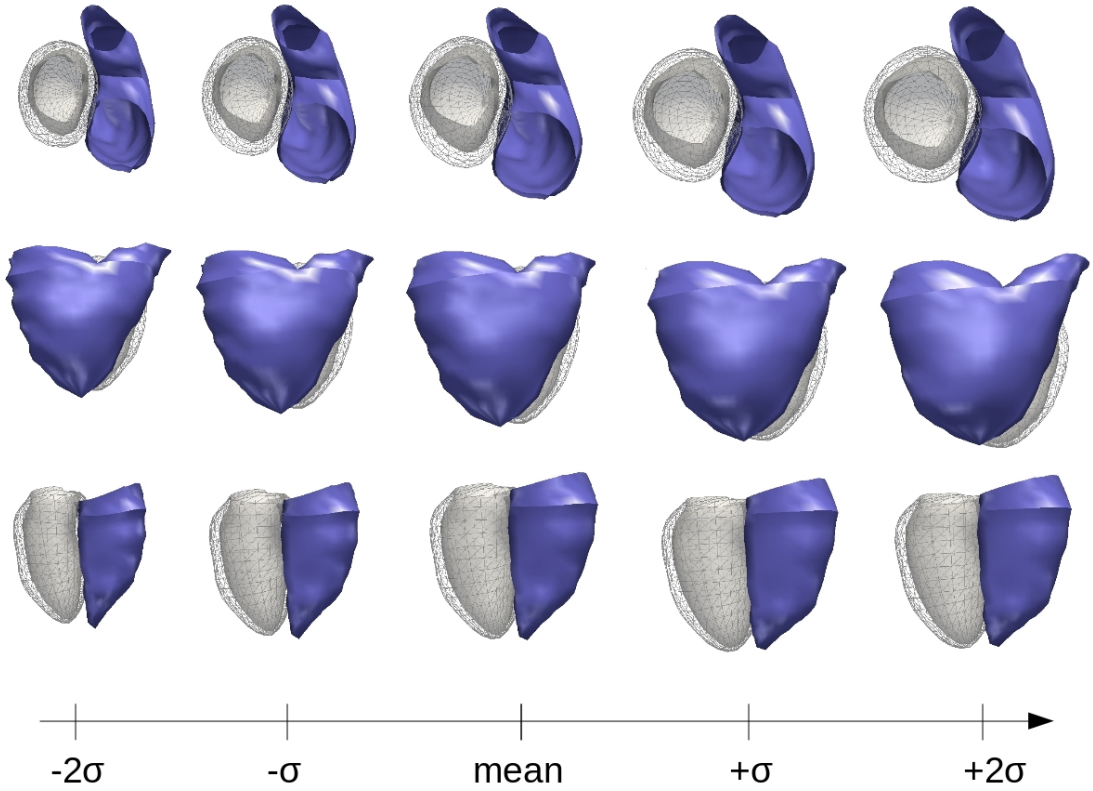

Figure 4.10: Mean growth model computed from a population of 13 rToF patients. Both ventricles grow as BSA increases

Given a larger dataset this model can be improved further by increasing the certainty in the model and by capturing more variability in shape observed in a wider population. As well, given more data we can divide the patients according to an external parameter such as treatment group to formulate a growth model for a given course of treatment. In the case of ToF, this could allow clinicians to have a better idea of how the heart re-models after different types of valve replacement surgery and

more importantly, the effect of the initial surgery on the long-term outcome. This is the key question.

4.4 Conclusion

In this chapter we presented methods for computing statistics on shapes. The proposed methods rely on currents to represent the anatomical shapes in a consistent way without the need for defining landmarks or point correspondences between shapes. This allows the computation of population statistics such as the mean and variance observed within a population and to correlate shape with clinical indices, for instance to quantify the severity of a disease. We also present a framework for formulating a generative statistical growth model to simulate the growth of an organ over time. This is especially important for our clinical application where understanding the shape remodelling of the heart in congenital diseases like Tetralogy of Fallot is crucial to better understand the evolution of the disease and ultimately to aid for therapy planning.

Chapter 5

Statistical Model of Cardiac Motion

– This chapter is based on [McLeod et al., 2015]: McLeod, K., Sermesant, M., Beerbaum, P., and Pennec, X. Spatio-temporal tensor decomposition of a polyaffine motion model for a better analysis of pathological left ventricular dynamics. *IEEE Transactions on Medical Imaging*, 34(7):1562–1575, July 2015. ISSN 0278-0062.

5.1 Introduction

Cardiovascular disease is a worldwide issue, being the leading cause of death and affecting the day-to-day life of millions of individuals. Heart disease can affect the motion dynamics of the heart over the cardiac cycle. Understanding the abnormal dynamics can thus potentially give insight into a pathology and provide information that can aid with diagnosis, therapy planning, and for determining the prognosis for a given patient. Quantitatively defining what are "normal" motion patterns is not straightforward given the complex dynamics and coupling between the ventricles and atria. In patients with heart conditions that affect the shape of the ventricles, the motion dynamics can be affected by the abnormal shape, resulting in poor pumping function in one or both of the ventricles, ultimately leading to increased workload on the heart. For patients with stenosis in the arteries or poor valve function, the motion dynamics can be affected by the excess load of the heart trying to pump blood to get enough oxygen to the body. Given the heavy workload on the heart in a lifetime, maintaining healthy heart function is crucial to maximise longevity.

The motion of the heart can be measured by placing markers on the myocardial tissue, which are then tracked over time. However, this kind of measure is invasive and not applicable on a large-scale basis or in all populations. For this reason, medical images are commonly used to non-invasively visualise the motion of the heart as it beats using magnetic resonance imaging (MRI), echocardiography (ECHO), or computed tomography (CT), for example. Using such images, the temporal evolution of the heart can be visualised in 2D or 3D. Such image sequences can be used to qualitatively analyse the motion dynamics. Some medical scanners are also able to compute global measures directly from the images such as ventricular volume, or 1D blood flow measures, however, 3D measures are not currently available in standard scanners. Also, more in-depth measures of cardiac function cannot be extracted directly from the images and quantitatively comparing motion in different subjects beyond strain or global measures is an ongoing challenge.

Quantitatively tracking cardiac motion can provide further insight into the 3D dynamics to obtain measures of cardiac function by analysing how efficiently the heart is beating and by identifying patterns related to normal (healthy) motion, and patterns characteristic of a given pathology. Myocardial deformation and strain can give early indicators of poor function and disease evolution. A number of methods for tracking cardiac tissue in a single subject have been proposed using image registration techniques to compute the deformation between images in the cardiac cycle. These methods are further discussed in Sec. 5.1. Methods for population-based analysis of cardiac motion have been proposed to study the functional dynamics of the heart at a population-wide level. A brief introduction of these methods is given in Sec. 5.1.

Cardiac Motion Tracking using Non-rigid Registration

A number of non-rigid image registration techniques for cardiac motion tracking have been proposed in recent years. A recent review of these is given in [Frangi et al., 2001; Wang and Amini, 2012]. Key features of these methods include ensuring that the deformations are diffeomorphic (smooth transformations that preserve the structure of the material to prevent non-physiological transformations such as folding) and including an incompressibility term to prevent large volume change in the myocardium. The challenge in cardiac motion tracking of cine MRI images is that the tissue is represented homogeneously in the images, giving little texture information to track besides the endocardial and epicardial contours. Thus, it is difficult to capture the strain purely from image-driven registration algorithms, particularly the circumferential strain. Voxel-based methods, which essentially model the correspondences between voxels in pairs of images, have been widely used for cardiac registration [Tautz et al., 2011],[Mansi et al., 2011a]. These methods have the advantage of defining the motion in every voxel in the image. However, since the displacement fields are dense, the number of parameters needed to describe the motion is large. For comparative population-wise studies, such a parameterisation reduces the robustness in group-wise analysis since comparing large parameter sets is difficult. Methods parameterised by B-spline transformations on the other hand have a lower number of parameters since the deformation is parameterised by the motion of control points, hence such methods have been used for cardiac motion tracking, for example in [Chandrashekara et al., 2004], [Shi et al., 2012], [Heyde et al., 2012], [De-Craene et al., 2011]. However, from B-spline based tracking, the total number of parameters relies on the sampling of control points, which is a trade-off between the accuracy of the tracking and maintaining a low number of parameters, since the motion is defined only at the control points. Simple models that can accurately represent the full deformation with a small number of parameters could provide a more insightful basis for motion analysis. The Polyaffine model [Commowick et al., 2008; Arsigny et al., 2009] provides such a framework by combining regional affine transformations in a smooth, global manner and has previously been applied in cardiac and cardiovascular image registration [Zhang et al., 2007; Hansen et al., 2012; McLeod et al., 2012; Mcleod et al., 2013b]. The Polyaffine model has the advantage of providing a regional-level analysis of the motion, and since the deformation parameters are affine, the parameters themselves are consistently defined from one sequence to another.

Population-based Motion Analysis

In [Qian et al., 2011], myocardial strain extracted from tagged MRI was used to identify and localise regional abnormal cardiac motion patterns, by describing the spatio-temporal motion as a tensor, where the tensor contains regional strain information for 20 regions of the left ventricle. This results in a tensor of size 60×10 (3 strain directions $\times$ 20 regions $\times$ 10 frames from end diastole to end systole) that is used to classify healthy/abnormal motion patterns. A key advantage of this work is the analysis of the parameters separately for space and time using 2D linear discriminant analysis (2DLDA) and a k-nearest-neighbour method to classify subjects as healthy or diseased. The method provides an interesting framework for population-specific function analysis, but is limited to 1D strain analysis. Therefore, some of the more complex 3D dynamics are not described with this model. Displacement fields were compared across subjects in [Rao et al., 2002] by first extracting the motion parameters using a B-spline model, then transforming the motion field to a common space by transforming each displacement vector by the inverse Jacobian matrix of the transformation. This was extended to construct a cardiac motion atlas in [Rao et al., 2003] by simply averaging the transformed motion fields from a group of subjects drawn from the same population. A 4D statistical atlas of the cardiac anatomy was developed using a B-spline model to represent the transformations in [Perperidis et al., 2004] by first performing spatio-temporal alignment [Perperidis et al., 2003]. This model was used to differentiate between normal motion and the motion of patients with hypertrophic cardiomyopathy. A cardiac motion atlas was constructed in [Rougon et al., 2004] by performing principal component analysis (PCA) on subject-specific motion fields after first spatio-temporally aligning the fields. Regional measures are then computed by averaging over the 17 American Heart Association (AHA) regions of the left ventricle.

5.1.1 Aim and Paper Organisation

Previous methods for performing population-based motion analysis have been directed towards analysis of dense motion fields, or of regional strain values. In terms of comparing 3D displacements, the analysis may require alignment of either images or displacement fields both spatially and temporally. In general, the spatio-temporal alignment of either images or displacement fields creates a bottleneck in population-based analysis due to the difficulty of aligning high dimensional objects. A key point missing in previous population-based work is further analysis towards understanding motion abnormalities (beyond identifying or classifying motion abnormalities).

In the present work, we are interested in performing group-wise analysis of a small set of displacement parameters obtained from the cardiac-specific PolyLogDemons algorithm of [McLeod et al., 2012; Mcleod et al., 2013b] as well as including image-driven spatial features to the model. We are particularly interested in analysing motion from short axis cine-MR images, given that this image sequence is commonly used in routine clinical practice (and thus cine-MR images are more readily available), and has the advantage of capturing the motion with reasonable spatial resolution (compared to ECHO for example). Rather than performing PCA on motion fields as in [Chandrashekara et al., 2003], or tensor decomposition of regional strain values as in [Qian et al., 2011], we perform analysis on Polyaffine parameters, and compute spatial and temporal bases by performing Tucker tensor decomposition on the parameters of a set of subjects. In contrast to the method proposed in [Xue et al., 2006] that was proposed to represent high-dimensional deformation fields in the context of brain image warping by a 3D statistical representation, we represent the deformation fields directly with Polyaffine transformation parameters.

Preliminary versions of this work have been published describing the motion tracking [McLeod et al., 2012], analysis of the trace of affine matrices [Mcleod et al., 2013b], and a preliminary investigation of matrix-based parameter decomposition to analyse spatial and temporal behaviour [Mcleod et al., 2013a]. The main contributions of the present work extending on these previous articles are summarised below:

- Image-driven spatial priors were added to [McLeod et al., 2012; Mcleod et al., 2013b]
- A framework for spatio-temporal alignment of Polyaffine parameters is proposed
- A method for the construction of a generative mean motion model is proposed
- Tensor decomposition of Polyaffine parameters is proposed to compare dominant spatial and temporal features between populations

The remainder of this paper is organised as follows. The methods section (Sec. 5.2) begins with a brief introduction of the cardiac-specific PolyLogDemons algorithm of [Mcleod et al., 2013b] that is used to obtain the transformation parameters that are used in the population-based analyses (Sec. 5.2.1). The additional image-based model priors that are added to the model are described in Sec. 5.2.1. The proposed spatio-temporal alignment of all Polyaffine parameters is described in Sec. 5.2.2. Methods for performing population-based motion analysis using Tensor decomposition of Polyaffine parameters are proposed in Sec. 5.2.3. The validation section (Sec. 5.3) describes first; the validation of the motion tracking (registration) using ground-truth motion landmarks (Sec. 5.3.1), second; the validation of the mean motion model in Sec. 5.3.2, third; an analysis of the predictive power of the mean models (Sec. 5.3.3) and finally; validation of the tensor-based analysis (Sec. 5.3.4).

5.2 Methods

5.2.1 Transformation Parameter Estimation using a Polyaffine Model

For a given set of regions, the transformation in each region i can be modelled by an affine deformation parameterised by a 3×4 matrix M_i. The M_i matrices can be fused to a global deformation field

using the Polyaffine model:

$$\vec{v}_{poly}(x) = \sum_i \omega_i(x) M_i \tilde{x}, \tag{5.1}$$

where ω_i is a parameter controlling the weight of the i^{th} region for each voxel x written in homogeneous coordinates [Arsigny et al., 2009].

As shown in [Seiler et al., 2012], Eq. 5.1 can be estimated by a linear least squares projection from an observed velocity field $\vec{v}(x)$ (in this case computed using the LogDemons algorithm) to the space of Log-Euclidean Polyaffine Transfomations (LEPT's). The log affine parameters M_i can be estimated by the following least-squares regression:

$$C(M) = \int_\Pi \parallel \sum_i \omega_i(x) \cdot M_i \tilde{x} - \vec{v}(x) \parallel^2 dx.$$

Using the Frobenius inner product $\parallel W \parallel^2 = Tr(W^T W)$, the solution at the optimum $\nabla C_M = 0$ is given by $M = B \cdot \Sigma^{-1}$ [Seiler et al., 2012], which in vector form is equivalently $vect(M) = (\Sigma \otimes Id_3)^{-1} \cdot vect(B)$, where $M = [M_1 M_2 \cdots M_3]$, $B_i = \int_\Pi \omega_i(x) \cdot \vec{v}(x) \cdot \tilde{x}^T dx$ and $\Sigma_{ij} = \int_\Pi \omega_i(x) \cdot \omega_j(x) \cdot x \cdot x^T dx$.

In [McLeod et al., 2012], the authors showed that an incompressibility penalisation and a neighbouring region regularisation can be added to this model by penalising the trace of the gradient of the Polyaffine velocity field, and by regularising the similarity between neighbouring regions via a distance term. Both terms were added in the least squares minimisation to obtain a penalised least squares error term, still with a linear solution in terms of M. The penalisation term was derived as:

$$\alpha \int_\Pi Tr(\nabla \vec{v}_{poly})^2 dx, \tag{5.2}$$

where the parameter α is used to control the strength of the penalisation. An additional term was added for the regularisation:

$$\beta \sum_i \Omega_{ij} dist(M_i, M_j), \tag{5.3}$$

where β controls the strength of the regularisation. Ω_{ij} is defined as:

$$\Omega_{ij} = \int_\Pi \omega_i(x) \omega_j(x) dx. \tag{5.4}$$

The new solution for M is given by:

$$vect(M) = (\Sigma \otimes Id_3 + \alpha V + \beta R)^{-1} . vect(B), \tag{5.5}$$

where R and V are the matrices controlling the regularisation and incompressibility respectively, as described in [McLeod et al., 2012].

The Polyaffine regions used in [McLeod et al., 2012; Mcleod et al., 2013b] were defined as cardiac-specific regions for the left ventricle using the 17 American Heart Association (AHA) regions. In [Mcleod et al., 2013b], the Polyaffine weight functions were computed in prolate spheroidal (PSS) coordinates rather than in the Cartesian frame using the method of Toussaint et. al [Toussaint et al., 2013] (see Fig. 5.1). Using the prolate spheroidal coordinates provides more anatomically grounded shapes of the weights to smooth the Polyaffine fusion around the ventricle. These coordinates have been previously used in a number of cardiac motion tracking applications, such as in [Bistoquet et al., 2007],[Heyde et al., 2012] for example.

Image-based Priors

Image Gradient Based Velocity Weighting Image-based spatial priors can be included in the model to weight the input velocity field to give more influence on velocity vectors in regions of high gradient in the image (regions that drive the LogDemons registration). In [McLeod et al., 2011], the region of interest, Π, was defined as a binary mask, where $\Pi = 1$ inside the mask, and $\Pi = 0$ outside. In this way, equal weight is given to the inner part of the tissue in the myocardium. In cine

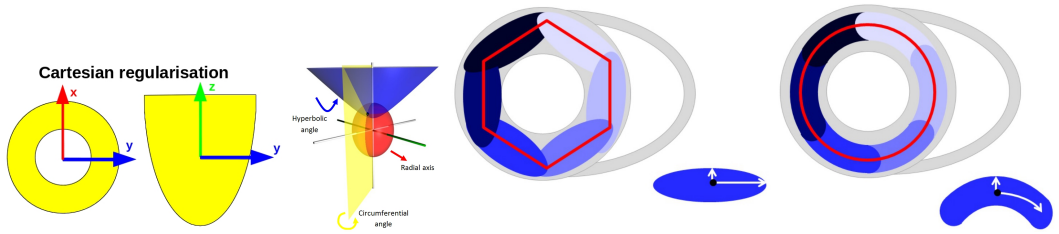

Figure 5.1: Regularisation direction for Cartesian coordinates (top left) and prolate spheroidal (PSS) coordinates (top right). The difference between Cartesian and PSS weights shown from above on a spheroid and the directions of the covariance matrix shown on an oval (bottom left - lower right corner) and curved segment (bottom right - lower right corner). The red lines emphasise the different shapes captured by the different weights, where the Cartesian weights sum to a hexagon (left) and the PSS weights sum to a circle (right).

MR images, however, there is little texture information in the inner part of the tissue. Therefore, the boundary of the tissue is the region that drives the registration, since this is the region of highest gradient. In fact, given the Gaussian nature of the Polyaffine weights, more weight is given to the centre of the tissue than the boundaries. To account for this, we introduce a spatial prior on the LogDemons correspondence field by giving higher confidence to the vectors in regions with high gradients in the image. This prior can be easily incorporated into the model by modifying the mask over which we integrate the terms in Eq. 5.2.1 (Π). Rather than using a standard binary mask, we can incorporate a confidence on the input velocity field (the LogDemons correspondence field) by taking the smoothed gradient magnitude image of the fixed and moving images (or similarly, we could use the structure tensor as used in [Le Folgoc et al., 2014]). For the reference image, however, the gradient of the binary mask image can be used since this is already defined (since it is needed for the computation of the weights). By taking the addition of these two images for the fixed and moving frames, we obtain an image with the added confidence between the fixed and moving images, which can be used to weight the input velocity field to give higher confidence to the velocities in voxels on the boundary of the tissue.

Epicardial constraints A second prior can be added to restrict the displacement in the epicardium, preventing the registration from being dragged by the endocardial motion. This is to account for the fact that the epicardial borders remain more fixed due to the constraint on the motion from the pericardium. This prior can be included in the model by down-weighting the input velocity field at the epicardium by a factor τ, where $0 < \tau < 1$, and $\tau = 1$ in regions of high gradient (thus leaving the velocity vectors unchanged). We can define τ as $(1 - (1 - C(x)) \times E(x))$, where $E(x)$ defines the epicardial border, and $C(x)$ is the magnitude of the image gradient. In practice, this can be the gradient magnitude image of the epicardial mask. The term $1 - C(x)$ is included to prevent the velocity from being restricted in regions where there is high gradient in the image (and thus in regions where we should trust the velocity).

Using this cardiac-specific PolyLogDemons method, a low-dimensional, regional, and consistent definition of the motion can be obtained for a different subjects. Moreover, the obtained deformations are physiologically grounded and the method makes use of image-specific intensity features.

5.2.2 Spatio-Temporal Parameter Alignment

Given the wide variability of cine MRI data, including temporal shifts, different cycle lengths, and different coordinate spaces for different acquisitions, spatio-temporal alignment is needed. We propose to perform the alignment directly on the transformation parameters to align all the parameters to a common space rather than pre-aligning the images or post-aligning the displacements. A method for temporally resampling the parameters so that all subjects have the same number of frames is proposed in Sec. 5.2.2, followed by a method for temporally aligning the parameters in Sec. 5.2.2,

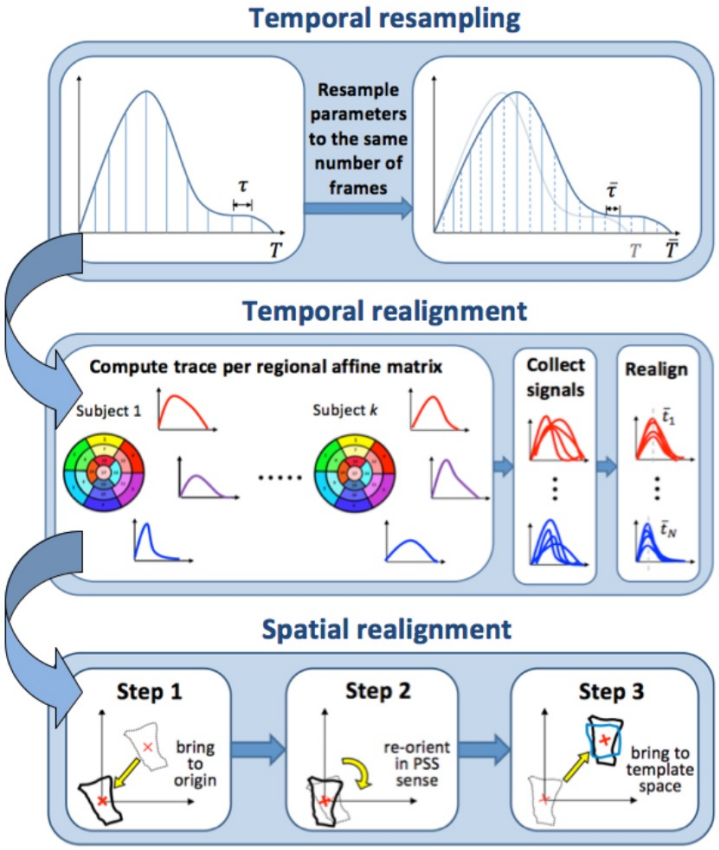

Figure 5.2: Spatio-temporal alignment pipeline starting with a temporal resampling step to resample the parameters so that there are an equal number of frames for all subjects. Temporal realignment is then performed regionally to align the parameters by the regional mean peak of the trace of the affine matrix. Spatial alignment is performed to align all parameters to a common coordinate space, by transporting the parameters to be centred at the barycentre of the region for the reference, and reoriented in a prolate spheroidal sense.

and finally a method for spatially aligning the parameters to a common space in a prolate spheroidal sense in Sec. 5.2.2. The steps for aligning Polyaffine transformation parameters are summarised in Fig. 5.2.

Temporal Resampling

In cine MR imaging, there is not a fixed number of frames acquired for each subject. In practice, the cycle length (from the R peak to the next R peak) is divided into a given number of frames (typically 10-30), and the cine movie is constructed from the information gathered over several heart beats (see Fig. 5.3). Such sequences are acquired while subjects hold their breathe, to remove lung motion artifacts. Therefore, since the cycle length differs from one acquisition to another, we need to temporally resample the parameters to a common space to have an equal number of frames for all subjects (in order to be able to directly compare the parameters). This is done simply by interpolating between frames to resample the number of observations to be the same for all subjects. This is represented in Fig. 5.2, step 1.

Regional Temporal Alignment

Cine MR image sequences are generally gated by electrocardiogram (ECG) signals, so that the first frame corresponds to the end diastolic frame, and so that an image sequence covers one cardiac cycle. Standard acquisition is acquired by waiting a given amount of time after the R wave before initiating

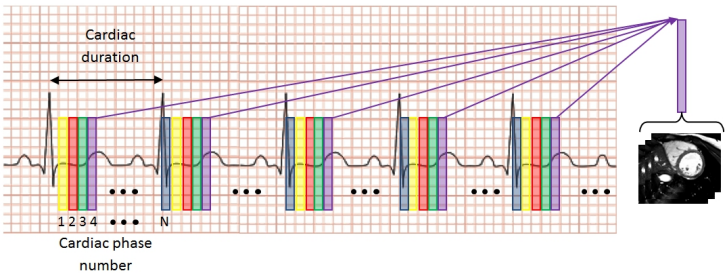

Figure 5.3: For a cine image sequence, the cardiac cycle is divided into N phases and the acquisition is averaged for each phase over several cycles. The number of phases is variable from one acquisition to another.

the sequence (see Fig. 5.4) and images are acquired between the R-to-R cycle. However, sometimes the first frame does not correspond exactly to the end diastolic frame and thus the sequence is slightly offset. Furthermore, some sequences do not loop back exactly to the end diastolic frame, where some frames may be missing, or too many frames may be included in the sequence. Also, the ECG signal may be weak in some patients, such as those with large pericardial effusion, making the ECG gating difficult. Subjects may also differ in the duration of the cardiac cycle, therefore, the peak frame does not always overlap for a group of patients. To account for this, the transformation parameters can be aligned temporally per region, by computing the trace of the affine matrix per region over time. The trace of the affine matrix corresponds to the volume curve, through properties of Lie algebra, so this essentially amounts to aligning the parameters according to the volume curves. In this way, the mean peak frame can be computed for a group of patients, and all the transformation parameters can be aligned to the mean peak frame (see Fig. 5.5). We assume that the transformation starts and finishes at the identity transformation. A temporal shift in one patient of five frames would set the first five frames to the identity transformation. This has the effect of not implying any information for these frames when the values are unknown, and thus the mean for these frames is computed only from the subjects in which the transformation is given.

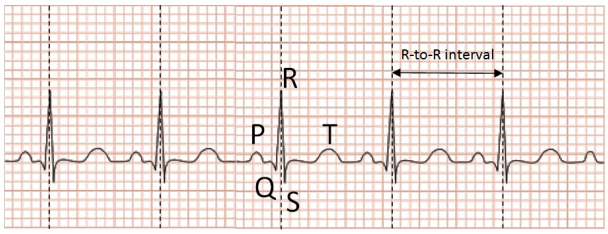

Figure 5.4: The ECG signal is used to detect the R peak. Acquisition is started a fixed amount of time after the R peak, and one cycle is considered as the R-to-R duration. Gating the cine MR sequences in this way can result in different acquisition lengths, especially for patients with low ECG signal.

Spatial Alignment

In order to be able to construct a mean motion model, we first need to transport all the parameters to a common space. Rather than aligning all the images, which would amount to rigidly registering all images to a common space prior to performing the motion tracking, as was done in [Mcleod et al., 2013a], we rather align the transformations after performing the motion tracking. Given the low dimensional representation of the motion given from the registration algorithm summarised in the previous section, this is a matter of simply transporting the affine matrices to a common coordinate space. By choosing one subject (at random) to be the reference subject, we can transport all the other subjects to this space. We are interested in analysing the motion at a regional level, hence we

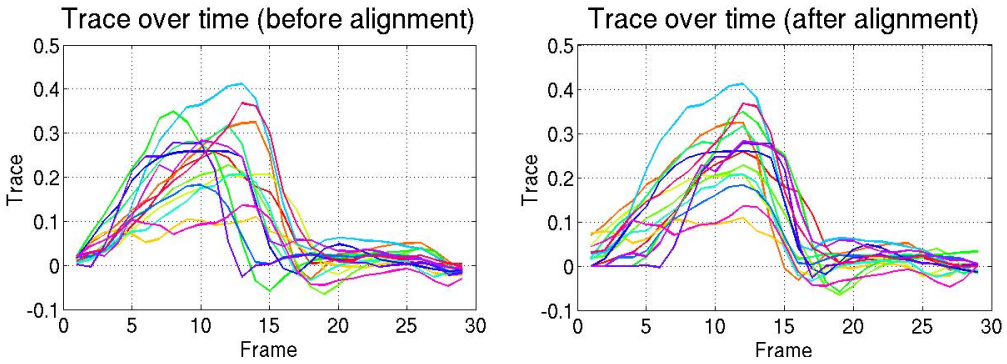

Figure 5.5: Trace of the affine matrix for a single region plotted over time for a group of subjects shown before alignment (left) and after alignment (right). Linearly aligning the curves brings the peaks to the same frame, to give the amount of shift needed to align the parameters.

are interested in aligning the matrices at a regional level independently from other regions. Therefore, we can align all matrices by first re-centring each matrix around the origin using the barycentre per region. The regions then need to be re-oriented to be aligned in a common manner. Since the Polyaffine weights are defined in PSS coordinates, it follows that the matrices can be oriented in a prolate spheroidal sense (see Fig. 5.1) by taking the Jacobian matrix computed at the barycentre. The same approach is applied to re-orient the result to match the template orientation, followed by a translation to bring the matrix to the template space. A simplification of this pipeline is shown in Fig. 5.2, step 3. The prolate spheroidal coordinates were computed using the method of Toussaint et. al [Toussaint et al., 2013].

5.2.3 Population-based Motion Analysis

Mean Motion Model Construction

Once all the matrices are aligned to a common space for all subjects, the mean of these observations can be easily computed using basic arithmetic operations. The mean M_t at time t can be computed by:

$$\bar{M}_t = \frac{1}{N_k} \sum_{i=1}^{N_k} M_{k,t}, \tag{5.6}$$

where k is the subject index, N_k is the number of subjects, and $M_{k,t}$ is the transported matrix for subject k at time t. By stacking all the matrices of a given subject to form a column vector of [time $\times$ number of regions $\times$ affine parameters], we can similarly compute the mean trajectory $\bar{M}$ by taking the average of these vectors.

Simulated Motion from the Mean Model

Given the estimated mean trajectory, the motion can be simulated on a new subject, given that the subject is in the same coordinate space as the reference, by simply applying the mean M_t to the first image of the sequence: $I_t = M_t * I_0$ (see Fig. 5.6).

In general, new subjects will not be in the same coordinate space as the template. Therefore, the mean trajectory $\bar{M}_t$ first needs to be transported to the subject space. This can be done in a similar way to the pipeline for aligning the subjects. Given the barycentre and Jacobian matrix for each region of the new subject, $\bar{M}_t$ can be transported to the subject space by:

$$M_r^k = T_r^k \cdot (\bar{T}_r)^{-1} \cdot \bar{M}_r \cdot \bar{T}_r \cdot (T_r^k)^{-1}, \tag{5.7}$$

where M_r^k is the mean motion model in region r in the subject-specific space for subject k, T_r^k is

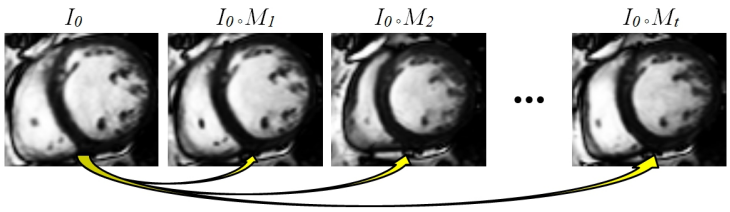

Figure 5.6: The mean motion model applied to an image requires simply applying the mean transformation per frame to the reference end-diastolic image.

the matrix:

$$T_r^k = \left[\begin{array}{cc} J_r^k & b_r^k \\ \hline 0 & 1 \end{array}\right]$$

with b_r^k the barycentre of region r for the k^{th} subject (in Cartesian coordinates), and J_r^k is the Jacobian matrix at the barycentre in the local (prolate spheroidal) coordinates. $\bar{T}_r$ is equivalently defined for the mean at the barycentre of region r in the reference space.

5.2.4 Spatial and Temporal Mode Construction using Tensor Decomposition

Rather than performing PCA on stacked matrices of all parameters for each subject or singular value decomposition (SVD) on parameters stacked either temporally or spatially as in [Mcleod et al., 2013a], the tensor $\mathcal{T}$ of all parameters can be decomposed directly. A number of methods for tensor decomposition have been proposed, the most common being the CANDECOMP/PARAFAC (CP) decomposition [Carroll and Chang, 1970; Harshman, 1970] and the Tucker decomposition [Tucker, 1963, 1966] (see Fig. 5.7). A review of these methods, as well as other tensor decomposition methods, is given in [Kolda and Bader, 2009]. The CP decomposition is the generalisation of SVD to tensors, in which a tensor is factored into the sum of rank-one tensors (tensors that can be written as the outer product of vectors). The Tucker decomposition (also known as higher-order PCA), rather decomposes the tensor into a core tensor and factor matrices corresponding to each axis (see Fig. 5.7). In this work, we focus on the Tucker decomposition, to give decoupled "loadings" of the modes (whereas in the case of the CP decomposition, there is a single loading for each axis, meaning that the n^{th} modes are coupled in some way).

Tensor Decomposition Using the Tucker Method

The Tucker decomposition (a.k.a higher-order PCA/SVD, N-mode SVD/PCA) computes an orthonormal space associated with each axis of the tensor $\mathcal{T}$. For a three-way tensor, the Tucker decomposition of $\mathcal{T}$ is expressed as an n-mode product:

$$\begin{aligned} \mathcal{T} \approx \mathcal{G} \times_1 A \times_2 B \times_3 C &= \sum_{p=1}^{P} \sum_{q=1}^{Q} \sum_{r=1}^{R} g_{pqr} a_p \circ b_q \circ c_r \\ &= [[\mathcal{G}; A, B, C]], \end{aligned} \tag{5.8}$$

where $\times_n$ denotes the mode-n tensor-matrix product, and $\circ$ denotes the vector outer product. A, B, and C are loading matrices in each direction that can be thought of as the tensor equivalent of principal components for each axis. The core tensor $\mathcal{G}$ gives the relationship between the modes in each direction and describes how to re-combine the original tensor $\mathcal{T}$. Computing such a decomposition is not straightforward. One method for doing so is to matricise the tensor (in the three-way case), similar to the decomposition described in [Mcleod et al., 2013a]. Another method, known as the *Tucker1* method, is to compute optimal components to capture the variation in the n^{th} axis, independently from the other axes. Alternatively, the factors can be estimated using an iterative

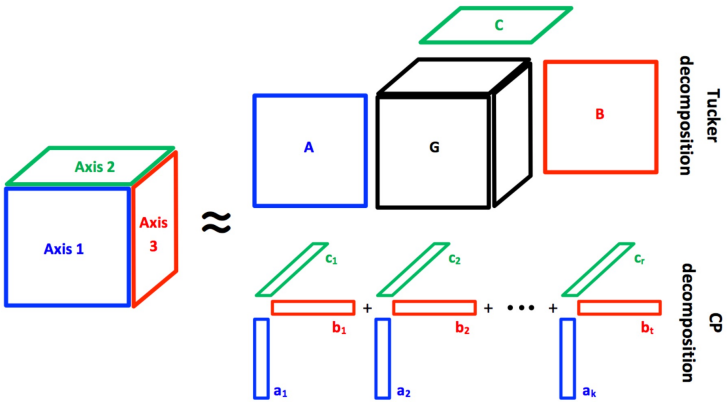

Figure 5.7: Visual representation of the Tucker decomposition (top right) and CP decomposition (bottom right) on a three-way tensor.

alternating least squares strategy (ALS), an alternating slice-wise decomposition (ASD), non-linear conjugate gradient method (NCG) and using a direct multi-linear decomposition (DMLD). Further details on the ALS strategy used in this work for computing a Tucker decomposition is given in the Appendix.

The tensor decomposition can be performed on a tensor stacked in a number of different ways, and would provide different levels of analysis of the parameters. In order to compute the spatial and temporal modes separately, all the spatial parameters can be stacked as a single vector of all affine parameters for all regions, along time, and for all subjects (namely a 3-way tensor of $space \times time \times subject$). This decomposition enables separate spatial and temporal mode analysis to be performed so that the reduced-order model can be validated by comparing to known spatial and temporal dynamics. It is also possible to decouple the spatial features into the respective regional and affine components in order to give a more detailed analysis of the regional motion differences and to extract the dominant affine components. Since this decomposition cannot be validated, it is not addressed in this work. More detailed constructions are also possible to separate the space parameters, such as using separate tensors for each region to provide another type of regional analysis.

5.2.5 Understanding Pathology-specific Motion Abnormalities

Identification of cardiac motion abnormalities and classification of normal vs. abnormal motion patterns is an important step towards better understanding cardiac diseases that affect function. Given the formulation of the proposed methods, in which the motion is defined with a low number of parameters (the Polyaffine parameters), and given that the parameters can be aligned to a chosen reference space (using the methods described in Sec. 5.2.2), different subjects can be compared, and models representing the mean motion of a population can be constructed (as in Sec. 5.2.3) in order to analyse population-specific motion patterns. Mean motion models computed on different populations could be compared to the Polyaffine parameters from a patient-specific simulation to help to classify patients according to different diseases or different stages of a given disease, to aid in cases where there is uncertainty in the diagnosis of a specific patient. This classification could be combined with standard clinical measures to give a more informative picture of the patient's condition. Also, by applying the mean model to a new subject (following the method described in Sec. 5.2.3), synthetic sequences can be generated to, for example, create a database of sequences with known ground-truth deformation to test cardiac models. A key advantage of the proposed mean motion model formulation is the ability to create full 3D sequences from the different models, to better understand the motion abnormalities. Such models could be used to complement existing methods to identify abnormal regions (strain or wall motion analysis for example), by providing more detail on what may be causing abnormal motion patterns in a population by visually analysing the motion dynamics.

5.3 Validation

In order to test the methods described in the previous sections, 4D sequences of two populations were studied. The first; a data-set of healthy controls, to establish normal motion patterns, and the second; a data-set of patients with Tetralogy of Fallot, to establish motion patterns related to this pathology.

a) Healthy Volunteers We illustrate these tools on 15 healthy adults (3 female, mean age $\pm$ SD $= 28 \pm 5$) obtained from the STACOM 2011 MICCAI cardiac motion tracking challenge database [Tobon-Gomez et al., 2013]. Steady-state free precession magnetic resonance images were acquired using a 3T scanner (Philips Achieva System, Philips Healthcare) in the short axis view covering entirely both ventricles (12-16 slices; isotropic in-plane resolution:$1.15 \times 1.15 mm^2$ to $1.25 \times 1.25 mm^2$; slice thickness: $8mm$; 30 frames).

b) Tetralogy of Fallot Patients To test the methods on pathological cases, we applied the described method to ten patients with repaired Tetralogy of Fallot (5 female, mean age $\pm$ SD $= 21 \pm 7$). These patients all had a full repair early in infancy, resulting in the destruction of the pulmonary valves. Steady-state free precession magnetic resonance images were acquired for each patient in the short axis view covering entirely both ventricles (12-15 slices; isotropic in-plane resolution: $1.21 \times 1.21 mm^2$ to $1.36 \times 1.36 mm^2$; slice thickness: $8mm$; 15-19 frames).

5.3.1 Validation of the Motion Tracking

Since the proposed population-based motion analysis is based on the initial motion tracking, the accuracy of the motion tracking has a large impact on the subsequent analysis. In order to examine the accuracy of the motion tracking, the cardiac-specific PolyLogDemons method was applied to the STACOM 2011 MICCAI cardiac motion tracking challenge database [Tobon-Gomez et al., 2013]. The primary goal here was to validate the choice of parameters used in the model to determine if the input parameters, the number of regions, and the choice of weight functions, provide sufficiently accurate tracking on a level equivalent to state-of-the-art methods.

The STACOM 2011 cardiac motion tracking challenge was open to all willing participants. Of the four competitors that applied for the challenge, only two applied their methods to the cine MR sequences. These were the Temporal Diffeomorphic Free Form Deformation (TDFFD) method of De Craene et. al [De-Craene et al., 2011] and the iLogDemons method of Mansi et. al [McLeod et al., 2011; Mansi et al., 2011a]. The principle behind the TDFFD method is to model the deformations as B-splines. The iLogDemons is rather a gradient-driven optical flow method based on the Demons method. As with the method used in this work, both of these methods require a mask of the myocardium as input.

Evaluating the accuracy of the provided ground truth landmark tracking is not the objective of this work. Rather, we are interested in quantitatively comparing the registration results of the proposed method to state-of-the-art methods applied to the same sequences. Given that the ground truth computation is subject to errors from the landmark allocation itself (inter- and intra-observer bias), and in alignment between the tagged MR and cine MR sequences (subjects may move between acquisitions), and noting the large slice thickness (8mm), we are interested in evaluating how greatly the errors vary from the other methods, rather than the absolute error itself. Furthermore, we expect higher errors than for ECHO or tagged MR for instance, since there is little or no texture information in the myocardium to drive the registration [Wang and Amini, 2012].

We applied the same work-flow for computing the error as described in [Tobon-Gomez et al., 2013] to be able to directly compare the errors between the different methods. Based on the experiments described in [Mcleod et al., 2013b], [McLeod et al., 2012], the chosen parameters were $\alpha = 1, \beta = 1, \kappa = 0.5, \mu = 1$, with PSS weights, and three multi-resolution levels. The l^2 norm error, between the annotated landmarks at end diastole and end systole and the deformed landmarks at the corresponding frames, was computed. The median error value of the two time points was 3.07 for the proposed method. This can be directly compared to the median values for the iLogDemons

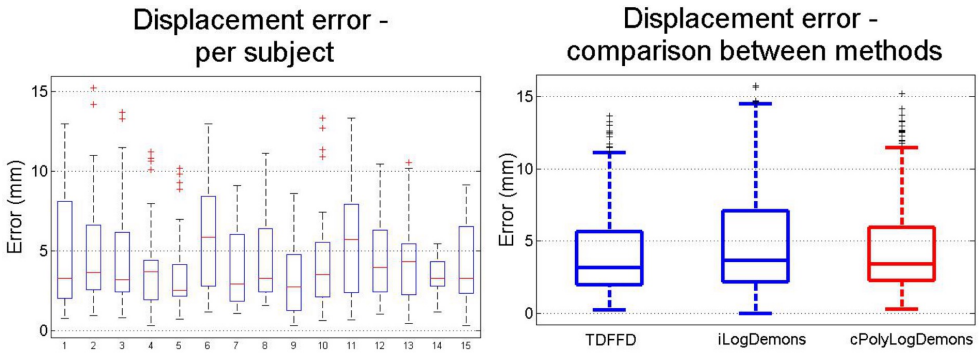

Figure 5.8: Box plot of errors per subject from the 12 4D annotated landmarks at end diastole and end systole (top). The average over the population is plotted for the TDFFD algorithm, iLogDemons algorithm, and the cardiac PolyLogDemons method (bottom). The cardiac PolyLogDemons method is on the same order of accuracy as both the TDFFD and the iLogDemons method.

algorithm (4.82) and for the TDFFD algorithm (3.17). Therefore, the errors are on the same order of magnitude as these methods. The errors are plotted in Fig. 5.8 (top) for each of the 15 volunteers. The error over all the subjects is shown in Fig. 5.8 (bottom) along with the box plots for the TDFFD and iLogDemons methods for comparison.

5.3.2 Validation of the Mean Motion Model

A mean normal (healthy) motion model was computed from the 15 healthy volunteers. The first volunteer was chosen to be the reference, and all other subjects were aligned to this space. Note that the choice of reference is arbitrary since the parameter space is the space of affine transformations described in Cartesian coordinates. To visualise the mean motion models, the models were transported to the space of one of the volunteers. The first image was deformed by each motion model using the method described in Sec. 5.2.3. In order to analyse the results, we compare the mean models to both the Polyaffine model and to the original sequence. The images at three frames (frame 5, 10 and 20) are shown in Fig. 5.9. The healthy mean motion model gives a reasonable motion pattern, and actually gives smoother motion than the Polyaffine model. As shown in the second column for the Polyaffine sequence, the radial contraction is underestimated in the regions close to the junctions of the right ventricle with the left ventricle (as shown by the yellow arrow). The Tetralogy of Fallot mean motion model shows abnormal dynamics, with abnormal flattening of the left ventricle free wall towards the septum. This abnormal flattening at the septum has been observed in many Tetralogy of Fallot patients, and may be due to a high prevalence of post-repair right bundle branch block in the ECG (through a patch to repair the ventricular septal defect (VSD)) [Jing et al., 2014], the effect of the VSD-patch itself [Knauth et al., 2008], and mediated through the persisting right ventricular volume and/or pressure load resulting from chronic pulmonary regurgitation/stenosis [Hui et al., 2014]. As a result, inter- and intra-ventricular dyssynchrony is highly prevalent and is regarded as an important contributor to both right ventricle and left ventricle dysfunction. More circumferential motion is also observed in the Tetralogy of Fallot mean motion sequence, as can be seen in the video of all of the sequences (see the supplementary video). Note that the key region of interest in these sequences is the myocardium of the left ventricle. Since the first image is deformed by each model, there are some motion artefacts in the blood pool caused by the trabeculae present in the first image. Also, the surrounding regions move due to the nature of the smooth Polyaffine weights.

A leave-one-out experiment was performed to test the ability of the mean model to approximate the motion of a new subject drawn from the same population by using 14 subjects as the training set, and testing on the 15^{th} subject. The residual error between the mean motion model (in the k^{th} subject space) and the original Polyaffine transformation parameters (before realignment) was computed for subjects in the training set as well as for subjects in the testing set. The errors are plotted over time in Fig. 5.10 for the training set (top) and the testing set (bottom). The errors are

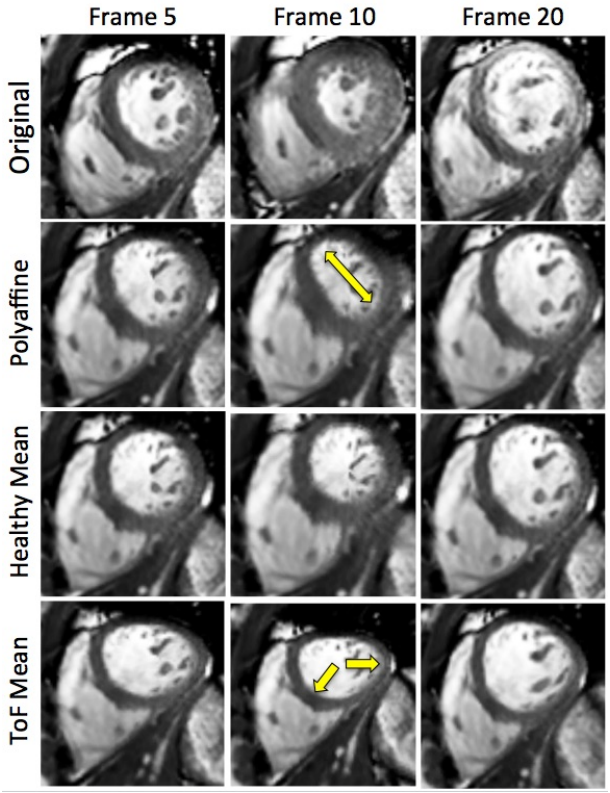

Figure 5.9: Original sequence (top row), Polyaffine Model (second row), healthy mean motion model (third row) and Tetralogy of Fallot mean motion model (bottom row) at frame 5 (left column), 10 (centre) and 20 (right column) for one subject. The Polyaffine model underestimates the radial motion in some regions (indicated with the yellow arrow on frame 10), whereas the healthy mean motion captures smoother, more physiological motion. The Tetralogy of Fallot mean motion model shows abnormal motion dynamics, with inward motion at the left ventricle free wall and expansion, rather than contraction at the junctions of the left and right ventricles (shown in the bottom row, centre column with yellow arrows).

within the same range for the training and testing set, indicating that the model is able to predict the motion of healthy subjects.

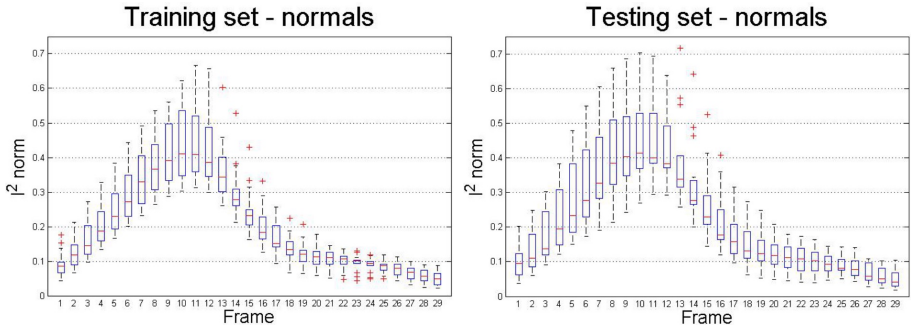

Figure 5.10: Box plots of the residual norm between the Polyaffine transformation and the normal mean model transformation over time for subjects used in the training set (top), and for subjects not used in the training set (bottom) for the healthy volunteers.

Performing the same leave-one-out experiment on the Tetralogy of Fallot patients, we find that the residual errors are also not higher for the training set than for the testing set, as shown in Fig. 5.11. Therefore, this suggests that the mean Tetralogy of Fallot motion model is able to capture the motion dynamics of these patients reasonably well.

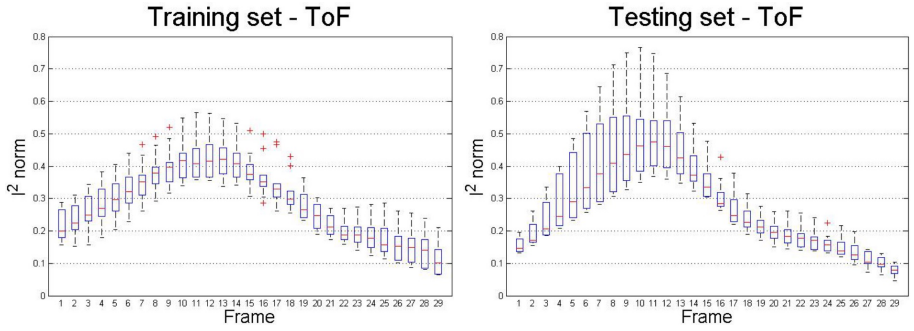

Figure 5.11: Box plots of the residual norm between the Polyaffine transformation and the normal mean model transformation over time for subjects used in the training set (top), and for subjects not used in the training set (bottom) for the Tetralogy of Fallot patients.

5.3.3 Analysis of the Predictive Power of the Mean Models

To test the ability of the mean normal model to capture the motion of Tetralogy of Fallot patients, the mean motion model was applied to each patient, and the weighted residual error between the model and the Polyaffine parameters was computed. Note that this distance measure was chosen to take into account the standard deviation of the data without requiring the computation of the inverse of the covariance matrix, as in the standard Mahalanobis distance (since the covariance matrix is ill-conditioned). The box plot of the error is given in Fig. 5.12 (top) alongside the box plots of the training and testing set of the healthy volunteers. As expected, the errors are higher for the Tetralogy of Fallot patients, indicating that the healthy model is insufficient in capturing the motion dynamics in these patients. This suggests that there are abnormal motion dynamics observed in these patients that are not captured in the healthy model.

As a further test to quantify the differences between the populations and to overcome the issue of inverting the covariance matrix in the standard Mahalanobis distance computation, a projected Mahalanobis distance was computed. By projecting the parameters to a 1D plane, the Mahalanobis

distance was computed directly from the projections γ_i given by:

$$\gamma_i = \frac{(V_i - \bar{V})^T(\bar{V}_{ToF} - \bar{V})}{\|\bar{V}_{ToF} - \bar{V}\|^2}, \tag{5.9}$$

where V_i is the vector of parameters for subject i ($i = 1, \ldots, 25$), $\bar{V}$ is the mean of the health controls, and $\bar{V}_{ToF}$ is the mean of the Tetralogy of Fallot patients. In this formulation, if a subject is close to the mean of the healthy controls, then $\gamma \simeq 0$, if a subject is close to the mean of the Tetralogy of Fallot patients, then $\gamma \simeq 1$. A leave-one-out experiment was performed with the mean computed on 14 subjects and the projected Mahalanobis distance computed on the 15^{th} subject, as well as on the Tetralogy of Fallot patients (see Fig. 5.12 - bottom). The mean for the healthy subjects was 0.8986, which can be compared to the Tetralogy of Fallot patients with 4.4513. Therefore, there is a statistically significant difference between the populations ($p < 0.05$).

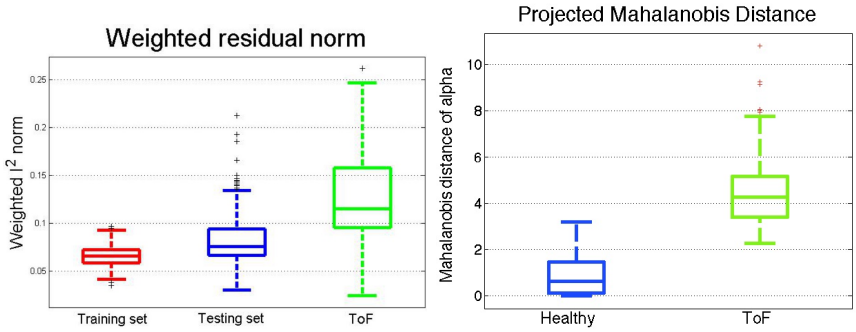

Figure 5.12: Top: Box plots of the weighted residual norm (l^2 norm weighted with respect to the standard deviation of the mean model) between the Polyaffine transformation and the normal mean model transformation for subjects used in the training set (left - red), for healthy subjects not used in the training set (centre - blue) and for Tetralogy of Fallot patients (right - green). Bottom: Projected Mahalanobis distance measure on the alpha indices from Eq. 5.9 for the healthy subjects (blue) and Tetralogy of Fallot patients (green).

In order to determine the classification power of the models for each population, two-dimensional linear discriminant analysis (2DLDA) [Liang et al., 2008] was performed using the openly available Matlab code from Mathworks file exchange. Following the application of this method described in [Qian et al., 2011] to discriminate between different populations by setting the two dimensions in the 2DLDA formulation as the spatial and temporal dimensions, a classifier was trained in a leave-one-out nature on all the transformations. The subjects were labelled as either healthy or Tetralogy of Fallot, and the classifier was tested on the excluded subject. Setting the parameters p and q for the dimensions of the reduced subspace as $p = q = 15$, and running a k-Nearest-Neighbours classifier on the testing subject (with 3 neighbours), the classifier correctly predicted the population group with 100% accuracy. Reducing the dimension of the acquired subspace to $p = q = 5$ yielded a classification accuracy of 92%.

5.3.4 Validation of the Tensor Decomposition

In order to capture the spatial and temporal aspects of the motion, a 3-way tensor of all the spatial parameters (affine parameters for all regions) stacked along time and for all subjects was constructed. Stacking the tensor in this way gives a decomposition in terms of the spatial components and temporal components separately (though other constructions are also possible). The Tucker tensor decomposition was performed using the Sandia National Laboratories Tensor Toolbox [Bader et al., 2012], implemented in MATLAB. Using these tools, the three-way tensors of [$space \times time \times subject$] of the healthy controls and of the Tetralogy of Fallot patients, were decomposed into factor and core matrices. Using the Tucker decomposition, we obtain temporal bases for each loading related to the spatial bases.

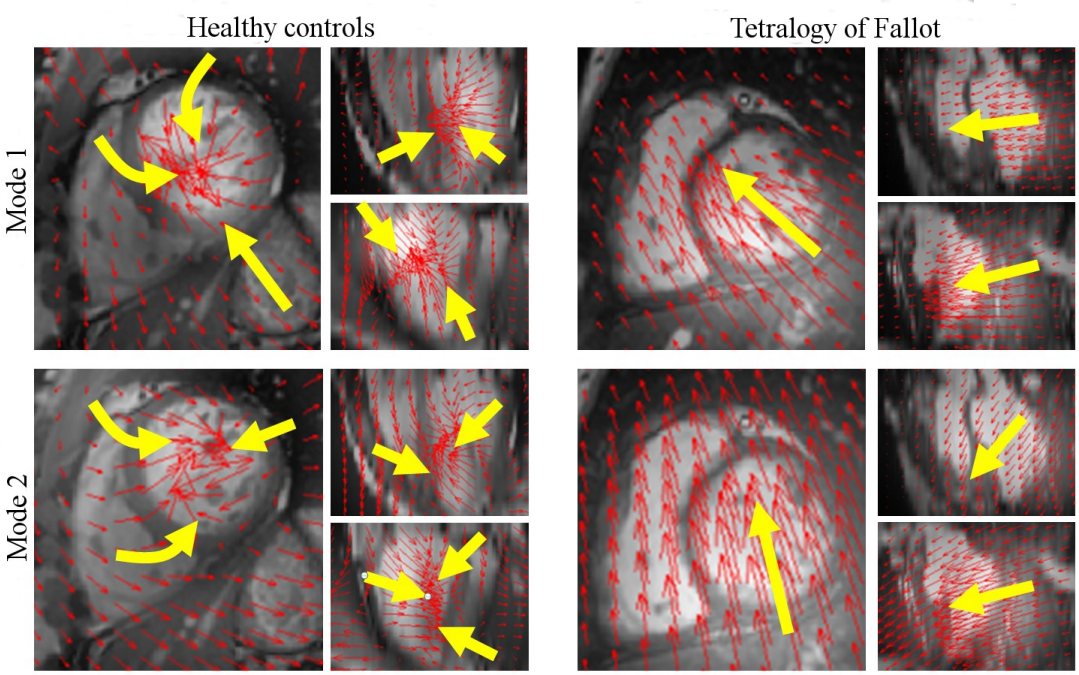

Figure 5.13: Three views of the first (top row) and second (bottom row) spatial modes for the healthy controls (left) and for the Tetralogy of Fallot patients (right). The modes for the healthy controls represent the radial contraction and circumferential motion, whereas the modes for the Tetralogy of Fallot patients represent the translation towards the right ventricle. Yellow arrows indicate the general direction of motion.

The first two spatial modes for the healthy controls are shown in Fig. 5.13 (left) and for the Tetralogy of Fallot patients (right). The first mode for the healthy controls appears to capture both the radial contraction and the circumferential motion (shown in block yellow arrows). The Tetralogy of Fallot modes, on the other hand, appear to capture a translation of the free wall and septal wall towards the right ventricle (RV). This abnormal motion is evident in the image sequences of these patients.

The temporal modes are shown in Fig. 5.14 (corresponding to the first loading of the spatial modes) for the first five temporal modes, shown for the healthy controls (top) and Tetralogy of Fallot patients (bottom). These plots show the dominant temporal mode in blue, which corresponds well to the expected volume curve for healthy subjects, but may indicate slower contraction and slower filling for the Tetralogy of Fallot patients.

The volume curves for the Tetralogy of Fallot patients were computed for the left ventricle from 4D segmentation performed using the MedViso Segment software (openly available for research purposes [Heiberg et al., 2010]), as shown in Fig. 5.15. The mean curve (shown in gray) corresponds well to the dominant temporal mode for these patients shown in Fig. 5.14, which indicates that the end systolic phase is delayed compared to healthy subjects and confirms the findings for the first temporal modes.

5.3.5 Implementation and Processing Time

The implementation of the described methods requires a number of key steps, including pre-processing of the images, segmentation of the ventricle and division into the Polyaffine regions (the AHA regions), computation of the Polyaffine weights, execution of the motion tracking registration, tensor construction, and model reduction. The pre-processing of the images requires image contrast enhancement and isotropic voxel resampling for the LogDemons part of the registration (which is computed on a regular grid and thus requires the voxel size to be isotropic). The left ventricle needs to be segmented in order to define the AHA regions and to compute the Polyaffine weights (which

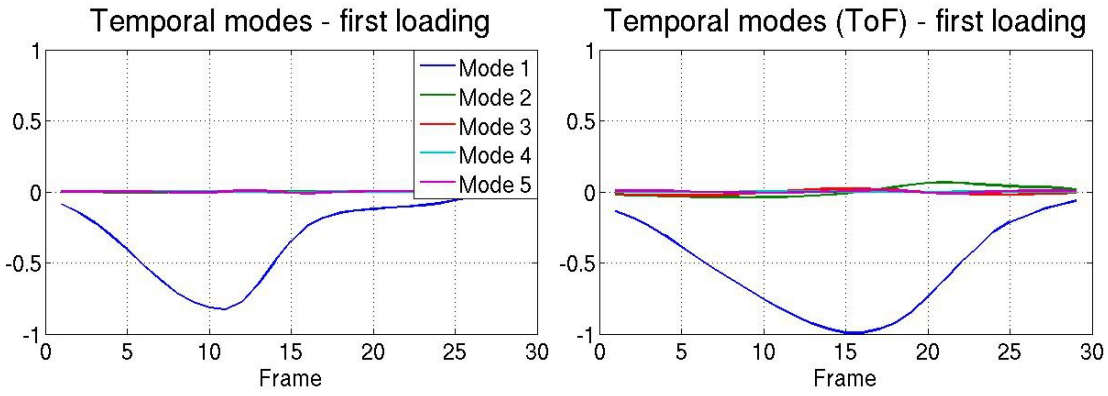

Figure 5.14: Temporal modes for the first five loadings corresponding to the first spatial mode for the healthy controls (top), and for the Tetralogy of Fallot patients (bottom). The first loadings show interesting differences for the Tetralogy of Fallot patients, with slower contraction and slower filling than for the healthy subjects.

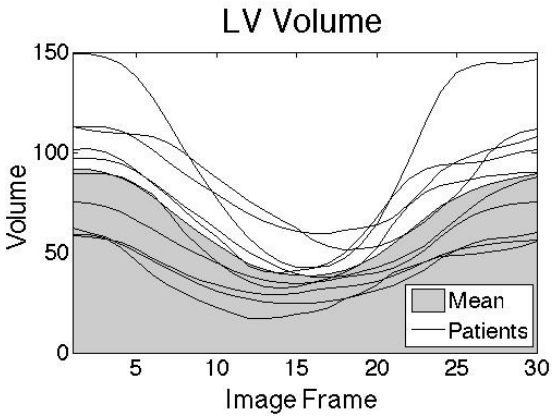

Figure 5.15: Left ventricle volume curves over time for the 10 Tetralogy of Fallot patients (in black) and the mean volume (shaded gray), which shows similar trends to the principal temporal mode shown in Fig. 5.14.

can both be performed automatically given the segmentation as well as the labelling of the apex, base and the junctions between the left and right ventricles). Given the regions and the weights, the registration algorithm can be launched by sequentially computing the registration of the current frame to the reference frame (the end-diastolic frame) and initialising the registration with the previous frame-to-reference velocity field. The registration is computed using ITK and C++ functions, building from the ITK implementation of the LogDemons algorithm [Dru and Vercauteren, 2009]. Constructing the tensor from the computed parameters is simply tensor manipulation and stacking. The model reduction on the constructed tensor was performed in Matlab using the tensor decomposition methods from Sandia National Laboratories [Kolda and Bader, 2009]. In terms of implementation, the key bottleneck is in the segmentation of the left ventricle, which in this case was performed using semi-automatic tools which requires on average 30 minutes per surface, and can take more than an hour in difficult cases (where there is large slice misalignment for example). Computation of the regions and weights is fully automatic and reasonably fast with C++ programming. The registration itself takes around 30 minutes per registration, therefore, given the sequential nature of the computation for a full heart cycle, it can take several hours for one cardiac sequence. Finally, the tensor construction and decomposition can be quickly computed in Matlab (in minutes). Ideally, the steps could be automated and the computation time could be improved by taking advantage or parallel computing architectures and by minimising the need for user intervention with fully automatic segmentation and landmark detection tools.

5.4 Discussion and Perspectives

In the current work, we proposed to use statistical methods to create a mean motion model, and to extract the modes of variation in terms of the spatial and temporal components using image registration, statistical model reduction, and tensor decomposition methods. The proposed method uses the parameters of the cardiac PolyLogDemons algorithm [Mcleod et al., 2013b], which gives transformations described by a small number of parameters extracted from cine MR image sequences. The analysis of cine MR images was chosen specifically for the frequency of use in standard clinical practice (no radiation risks and short axis cine loops are standard in the clinical protocol for many diseases), which allows for more wide-spread application of the method, as well as for the good spatial resolution, which allows for better visualisation of the myocardial borders.

The proposed methods were applied to motion tracking of the left ventricle only. The reasons behind this choice are described in Sec. 5.4. Spatio-temporal alignment of the parameters was performed prior to the analysis. The techniques used for the alignment are further discussed in Sec. 5.4. A mean motion model was constructed by taking the average of the aligned parameters. The mean model construction is further discussed in Sec. 5.4. From the obtained Polyaffine transformation parameters, statistical model reduction was applied to the parameters after spatio-temporal alignment. The statistical methods used are discussed in Sec. 5.4. A brief discussion on an interpretation of the results and how the proposed methods can be used to gain further insight into pathology-specific functional abnormalities is described in Sec. 5.4.

Bi-ventricle Motion Analysis

The present work is focused primarily on the left ventricle since the current ground truth data for the motion is available for the left ventricle only. As a proof of concept article it does not seem viable to draw any conclusions from the statistical model (namely the tensor decomposition) built from the motion tracking (the cardiac PolyLogDemons method) without having some validation of the motion tracking parameters. Furthermore, investigating left ventricular dynamics in Tetralogy of Fallot subjects is of interest for clinicians since left ventricle dysfunction has been identified as a predictor for mortality in adults with this disease [Ghai et al., 2002]. For future applications to clinical data the method can be extended to bi-ventricular (i.e. left and right ventricle) motion analysis, provided that anatomically relevant weights can be defined on the right ventricle.

Parameter Realignment

Spatio-temporal alignment was performed by making use of the trace of the affine matrices to align the transformations temporally, and making use of the prolate spheroidal coordinates to align the transformations spatially, in an anatomically meaningful manner. The temporal realignment used in this work was a simple rigid transformation of the parameters, to translate the parameters regionally to the mean peak of the trace. However, this may have the effect of removing relevant parameters. Therefore, a non-rigid transformation may allow more intuitive analyses by fixing the first frame and stretching (or shrinking) the parameters to the mean peak of the trace, and stretching (or shrinking) to the relaxation phase, similar to the temporal alignment described in [Perperidis et al., 2005]. Both the temporal and spatial alignment were performed at a regional level. This was due to the fact that we are interested in region-wise analyses, rather than global analyses. However, it is also possible to temporally align the transformations to a global peak frame. Spatially, however, the current formulation relies on the regional construction. The parameters could be spatially aligned by the barycentre of the ventricle, however, further data-points would be needed such as the base, apex and the junctions between the left and right ventricles.

Mean Motion Model Construction

From the mean motion model constructed from healthy subjects, we found that the model is able to approximate the motion of other healthy subjects reasonably well, however, the motion of Tetralogy of Fallot patients was not fully captured from this model. This was expected given the abnormal motion dynamics observed in Tetralogy of Fallot patients. Interestingly, the motion model constructed from 9 Tetralogy of Fallot patients was sufficient to capture the motion dynamics of the 10^{th} subject (based on the results of the leave-one-out experiment). Given that these patients have followed different treatment paths, and are at different stages due to the range of patient age (some patients are children, others adults), we expected to require a larger number of patients to capture the dynamics in this population. However, the related factor between these patients is a missing pulmonary valve, caused by the initial surgery. Therefore, the regurgitated blood from the pulmonary artery may be the key factor affecting the motion dynamics of these patients. Ideally, given more patients with similar treatment history, treatment-specific models could be constructed to distinguish the key differences in the motion dynamics for patients treated with one treatment over another. In future work, the mean motion models could also be used to generate synthetic sequences for new subjects in which only the end diastolic image is available.

Statistical Model Reduction

A number of statistical model reduction techniques were used in this work to attempt to understand the underlying motion variability of the two populations. We extend on the work in [Mcleod et al., 2013a], in which model reduction is performed block-wise on matrices stacked either column- or row-wise to obtain temporal and spatial population bases. In the current work, we perform model reduction on the full tensor using the Tucker decomposition to obtain spatial and temporal bases directly. The advantage of performing model reduction directly on the tensor is that the bases are decoupled and can be recombined independently. However, tensor decomposition is not straightforward and requires numerical methods for estimating the modes, compared to matrix decomposition which can be performed simply with SVD, PCA, partial least squares, etc. The tensor decomposition used in this work was the Tucker decomposition, though a number of other methods for decomposing a tensor have been proposed and could be applied (such as CP decomposition, 2DPCA, etc.).

Population-wide Analysis of 4D Motion

The validation section (Sec. 5.3) showed the ability of the proposed population-based analysis methods for extracting the dominant patterns observed in a population. For healthy subjects, these were the radial, circumferential, and longitudinal motion representing the key spatial patterns, and the temporal trigger which follows the pattern of the volume curve in the ventricle. In contrast, the

typical motion patterns for Tetralogy of Fallot patients are less well known. The presented method identified the dominant spatial pattern in these hearts as being a translation from the left ventricle free wall to the septum, which is consistent with qualitative analysis of the motion visible for some patients, in which the left ventricle appears to be dragged towards the right ventricle. The identified temporal trigger indicates that there is a slower contraction of the left ventricle, which was verified by computing the volume over time for all patients using image segmentation. These experiments may provide further insight into the function of the left ventricle for Tetralogy of Fallot patients, with more efficiency than manual analysis (i.e. 4D segmentation of several hearts may be time-consuming and subject to user bias) and may provide more detail than simpler methods (such as 1D measures of strain or wall thickening).

4-Way Tensor Decomposition

The goal of the proposed methodology is to gain insight into pathology-specific functional behaviour by analysing the motion to extract information that may currently be unknown. The experiments described in the validation section showed that both the mean motion model and the tensor decomposition of grouped motion parameters give meaningful results in terms of extracting already known information automatically from the data (such as spatial and temporal behaviour). In future work, the analysis will go deeper to investigate and compare different populations. In order to analyse the spatial motion features independently (in terms of regional and affine components), 4-way Tucker Decomposition can be performed on tensors stacked by [affine parameters $\times$ region $\times$ time $\times$ subject]. Further work is required for such analysis in terms of optimising for the number of dimensions needed in the reduced model and describing the parameters in a more physiological sense.

5.5 Conclusion

In this work, we propose a novel method for analysing population-wide motion patterns in terms of the dominant spatial and temporal patterns. Using a Polyaffine model to describe the transformation from one image to another, we perform group-wise analysis on these parameters to construct a mean motion model by averaging spatio-temporally aligned transformation parameters from a group of subjects in the same population (healthy or pathological). Further population-based statistical analyses were performed by computing a tensor decomposition on the transformation parameters directly. From the analyses we obtained meaningful differences between the healthy population and the pathological population of Tetralogy of Fallot patients in terms of motion patterns (both spatially and temporally) and were able to detect potentially meaningful motion information for Tetralogy of Fallot patients such as an abnormal triggering of contraction.

Appendix

5.5.1 Tucker Tensor Decomposition using Alternating Least Squares

The alternating least squares (ALS) method for computing a rank-$(R_1, \cdots, R_N)$ Tucker decomposition is described briefly here. Note that the n-Rank of a tensor $\mathcal{T}$ is not the same as the rank of a tensor (the minimum number of rank-one components). R_n is the column rank of the n^{th} axis of $\mathcal{T}$. In this work, we take $R_n = rank_n(\mathcal{T})$ to find an exact Tucker decomposition of $\mathcal{T}$, rather than computing a truncated Tucker decomposition (which gives an inexact decomposition rather than the truncation of an exact decomposition).

The ALS method essentially approximates the factors that minimise the least squares criterion:

$$C(\mathcal{T}) =: \min_{\mathcal{G}, \mathcal{A}^{(n)}} \parallel \mathcal{T} - [[\mathcal{G}; \mathcal{A}^{(1)}, \mathcal{A}^{(2)}, \cdots, \mathcal{A}^{(N)}]] \parallel \tag{5.10}$$

given $\mathcal{G} \in \mathbb{R}^{R_1 \times R_2 \times \cdots \times R_N}$ and $A^{(n)} \in \mathbb{R}^{I_n \times R_n}$ is column-wise orthogonal for all n. The algorithm for computing a rank-$(R_1, \cdots, R_N)$ decomposition is given is Algorithm 3 [Kolda and Bader, 2009].

Algorithm 3 ALS rank-$(R_1, R_2, \cdots, R_N)$ Tucker decomposition

Require: Initialisation: $\mathcal{A}^{(n)} \in \mathbb{R}^{I_n \times R}$ for $n = 1, 2, \cdots N$
  loop {*until convergence*}
    for $n = 1, \cdots N$ **do**
      $y \leftarrow \mathcal{T} \times_1 \mathcal{A}^{(1)T} \cdots \times_{n-1} \mathcal{A}^{(n-1)T} \times_{n+1} \mathcal{A}^{(n+1)t} \cdots \times_N \mathcal{A}^{(N)T}$
      $\mathcal{A}^{(n)} \leftarrow$ the $R^{(n)}$ leading singular vectors of y
    end for
  end loop
  $\mathcal{G} \leftarrow \mathcal{T} \times_1 \mathcal{A}^{(1)T} \times_2 \mathcal{A}^{(2)T} \cdots \times_N \mathcal{A}^{(N)T}$
  return $\mathcal{G}, \mathcal{A}^{(1)}, \cdots, \mathcal{A}^{(N)}$

Part III

When Biophysics Meets Statistics

Chapter 6

Learning from Model-based Synthetic Images

– This chapter is based on [Prakosa et al., 2014]: Prakosa, A., Sermesant, M., Allain, P., Villain, N., Rinaldi, C. A., Rhode, K. S., Razavi, R., Delingette, H., and Ayache, N. Cardiac electrophysiological activation pattern estimation from images using a patient-specific database of synthetic image sequences. *IEEE Transactions on Biomedical Engineering*, 61(2):235–245, 2014.

6.1 Introduction

Since electrophysiological activation controls the onset of the mechanical contraction, important information about the electrophysiology could be gathered from the detailed observation of the resulting motion patterns. Abnormal patterns of this activation are at the origin of important cardiovascular diseases (e.g. arrhythmia, asynchrony). However, only catheter-based intracardiac electrical mappings are available to obtain such information, and these invasive procedures are not classically used for diagnosis but rather for planning and guiding a therapy. Electrocardiographic imaging [Ghanem et al., 2005] (*a.k.a.* body surface potential mapping) is a non-invasive technique for imaging activation times of the myocardium but still remains to be validated thoroughly and is not widely available in clinical centres. First application of ECGI in human subject was done in [Ramanathan et al., 2004] to image the activation pattern of normal heart, heart with right bundle branch block, heart with pacing and also atrial flutter. In a recent study [Wang et al., 2011b], the invasive catheter-based electrophysiology study findings were compared with the non-invasive ECGI method to image a large diversity of human ventricular tachycardia activation patterns. Recent validation studies were done in rabbit [Han et al., 2011], canine [Han et al., 2012] and swine [Liu et al., 2008] for another technique which also uses the body potential mapping, namely the three-dimensional cardiac electrical imaging (3DCEI), to non-invasively reconstruct the three-dimensional ventricular activation sequence. Another method which also used the body surface potential maps and an ultra-fast computerised tomography scanning was developed in the 3-D electrocardiographic imaging technique (3-DEIT) [Zhang et al., 2005] and was compared with the 3-D intracardiac mapping in rabbits. In [Berger et al., 2006], the feasibility of the non-invasive imaging of cardiac electrophysiology (NICE) in patients with the Wolff-Parkinson-White syndrome was investigated. The result was compared with the standard invasive electroanatomical mapping. Therefore there is a strong need to quantitatively assess a patient electrophysiological condition from non-invasive imaging modalities. The proposed method could help in constraining the notoriously ill-posed inverse problem of electrocardiography.

Despite advances in both medical image analysis and intracardiac electrophysiological mapping technology, the understanding of the relationship between the cardiac electrophysiology and the cardiac motion visible in images is only partial. Since non-invasive cardiac imaging is readily available, unlike non-invasive detailed electrophysiology maps, it is important to investigate how the cardiac electrophysiology function can be estimated from the analysis of cardiac motion. This is specifically

relevant, for example, in the evaluation of the Cardiac Resynchronization Therapy (CRT) where the placement and tuning of pacemaker leads play a crucial role in the outcome of the therapy. In this context, cardiologists need to interpret time series of cardiac images in order to detect and characterise kinematic patterns (motion asynchrony, delayed contraction) and then infer possible electrical conduction disorders. However, currently 30% of the patients with CRT show no benefit from this therapy [Helm et al., 2007], which may be caused by the suboptimal implementation of the therapy. Providing activation maps from a time series of cardiac images would be of great interest to better select patients and to optimise the lead placements and delays during and after therapy. For instance, in a recent study, Sohal et al. [Sohal et al., 2013] use time-volume curves of left ventricular segments to identify two classes of contraction patterns, which seem to be correlated with CRT response in patients with left bundle branch block (LBBB). More fundamentally, understanding the relationship between cardiac motion and electrophysiology is essential to improve the diagnosis and therapy of patients suffering from heart failure.

While there is an important literature on the estimation of the cardiac kinematics from cardiac sequences (see for instance [McLeod et al., 2011; Tobon-Gomez et al., 2012; Mansi et al., 2011a; Elen et al., 2008] and references therein), there exists no such tools to estimate the electrical wave propagation from such image sequences. However, the relationship between cardiac motion and electrical activation has been investigated in several studies [Prakosa et al., 2011, 2010; Otani et al., 2010; Provost et al., 2010; Sanchez-Ortiz et al., 2004].

Electromechanical Wave Imaging (EWI) modality has been recently introduced to image the Electromechanical Wave (EW) which was shown to correlate with the myocardium electrical wave propagation [Provost et al., 2010; Konofagou and Provost, 2012]. In [Provost et al., 2011], it was shown that the EW was able to be reproduced by an E/M model. This imaging modality uses high ultrasound frequency to map the small, transient deformation of the EW. However, this method is limited to this specific modality, which has only been demonstrated in 2D (whereas the propagation pattern is 3D) and is not often available clinically.

In this paper, we propose to study the inverse electro-kinematic relationship through the creation of a patient-specific database of synthetic time series of cardiac images based on our previous study in [Prakosa et al., 2011]. Because it is difficult to obtain a large number of cases where both electrophysiological mapping and time series of 3D images are available, we use an E/M model of the heart to produce synthetic but visually realistic image sequences for which the electrical stimulation is known using our method [Prakosa et al., 2013]. On this database, invariant kinematic descriptors were extracted from each synthetic sequence and then fed to a machine learning algorithm which estimates the electrical pattern from kinematic descriptors during the cardiac cycle. The creation of this database allows us to develop this machine learning based study. Recently, many medical image analysis studies are motivated by machine learning, for example in [Tobon-Gomez et al., 2008] where a virtual population is created to train an active shape models. As the electro-kinematic relationship is very complex, we prefer here to generate a patient-specific database, so that the learning is done on cases relatively close to the patient condition. The hypothesis of this study is that the clinician already has some knowledge on the pathology when asking for the MR images, e.g. LBBB from a standard ECG using QRS shape and width. Therefore the aim is not to help for diagnosis but for therapy planning. We believe that solving the general case without any information on the diagnosis of the patient would lead to a huge number of possibilities and make the inverse problem even more difficult.

Previous works [Provost et al., 2010; Sanchez-Ortiz et al., 2004] have mainly focused in detecting E/M wave directly from the displacement and strain patterns estimated from image sequences during the contraction and relaxation of the myocardium. Since the relationship between those mechanical waves and electrical waves is very complex, our approach is to learn it through an E/M model of the heart at a larger spatial and temporal scale. In [Sanchez-Ortiz et al., 2004] the cardiac motion descriptors are combined in order to obtain the electrical activation time, but the weights are assigned manually for the descriptors. Another study by McVeigh et al. [McVeigh et al., 1998] considers only the circumferential strain estimated from tagged MR images as the mechanical activation measure. Another approach has been developed using a mathematical based computational technique to image

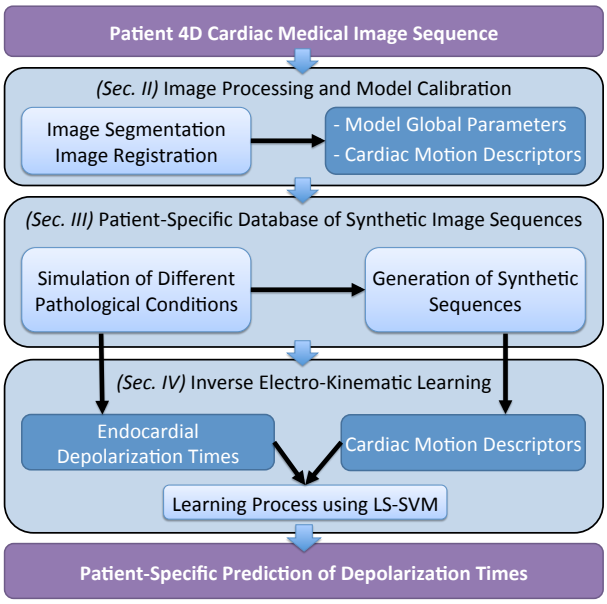

Figure 6.1: **Estimation of Electrophysiological Activation Pattern from Images.** A cardiac mesh is created from image segmentation. Different electromechanical conditions are simulated close to the patient condition to generate the database of electrophysiological patterns and synthetic cardiac sequences.The relationship between the motion descriptors and the activation patterns is learned from this database. The result is used to predict the patient electrophysiological activation pattern.

the active stress from the displacement using an inverse model [Otani et al., 2010]. This method was able to reconstruct travelling plane wave of active stress from a mechanical deformation. The active stress was initially used to generate this deformation using a forward model. However, this method would still need to be evaluated in clinical application. Compared to [Prakosa et al., 2010], instead of estimating displacements and strains directly from the E/M model, we propose a more realistic estimation by first simulating 3D images and then using an image-based motion tracking algorithm. Furthermore, rather than learning the activation forces over time, we have chosen to learn the depolarisation times of all American Heart Association (AHA) segments. Finally, our learning approach is optimised in order to detect which kinematic descriptor is most correlated with the electrophysiology waves.

The overall approach is described in Fig. 6.1 and mainly consists in three stages. First, right and left ventricles are segmented from an input cardiac image sequence and the cardiac motion is tracked. An electromechanical model of the heart is mechanically calibrated from this data. In a second stage, a training set, *a.k.a* patient-specific database, is created from this E/M model by changing electrophysiological parameters related to different pathological conditions. For each set of electrophysiology parameters, a different cardiac motion is simulated and a realistic synthetic image sequence is created. In the third stage, motion descriptors are estimated from each sequence. A learning method is then trained to relate those descriptors with the endocardial depolarisation times. Finally, the depolarisation times of the original sequence are estimated from the knowledge of its motion descriptors. Evaluation of the inverse electro-kinematic learning process on three patients is discussed in Sec. 6.5.

6.2 Image Processing and Parameter Calibration

6.2.1 Image Segmentation and Registration

First we need to apply two image processing steps to the patient clinical image sequence. These steps are the segmentation of the end diastolic (ED) myocardium and the estimation of the myocardium motion. The purpose of the segmentation is to personalise the cardiac mesh geometry required for the cardiac E/M simulation. Furthermore, the estimation of patient cardiac motion allows us to also

estimate the patient's endocardial left ventricle (LV) volume curve. Using this information, The E/M simulation can be calibrated with respect to this volume curve so that the simulated ejection fraction as well as the ejection and filling rates are similar to the measured ones [Marchesseau et al., 2012a].

The 3D epicardium and endocardium of the left and the right ventricles of the ED clinical image were delineated using an interactive tool available within the CardioViz3D software [Toussaint et al., 2008]. These delineations were then used to create the myocardium segmentation. Using CGAL software [Rineau et al., 2009], a computational tetrahedral mesh was created from the binary mask of the compact myocardium segmentation (cf. Fig. 6.2). We label the different tetrahedra of the mesh in order to set different electrical conduction parameters for each labeled region (Sec. 6.3.1). The labels include the scar, the Purkinje network (the tetrahedra next to the endocardial surface), the scarred Purkinje network (the intersection of the scar and the Purkinje network) and the cardiac muscle (the remaining tetrahedra). To create bull-eyes plot, we also label the left ventricle according to the 17 AHA segments.

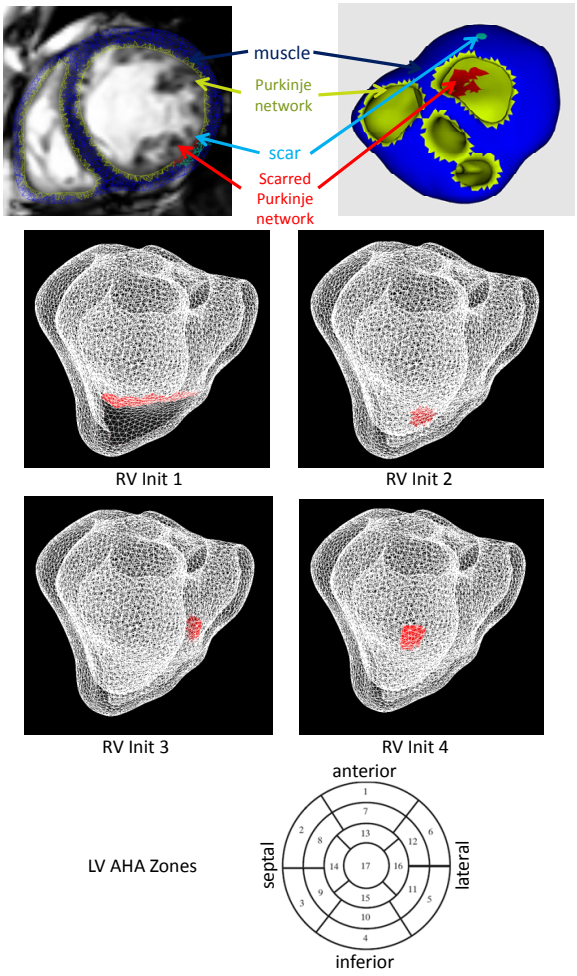

Figure 6.2: **Cardiac Geometry and Electrical Stimulation.** A personalised cardiac mesh is created from the myocardium delineation of the clinical image. The region on the surface of the LV and RV endocardium is set to have higher electrical conduction velocity to simulate the Purkinje network. Different RV initial electrical activation position is set to simulate the extremities of the Bundle of His. These positions are approximately set based on the septal LV AHA Zones.

Applying a non-linear registration to pairs of medical images is a common method to estimate the motion of the tissue in the image. Here we use the symmetric log-domain diffeomorphic demons (LogDemons) [Vercauteren et al., 2008] non-rigid registration method to align the template image $T_i(\mathbf{x})$ to a reference image $R(\mathbf{x})$, which is the ED image of the clinical sequence, by estimating a dense non-linear transformation $\phi_i(\mathbf{x})$, where $\mathbf{x} \in \mathbb{R}^3$ is the space coordinate. $T_i(\mathbf{x})$ is the image at each time frame i in the cardiac sequence. This transformation $\phi_i(\mathbf{x})$ is associated with the

displacement vector field $u_i(\mathbf{x})$ and is parameterized by the stationary velocity field $v_i(\mathbf{x})$ which ensures the invertibility of the deformation since we are working in the log-domain. By having this estimated displacement field, we are also able to estimate the patient's endocardial LV volume curve in time. We deformed the ED tetrahedral mesh using the estimated displacement field $u_i(\mathbf{x})$ and then computed the endocardial LV volume of the deformed mesh in time.

6.2.2 Electromechanical Model Calibration

We used the Eikonal model to simulate the electrophysiological activation patterns. This model has the advantage to be fast to compute and involves few parameters. More detailed models [Ten Tusscher et al., 2004; Mitchell and Schaeffer, 2003] could also have been used however such additional level of complexity is not necessary since we are only interested in providing main patterns of conduction driven by few parameters. The Eikonal equation $v\sqrt{\nabla T_d^t D \nabla T_d} = 1$ was solved using Multi-Front Fast Marching Method [Sermesant et al., 2007] to calculate the depolarisation time T_d at each point of the mesh. v is the local conduction velocity and $D = (1-r)f \otimes f + r.I$ is the anisotropic conductivity tensor where f is the fibre orientation, r is the conductivity anisotropy ratio and I is the identity matrix.

We base our approach on the Bestel-Clément-Sorine (BCS) E/M model [Chapelle et al., 2012] composed of a passive non linear elastic part and an active part that describes the binding and unbinding process of the actin and myosin filaments in the sarcomere by a differential equation that controls the active stress τ_c and the sarcomere stiffness k_c:

$$\begin{cases} \dot{k_c} = -(\mid u \mid + \alpha \mid \dot{e_c} \mid)k_c + n_0 k_0 \mid u \mid_+ \\ \dot{\tau_c} = -(\mid u \mid + \alpha \mid \dot{e_c} \mid)\tau_c + \dot{e_c} k_c + n_0 \sigma_0 \mid u \mid_+ \end{cases} \tag{6.1}$$

where α is a constant related to the cross-bridge release due to a high contraction rate, k_0 and σ_0 are respectively the maximum stiffness and contraction. n_0 is a reduction factor that allows to take into account *the Starling effect* by which the maximum contraction depends on the fiber strain e_c. The control variable u is derived from the electrical activation model and is a function of the free calcium concentration only. It is modeled using electrophysiological inputs such as depolarization times (T_d) and action potential durations (APD). The four-element Windkessel model is used to model the arterial pressure [Marchesseau et al., 2012a].

The BCS E/M model was implemented in the SOFA simulation platform [Faure et al., 2012] and to assess the mechanical parameters of the model, we used the algorithm derived from the Unscented Transform [Julier and Uhlmann, 1997], and described in [Marchesseau et al., 2012a,b]. The algorithm finds a set of parameters that enable the simulation to match observations on the endocardial LV volume (the minimum volume, the minimum and maximum of the flow) in one iteration through the analysis of the covariance matrix between the simulated observations and the variation of each parameter independently. The assessed calibrated parameters of the BCS E/M model are σ_0, K, μ, APD and Rp. K is the Bulk modulus of the passive part and μ is the viscosity parameter of the active part. APD is the cell excitation duration. Rp is the peripheral resistance, one of the Windkessel parameters.

6.3 Patient-Specific Database of Synthetic Image Sequences

A database of visually realistic synthetic cardiac sequences is created using the method proposed in [Prakosa et al., 2013]. This database is required to train the machine learning algorithm. This synthetic sequence generation method consists in the combination of the simulated motion and the real motion estimated from the patient image sequence. The database is built using different scenarios which are performed to simulate a variety of conditions close to clinical condition of this patient. Since these datasets are taken from patients with a left bundle branch block (LBBB), the scenarios consist of different variations of electrophysiological and mechanical parameters that simulate this specific pathology.

6.3.1 Simulated Electromechanical Conditions

Electrical Onset Position	Conduction Velocities in cm/s of: Muscle v_m	Purkinje v_p	Scar v_s	Scarred Purkinje v_{sp}
1-2-3-4	40-50-80-110	160-240-350	5-10-20	120

Table 6.1: **Patient-Specific Database of 144 Simulated Cases.** We varied the initial electrical activation position of the LBBB and the conduction velocities of the different components of the electrophysiological model.

An electrophysiological activation pattern which corresponds to each scenario is generated using the Eikonal model in the personalized cardiac mesh geometry. The scenarios are created based on a variation of the parameters of the Eikonal model around the standard values. The varying parameters are the conduction velocity value of the Purkinje network v_p, the value in the cardiac muscle v_m, and also the initial electrical activation position which simulates the extremities of the Bundle of His. For datasets containing a scar region, a variation of the conduction velocity value for this region v_s and also a value of the scarred Purkinje network v_{sp} are also included in the scenarios (cf. Table 6.1 and Fig. 6.2).

Electrical Onset Position	Conduction Velocities in cm/s of: Muscle v_m	Purkinje v_p	Block v_b	Blocked Purkinje v_{bp}
1-2-3-4	30-50-80	130-210-320	none- 30 (Anterior)- 30 (Posterior)	none- 30-90 (Anterior)- 30-90 (Posterior)

Table 6.2: **Patient-Specific Database of 180 Simulated Cases.** Additional configurations with low conduction velocity in the anterior lateral region or in the inferior lateral region are added to mimic the functional block.

For datasets that do not contain a scar region, we set a low conduction velocity in the anterior lateral region (zone 6, 12, and 16 of the AHA segments) or in the inferior lateral region (zone 5, 11, and 16 of the AHA segments) in order to mimic the occurrence of a functional block in those regions (cf. Table 6.2). The overall conduction velocities are also set lower compared to Table 6.1.

6.3.2 Generation of Synthetic Image Sequences

Visually realistic synthetic time series of MR images were created using the previously simulated deformation which was combined to the real clinical sequence estimated displacement using the method proposed in [Prakosa et al., 2013]. This method applied non-rigid registration algorithm to extract the motion of the real clinical MRI sequence. This extracted motion was then combined with the E/M simulated motion in the log domain and then used to warp the original images in order to create the synthetic cardiac sequence. With this method, a database of realistic images of the patient was generated for which the underlying cardiac motion and electrophysiological parameters are known. This database served as the training set in our machine learning based study. For each different initial electrical activation position (RV Init 1, 2, 3 and 4) (cf. Fig. 6.2, Table 6.1 and Table 6.2), a mechanical calibration is performed as described in section 6.2.2. Therefore, the variation of the mechanical parameters were included as well in the database.

With the method described previously, a large database of synthetic 3D MR images was created. We then tracked the cardiac motion from those synthetic images by using the symmetric log-domain diffeomorphic demons (LogDemons) registration algorithm [Vercauteren et al., 2008]. More precisely, we registered all the images of the synthetic sequence to its reference ED image as we did to the real clinical sequence.

6.4 Inverse Electro-Kinematic Learning

6.4.1 Cardiac Motion Descriptors

As an input to a machine learning algorithm, we needed to first extract kinematic descriptors which describe in a compact and discriminative way the cardiac motion for each time point in the cardiac cycle. We wanted these descriptors to be regional, as we aim for an activation pattern rather than local activation times, and also intrinsic (frame invariant) as the orientation of the heart in the images varies.

To this end, we first characterized the motion of each AHA segment by fitting in the least-squares sense an affine transformation $f(p) = Ap + B$ to the LogDemons estimated displacement field. The strain tensor E was then computed from the affine matrix A as: $E = (A^T A - I)/2$.

We then extracted kinematic descriptors at each time of the cardiac cycle that are invariant to any change of reference frame (or rigid transformation). For the strain matrix E, the three Euclidean invariants are computed as:

$$x_1 = \text{trace}(E),\ x_2 = \text{trace}(E^2),\ x_3 = \det(E)$$

For the displacement vector, we only extracted its norm as invariant:

$$x_4 = \|u\| = \|Ab + B - b\|,$$

where $\|u\|$ is the displacement norm of the zone centroid with b the initial position of the centroid. We also used the strain in the direction of displacement as the invariant:

$$x_5 = (u^T E u)/(2\|u\|^2)$$

Compared to our previous study [Prakosa et al., 2011], we added here more descriptors which are usually found in clinical records. We added the QRS duration $x_6 = t_{QRS}$ which is the time needed for the whole myocardium to be activated. We also added the LV volume curve $x_7 = V$ and the regional LV volume curve $x_8 = V_{reg}$ computed for each AHA segment. More precisely, we divided the LV endocardial surface according to the AHA segment surfaces and then computed the volume of the region created by each displaced segment surface and the barycenter of the LV (cf. Fig. 6.3).

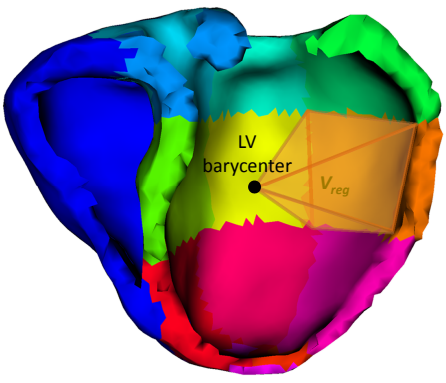

Figure 6.3: **Regional LV Volume.** The V_{reg} is the volume of the region created by the LV AHA segment surface and the LV barycenter.

Furthermore, in order to learn the influence of the dynamics of some descriptors, we added the derivative of the trace of the strain tensor, of the displacement, and of the global and regional volume curves:

$$x_9 = d\,\text{trace}(E)/dt,\ x_{10} = d\|u\|/dt,$$
$$x_{11} = dV/dt, x_{12} = dV_{reg}/dt$$

These descriptors, except for the volume curve x_7, its derivative x_{11} and the QRS duration x_6, are evaluated regionally for the 17 AHA zones during the n time instances. The value n depends on the

temporal resolution of the original clinical sequence, n = number of frames -1. The volume curve x_7 and its derivative x_{11} are vectors with length of n and the QRS duration x_6 is a single scalar value.

The difficulty in using a simulated database for machine-learning is that there are limitations in both the electromechanical model used to simulate the motion and the image processing methods used to extract the descriptors. Therefore there can be discrepancies between the descriptors used in the learning phase compared to the descriptors extracted from the real images.

In order to cope with this, and also because we are more interested in the relative dynamics of these descriptors which is related to the activation pattern than in their absolute values, we normalized each descriptor. This normalization was done regionally for the descriptors taken from the 17 AHA regions. With this normalization, each descriptor has a range of values from 0 to 1, as we use the relationship $x = (x - x_{min})/(x_{max} - x_{min})$, where x_{max} and x_{min} are the maximum and the minimum values of x respectively. .

Number	Descriptor	Vector Size
x_1	trace(E)	17$\times n$
x_2	trace(E^2)	17$\times n$
x_3	det(E)	17$\times n$
x_4	$\|u\|$	17$\times n$
x_5	$(u^T E u)/(2\|u\|^2)$	17$\times n$
x_6	t_{QRS}	1
x_7	V	n
x_8	V_{reg}	17$\times n$
x_9	dx_1/dt	17$\times n$
x_{10}	dx_4/dt	17$\times n$
x_{11}	dx_7/dt	n
x_{12}	dx_8/dt	17$\times n$

Table 6.3: **List of the Descriptors.** The descriptors are extracted from the estimated cardiac motion, their temporal derivation and also the QRS duration. n = the number of frames in a cardiac cycle - 1.

These 12 descriptors (cf. Table. 6.3) were used to create a kinematic descriptor vector $\mathbf{x} = (x_i)_{i\in[1,12]} \in \mathbb{R}^d$ for each simulation with

$$\begin{aligned} d &= 9(\text{Descriptors}_{1,2,3,4,5,8,9,10,12}) \times n(\text{Times}) \times 17(\text{Zones}) \\ &\quad + 2(\text{Descriptors}_{7,11}) \times n(\text{Times}) \\ &\quad + 1(\text{Descriptors}_{6}) \\ &= 155n + 1 \end{aligned}$$

For a cardiac image sequence with 30 images, the dimension d of the complete vectorial kinematic descriptor is:

$d = 155 \times (30 - 1) + 1 = 4496$.

6.4.2 Machine Learning Method

In the inverse electro-kinematic learning process, the non-linear relationship between the kinematic descriptors and the electrical propagation was estimated based on a training set extracted from the

synthetic database. To represent the cardiac electrophysiology, we considered the activation time when the electrical potential starts to depolarize at a point of the myocardium. The activation time was averaged for all points of the LV endocardial surface in each AHA segment. Therefore, the vector characterizing electrophysiology for each simulation is $\mathbf{y} = (y_i) \in \mathbb{R}^{\text{r=17 (AHA Zones)}} = log(\text{Activation Times})$.

We modeled the non-linear relationship using Least-Square Support Vector Machine (LS-SVM) for regression [Cawley, 2006] which is similar to the Kernel Ridge Regression (KRR).

LS-SVM extends the KRR method by adding a bias term. KRR itself is the non-linear extension of Ridge Regression (RR) which searches a linear function $\mathbf{y} = \mathbf{w}^T\mathbf{x}$ that models the dependencies between the descriptor vectors $\mathbf{x} = \mathbf{x}_i \in \mathbb{R}^d$ and response vectors $\mathbf{y} = \mathrm{y}_i \in \mathbb{R}^r$ (all vectors are column vectors) from a set of N examples $(\mathrm{x}_1, \mathrm{y}_1), (\mathrm{x}_2, \mathrm{y}_2), ..., (\mathrm{x}_N, \mathrm{y}_N)$. The use of nonlinear kernels allows to capture the complex relationship between activation times and motion in a way that will decrease the influence of some descriptors when far from the ones used in the training phase.
Ridge Regression can be extended to Kernel Ridge Regression by rewriting the solution

$$\begin{aligned} \mathrm{y} &= \mathrm{w}^T\mathrm{x} \\ &= Y^T(\lambda\mathrm{I} + K)^{-1}\mathrm{k} \end{aligned} \tag{6.2}$$

with $K = XX^T$, $\mathrm{k} = X\mathrm{x}$, $\lambda > 0$ is the regularization parameter, $X = (\mathrm{x}_1, \mathrm{x}_2, ..., \mathrm{x}_N)^T$ is a $N \times d$ matrix and $Y = (\mathrm{y}_1, \mathrm{y}_2, ..., \mathrm{y}_N)^T$ is a $N \times r$ matrix. In this form, other type of Kernel function can be used to substitute the linear Kernel function $K = K(\mathrm{x}_i, \mathrm{x}_j) = \mathrm{x}_i^T\mathrm{x}_j$.

We modeled the non-linear relationship using Kernel Ridge Regression with a bias term or Least-Square Support Vector Machine (LS-SVM) for regression

$$\mathrm{y} = f(\mathrm{x}) = A\mathrm{k}(\mathrm{x}_i, \mathrm{x}) + \mathrm{b} \tag{6.3}$$

with matrix A is computed as $A = Y^T(\lambda\mathrm{I} + K)^{-1}$ and $\mathrm{k}(\mathrm{x}_i, \mathrm{x})$ is a kernel vector. We chose the Radial Basis Function (RBF) $K(\mathrm{x}_i, \mathrm{x}_j) = \sum_{k=1}^{D} e^{-z_k}$ as the Kernel function where $z_k = \left(\left|\mathrm{x}_i^k - \mathrm{x}_j^k\right| / (\sigma_k\alpha_k)\right)^2$, $i, j = \{1, ..., N\}$ and D is the number of descriptors. In this kernel function, σ_k is the standard deviation of each descriptor and α_k is a dimensionless coefficient which weights the importance of each descriptor in the learning process, where $\sigma_k^2 = (1/N)\sum_{i=1}^{N}\left\|\mathrm{x}_i^k - \mu\right\|^2$ and $\mu = (1/N)\sum_{i=1}^{N}\mathrm{x}_i^k$.

6.4.3 Parameter Optimization

The chosen λ and α parameters are optimized by using leave-one-out estimates which train the model with all members of the training set but one and test the performance on the singleton. The process is repeated for all the singletons in the training set. We use Allen's PRESS (Predicted Residual Sum of Squares) criterion for the optimization of the λ and α parameters $PRESS = \sum_i^N \mathrm{e}_{(i)}^2$ [Cawley, 2006] where $\mathrm{e}_{(i)} = \mathrm{y}_i - \hat{\mathrm{y}}_{(i)}$ is the residual for the *i*th example with the *i*th example excluded from the training process and $\hat{\mathrm{y}}_{(i)}$ is the predicted response for the *i*th example based on the training process. Fortunately, we have $e_{(i)} = e_i/(1 - h_{ii})$ where $e_i = \mathrm{y}_i - \hat{\mathrm{y}}_i$ is the residual for the *i*th example in the training process which includes all examples and $\hat{\mathrm{y}}_i$ is fitted response based on this training. h_{ii} is the *i*th element of the leading diagonal of the hat matrix $H = X(\lambda\mathrm{I} + X^TX)^{-1}X^T = XX^T(\lambda\mathrm{I} + XX^T = K(\lambda\mathrm{I} + K)^{-1}$. Therefore, in the end, we can have the PRESS for the chosen parameters λ and α in one iteration without having to do N iterations for the leave-one-out cross validation. We use the Powell's BOBYQA [Powell, 2009; Johnson, 2012] method to optimize these parameters to have the smallest PRESS.

6.5 Results

6.5.1 Activation Pattern Validation on Synthetic Data

First, we evaluated the learning process on the generated synthetic data and estimated the minimum size of the training set to have a small regression error for the remaining entries of the database.

Fig. 6.4 shows a good generalization with a root mean square (RMS) error of less than 8 ms of residual by using at least 13, 18 and 44 training datasets for the Database I, II and III respectively. The Database I, II, and III are the patient-specific databases for patient I, II and III respectively described in Sec. 6.5.2. These numbers are less than 25% of the size of datasets of each database.

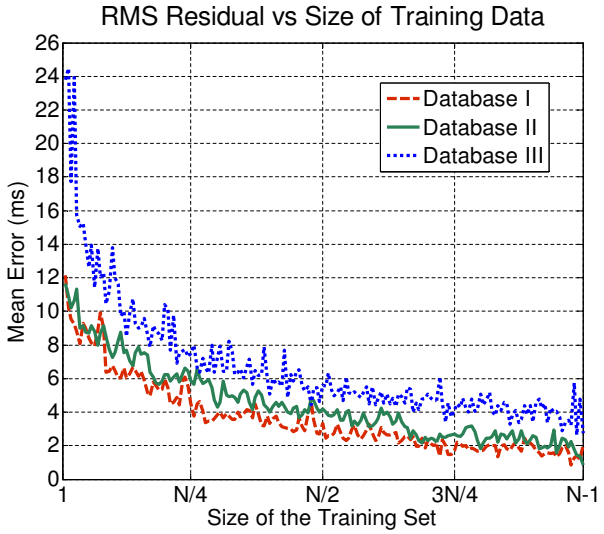

Figure 6.4: **RMS Residual vs Size of Training Data.** Less than 8 ms RMS residual is obtained by using more than 13, 18 and 44 training cases for the Database I, II and III respectively. The Database I, II, and III are the patient-specific databases for patient I, II and III respectively described in Sec. 6.5.2. This means that a good generalization is obtained by using less than 25% of the whole dataset.

6.5.2 Activation Pattern Evaluation on Clinical Data

We applied our proposed approach on three clinical cases from patients with different pathologies and etiologies or causes of diseases. However, in all three of them there was a modified activation pattern due to scars or functional blocks, as well as poor ejection fraction, which are the characteristics of the patient groups we are aiming at.

The first patient was a 60 years old woman with heart failure and NYHA class III symptoms. She had subendocardial postero-lateral scar in the left ventricle. Her left ventricular ejection fraction was 25% on maximal tolerated heart failure medication. The surface ECG demonstrated significant conduction disease with left bundle branch block (LBBB) QRS duration of 154 ms (normal QRS is less than 120 ms). Echocardiography, including Tissue Doppler, confirmed significant mechanical dyssynchrony in keeping with the ECG findings.

The second patient was a 72 years old male patient with ischemic heart disease. He had a myocardial infarction in the infero-lateral wall. His left ventricular ejection fraction was 35% with the QRS duration of 99 ms.

The third patient was a seventy-seven year old woman with a much more developed dilated cardiomyopathy. She was in NYHA class III heart failure with a LV ejection fraction of 18%, LBBB and a QRS duration of 200 ms. There was no late gadolinium enhancement images acquired but functional conduction block was observed in the electrophysiological mapping. We proposed to add different virtual functional blocks in the simulated database in order to be able to correctly estimate the activation patterns in non ischemic cases, which often also present conduction blocks.

For all the cases, dynamic cardiac MRI (Philips 1.5T Achieva, Phillips Healthcare, Best, The Netherlands) consisted of multiple slice cine steady state free precession (SSFP) scans performed in short-axis orientation to assess the ventricular function (TR/TE $= 2.9/1.5$ms, resolution $2.2 \times 2.2 \times 10\ mm^3$, around 30 heart phases, breath-hold). The images were then resampled in a resolution of 1.6 mm^3 and centered on the heart region with a region of interest of around 100^3 voxels. A non-contact mapping study was performed using the Ensite 3000 multi-electrode array catheter system

(St Jude, Sylmar, CA). The array records intracavity far-field potentials that are sampled at 1.2 kHz and digitally filtered at 0.1-300 Hz. The resulting signals allow the reconstruction of over 3000 virtual unipolar electrograms superimposed on a model of the left ventricle created using a locator signal on a roving endocardial catheter. The XMR fusion provided the location of the Ensite mapping with respect to the MR-derived information.

For each patient, a database of synthetic sequences which contains the scenarios described in Sec. 6.3.1 was built. For the first patient, the total generated synthetic 3D MR images are 144 (scenarios) $\times$ 29 (number of frame - 1) $=$ 4176.

We did a first evaluation of this learning process on the clinical 3D MR sequence of the patients. Using the relationship or the optimized parameters previously found, we are able to predict the LV endocardial electrical activation time of the patient. We apply the same processing to this sequence as we did for the synthetic sequence.

After optimizing the PRESS criterion on the whole synthetic database of each patient, the obtained LS-SVM parameters are shown in Table. 6.4. We listed the descriptors with their $(\alpha_{max} - \alpha_i)/(\alpha_{max} - \alpha_{min})$ value which describes the increasing importance of the descriptor i (cf. Table. 6.4). α_{max} and α_{min} are respectively the maximum and minimum α value of the descriptors for a patient database. Therefore the value range is from 0 for the least important descriptor to 1 for the most important one. Table. 6.4 shows that the kinematic descriptors $x_1 = \text{trace}(E)$ and $x_5 = (u^T E u)/(2\|u\|^2)$ are consistently the most important ones to learn the electro-kinematic relationship from the three databases since they have smaller optimized α_i values compared to the other descriptors.

Descriptor	$(\alpha_{max} - \alpha_i)/(\alpha_{max} - \alpha_{min})$		
	Patient I	Patient II	Patient III
trace(E)	1.000	0.522	0.514
trace(E^2)	0.541	0.431	0.446
det(E)	0.506	0.000	0.464
$\|u\|$	0.428	0.823	1.000
$(u^T E u)/(2\|u\|^2)$	0.659	1.000	0.998
t_{QRS}	0.000	0.167	0.040
V	0.046	0.227	0.097
V_{reg}	0.103	0.203	0.053
d trace(E) / dt	0.367	0.189	0.171
$d\ \|u\| / dt$	0.597	0.282	0.078
$d\ V / dt$	0.239	0.520	0.232
$d\ V_{reg} / dt$	0.218	0.279	0.000
α_{min}	1.038	1.690	0.985
α_{max}	2.263	2.282	2.583

Table 6.4: **Rank of the Optimized LS-SVM Parameters.** The value of the parameters $(\alpha_{max} - \alpha_i)/(\alpha_{max} - \alpha_{min})$ after optimizing the PRESS criterion gives the importance of each descriptor.

After performing LogDemons non-rigid registration and extracting the vector $\mathbf{x}$ of kinematic descriptors from the estimated displacement field, the electrophysiology vector $\mathbf{y}$ was estimated from the LS-SVM. Since we have the ground truth LV endocardial electrical activation time of the patient acquired using non-contact mapping study, we are able to compare our prediction with this measurement. Similar estimated depolarization times were obtained for this patient (cf. Fig. 6.5) with the root mean square error RMSE $=$ 11.20 ms for the patient I, 13.51 ms for the patient II and

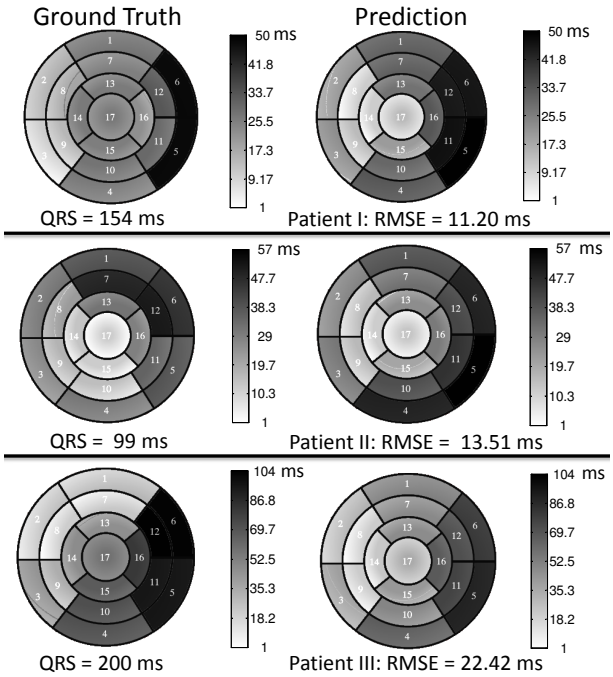

Figure 6.5: **Depolarization Time Estimation from Clinical 3D MR Sequences.** First evaluation of the learning process in the prediction of the LV endocardial surface depolarization time on three patients (right) is compared to the ground truth value (left). Similar patterns in the same range are observed on the three of them.

22.42 ms for the patient III.

We computed the mean and variance of the electrophysiological database created previously with the patient's LV endocardial electrical activation time ground truth value. Then, we were able to compare our prediction with these values (cf. Fig. 6.6).

We can observe similar RMS errors for the activation time for different parameter sets, which is mostly due to the influence of the Purkinje network. The high electrical conductivity of the Purkinje network produces similar endocardial activation patterns. However, the activation pattern for the whole myocardium is significantly different for each parameter set, which makes the resulting motion pattern different.

6.6 Discussion

In this study, we created patient-specific database of synthetic sequences in order to learn the cardiac inverse electro-kinematic relationship. In the end, we used the learned relationship to estimate patient's left ventricle endocardium electrical activation time. For each dataset, the prediction error (cf. Fig. 6.5) is in the order of 15 ms which represents typically between 21% and 24% of the total LV endocardium surface activation and between 7% and 14% of the QRS duration. This is reasonable given the spatial and temporal accuracy of the invasive intra-cardiac mapping systems and even more compared to the accuracy of non-invasive ECGI systems.

A current limitation of the method is the spatial resolution of the predicted map. The spatial resolution of the estimated activation pattern could be increased to more than 17 regions as the electromechanical model spatial resolution is much finer. However given the resolution of the images and the uncertainty on the invasive EP data (due to acquisition and registration errors), predicting depolarization times at a greater spatial resolution would be difficult to validate with the current data. However, the modeling and the learning phases can handle higher resolution data therefore the method would be unchanged. We are working on acquiring higher resolution contact maps to allow us to have a better validation for a finer model.

The prediction error is also smaller compared to the average error in the database (cf. Fig. 6.6).

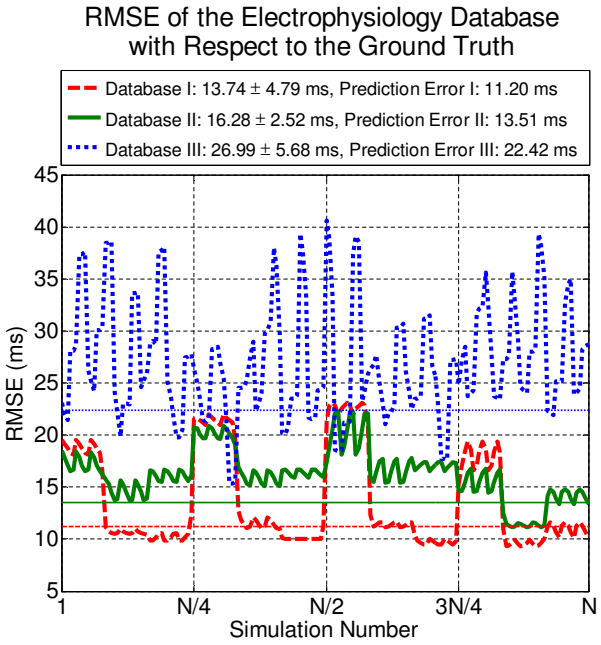

Figure 6.6: **Distance (RMSE) of Each Simulated Electrophysiology with respect to the Patient's Ground Truth.** For each patient's database of simulated electrophysiological patterns, the difference of each pattern with the patient's electrophysiological pattern ground truth is calculated. These differences are shown in a curve which describes the variation of the simulated electrophysiology. The mean and standard deviation of each curve for each patient are shown in the legend. The prediction errors in Fig. 6.5 are shown as horizontal lines with the values shown in the legend.

Patient I: 11.20 ms $<$ 13.74 ms, Patient II: 13.51 ms $<$ 16.28 ms, Patient III: 22.42 ms $<$ 26.99 ms. This shows the proper behavior of the LS-SVM method since it basically consists in interpolating the depolarization times of the entries in the learning set that are closest to the input kinematics descriptors. Ideally, a measure of confidence in the prediction should be provided, but the LS-SVM regression method does not provide any covariance on the activation times. Covariance can only be estimated on the activation parameters if covariance on the motion descriptors is available which is not the case here.

With this learning process, the prediction error combines several types of possible errors: noise in the non-contact mapping acquisition, errors in the learning process, errors in modeling the cardiac electromechanics and discretization errors. Due to the non-contact nature of the mapping, it is often difficult to have an accurate match between the electrophysiology maps and the endocardial surface reconstructed from MR imaging. For example for Patient II, there is an uncertainty in the ground truth data since the latest activated area is not in the region where the scar is. Applying 30° of clockwise rotation to the ground truth data would make the scarred region last activated and reduce the prediction error from 13.51 ms to 8.73 ms. The learning error mostly depends on the size of the electrophysiology scenarios as they should be vast enough to include the actual pathology of the patient. In this paper, we have restricted ourselves to LBBB cases with 5 parameter categories (onset position, conduction velocity...) leading to between 144 and 180 simulated cases. Adding more hypothesis of electrophysiology parameters in the training set would help capturing more complex electrophysiology and kinematics patterns. However, this would also lead to a much increased number of simulations and therefore a trade-off must be found between the range of pathologies and the computational requirements.

Then prediction errors also depend on the accuracy of the electrophysiology model. For instance, applying an automated personalization method [Relan et al., 2011b] of an electrophysiology model on the 3 patients' datasets described previously leads to errors of 10.19 ms, 9.19 ms and 16.51 ms respectively. These errors after personalization capture the combined effect of acquisition, discretiza-

tion and model errors. Given that the prediction errors are respectively 11.20 ms, 13.51 ms and 22.42 ms, it appears that the errors due to the learning process are relatively small. To decrease further those errors may require to use a more complex electrophysiological model or a finer mesh. However, it is probable that improving the acquisition protocol leading to higher spatial resolution would be most beneficial. In practice, obtaining ground truth electrophysiology data is currently difficult due to the invasive nature of the endocardial mapping systems. Using less invasive electrophysiology data from body surface potential mapping would allow to broaden the number of test cases.

In addition, to decrease the prediction errors, it is important that the electromechanical model produces realistic simulations of the cardiac motion. This not only implies that the cardiac physiology is well described by the chosen E/M model, but it also means that this model is sufficiently well personalized. In our approach, the chosen E/M has been shown to produce realistic simulations of the cardiac motion and also shown good predictive behavior for the electrophysiology and mechanics [Sermesant et al., 2012]. Furthermore, in this study, we have performed four different mechanical calibrations for each onset position, in order to have similar volume curves between the simulation and the patient data. To improve the prediction, one would probably need to perform a calibration and even a personalization of the mechanical parameters for each electrophysiology scenario. Indeed, the calibration stage only tries to match the endocardial volume curves whereas the personalization stage tries to match more regional or local kinematic indices (regional volume curves, estimated displacement...). The weighting of the descriptors was learned on the simulated database, therefore it is important that the link between electromechanics and deformation is well captured by the model. Any improvement of the model can be readily used in this method by re-running the learning phase.

The learning phase will be also influenced by the observability of the deformation features in the motion extracted from the simulated images. Any improvement in cardiac motion tracking from images would help in better learning the link between the simulations and the resulting features. More sophisticated methods for cardiac motion analysis, e.g. atlas-based ones, could be used as input to the learning process, however they still need a large scale validation therefore we focused here on motion descriptors already available in a clinical setting.

One limitation of this study is that the created database is patient-specific. Therefore, numerous simulations need to be performed in order to predict another patient's depolarization time. Currently, predictions from one training set built from one patient does not generalize to another patient because of the difference in their kinematic descriptors. The use of an atlas may overcome this limitation but meaningful strategies to transport the kinematic descriptors between patients have to be found.

6.7 Conclusion

As the generated synthetic cardiac MR sequences have electro-kinematic "ground truth" information, we have performed an inverse electro-kinematic learning on this patient-specific database. Invariant kinematic descriptors were extracted from the displacement field obtained from the sequence registration. The non-linear inverse relationship between the electrical activation times and the kinematic descriptors was modeled using LS-SVM. Evaluation of the learning process for the database of synthetic sequence shows good generalization and a first evaluation on three clinical MR sequences shows encouraging results.

We presented here results on patients with a LBBB in order to reduce the span of possible onset locations and have a relatively slower propagation (large QRS). However we tested the method on both ischemic and non-ischemic patients. The results are better for the ischemic patients, as the scar locations are known, while for the non-ischemic patients we need to find where the potential functional block is. Extension of this method to more complex activation patterns should be possible, but the evaluation of the observability of such patterns from the available time resolution of the images has to be explored.

This approach opens the possibility of using non-invasive cardiac motion imaging as a way to estimate electrophysiological patterns. This could provide additional information to the cardiologist during the optimization of the Cardiac Resynchronization Therapy (CRT), for example allowing the placement of the pacemaker leads in the cardiac region which is lately activated. An extension of

this work would be the application of this method to different imaging modalities. This can be done since the synthetic sequence generation method is generic and was already demonstrated for different imaging modalities [Prakosa et al., 2013].

Chapter 7

Probabilistic Personalisation of Cardiac Electrophysiology

– This chapter is based on [Konukoglu et al., 2011]: Konukoglu, E., Relan, J., Cilingir, U., Menze, B., Chinchapatnam, P., Jadidi, A., Cochet, H., Hocini, M., Delingette, H., Jaïs, P., Haïssaguerre, M., Ayache, N., and Sermesant, M. Efficient probabilistic model personalization integrating uncertainty on data and parameters: Application to Eikonal-diffusion models in cardiac electrophysiology. *Progress in Biophysics and Molecular Biology*, 107 (1):134–146, 2011.

7.1 Introduction

Modeling of physiological processes and pathologies is important for understanding the underlying phenomena and also for designing better clinical systems for diagnosis and therapy planning. The research community has focused on the mathematical models for a long time aiming to create more realistic and multi-scale models [Murray, 2002]. Recently, thanks to the advances in clinical imaging and mapping, modeling research broadened its interest and started to focus on a different type of problem, *model personalization*. Model personalization is the adaptation of a generic model to a specific patient based on the available clinical data. This is crucial both for transferring mathematical models into clinical practice and for validating models with patient data. In this chapter we concentrate on the estimation of patient specific parameters.

Parameter estimation from clinical data is a challenging task due to the nature of the clinical observations and the complexity of the mathematical models, even in simplified cases [He and Keyes, 2007]. The challenge mainly arises due to the following reasons:

i. *Sparsity* of the data: The temporal (frequency) and spatial (resolution) sampling of the acquired clinical observations are much lower than the corresponding scales of the underlying processes. For example, during a cycle of a healthy heart the electrical wave passes through all the cells in the cardiac tissue. The cardiac mappings on the other hand, samples at best a few hundred points at 1 Hz on the boundary of the heart.

ii. *Uncertainty* on the data: The measurements obtained from clinical data are often gathered through invasive and/or indirect procedures. For example, cardiac electrophysiology mapping can either be achieved by catheterization or indirectly derived from body surface potentials. In the first case the contact points are on a moving heart and can slide due the beating of the heart and the breathing motion. Furthermore, the matching between the measurement points and the computational mesh used in the simulations - which is extracted from medical images - is ambiguous. Both the motion and the ambiguous matching are sources of uncertainty on the measured values.

iii. *Complexity* of the model: The mathematical models describe complex dynamics resulting in nonlinear formulations. The interactions between the model parameters, the model variables

and the observations are therefore not trivial. Furthermore, models often include large number of parameters that must be estimated. The parameter estimation problems for such models are in general hard and often results in non-unique solutions in the sense that observations could have resulted via a range of possible parameter sets instead of a single one.

iv. *Assumptions* of the model: Modeling is by definition a simplification, thus the degree of realism of the model compared to the observations is limited by the assumptions that make the model valid. Finding the right level of details in a model in order to be able to both adjust it to the data and achieve meaningful predictions is not simple.

These challenges undermine the uniqueness of the parameter estimation problem. Under these settings one can expect multiple parameter sets satisfying the observations with the same accuracy. Methods for estimating patient-specific parameters should take these challenges into account in providing not only a single value for the parameters but also ranges of possible parameters and confidence margins.

Most physiological models used today are continuum models based on systems of partial differential equations (PDEs) [Murray, 2002]. Parameter estimation problems are well studied for PDE systems [Tarantola, 2005]. Approaches can be coarsely classified as deterministic or probabilistic [Kaipio and Somersalo, 2005]. Deterministic approaches are based on minimizing a cost function that measures the difference between the observations and the model solutions. The solution giving the minimum value then serves as the estimate. The most common techniques involve variational (e.g. adjoint model) or sequential (e.g. Kalman filter) methods [Tarantola, 2005; Voss and Timmer, 2004]. These methods are very popular due to the tractability of the estimation and the well studied control theory. On the other hand, it is well known that these methods are prone to local minima and the sensitivity analysis can become cumbersome in complex models where it is not easily derived analytically. In the case of sparse and uncertain observations these drawbacks become important issues.

Probabilistic or statistical methods are based on the theories of Bayesian inference and numerical schemes to generate the posterior distributions for the parameters. The problem of parameter estimation is cast as a probabilistic model defining a joint probability distribution between observations, parameters and variables. The estimation task is then defined as computing the posterior distribution for the parameters given the observations. These distributions provide much richer information than the point estimates obtained in deterministic methods. They contain information about how well all possible sets of model parameters fit the observations. They can be used to obtain point estimates (e.g. Maximum-A-Posteriori (MAP) estimates) as well as confidence on these estimates. Another advantage of probabilistic methods is that they are less sensitive to local minima since they estimate the whole distribution.

The main disadvantage of the probabilistic methods is their computational cost. In general posterior distributions cannot be computed analytically and must be approximated numerically. The conventional numerical method for this task is sampling through Markov-Chain Monte-Carlo (MCMC) methods [Kaipio and Somersalo, 2005]. MCMC methods is based on simulating the model with many number of different parameter sets and approximating the posterior distribution using these samples. Obtaining an accurate estimate using probabilistic methods requires a large number of sample simulations to be done. When a single model simulation can take a considerable amount of time on a high performance computer, as it can be the case in organ-scale biophysical models, running thousands of them becomes impractical.

Recent advances in uncertainty quantification (UQ) and numerical methods for stochastic PDEs provide solutions for reducing the computational cost of Monte-Carlo simulations of PDE systems [Ghanem and Doostan, 2006; Xiu and Karniadakis, 2002]. These methods are based on polynomial chaos (PC) expansions of random variables and spectral representations of the equations. Through spectral approximations, the Monte-Carlo simulations can be executed using only linear combinations of spectral basis functions rather than solving the PDE for each random parameter set. This yields faster Monte-Carlo simulations and faster uncertainty quantification, which have significant impact on probabilistic methods for sensitivity analysis and parameter estimation [Ghanem

and Doostan, 2006; Xiu and Karniadakis, 2002; Marzouk et al., 2007; Marzouk and Najm, 2009; Marzouk and Xiu, 2009; Ma and Zabaras, 2009; Doostan et al., 2009; Xiu, 2007, 2009].

In this chapter we propose and demonstrate an efficient Bayesian inference method for the parameter estimation problems involving a large (> 10) number of parameters. In order to demonstrate the interactions between uncertainty on the data and the model parameters we focus on the parameter estimation problem in Eikonal-Diffusion (ED) type models for cardiac electrophysiology (EP). We formulate the Bayesian inference problem for the ED model and demonstrate the inference method. In Section 7.2 we briefly discuss the cardiac electrophysiology model used in this work. Section 7.3 explains the probabilistic formulation and the Bayesian inference problem. In Section 7.4 we explain the inference algorithm (mathematical details are given as appendices). The proposed methodology is demonstrated both on synthetic and clinical data. Sections 7.5 and 7.6 present these results. Finally we conclude this chapter with discussions on the methodology.

7.2 Eikonal-Diffusion Model

Among the different models describing the electrical activity in the cardiac tissue [Clayton et al., 2011b], here we chose to focus on the Eikonal-Diffusion (ED) model [Colli Franzone et al., 1990], as it allows a compact formulation while still including important nonlinearities. Moreover, by using the Fast-Marching Method [Konukoglu et al., 2007], Eikonal models can achieve fast computations which makes them suitable for clinical applications [Chinchapatnam et al., 2008] and treatment simulations [Pernod et al., 2011].

7.2.1 The Eikonal-Diffusion Model

The ED model describes the depolarisation time $T(\mathbf{x})$ in the cardiac tissue $\mathbf{x} \in \Omega \backslash \Omega_E$, through the nonlinear PDE

$$c_0 D(\mathbf{x}) \left(\sqrt{\nabla T^t \mathbf{M}(\mathbf{x}) \nabla T} \right) - \nabla \cdot (D(\mathbf{x}) \mathbf{M}(\mathbf{x}) \nabla T) = \tau, \tag{7.1}$$

$$T(\mathbf{x}) = 0, \ \mathbf{x} \in \Omega_E, \tag{7.2}$$

where the boundary conditions depicts the initialisation of the excitation (electric wave) at location Ω_E, *the onset location* (which is a set of points in the discrete setting). In this equation the superscript t denotes the transposition, c_0 is the dimensionless constant related to the cell membrane and τ is the cell membrane time constant. $D(\mathbf{x})$ is the square of the local tissue space constant and is related to the specific conductivity of the tissue. The tensor quantity $\mathbf{M}(\mathbf{x})$ incorporates the local fibre orientation to represent the anisotropy in conduction velocity of the cardiac tissue (see [Tomlinson et al., 2002] for further details on the Eikonal-Diffusion model parameters).

The parameters of interest in this equation are the conductivity $D(\mathbf{x})$ and the onset location Ω_E. $D(\mathbf{x})$ is a spatially varying conductivity function with specific structure. Its value in the cardiac myocardium volume is taken as a global parameter. But on the endocardium surface, it varies spatially due to the existence of the Purkinje network extremities. This network creates important fast conduction pathways but cannot be observed using medical imaging. The goal of the inverse problem is to find the global myocardium conductivity and the locally varying conductivity on the endocardium. We represent $D(\mathbf{x})$ with a radial basis function approximation as often done in the literature [Nobile et al., 2008; Ma and Zabaras, 2009].

$$D(\mathbf{x}) = \begin{cases} D_0 & \text{if } \mathbf{x} \in \Omega_{myo}, \\ \frac{1}{Z(\mathbf{x})} \sum_{m=1}^{M} D_m \exp(-(\frac{||\mathbf{x}-\mathbf{x}_m||^2}{\sigma^2})) & \text{if } \mathbf{x} \in \Omega_{endo}, \end{cases} \tag{7.3}$$

where Ω_{myo} is the myocardial tissue, Ω_{endo} is the endocardial surface, $Z(\mathbf{x}) = \sum_{m=1}^{M} \exp(-(||\mathbf{x} - \mathbf{x}_m||^2/\sigma^2))$ is a normalisation term, D_0 is the muscle tissue conductivity, $\mathbf{x}_m$ are pre-defined radial basis centres, $||\cdot||$ is the geodesic distance on the endocardium surface and D_m's are scalar weights. Based on this representation the inverse problem for $D(\mathbf{x})$ is defined as estimating the vector $\overline{D} =$

$[D_0, ..., D_M]$. Alternative representations can also be used [Marzouk and Najm, 2009; Marzouk and Xiu, 2009]. Ideally one would represent $D(\mathbf{x})$ as a different value at each discretisation point in the computation domain. This however, yields a high dimensional inverse problem creating a high computational cost [Kaipio and Somersalo, 2005].

We model the onset location Ω_E as a point on the septum wall on the endocardium. Although a more realistic model would formulate this as a set of different junctions we currently approximate this with a single point and endocardial areas of fast conduction. Based on this assumption we represent the location of the Ω_E with two spatial coordinates on the septum of the endocardial surface x_E, y_E.

7.2.2 The Observation Model

The clinically available observations are depolarisation times on the left ventricular endocardium (from catheter-based mapping) and depolarisation times on the epicardium, from catheters or computed from the inverse problem of electrocardiography. These observations are mathematically represented as $\tilde{T}(\mathbf{x}) = T(\mathbf{x}) + \epsilon(\mathbf{x})$ for $\{\mathbf{x}_i\}_1^N \subset \partial\Omega$ on the boundary of the heart, where $\epsilon(\mathbf{x})$ is the observation noise and $\{\tilde{T}(\mathbf{x}_i)\}_1^N$ forms the observation vector. The observation noise approximates the following sources of uncertainty:

- During the acquisition procedure the catheters position changes due to the beating of the heart and the breathing motion.
- The position of each observation point is projected on the computation domain Ω which is extracted from medical images taken either before or after the acquisition. Therefore, these points do not necessarily correspond to each other.
- The depolarisation times are estimated from the electrical potentials measured by the catheter. This estimation is also prone to noise [Steinhaus, 1989].

An in depth analysis of each of these sources of error would be very beneficial however, this is beyond this presented work. Here we approximate the contribution of all of these sources with the observation noise $\epsilon(\mathbf{x})$.

7.3 Probabilistic Modelling of Parameter Estimation

Different method were proposed to adjust cardiac electrophysiology models, including for instance genetic algorithms for the fast conduction system [Camara et al., 2010], Maximum A Posteriori state estimation [Wang et al., 2011a], or in similar conditions using a deterministic approach and a trust-region minimizations [Chinchapatnam et al., 2008; Relan et al., 2011a]. Up to the best of our knowledge non of these approaches use a full probabilistic treatment of the problem.

The probabilistic approach taken here formulates each model parameter as a random variable. The distributions for these random variables reflect the possible ranges of the parameters as well as their expected value. Under this randomness the relationship between the model parameters and the model variables T can be written as a joint probability distribution. This distribution can be decomposed based on the conditional dependencies of the PDE, i.e. different parameters leading to different solutions. The joint distribution for the ED model described above can be written as

$$\begin{aligned} p(\tilde{T}, T, D(\mathbf{x}), c_0, \tau, \mathbf{M}(\mathbf{x}), \Omega_E) &= p(T|D(\mathbf{x}), c_0, \tau, \mathbf{M}(\mathbf{x}), \Omega_E) \\ & \quad p(\tilde{T}|T)p(D(\mathbf{x}), c_0, \tau, \mathbf{M}(\mathbf{x}))p(\Omega_E) \end{aligned} \tag{7.4}$$

where the $\tilde{T} = \{\tilde{T}(\mathbf{x}_1), \tilde{T}(\mathbf{x}_2), ..., \tilde{T}(\mathbf{x}_N)\}$ is the set of observations, $p(\Omega_E)$ is the prior distribution for the onset location and $p(D(\mathbf{x}), c_0, \tau, \mathbf{M}(\mathbf{x}))$ is the prior distribution for the model parameters. On the right hand side of this equation, the first term describes the probability that for a given parameter set the simulated depolarization times will be T, the second term describes the probability of observing $\tilde{T}$ when the simulation result is given as T and the last two terms are the prior distributions for the parameters. Here we only focus on the conductivity $D(\mathbf{x})$ and the Ω_E therefore we can drop the

other parameters in the formulation and use the approximation given in Eq. (7.3). Furthermore, we assume that the observation noise $\epsilon(\mathbf{x})$ is an independent random variable for each point - a common assumption for the probabilistic models [Kaipio and Somersalo, 2005]. Considering the independent nature of contact mappings this assumption can be justified for the catheter based observations. This assumption allows us to state that for a given location $\mathbf{x}$ if $T(\mathbf{x})$ is given then the $\tilde{T}(\mathbf{x})$ does not depend on the observations taken from other locations $\mathbf{y}$ (however, we would also like to note that this independence assumption could also be changed without greatly affecting the overall method.). Based on this conditional independence the formulation becomes

$$p(\tilde{T}, T, \overline{D}, x_E, y_E) = \prod_{i=1}^{N} \left\{ p(\tilde{T}(\mathbf{x}_i)|T(\mathbf{x}_i)) p(T(\mathbf{x}_i)|\overline{D}, x_E, y_E) \right\} p(\overline{D}) p(x_E, y_E). \tag{7.5}$$

In the case of parameter estimation for PDEs, given a boundary condition and a set of parameters the forward simulation provides a unique $T(\mathbf{x})$ function. This is integrated as an additional simplification: $p(T(\mathbf{x}))|\overline{D}, x_E, y_E) = \delta_{T(\mathbf{x}|\overline{D}, x_E, y_E)}$, where we use $T(\mathbf{x}|\overline{D}, x_E, y_E)$ to represent the solution of the model Eq. (7.1) given a specific parameter set and δ is the Dirac's delta function. We can then compute the posterior distribution for the parameters, $p(\overline{D}, x_E, y_E, |\tilde{T})$, given an observation vector:

$$\mathcal{L}(\tilde{T}|\overline{D}, x_E, y_E) = \prod_{i=1}^{N} p(\tilde{T}(\mathbf{x}_i)|T(\mathbf{x}_i|\overline{D}, x_E, y_E)) p(\overline{D}) p(x_E, y_E), \tag{7.6}$$

$$p(\overline{D}, x_E, y_E, |\tilde{T}) = \frac{\mathcal{L}(\tilde{T}|\overline{D}, x_E, y_E)}{\int_{\overline{D}, x_E, y_E} \mathcal{L}(\tilde{T}|\overline{D}, x_E, y_E) d(\overline{D}) dx_E dy_E}, \tag{7.7}$$

where $\mathcal{L}(\tilde{T}|\overline{D}, x_E, y_E)$ is the likelihood function (what is the probability of observing a set of $\tilde{T}$ for a given set of parameters) and the integral in the denominator of the posterior distribution is over all the possible parameter sets. One can see the advantage of probabilistic methods in this formulation. The posterior distribution $p(\overline{D}, x_E, y_E, |\tilde{T})$ not only provides us with the best possible parameter set that fits the observation, but also contains information on how all other possible parameter sets fit the observations.

In principle the prior distributions for the conductivity values and the onset locations can be obtained through populations statistics. In order to keep the definitions flexible and general, here the prior distributions are set to uniform distributions, namely the uninformative priors

$$\begin{aligned} D_m &\sim \mathcal{U}(D_m^a, D_m^b), \ m = 0, ..., M \\ x_E \sim \mathcal{U}(x_E^a, x_E^b), \ y_E &\sim \mathcal{U}(y_E^a, y_E^b). \end{aligned} \tag{7.8}$$

The values for the upper and lower limits of the distributions will be specified in the experiments section.

7.4 Fast Bayesian Inference

Bayesian inference corresponds to computing the posterior distribution $p(\overline{D}, x_E, y_E, |\tilde{T})$ for a given observation set. Equation (7.6) admits an analytical solution only if the term $T(\mathbf{x}|\overline{D}, x_E, y_E)$ can be written analytically. For most models, as is the case for this one, solutions cannot be written analytically. They are found by numerically solving the PDE systems. The common approach to compute $p(\overline{D}, x_E, y_E|\tilde{T})$ is to use sampling methods such as MCMC [Kaipio and Somersalo, 2005]. MCMC methods evaluate the numerator in Equation 7.6 (the likelihood function) sequentially at many random points and approximate the posterior distributions using these samples (we would like to note here that the independence assumption on $\epsilon(\mathbf{x})$ only determines the method of computation of this numerator and it can easily be interchanged with another observation model). One can immediately see the bottleneck here: evaluation of the model, $T(\mathbf{x}|\overline{D}, x_E, y_E)$. Simulating models often takes time and this is the reason of the high computational cost of probabilistic methods.

Spectral representations based on polynomial chaos expansions efficiently approximate $T(\mathbf{x}|\overline{D}, x_E, y_E)$ and yield substantial speed ups [Ghanem and Doostan, 2006; Xiu, 2009; Marzouk and Najm, 2009].

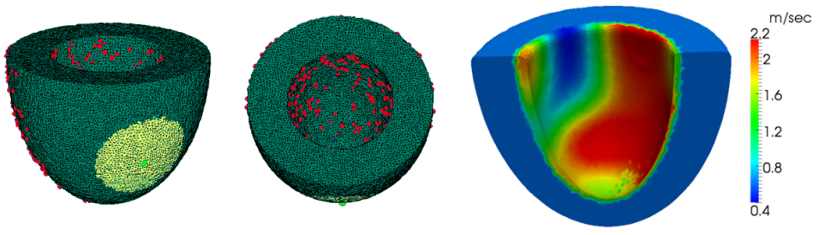

(a) (b) (c)

Figure 7.1: Geometric setting: (a) Simulation domain. Green point: onset location for experiments 1. Yellow disc: region of unknown onset location in experiment 2, (b) Observation points, (c) Ground truth varying conductivity. Muscle conductivity: $D_0 = 0.06\ mm^2$ (the conduction velocity $v = c_0\sqrt{D_0}/\tau = 0.6\ m/s$). Endocardial conductivity set using Eq. (7.3) with $M = 17$.

It has already been used for the sensitivity analysis of the direct problem of electrocardiography at the macroscopic scale, where number of parameters is small and the underlying equation is linear [Geneser et al., 2008]. The spectral approximation for the probabilistic formulation of the ED model given above can be given as

$$T(\mathbf{x}|\overline{D}, x_E, y_E) \approx \sum_{i=0}^{P} T_i(\mathbf{x})\Phi_i(\overline{D}, x_E, y_E), \tag{7.9}$$

where $T_i(\mathbf{x})$ are so-called the spectral basis, Φ_i are multivariate orthonormal Legendre polynomials of increasing order and P is the total number of spectral components involved in the approximation. The summation on the right hand side approximates the solution of the model equation. One can see that the computation of this summation can be executed much faster than numerically solving the model equation because it only involves addition of functions. Therefore, in the Bayesian inference this approximation can be used to compute the samples necessary to build the posterior distribution. For the ease of explanation we do not provide the mathematical details at this stage please refer to 7.A for these details.

The computation of the spectral basis $T_i(\mathbf{x})$ for high number of parameters is in general a computationally expensive task. However, for the ED model, compressed sensing can be used to determine the basis in a fast manner [Doostan et al., 2009]. Therefore, one can compute the basis functions easily and in an efficient manner (see 7.B for a brief explanation). Using these two improvements together, we can then apply Bayesian inference on such non-linear 3D models in a tractable way. We will provide computational times in the experiments section to elaborate on this advantage.

7.5 Validation on Synthetic Data

In this section we demonstrate the proposed Bayesian inference method on synthetic data where the ground truth for the local cardiac muscle conductivity is known. Using the synthetic problem we aim to demonstrate the influence of the data uncertainty on the confidences of the estimated parameters. We use an idealised left ventricle geometry (see Fig. 7.1). The computation domain is discretized as a Cartesian grid in 3D, its size is $15 \times 15 \times 10\ cm^3$ and the resolution of each voxel is $1 \times 1 \times 1\ mm^3$. The ED model Eq. (7.1) is solved within the volume enclosed by the mesh shown in Fig. 7.1a (mesh is only shown for visualization purposes and the computations were done on a Cartesian grid for this synthetic study) using a Fast-Marching approach. The parameters – which are assumed to be known and constant for the presented experiment – are $c_0 = 2.5$, $\tau = 1$ and $\mathbf{M}$ is here an isotropic tensor.

7.5.1 Problem Setting

We generated a ground truth conductivity function using Eq. (7.3) and simulated data similar to what can be acquired in a clinical environment: a set of endocardial depolarization times as measured with a catheter [Dong et al., 2006; Richmond et al., 2008] and a set of epicardial depolarization times, as measured either by a catheter [Sacher et al., 2010] or from body surface potential mapping [Ramanathan et al., 2004]. Using the simulated data we infer the conductivity function under different settings. The presented experiments encompass some of the main difficulties of this inverse problem: the spatial variation of conductivity on the endocardium from very low values (scars) to very high values (Purkinje extremities), and the uncertainty on the onset location.

In order to exclude the onset from the data, we simulate a Left Bundle Branch Block, therefore we initiate the electrical onset on the right ventricular septum (green point in Fig 7.1a). In the first experiment this location is known, and in the second experiment we relax this assumption and perform a joint inference of both the onset location and the conductivity function. The yellow region shown in Fig. 7.1a denotes possible locations of the onset point for this second experiment.

The ground truth conductivity common to both of the presented experiments is shown in Fig. 7.1c. In this figure and all the following figures, we show the conduction velocity $v = c_0\sqrt{D}/\tau$ rather than the D value due to its clinical relevance. For completeness we will provide numerical values for both D and v. To model the scars and the existence of Purkinje extremities, the conductivity on the endocardium varies from very low values ($0.0016\ mm^2 \sim 0.1\ m/s$) to very high values ($0.9\ mm^2 \sim 2.4\ m/s$), as seen in Fig. 7.1c. We construct the conductivity function as given in Eq. (7.3). We used an 18 dimensional $\overline{D}$, with $M = 17$ radial basis functions defined on $\{\mathbf{x}_m\}$ which are equally spaced on the surface and the ground truth muscle conductivity is taken as $D_0 = 0.06\ mm^2 \sim 0.6m/s$.

Using the model Eq. (7.1) and the parameter settings described above, we simulated data at different observation points on the endocardium (200 points) and the epicardium (300 points). The epicardial data were assumed to be only on the opposite side of the onset point since the region around the onset would normally be located inside the right ventricle and not accessible. In Fig. 7.1a and b we show these observation points as red spheres on the surface. As explained in Section 7.2.2 the observed depolarization times can be uncertain due to several factors. In order to integrate this into our synthetic experiment we added Gaussian noise to the simulated depolarization times with variance of 25 ms (simulated depolarization times varied between 35 ms to 125 ms at the observation points).

7.5.2 Probabilistic Model Details and Computational Aspects

The parameters of the presented method are the limits of the uniform distributions given in Equation 7.8 and the number of spectral components P to be included in the spectral approximation. For the $\overline{D}$ parameter the ranges for the synthetic problem are set as $(D_0^a, D_0^b) = (0.01, 0.09)\ mm^2 \sim (0.25, 0.75)\ m/s$ and $(D_m^a, D_m^b) = (0.001, 0.9)\ mm^2 \sim (0.08, 2.4)\ m/s$ for $m = 1, ..., 17$. On the other hand for the onset location Ω_E the prior distribution is defined as the uniform distribution defined over the yellow region shown in Fig. 7.1a, which is a disc of 6 cm in diameter on the surface. Using this probabilistic setting we computed the spectral basis $\{T_i(\mathbf{x})\}_{i=0}^P$ on all the observation points. In our experiments we set $P = 10626$ containing all 20 dimensional multivariate Legendre polynomials of maximum order 4.

In terms of computational times the construction of the spectral basis is the most expensive part. However, as explained in Section 7.4 compressed sensing framework speeds up this construction. In the synthetic example the computation of the $\{T_i(\mathbf{x})\}_{i=0}^P i$ took about 2.5 hours for all the 500 observation points.

7.5.3 Estimation Experiments

We present two different experiments using the setting explained above: 1) inference of $\overline{D}$ using observations taken on endocardial and epicardial surfaces assuming the knowledge of Ω_E and 2) joint inference of $\overline{D}$ and Ω_E. All the inferences are done using the formulation and the method explained in Sections 7.3 and 7.4. Once the spectral basis is constructed the inference for each of

the experiments took *less than 5 minutes* for both of the experiments. The MCMC algorithm we used is described in [Girolami and Calderhead, 2011]. The posterior distributions were approximated through generating 15000 samples where first 5000 samples were discarded as burn-out. As it is not feasible to visualize the high dimensional posterior distributions $p(\overline{D}|\tilde{T})$ and $p(\overline{D}, x_E, y_E|\tilde{T})$ in the experiments we present the mean of the posterior distribution and the marginal standard deviations on these estimates.

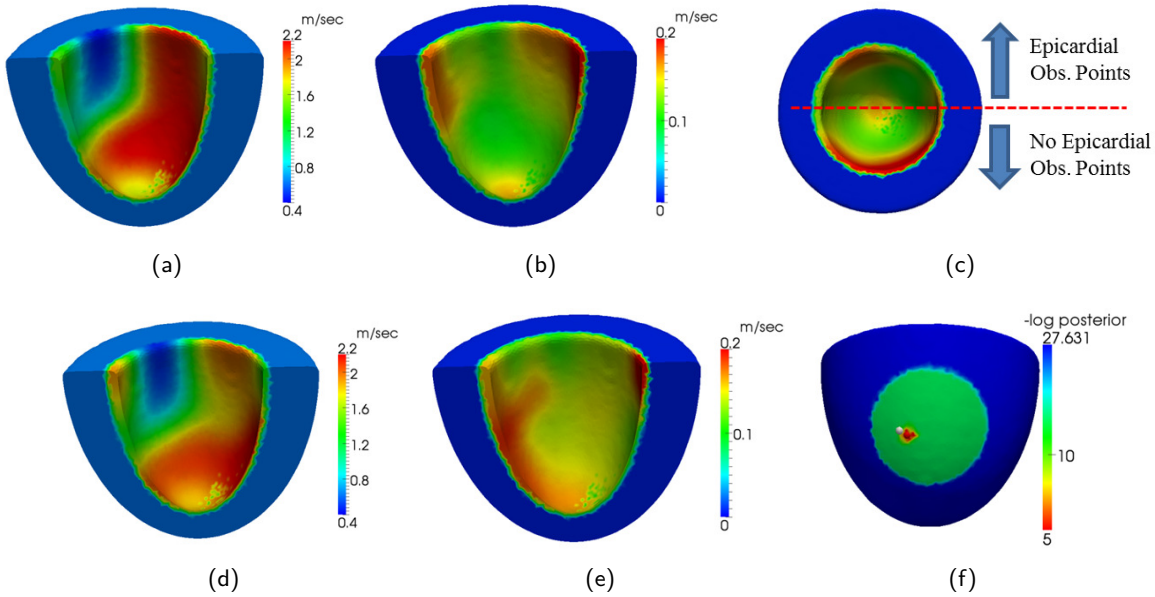

Figure 7.2: Mean estimate of the conductivity function (a) for experiment 1, and (d) for experiment 2. Standard deviation of the conductivity estimate (b) for experiment 1 and (e) for experiment 2. (c) Distribution of the marginal standard deviation (inverse of the confidence in estimation) with respect to the location of epicardial observation points. Notice that where there are more observations the standard deviation on the estimation is lower. (f) -log posterior distribution of the onset location given the observations. The white point denotes the ground truth and the red point denotes the mean of the posterior distribution.

In Fig. 7.2a and b we show the mean of the posterior distribution of the conductivity estimate and its marginal standard deviation for $\overline{D}$ obtained from the first experiment. We observe that the estimate is very similar to the ground truth both quantitatively and qualitatively (the RMS error between the simulated depolarization times and the measurements is 1.7 $msec$). The standard deviation is low showing the higher confidence in the estimation. The posterior average and the standard deviation of muscle conductivity estimate in this case is $0.061 \pm 0.001\ mm^2 \sim 0.62 \pm 0.01\ m/s$. In Figure 7.2c we show the standard deviation of the estimation from the top view. Notice that the standard deviation is higher for the regions where there are no epicardial observation points. This is as expected since the sparsity of observation in that side of the synthetic left ventricle increases the uncertainty in the estimated parameters. Furthermore, we also notice that the standard deviation increases towards the top of the left ventricle where the number of observation points is smaller, in other words the observations are sparser.

For the second experiment we defined the onset location as a random parameter of the system as well. In the first experiment the onset location was centered in the allowable region. In order to show that the proposed methodology indeed works for the whole region we changed the ground truth onset location to the white sphere shown in Fig. 7.2f. In Fig. 7.2d we show the mean of the posterior distribution of the conductivity estimate of the conductivity. Observe that again the locations of the low and high conduction regions are well captured (the RMS error on the depolarization times is 3.5 $msec$). Moreover the standard deviation for this estimate shown in Fig. 7.2e demonstrates that again the difference between the ground truth and the estimate is captured within the standard

deviation of the estimate. Comparing Figures 7.2b and e we notice that the standard deviation on the estimated conductivity function increases slightly. This is as expected since the posterior distributions for the parameters captures all possible parameter sets that fit the (noisy) observation. Therefore, by introducing the onset location in the parameter estimation we enlarge the possible parameter sets that would have a close fit with the observations. This increases the standard deviation leading to a decrease our confidence. The muscle conductivity in this case is estimated as $0.062 \pm 0.001\ mm^2 \sim 0.62 \pm 0.01\ m/s$. In Fig. 7.2f we show the mean of the posterior distribution of the onset location (small red sphere) and the negative log posterior distribution $-\log(p(\Omega_E|\tilde{T}))$. The mean of the posterior distribution well estimates the ground truth onset location ($4.4\ mm$ apart).

7.6 Evaluation on Clinical Data

In order to evaluate this method on clinical data, we used contact mapping of the myocardium, acquired during an electrophysiology study for ventricular tachycardia radio-frequency ablation. This study comprises both endocardial and epicardial mapping, which is rare in clinical routine but enables to precisely evaluate the impact of both measurements on the estimated parameters and its associated confidence. We used either the 20-polar 5-spline PentaRay I (Biosense-Webster, CA) or the 30-polar 5-spline PentaRay II (Biosense-Webster, CA) catheters for high density endo- and epicardial mapping. The PentaRay II catheter enables simultaneous multi-electrode contact mapping of up to 60 mm^2 myocardial surface, when fully expanded. This novel technique of high density map acquisition enables rapid high-density mapping. The mean duration for acquiring a high-density map is about 5-10 minutes. The EP measurements were processed to estimate the depolarisation times [Steinhaus, 1989] at 958 observation points (both endocardial and epicardial) which were then used to adjust the model.

Magnetic Resonance Images (MRI) of the patient were also acquired, both anatomical images and late-enhancement ones, in order to locate scar tissue (this patient has a large aneurysm in the left ventricle). The 3D anatomical image was segmented to generate the myocardial mesh and late-enhancement MRI was segmented and used to label scar tissue and peri-infarct area (border zone) in the mesh. The extra-cellular potential measurements obtained with the catheters were then globally manually registered to this mesh, and projected on the mesh surface. In Fig. 7.3 we present the mesh extracted from the MR images and the observation points projected onto the mesh. The colour of the points corresponds to the distance between the location of the observation point during the procedure and the mesh surface extracted from the MR image. Notice that these distances can be quite large and contribute to the uncertainty on the observation values.

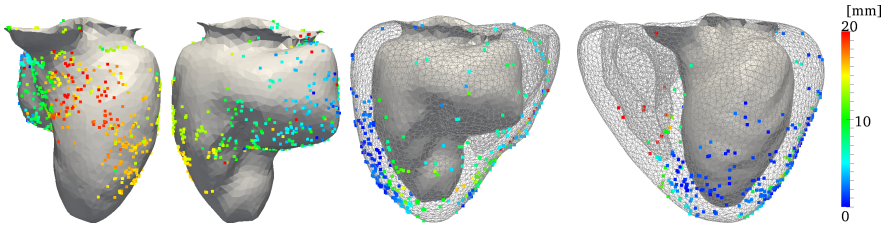

Figure 7.3: The computational mesh extracted from the MR images and the observation points. On the left two views of the endocardial surface is shown with the observation points plotted on top. On the right two views of the epicardial surface is also drawn (as a wire mesh). The observation points on the two surfaces are depicted in the images where the colors correspond to the *distance each point was projected to the mesh surface*.

7.6.1 Probabilistic Model Details and Computational Aspects

The parameters we focus on are: the onset location, the fast conduction system on the endocardium, and the myocardium / scar / border zone conductivities. As in the synthetic case, we determined 17

anatomical regions on the endocardial surface and use the formulation given in Equation 7.3 to describe the endocardial conductivity function. This (together with the myocardium/scar/border zone conductivities) in total yields 20 conductivity parameters to estimate. The conductivity parameters were again formulated as uniformly distributed random variables with ranges: i) myocardium and border zone - $(0.1, 1.6)\ mm^2 \sim (0.25, 1)\ m/s$, ii) scar - $(0.03, 0.4)\ mm^2 \sim (0.15, 0.5)\ m/s$ and iii) each endocardial parameter - $(0.1, 1.9)\ mm^2 \sim (0.8, 3.5)\ m/s$. In addition to these we formulated the uncertainty on the onset location as a uniform distribution on the septum (the yellow regions shown in Figures 7.4c and 7.5c) yielding two extra parameters, 22 parameters in total to estimate. For this 22 dimensional problem we used $P = 14950$ containing 22 dimensional multivariate Legendre polynomials of maximum order 4 similar to the synthetic examples shown before.

The ED model was solved on a tetrahedral mesh with an average element volume of 10 mm^3. The parameters $\tau = 1\ msec$ and $c_0 = 2.5$ were used as in the synthetic experiments. The tensors $\mathbf{M}$ in this case were generated using an analytical model of cardiac fiber orientations where the anisotropy ratio between the principal direction and the others is 0.15 (which corresponds to a conduction velocity three times faster along the fibre). The total time elapsed for the computation of $\{T_i(\mathbf{x})\}_{i=0}^{P}$ took 4.2 hours for all the observation points. In the phase of inference we used 30 000 samples (after the first 5000 samples that were discarded as burn-out) to compute the posterior distributions for the parameters under investigation. Each inference process took 15 minutes on average.

7.6.2 Noise Model

Different sources of uncertainty acting on the cardiac mapping data explained above are: i) the displacement of the catheter contact points on the cardiac surface due to the motion of the heart, ii) the estimation of the depolarization times from the EP measurements and iii) the registration and the projection of the observation points onto the cardiac surface. All these sources affect the interaction between the model and the observed data and therefore, influence the parameter estimation problem. In depth understanding of these effects are crucial to model this interaction accurately. As a preliminary step in this work we used a simplified uncertainty model for the observations. The contributions of the first two sources are modeled as Gaussian noise with homogeneous variance over all the observation points, $\epsilon_1(\mathbf{x}) \sim \mathcal{N}(0, 400\ msec^2)$. The contribution of the third source is modeled as a Gaussian noise with inhomogeneous variance. The variance is modeled to depend on the distance between the mesh surface and the location of the observation point which is available through projection distances for each mapping point, see Figure 7.3. This is formulated in a very simple form as $\epsilon_2(\mathbf{x}) \sim \mathcal{N}(0, \rho_{proj}(\mathbf{x})^2\ msec^2)$ where $\rho_{proj}(\mathbf{x})$ is the projection distance for the observation point at $\mathbf{x}$. The overall noise model for each observation point is then given as the Gaussian noise $\epsilon(\mathbf{x}) = \epsilon_1(\mathbf{x}) + \epsilon_2(\mathbf{x}) \sim \mathcal{N}(0, 400 + \rho_{proj}(\mathbf{x})^2 msec^2)$.

7.6.3 Estimation Experiments

Using the proposed Bayesian formulation and the inference method three different experiments were conducted. In all experiments the different conductivity values and the onset location are estimated as explained in Section 7.6.1. In the first experiment all the 958 observation points (both endocardial and the epicardial) were used in the inference to compute the posterior distributions for the parameters. In the second experiment only the observation points on the epicardial surface (observation points shown in the right two most surfaces in Figure 7.3) were used in the inference. The computed posterior distribution for the parameters is then used to predict depolarisation times for the points on the endocardial surface. These predictions are given as ranges of possible personalised model simulations based on the posterior distributions of the model parameters. The ranges are obtained using the probabilistic framework and the fast sampling scheme presented in Sections 7.3 and 7.4. Comparisons with the measured values - which were not used during the estimation - is presented. In the third experiment, only the endocardial observation points were used in the inference and the predictions are done for the epicardial depolarisation times. For ease of visualisation, we present most of the results on surfaces, but everything was computed on the volumetric myocardial mesh.

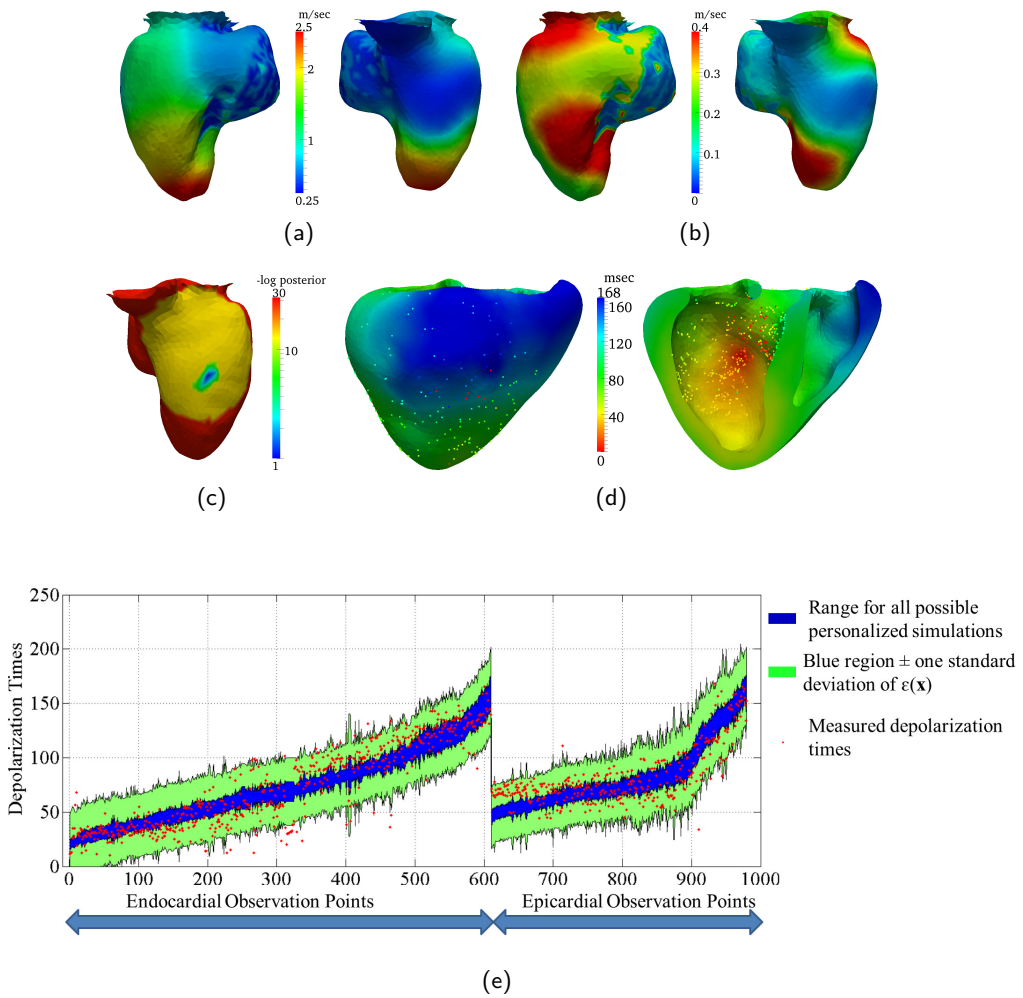

Figure 7.4: Estimation results for the experiment 1 - inference using all the measured points. (a) Mean estimates for the endocardial conductivity function shown from two views. (b) Marginal standard deviations on the estimated conductivity function. (c) $-log(p(\Omega_E|\tilde{T}))$ - the - log posterior for the onset location. (d) Depolarisation time isochrones simulated with the mean estimates where colour points represent the measurements and their depolarisation times. (e) Comparison between the measured depolarisation times and the probabilistic model fit. Range for all possible personalised simulations is computed through the posterior distributions for the parameters. The green region is the observation noise model added to the possible simulation range.

Results on Experiment 1 Figure 7.4 and the first row of Table 7.1 presents the results obtained for the first experiment where all the observation points were used in the estimation process. The posterior distribution for the endocardial conductivity function is presented through its mean (Fig. 7.4a) and the marginal standard deviation (Fig. 7.4b). The estimated volumetric conduction velocities are also given in Table 7.1, which are in the range of the values found in the literature. Notice that the standard deviations for the endocardial conductivities are higher in some regions. Comparing this with the locations of the observation points in the Figure 7.3, we see that the standard deviations are higher where the density of observation points is lower. This is intuitive as in the sense that our confidence on the estimated values is directly linked to the density of observation points. This shows that the presented probabilistic method well captures the interaction between the sparsity of the observations and the estimation of model parameters. Figure 7.4c shows that the posterior distribution for the onset location which is concentrated in a region. This is also in accordance with the density of the observation points.

Two different types of comparison between the model fit and the measured values are shown. In Figure 7.4d the isochrones on the mesh shows the depolarisation times obtained with the mean

	Myocardium	Aneurysm	Border Zone
Exp. 1: Inference all observations	0.88 $\pm$ 0.05	0.31 $\pm$ 0.05	0.58 $\pm$ 0.08
Exp. 2: Inference epicardial observations	0.95 $\pm$ 0.03	0.24 $\pm$ 0.05	0.31 $\pm$ 0.09
Exp. 3: Inference endocardial observations	0.48 $\pm$ 0.14	0.41 $\pm$ 0.07	0.58 $\pm$ 0.10

Table 7.1: Estimated conductivities (mean and standard deviation in m/s) for myocardium, aneurysm and border zone for the three different experiments.

estimates of the parameters. On the same figure the observation points are shown where their colour corresponds to the measured depolarisation time. The match between the mean model (model using the mean estimates for the parameters) and the measured values is $16\ msec$ in RMS error. The mean model however, does not show the rich information context of the probabilistic formulation. The posterior distribution for the parameters suggests a range of possible personalised models instead of a single one. This link between the uncertainties in the estimated parameters and the model simulations yields a possible range of model fits. Figure 7.4e presents a comparison between the measured depolarisation times and this possible range of model fits computed through the parameter posterior distributions. The blue region shows the range of all possible simulated (personalised) depolarisation times, i.e. the range of all the possible values of $T(\mathbf{x}|\overline{D}, \Omega_E)$ computed using $p(\overline{D}, \Omega_E|\tilde{T})$. The green region adds the noise model on this possible range, i.e. $\pm$ one standard deviation of the observation noise model $\epsilon(\mathbf{x})$ to the possible ranges for $T(\mathbf{x}|\overline{D}, \Omega_E)$. Notice that the width of the blue region is rather narrow showing confidence in the model fit. Furthermore, most of the observation points lie within the blue region while almost all of the remaining points lie within the green region.

Results on Experiment 2 The results for this experiment are presented in Figure 7.5 and the second row in Table 7.1. The surface meshes shown in (a) demonstrates that the mean of the posterior distribution for the parameters is structurally similar to the ones estimated in the first experiment with slight differences. The estimated volumetric conduction velocities given in Table 7.1 also show a similar trend. The standard deviations shown in Fig. 7.5b on the other hand are significantly higher compared to Fig. 7.4b. This suggests that only epicardial observations are not enough to confidently estimate endocardial conductivities. This is not surprising as the observations in this case are not directly taken from the endocardial surface. For most of the epicardial points the depolarisation times are influenced by different regions on the endocardium as well as the myocardial conductivity. Therefore, we do not have a direct observations that can confidently estimate the endocardial conductivity function. On the other hand, we notice the low standard deviations for the volumetric conductivities given in Table 7.1 showing that the epicardial observations are enough to confidently estimate the volumetric conduction velocities. Regarding the numerical differences between the estimated values, we will come back to this point while presenting the results for Experiment 3.

Observing Fig. 7.5b one notices that the standard deviations are higher on one side of the endocardium surface. This is as expected since the projection distances of epicardial observation points shown in Fig. 7.3 are higher on one side as well. Therefore, these points are more uncertain leading to lower confidences on the endocardial conductivity estimates on the corresponding side of the endocardium surface. This demonstrates that the presented method well captures the interaction between the uncertainty of the observations and the model parameter estimates.

Figure 7.5c shows that the posterior distribution for the onset location, which (almost) covers the one of Fig. 7.4c. However it is much more spread, also as expected. In Figure 7.5d the depolarisation times simulated by the mean model are shown along with the observations. On the epicardium, the mean model matches the measured depolarisation times with a RMS error of $12.9\ msec$. Using the estimated parameters, the depolarisation times for the endocardium are also predicted. The mean model prediction matches the measured values on the endocardium with a RMS error of $26.1\ msec$.

In Figure 7.5e the comparison between the measured values and the possible ranges for the depolarisation times simulated with the (probabilistically) personalised model are shown. For the

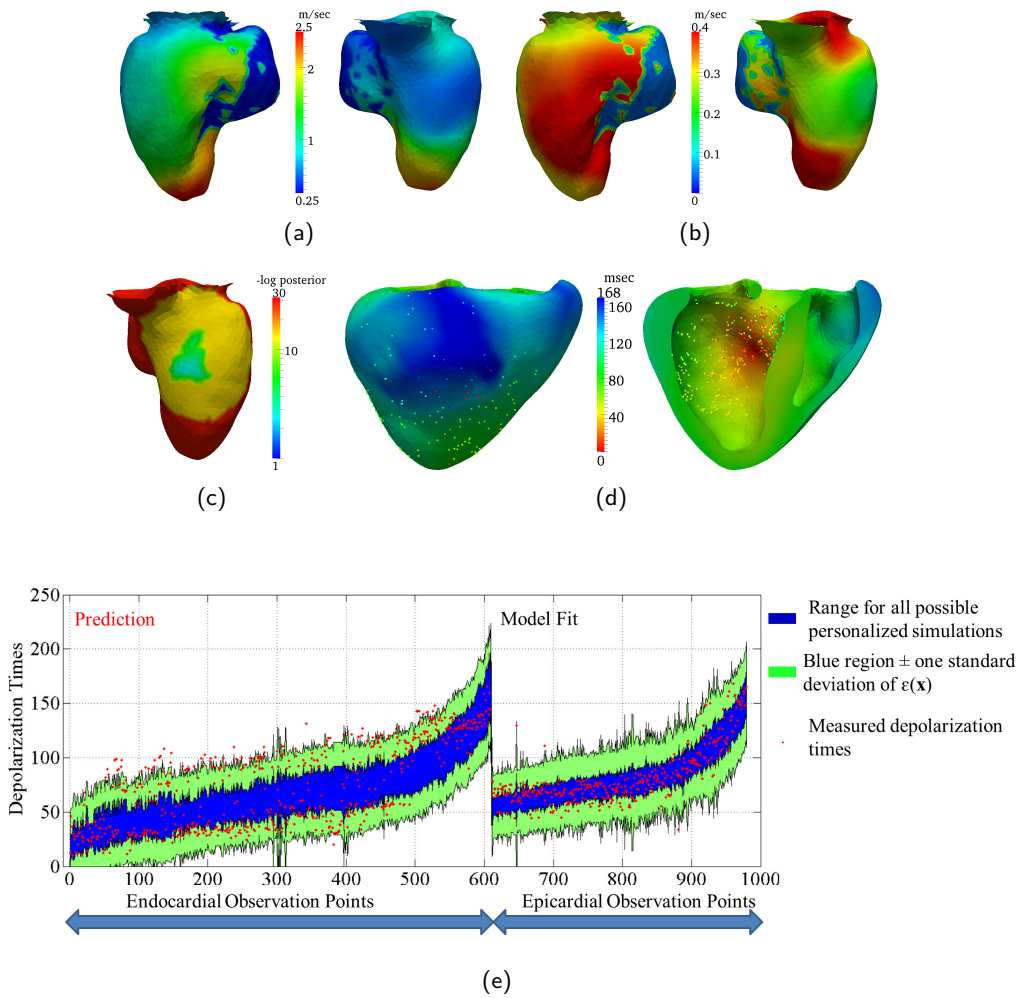

Figure 7.5: Estimation results for the experiment 2. (a) Mean estimates for the endocardial conductivity functions shown from two views. (b) Marginal standard deviations on the estimated conductivity functions. (c) $-log(p(\Omega_E|\tilde{T}))$ - the - log posterior for the onset location. (d) Depolarisation time isochrones simulated with the mean estimates where colour points represent the measurements and their depolarisation times. (e) Comparison between the measured depolarisation times and the probabilistic model fit and model prediction. The estimation uses only the epicardial observation points. The endocardial depolarisation times are predicted.

points that were used for the estimation - epicardial points - we see that the ranges are similar to the ones given in Fig. 7.4. The probabilistic model fit is similar in this case with a narrow range and almost all measurements lying within the blue region. The properties of the predicted endocardial depolarisation times are however, significantly different. The range for the possible predictions are much wider reflecting the uncertainties on the estimated endocardial conductivities. The measured endocardial depolarisation times remain within the model plus the observation noise region, however, the spread is much wider. Furthermore, this quantifies the importance of having observation points on both sides of the myocardium on the accuracy and confidence in the personalised model. We note that we used a different ordering of observation points while plotting Figure 7.4e and 7.5e to have a better visualisation.

Results on Experiment 3 The results for this experiment are presented in Figure 7.6 and the third row in Table 7.1. We notice that the mean of the posterior distribution for the conductivity function and the volumetric conductivity values are again structurally similar to the ones estimated in the previous experiments. The numerical differences between the three experiments demonstrates that the observations taken on the endocardium and the epicardium slightly disagrees on the exact values

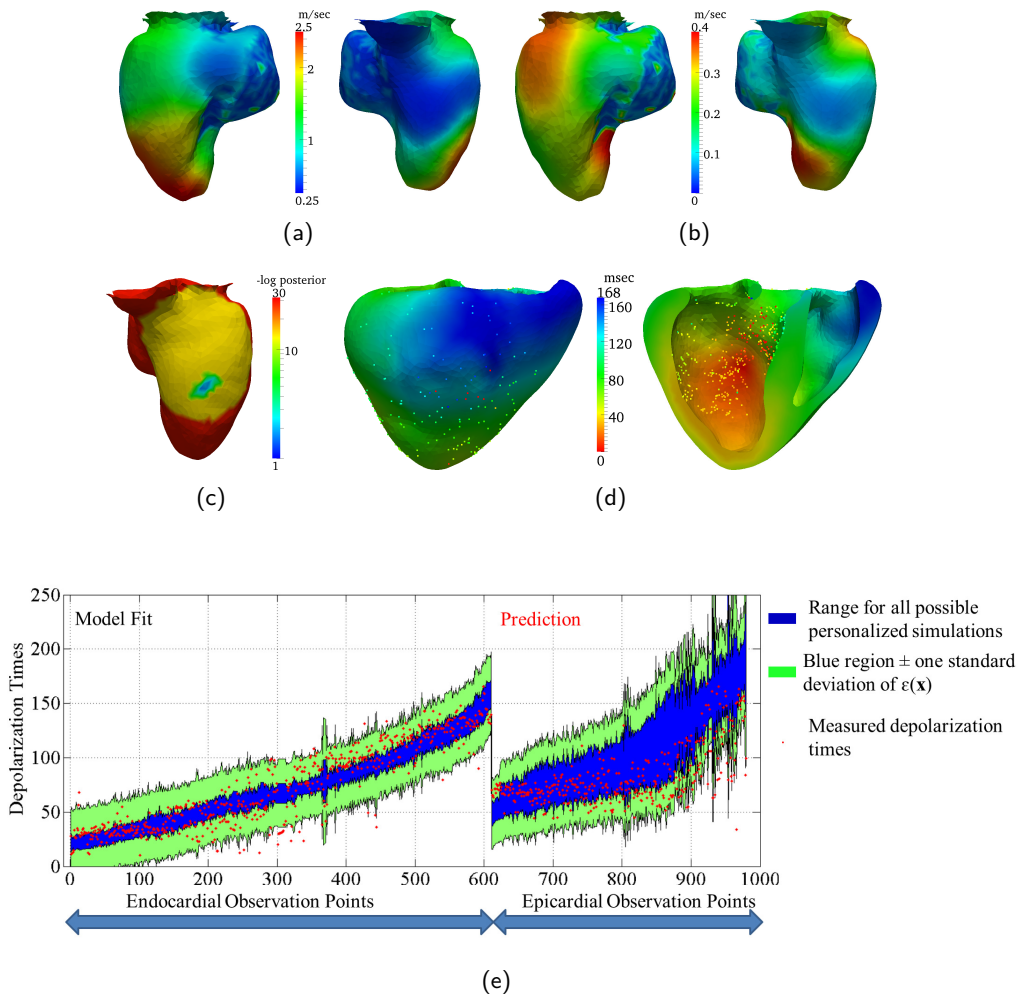

Figure 7.6: Estimation results for the experiment 3. (a) Mean estimates for the endocardial conductivity functions shown from two views. (b) Marginal standard deviations on the estimated conductivity functions. (c) $-log(p(\Omega_E|\tilde{T}))$ - the - log posterior for the onset location. (d) Depolarisation time isochrones simulated with the mean estimates where colour points represent the measurements and their depolarisation times. (e) Comparison between the measured depolarisation times and the probabilistic model fit and model prediction. The estimation uses only the endocardial observation points. The epicardial depolarisation times are predicted.

of the conductivities (comparing Figure 7.6a with Figure 7.5a and second row of the Table 7.1 with the third). This, we believe, is due to the discrepancy between the ED model and the underlying real dynamics. Two observations related to these discrepancies are: i) the mean estimates of Experiment 1 are - in loose terms - averaged between the mean estimates of Experiment 2 and 3, which is as expected and ii) the regions with high standard deviation shown in Figure 7.4b reflects the differences between the estimates given in Figures 7.5a and 7.6a demonstrating that the non-uniqueness of the model-observation interaction can be captured using the proposed method.

Observing Figure 7.6b we notice that the standard deviations are correlated to the density of the observation points as in the first experiment. Furthermore, as the inference is based on the observations taken only from the endocardial surface the standard deviation values shown in Figure 7.6b are lower than the other experiments. However, the high standard deviation on the myocardial conductivity given in Table 7.1 shows that the endocardial observations are not very informative about the muscle conductivity and one needs observations from the epicardium to confidently estimate this value.

The posterior distribution for the onset location (Figure 7.6c) shows similarities to the one obtained in the first experiment. In Figure 7.6d we show the depolarisation times simulated by the

mean model. The RMS model fit error between the mean model simulation and the endocardial measurements is $15.3\ msec$. The difference between the predicted epicardial depolarisation times and the measured ones has an RMS error of $32.2\ msec$.

As in the previous cases in Figure 7.6e we show the possible ranges for the depolarisation times simulated with the personalised model and the measured values. As expected we see that the range for possible simulated depolarisation times is narrower for the endocardial points where the model is fit to the observations. On the other hand, the range of possible predictions of the depolarisation times on the epicardium is much wider. Comparing Figures 7.5e and 7.6e we notice that the uncertainty on the predicted depolarisation times in the latter case is higher. This result is due to the fact that the epicardial observations contain information on the whole system since these depolarisation times are influenced by the endocardial conductivities as well as the volumetric ones. The endocardial observations on the other hand, contain much less information regarding the myocardial conductivity. Therefore, the predictions in this case have much wider possible range, i.e. have much less confidence. We note that this separation of the information content is partly due to the conductivity model we use as given in Equation 7.3.

7.7 Discussion

The presented results show the capabilities of the proposed probabilistic method and the fast inference framework. However, there are some important factors that influence the results of the method:

- *Data Noise Model:* The selected noise model has an important impact on the results. We used here some arbitrary values from our experience on such data, a more exhaustive process looking through the repeatability of the measures and the processing pipeline from the raw signal to the extracted depolarization time should be undertaken to properly define the noise model.

- *Model Parameter Variability:* The prior distributions used for the different model parameters also have an important impact on the results. Here uninformative priors have been used with large ranges. Narrower ranges or a different prior model such as Gaussian would have altered the variations on the estimated parameters as well as the ranges for the possible model fits and predictions. Analysis of a set of clinical cases should help in improving the relevance of the prior distributions used here.

- *Model Error:* The realism of the selected model has also obviously an impact on the success of such personalization. Some strategies were proposed to explicitly include the model error in such joint probabilities, including for instance the approximation errors [Arridge et al., 2006]. These methods can be integrated into the proposed framework.

Regarding the *clinical applications*, the presented probabilistic framework provides a confidence measure that can help the clinician in weighting the predictions of a model with respect to the other clinically available information in his decision process. Moreover it can also guide the data acquisition. For instance, we used here epicardial points, which mapping in clinical practice is exceptional, but being able to quantify the contributions of both endo and epi surfaces is important. It can help in deciding if the additional information given by this epicardial mapping will be quantitatively significant or not. One application is also to move from invasive to non-invasive methods, namely from endocardial catheters to epicardial data estimated from body surface potentials, and there is then a need to know how confident one can be in the estimated parameters when using only epicardial data.

7.8 Conclusion

In this work we presented an efficient probabilistic framework personalization of mathematical models. We also demonstrated the proposed framework for the parameter estimation problem for cardiac

electrophysiology. The proposed method is based on spectral approximations of partial differential equations and compressed sensing. In the experiments we showed that Bayesian inference for high dimensional parameters, i.e. locally varying conductivity, can be efficiently done *within few minutes*, given that the spectral basis is already computed. Moreover, we have shown that the spectral basis can be computed efficiently as well (within 5 hours). Considering the computational cost of conventional methods for Bayesian inference for PDEs, this is an important step in making stochastic personalization practical, and it already provides interesting results on clinical data. The interaction between the uncertainty on the observations and the uncertainty on the estimated parameters is a major phenomenon to consider when using biophysical models for personalized medicine. We demonstrated on clinical data how this interaction translates into the model parameters and predictions for patient data. Our future work is concentrated on analyzing the proposed methodology for different modeling problems (including reaction-diffusion models) and creating more realistic and yet tractable Purkinje network and myocardium interactions.

7.A Polynomial Chaos and Spectral Representation

Polynomial chaos (PC) expansion is an orthonormal basis representation for random functions [Xiu and Karniadakis, 2002]. For the ease of explanation let us concentrate only on the vector $\overline{D}$ where different components were modelled as random variables with uniform distributions. The PC expansion for the random vector $\overline{D}$ is given as

$$\overline{D} \triangleq \overline{D}(\boldsymbol{\xi}) = \sum_{i=0}^{\infty} \overline{d}_i \Phi_i(\boldsymbol{\xi}) \approx \sum_{i=0}^{P} \overline{d}_i \Phi_i(\boldsymbol{\xi}), \tag{7.10}$$

where $\boldsymbol{\xi} = [\xi_1, ..., \xi_Q]$ is a random vector of independent components with uniform distributions, $\{\Phi_i\}_0^\infty$ is the orthonormal (multivariate) Legendre polynomial basis and $\{\overline{d}_i\}_0^\infty$ are deterministic vectors – which we call the **spectral basis** for the $\overline{D}$ vector. The second part of Eq. (7.10) shows the computationally useful finite approximation of the PC expansion where the parameter P corresponds to number of components to include in the approximation. The orthonormality condition of the PC basis is defined as

$$< \Phi_i(\boldsymbol{\xi}), \Phi_j(\boldsymbol{\xi}) >= \int_{\Sigma(\boldsymbol{\xi})} \Phi_i(\boldsymbol{\xi}) \Phi_j(\boldsymbol{\xi}) p(\boldsymbol{\xi}) d\boldsymbol{\xi} = \delta_{i,j}, \tag{7.11}$$

$$\overline{d}_i = \int_{\Sigma(\boldsymbol{\xi})} \overline{D}(\boldsymbol{\xi}) \Phi_i(\boldsymbol{\xi}) p(\boldsymbol{\xi}) d\boldsymbol{\xi}, \;\; i, j \in \mathbf{N}_0, \tag{7.12}$$

where $\Sigma(\boldsymbol{\xi})$ is the range of the $\boldsymbol{\xi}$ vector, $p(\boldsymbol{\xi})$ is the distribution - a constant value in this case - and $\delta_{i,j}$ is Dirac's delta.

The definition of $\overline{D}(\boldsymbol{\xi})$ and the dimension of the vector $\boldsymbol{\xi}$ depend on the distribution of the vector itself and the random vector $\overline{D}$, [Xiu and Karniadakis, 2002]. Focusing on the inverse problem defined in Section 7.3, we defined each component of the random vector $\overline{D} = [D_0, ..., D_M]$ as uniformly distributed (noted $\mathcal{U}$) independent random variables. The PC expansion given in Equation 7.10 can then be written as

$$\boldsymbol{\xi} = [\xi_0, ..., \xi_M], \;\; \xi_m \sim \mathcal{U}(-1, 1), \;\; \forall m \in \{0, ..., M\}$$
$$\Rightarrow D_m = D_m(\xi_m) = \frac{D_m^b - D_m^a}{2} \xi_m + \frac{D_m^b + D_m^a}{2}. \tag{7.13}$$

The power of the spectral methods for PDEs is that the randomness of $T(\mathbf{x})$ – which is due to the randomness in parameters – can be represented using the same PC basis functions and the same random vector $\boldsymbol{\xi}$ as the parameters [Ghanem and Doostan, 2006; Xiu, 2009]. We can write

$$T(\mathbf{x}) \triangleq T(\mathbf{x}, \boldsymbol{\xi}) = \sum_{i=0}^{\infty} T_i(\mathbf{x}) \Phi_i(\boldsymbol{\xi}) \approx \sum_{i=0}^{P} T_i(\mathbf{x}) \Phi_i(\boldsymbol{\xi}), \tag{7.14}$$

where $T_i(\mathbf{x})$ are the spectral basis functions for $T(\mathbf{x})$. This representation provides the computationally efficient link between $\overline{D}$ and $T(\mathbf{x})$. Let $\tilde{D}$ be a single instance of $\overline{D}$ then there is a unique $\tilde{\boldsymbol{\xi}}$ such that $\tilde{D} = \overline{D}(\tilde{\boldsymbol{\xi}})$ due to the orthonormality of the spectral representation given in Equation 7.11. As a result

$$T(\mathbf{x}|\tilde{D}) = T(\mathbf{x}, \tilde{\boldsymbol{\xi}}) \approx \sum_{i=0}^{P} T_i(\mathbf{x})\Phi_i(\tilde{\boldsymbol{\xi}}). \tag{7.15}$$

As a result instead of solving Eq. (7.1) to compute $T(\mathbf{x}|\tilde{D})$ we can approximate it using the linear combination of Eq. (7.15). This provides substantial speed up yielding faster sampling.

The computationally expensive part in the given discussion is the estimation of the spectral basis functions $\{T_i(\mathbf{x})\}_{i=0}^{P}$. Two different methods that have been proposed in the literature are Galerkin projections [Xiu and Karniadakis, 2002; Ghanem and Doostan, 2006] and stochastic collocation methods [Ma and Zabaras, 2009; Nobile et al., 2008]. Both of these methods suffer from the curse of dimensionality [Doostan et al., 2009], i.e. when the dimension of the parameter $\overline{D}$ is high the construction of $T_i(\mathbf{x})$ becomes computationally impractical. Depending on the quality of the approximation, P, and the model equation, in the case of Galerkin projections one can end up solving a system of 2000 coupled PDEs [Xiu and Karniadakis, 2002] and in the case of stochastic collocation methods a substantial number of model simulations, $\mathcal{O}(10^5)$, might be needed [Ma and Zabaras, 2009].

In this work we overcome the curse of dimensionality by integrating compressed sensing based sparse reconstructions of $\{T(\mathbf{x}_i)\}_{i=0}^{P}$ in the Bayesian inference framework.

7.B Spectral Reconstructing using Compressed Sensing

Compressed sensing (CS) is a very active field of research in signal and image processing [Donoho, 2006; Lustig et al., 2008]. The main idea is that if a signal is sparse we need much less information to reconstruct it. This information, for example, can be in terms of number of samples taken in the frequency domain. The reason for this is that sparse signals contain only a small number of frequency components and therefore, a small number of random samples is enough for accurate reconstruction [Donoho, 2006]. In the context of PDEs this corresponds to the fact that in spectral expansion of the solution $T(\mathbf{x}, \boldsymbol{\xi})$, only a small number of components $T_i(\mathbf{x})$ are significantly larger than zero. Following the compressed sensing theory the significant components can be recovered using a small random set of $\hat{\boldsymbol{\xi}} = \{\boldsymbol{\xi}_n\}_{n=0}^{K}$ where $K << P$. This recovery is possible through the formulation

$$\begin{aligned} \arg\min_{\mathbf{T}(\mathbf{x})} \|\mathbf{T}(\mathbf{x})\|_1 \text{ subject to } \left\|T(\mathbf{x}, \hat{\boldsymbol{\xi}}) - \boldsymbol{\Phi}(\hat{\boldsymbol{\xi}})\mathbf{T}(\mathbf{x})\right\|_2 < \delta, \\ \mathbf{T}(\mathbf{x}) = [T_0(\mathbf{x}), ..., T_P(\mathbf{x})]^t \\ T(\mathbf{x}, \hat{\boldsymbol{\xi}}) = [T(\mathbf{x}, \boldsymbol{\xi}_0), ..., T(\mathbf{x}, \boldsymbol{\xi}_K)]^t, \forall \mathbf{x} \in \Omega \end{aligned} \tag{7.16}$$

where $\boldsymbol{\Phi}(\hat{\boldsymbol{\xi}})$ is the matrix of $K \times P$ with $[\boldsymbol{\Phi}(\hat{\boldsymbol{\xi}})]_{ij} = \Phi_j(\boldsymbol{\xi}_i)$, $\|\cdot\|_1$ is the L_1 norm, $\|\cdot\|_2$ is the L_2 norm and δ is the desired accuracy. This minimization problem is defined for each point $\mathbf{x}$ separately. In the case of Bayesian inference problem we solve it for all the observation points $\{\mathbf{x}_i\}_1^N$. Equation (7.16) is a linear program and can be solved efficiently and accurately using various available tools, for example [Tomioka and Sugiyama, 2009].

In [Doostan et al., 2009], Doostan *et al.* analysed the one dimensional linear diffusion equation (elliptic PDE). They have shown that the significant spectral coefficients obtained using the Eq. (7.16) were very similar to the exact coefficients. The advantage of this approach is that it requires a few hundred simulations to construct the significant spectral basis components while stochastic collocation based methods requires high number of simulations ($\mathcal{O}(10^5)$) to reach the same accuracy. The amount of decrease in the computational burden depends on the sparsity of the underlying equation. Although, for the general equations the applicability of this method is not know for the Eikonal-Diffusion models the sparsity holds and can be shown experimentally.

Chapter 8

Coupling Shape Statistics with a Reduced Model of Cardiac Flow

– This chapter is based on [Guibert et al., 2013]: Guibert, R., Mcleod, K., Caiazzo, A., Mansi, T., Fernández, M. A., Sermesant, M., Pennec, X., Vignon-Clementel, I., Boudjemline, Y., and Gerbeau, J.-F. Group-wise construction of reduced models for understanding and characterization of pulmonary blood flows from medical images. *Medical Image Analysis*, 18(1):63–82, Oct. 2013.

8.1 Introduction

Congenital heart disease (CHD) is a prominent cause of infant mortality around the world and decreases the quality of living and life expectancy of many. Abnormal heart rhythm and structure affect blood flow through the heart and into the arteries, which consequently influences the development of the organs and surrounding structures. CHD patients are monitored with several imaging modalities, which are chosen in medical practice based on the pathology and its severity [Puranik et al., 2010]. Anatomy can be easily visualized in the images extracted from typical cardiac imaging modalities such as cine-MR in magnetic resonance (MR) imaging, echocardiography and CT. However current methods for imaging blood flow in a three-dimensional volume are limited. Non-invasive imaging techniques such as phase contrast magnetic resonance imaging (PC-MRI) are used to quantitatively measure blood flow in clinical practice only if necessary, and are not easy to acquire at multiple locations, especially for CHD patients [Markl et al., 2012]. Compared to PC-MRI, cardiac MR volumetry has been shown to provide non-interchangeable cardiac function assessment in dobutamine stress testing of regurgitant repaired Tetralogy of Fallot (ToF) [Valverde et al., 2011]. Time-resolved 3D contrast-enhanced MR angiography has also been proposed to non-invasively assess lung perfusion in ToF [Tomasian et al., 2009]. 4D-MRI, while potentially providing velocity in a three-dimensional volume over time, is still a subject of research for its acquisition and post-processing [Markl et al., 2012]. Velocity can be measured with Doppler ultrasound machines, which are more often found in clinical practice, but the acquired data is limited to 1D.

This is one reason why computational simulations of blood flow have been developed in recent years in an attempt to better understand blood flow dynamics. The aim of such modeling is to gain insight into how hemodynamics change due to a pathology and wall shear stress (see, *e.g.*, [Yeung et al., 2006; Troianowski et al., 2011; LaDisa et al., 2011]). Conversely, pathology developments can depend on abnormal hemodynamics, such as in the absence of a functioning valve, as will be the case in this work. Computer hemodynamic simulations provide a tool to predict hemodynamic changes due to surgical repair [Vignon-Clementel et al., 2010b], explore different scenarios for treatment (see, *e.g.*, [Hsia et al., 2011; Yang et al., 2011]), non-invasively compute indices that are otherwise invasively measured such as fractional flow reserve (FFR) [Koo et al., 2011], and design artificial devices or conduits that are subject to blood flow (see, *e.g.*, [Prasad et al., 2011; Pant et al.,

2011]). Similarly, knowing the anatomy and hemodynamics of a patient, physicians can determine the suitability of a patient for surgical intervention and plan therapy [Morales et al., 2011].

Computational fluid dynamics (CFD) methods are commonly used to simulate blood flow among others in the larger arteries, by numerically solving the three-dimensional Navier-Stokes equations. However, the large computational cost of numerical simulations is still a relevant issue, especially when dealing with patient-specific geometries. On one hand, the computation time can be reduced by exploiting parallel computing and GPU implementations (see, *e.g.*, [Biswas, 2010]). It can also be drastically reduced when lower-dimensional models (i.e. 1D wave propagation or 0D lumped models) can efficiently replace 3D models [Moore et al., 2005; Blanco et al., 2009; Grinberg et al., 2011; Formaggia et al., 2012; Reymond et al., 2012]. However, 3D models are really warranted when pressure losses and velocity features are largely determined by the interplay between hemodynamics and complex geometry as in these repaired ToF cases. On the other hand, the issue of complexity has also been addressed by developing so-called model order reduction techniques, which aim to reduce the dimension of the problem by restricting the numerical solution to a pre-defined low order space.

Among others, in [Manzoni et al., 2011], the authors propose to extract a low dimensional parametrization of the computational domain and solve the parameterized flow equations with the reduced basis method. This work is able to gain speed in computational time but necessitates a shape parametrization of the object through control points assigned at regions of shape change. Here, we consider a model reduction based on the Proper Orthogonal Decomposition (POD, also known as Karhunen – Loève expansion or Principal Component Analysis – PCA), an approach which aims to find a low-order basis for the numerical solution starting from a set of pre-computed snapshots. In fluid dynamics, POD was introduced by Lumley in the late 1960s to study turbulent flows. For a more recent presentation of POD, we refer for example to [Volkwein, 1999; Bergmann et al., 2009; Rathinam and Petzold, 2004]. In the context of blood flows, POD was used by [Mcgregor et al., 2008; McGregor et al., 2009], to interpolate flow field measured on medical images.

In this paper, we construct reduced order models of blood flows through the pulmonary artery by transporting a POD basis from a reference geometry onto patient specific anatomies. The reference geometry is obtained by computing a centered atlas of a preliminary population, with a non-parametric method which is thus not dependent on a choice of control points. The general methodology was briefly presented in [McLeod et al., 2010] where we only assessed the capability of the reduced basis to approximate the solution of the full order model. In the present work, we extensively test our approach on a significant number of patients, varying not only the geometry but also the experimental conditions, and we actually use the reduced order model to solve the Navier-Stokes equations.

We apply the method to a data-set of 17 pulmonary arteries (PA) with repaired ToF (as shown in Fig. 8.1), where the structures are affected by a known shape abnormality due to both the pathology and the initial surgical repair. A schematic diagram showing the pipeline of this method is shown in Fig 8.2.

For this pathology, clinicians are interested in understanding how the artery remodels due to blood regurgitating back into the right ventricle of the heart, and reversely how blood regurgitates due to the deformed artery. Regurgitation results from the absence of a functioning pulmonary valve that maintains one-way blood flow from the right ventricle to the pulmonary artery. Previous ToF blood flow simulations have investigated regurgitation with lumped [Kilner et al., 2009] or idealized (geometry and boundary conditions) three-dimensional [Chern et al., 2008] models, as well as pressure losses for two repair options with either a one-dimensional [Spilker et al., 2007] or a steady three-dimensional [Chai et al., 2010] patient-specific model. In this paper, we combined realistic models of form (three-dimensional geometries) and function (physiological inflow and outlet boundary conditions) as in [Das et al., 2011]. This is particularly important for one of the aims of this paper: to test the robustness of model order reduction not only with respect to geometry deformation, but also against changes in the physiological boundary condition. Specifically, we investigated how the reduced method works for normal as well as pathological flows in the PAs, and its capability for simulating other physiological states, namely exercise and varying degrees of pathological regurgitation. This aspect has to our knowledge not been investigated before.

For follow-up treatment planning, clinicians are interested in determining first the optimal method

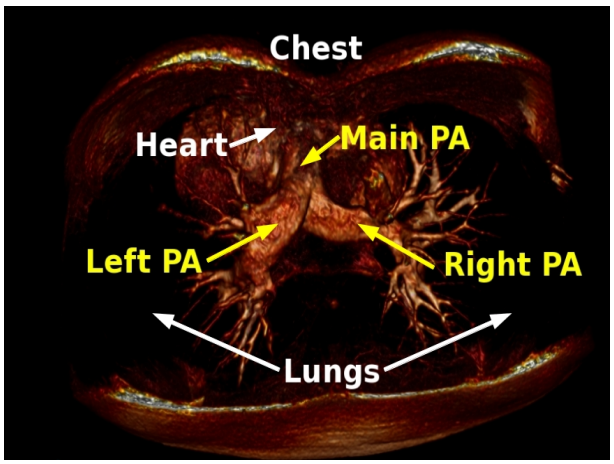

Figure 8.1: A 3D volume rendered image of one patient to visualise the location of the pulmonary artery (PA) with respect to the heart and lungs.

of intervention for each patient, be it surgical or non-invasive, as well as designing artificial devices to act in the same way as the pulmonary valve to enforce one way blood flow. Due to the complex and remodeled pulmonary artery, it is not always possible to insert existing devices in some patients. This work constitutes thus a first step towards the use of atlas-based reduced models to better understand hemodynamics in these patients and efficiently simulate hemodynamics for later device design.

The paper is structured as follows. In Sec. 8.2 the construction of the atlas which serves as the reference geometry is described. Sec. 8.3 is dedicated to blood flow simulations, describing the numerical method for the full simulations on the reference geometries and the model order reduction technique for the patient-specific reduced simulations. The procedure is assessed in Sec. 8.4 by comparing the reduced method to full CFD simulations in different clinically relevant situations. Finally, in Sec. 8.5 the results and future paths for improvements are discussed, while. Sec. 8.6 draws a few concluding remarks.

8.2 Computation of an average geometry

Let us assume to have a set of patient geometries drawn from a given population, and, for each patient, a surface representation of a region of interest (such as an organ, or artery), which is defined by delineating the boundaries of the organ on the images.

As a first step, given the set of such surfaces we would like to compute an *atlas*, i.e. an average surface representation of the population. In this case, the geometry of the atlas should be well-defined and centered with respect to the population. For this we use the framework proposed in [Durrleman et al., 2009a], which is described briefly in Sec. 8.2.1 - 8.2.3. Additionally, we also require a consistent method for computing individual maps from the original patient geometries to the atlas. We extend on the mathematical framework of [Durrleman et al., 2009a] to estimate a surface representation of the centered currents atlas, as described in Sec. 8.2.4.

8.2.1 Non-parametric representation of surfaces using currents

As in [Durrleman et al., 2009a], the patient meshes are represented by *currents* from the geometric integration theory. The basic idea is to characterize shapes by the flux of any vector field through them, somehow in the way 3D objects are probed by laser scanners from many locations to reconstruct their surfaces. Formally, current are elements of the metric dual of a Hilbert space of vector fields (the kernel trick from machine learning is used to provide a convenient metric), which gives a nice linear embedding space for anatomical surfaces. Currents are used to represent the observations (the patient geometries), the residuals (what is not captured by the geometrical model), and the deformations (used to map one geometry to another), in the same common framework. More

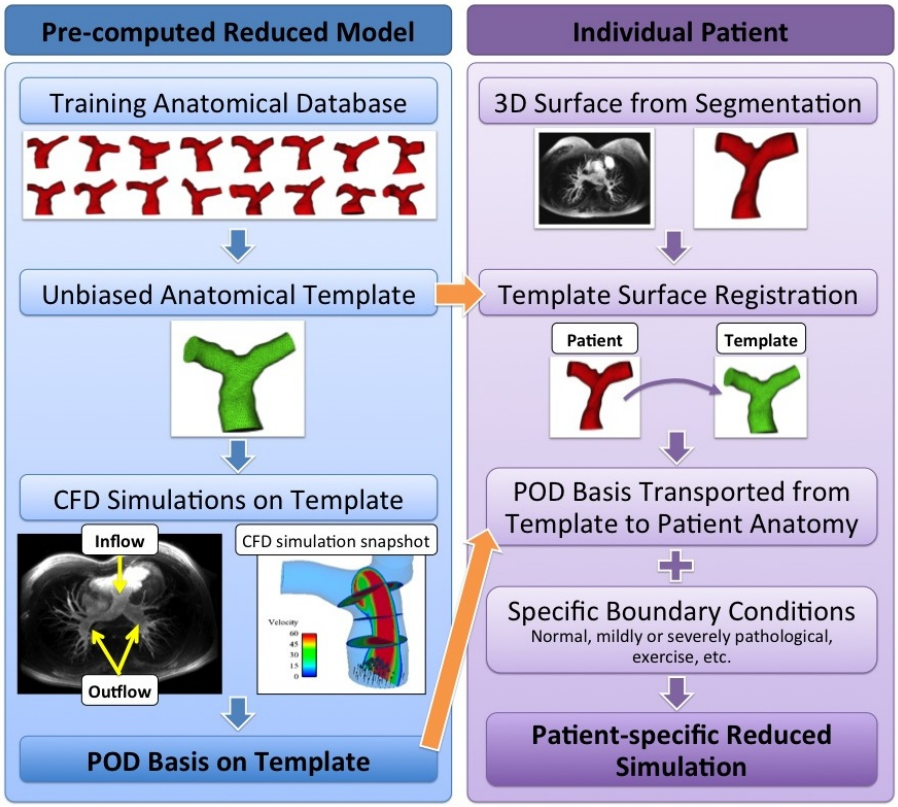

Figure 8.2: Schematic diagram to display the method which consists of an offline pre-computation step by simulating the blood flow on a reference geometry, and then reducing the output of the simulation to obtain a reduced-order basis. An individual flow simulation can be done by transporting the reduced-order reference basis to the individual, and solving the flow equations with the reduced basis in the patient space with patient-specific boundary conditions.

specifically, the space of currents forms a vector space, and we can compute the distance between two meshes in the space of currents, without requiring a point-to-point correspondence between the meshes [Durrleman et al., 2009a]. Moreover, we can apply statistical operations such as the mean and variance on surfaces.

The approach is summarized in more details in the Appendix (Sec. 8.6), while we refer the reader to [Durrleman et al., 2009a] for a complete derivation.

8.2.2 Surface-to-surface registration

After having represented the meshes as currents, we need a method for computing the deformations, i.e. the transformations from one geometry to another.

We would like to restrict the transformations to those which preserve the topology of the object and give a one-to-one (invertible) smooth transformation (i.e. a diffeomorphism). Restricting to diffeomorphisms gives non-linear deformations that allow local smooth variations to be captured in the registration. We use a group of diffeomorphisms to allow computations with discrete parametrization using the Large Deformation Diffeomorphic Metric Mapping (LDDMM) method. LDDMM was used for instance in [Beg et al., 2004] to find the deformations between full 3D images in the context of cardiac anatomy. Our choice is dictated by the ability of LDDMM to capture the large shape variability observed in the population. In particular, this method allows to estimate the optimal deformation (ϕ) from one surface to another. This deformation framework can also be used to register surfaces modeled as currents, as shown in [Vaillant and Glaunes, 2005]. A brief overview of the LDDMM method is given in the Appendix (Sec. 8.6).

8.2.3 Iterative estimation of the atlas

Let us denote with S_i, $i = 1, \ldots, N_P$ the set of patient surfaces. An atlas surface $\widehat{S}$ can be computed using a *forward* approach [Durrleman et al., 2009b] by modeling the observations (the patient meshes) as noisy deformations of the atlas:

$$S_i = \phi_i(\widehat{S}) + \epsilon_i \, .$$

In the latter, ϵ_i is a residual term that accounts for shape features not represented by the atlas. The deformations ϕ_i can be computed iteratively by minimizing the distance from the S_i's to the atlas, in order to center the atlas with respect to the observations (see Appendix). This approach is clearly disentangling the shape changes (encoded in the deformation) from the measurement noise (encoded in the residuals). Thus, statistical analyses can be done on the deformations and the residuals.

The iterative procedure can be summarized as follows (see Algorithm 4). The atlas is first initialized by taking the mean of the patient meshes in the space of currents. At each iteration N, the current atlas $\widehat{S}^N$ is then registered to each of the patients, individually computing individual deformations ϕ_i^N.

The new atlas is computed through a deformation, in order to minimize the error, for each patient, between the patient mesh S_i and the geometry generated from mapping the atlas onto the patient mesh. Formally, denoting with $\|.\|$ the L_2 norm (in the space of currents), we minimize the error:

$$\varepsilon(\widehat{S}^{N+1}) = \|S_i - \phi_i^N(\widehat{S}^N)\|^2 \tag{8.1}$$

(see [Durrleman et al., 2009a] for details on the minimization strategy). We then register the updated atlas to the individuals, recompute the atlas and loop until convergence using the forward model.

Algorithm 4 Atlas Estimation

Require: N segmented patient images (surface meshes).

1: Manual rigid alignment of meshes to a reference patient.
2: Create initial atlas $\widehat{S}^0$ as the mean of the patient meshes.
3: **loop** {*over* N *until convergence*}
4: Estimate the transformations ϕ_i that register the atlas $\widehat{S}^N$ to the individual S_i.
5: Update the atlas by minimizing the error $\varepsilon(\widehat{S})^{N+1}$ in Eq. 8.1 using the estimated transformations ϕ_i and the atlas $\widehat{S}^N$
6: **end loop**
7: **return** Final atlas $\widehat{S}^{N_{end}}$ and the related transformations $\phi_i^{N_{end}}$.

8.2.4 Surface representation of the atlas

Using the atlas-construction method described in Algorithm 4, we compute an atlas in the space of currents which can be visualized as the disjoint set of triangles (Dirac currents). This representation is sufficient for computing statistics between objects in the space of currents, however in this case we need a surface representation of the atlas in which to compute the "average" flow. A general practice for computing this surface is to register the closest patient (in the space of currents) to the computed atlas. Of course, this representation is biased by which patient is used. To reduce this bias, we followed the minimization strategy as in [Durrleman et al., 2008a] at a coarse scale, followed by an additional step to average the atlas-to-patient deformations. This average deformation was applied to the closest patient and this mesh was used to initialize the atlas construction pipeline at a finer scale. The initial optimization (Algorithm 4) is performed at a coarse scale to extract the regional differences in order to obtain a reasonable first estimate of the atlas, which is then refined to capture smaller local shape features (see Algorithm 5).

Algorithm 5 Atlas Refinement

1: Compute atlas at a coarse scale
2: Find the closest patient S_j to the atlas and deform the patient to the atlas to get a surface mesh $\widehat{S}_{S_j} = \phi_j(S_j)$
3: **loop** $\{$*over* N *until convergence*$\}$
4: Register $\widehat{S}^N_{S_j}$ to each patient to get $\phi^N_{\widehat{S}_{S_j},i}$
5: Average the deformation fields $\phi^N_{\widehat{S}_{S_j},i}$ for all i to get $\hat{\phi}^{N+1}_{\widehat{S}_{S_j}}$
6: Apply the average deformation field $\hat{\phi}^{N+1}_{\widehat{S}_{S_j}}$ to $\widehat{S}^N_{S_j}$
7: Use the result from Step 5 as initialization into the atlas construction at a reduced scale
8: **end loop**
9: **return** Final refined atlas $\widehat{S}^{N_{end}}$ and the related transformations $\phi_i^{N_{end}}$.

8.3 An atlas-based reduced order model of blood flow

8.3.1 Reference blood flow simulation and POD basis

In the following, let us denote by $\widehat{\Omega}$ the three-dimensional spatial domain enclosed by the atlas surface representation (Section 8.2.4). We will refer to $\widehat{\Omega}$ as the *reference geometry*. In the context of the computational fluid dynamics (CFD) in the pulmonary artery, we assume that the boundary of $\widehat{\Omega}$ is partitioned as

$$\partial\widehat{\Omega} = \Sigma_{\text{in}} \cup \Sigma_{\text{wall}} \cup \Sigma_{\text{out}},$$

which corresponds to the inflow, arterial wall and the outflow boundaries, respectively.

The reference simulation of blood flow is obtained by numerically solving the incompressible Navier-Stokes equations in $\widehat{\Omega}$, for the velocity $\hat{\mathbf{u}} : \widehat{\Omega} \times \mathbb{R}^+ \to \mathbb{R}^d$ and the pressure $p : \widehat{\Omega} \times \mathbb{R}^+ \to \mathbb{R}$

$$\begin{cases} \rho\partial_t\hat{\mathbf{u}} + \rho\hat{\mathbf{u}}\cdot\nabla\hat{\mathbf{u}} + \nabla\hat{p} - 2\mu\,\text{div}\,\boldsymbol{\epsilon}(\hat{\mathbf{u}}) = 0 & \text{in} \quad \widehat{\Omega}, \\ \text{div}\,\hat{\mathbf{u}} = 0 & \text{in} \quad \widehat{\Omega}, \\ \hat{\mathbf{u}} = \mathbf{u}_{\text{in}} & \text{on} \quad \Sigma_{\text{in}}, \\ \hat{\mathbf{u}} = 0 & \text{on} \quad \Sigma_{\text{wall}}, \\ \boldsymbol{\sigma}(\hat{\mathbf{u}},\hat{p})\mathbf{n} = -p_{\text{out}}\mathbf{n} & \text{on} \quad \Sigma_{\text{out}}. \end{cases} \tag{8.2}$$

In (8.2), ρ stands for the density of the fluid and the fluid Cauchy-stress tensor is given by

$$\boldsymbol{\sigma}(\mathbf{u},p) = -p\mathbf{I} + 2\mu\epsilon(\mathbf{u}), \quad \boldsymbol{\epsilon}(\mathbf{u}) \overset{\text{def}}{=} \frac{1}{2}\left(\boldsymbol{\nabla}\mathbf{u} + \boldsymbol{\nabla}\mathbf{u}^{\text{T}}\right),$$

μ being the dynamic viscosity of the fluid, $\mathbf{u}_{\text{in}}$ a given inlet velocity field and p_{out} an outlet pressure (defined below).

At the inlet we prescribe a parabolic velocity profile, whose flow rate varies in time according to a chosen physiological regime. At the outlet, a relationship between pressure and flow is prescribed, in order to represent the pulmonary vessels downstream of the 3D-fluid model. We consider an outlet boundary composed of two disjointed surfaces, i.e. $\Sigma_{\text{out}} = \Gamma_1 \cup \Gamma_2$. The outlet pressure p_{out} at each outlet boundary $\Gamma_i \subset \Sigma_{\text{out}}$ is defined by a lumped parameter model, in which $p_{\text{out}}(t)$ is related to the outgoing flux at Γ_i,

$$Q^i_{\text{out}}(t) = \int_{\Gamma_i} \mathbf{u}(t)\cdot\mathbf{n}ds, \tag{8.3}$$

in an analogous way as voltage and current are related in electric circuits. In particular, we used a 3-element Windkessel model [Frank, 1899] (see [Vignon-Clementel et al., 2010a] for recent applications in pulmonary artery modeling), in which the outlet pressure and flow are related by the ordinary differential equation:

$$p_{\text{out}} + R_{\text{d}}C\frac{\text{d}p_{\text{out}}}{\text{d}t} = (R_{\text{p}} + R_{\text{d}})Q_{\text{out}} + R_{\text{p}}R_{\text{d}}C\frac{\text{d}Q_{\text{out}}}{\text{d}t}, \tag{8.4}$$

where R_{p} and R_{d} model the resistance of the proximal and distal vasculature, respectively, and the capacity C takes into account the ability of the downstream vessels to store blood during peak flow and recoil when pressure decreases. The deformability of the vessels could also been taken into account in the 3D domain: fluid-solid interaction has been shown to influence both pressure and flow in pulmonary arteries, changing not so much the streamlines but more the pressure and wall shear stress, mostly for exercise conditions [Bazilevs et al., 2009]. However this requires knowledge of thickness and material properties of the wall, which cannot be easily extracted from the available MRI data. As a first step the wall is thus assumed rigid, although the proposed method could be also extended to the case of fluid-solid interaction.

Numerical approximation

Problem (8.2) is discretized in time with a Chorin-Temam projection scheme (see, e.g., [Guermond et al., 2006; Chorin, 1968; Temam, 1968]) in which velocity and pressure are solved separately in two substeps. Namely, let us denote with τ the time-step size, setting $t_n \overset{\text{def}}{=} n\tau$ for $1 \leq n \leq N$. For a given initial condition $\mathbf{u}^0 = \mathbf{u}_0$, the time iteration consists of solving the two problems:

1. Velocity step:

$$\begin{cases} \rho\dfrac{\hat{\mathbf{u}}^{n+1} - \hat{\mathbf{u}}^n}{\tau} + \rho\hat{\mathbf{u}}^n \cdot \boldsymbol{\nabla}\hat{\mathbf{u}}^{n+1} - 2\mu\boldsymbol{\nabla}\cdot\boldsymbol{\epsilon}(\hat{\mathbf{u}}^{n+1}) + \nabla\hat{p}^n = \mathbf{0} & \text{in} \quad \widehat{\Omega}, \\ \hat{\mathbf{u}}^n = \mathbf{u}_{\mathrm{in}}(t_{n+1}) & \text{on} \quad \Sigma_{\mathrm{in}}, \\ 2\mu\epsilon(\hat{\mathbf{u}}^{n+1})\mathbf{n} = \mathbf{0} & \text{on} \quad \Sigma_{\mathrm{out}}, \\ \hat{\mathbf{u}}^n = \mathbf{0} & \text{on} \quad \Sigma_{\mathrm{wall}}. \end{cases} \tag{8.5}$$

2. Pressure-Poisson projection step:

$$\begin{cases} -\dfrac{\tau}{\rho}\Delta\hat{p}^{n+1} = -\boldsymbol{\nabla}\cdot\hat{\mathbf{u}}^{n+1} & \text{in} \quad \widehat{\Omega}, \\ \dfrac{\tau}{\rho}\dfrac{\partial\hat{p}^{n+1}}{\partial\mathbf{n}} = 0 & \text{on} \quad \Sigma_{\mathrm{in}} \cup \Sigma_{\mathrm{wall}}, \\ \hat{p}^{n+1} = p_{\mathrm{out}}^{n+1} & \text{on} \quad \Sigma_{\mathrm{out}}. \end{cases} \tag{8.6}$$

The 3D-0D coupling on the outlet boundary condition is treated in a implicit fashion (see [Bertoglio et al., 2013]). The discretization in space of problems (8.5)-(8.6) is performed via continuous piecewise affine finite elements. We denote by $\boldsymbol{V}_h$ and Q_h the corresponding finite element spaces for the velocity and the pressure, respectively.

Proper orthogonal decomposition on the reference geometry

A proper orthogonal decomposition (POD) of a numerical solution (that is $\{\hat{\mathbf{u}}_h^n\}_{i=1}^N$ and $\{\hat{p}_h^n\}_{n=1}^N$ or, in general, of a given set of data, see [Bergmann et al., 2009; Rathinam and Petzold, 2004] for instance), consists of finding a set of basis functions (orthogonal w.r.t. a given scalar product) which, even containing a small number of elements, can represent sufficiently well the numerical solution. This approach, besides reducing the data size without losing relevant information, allows to perform faster numerical simulations, by restricting the space of the solution to the subspace generated by the POD basis functions.

Starting from a full CFD simulation on the reference geometry, we computed two POD bases for velocity and for pressure, denoted by $\hat{\boldsymbol{\Phi}} = \{\hat{\boldsymbol{\varphi}}_i\}_{i=1}^{M_{\mathbf{u}}}$ and $\hat{\Psi} = \{\hat{\psi}_i\}_{i=1}^{M_p}$ respectively.

Note that with $\hat{\boldsymbol{\varphi}}_i : \widehat{\Omega} \to \mathbb{R}^3$ and $\hat{\Psi}_i : \widehat{\Omega} \to \mathbb{R}$, these basis functions are given in terms of their natural decomposition on the finite element basis of $\boldsymbol{V}_h$ and Q_h, respectively. Note that in practice we have $M_{\mathbf{u}} \ll \dim(\boldsymbol{V}_h)$ and $M_p \ll \dim(Q_h)$. Hence, the main idea of model reduction is to perform the spatial approximation of (8.5) and (8.6) on the lower dimensional spaces spanned by $\hat{\boldsymbol{\Phi}}$ and $\hat{\Psi}$, respectively.

For instance, using the velocity POD basis $\hat{\mathbf{\Phi}}$, instead of the original finite element basis of $\boldsymbol{V}_h$, the discrete problem (8.5) can be formulated in terms of the reduced solution

$$\tilde{\mathbf{u}}(\mathbf{x},t) = \sum_{i=1}^{M_{\mathbf{u}}} \alpha_i(t)\hat{\boldsymbol{\varphi}}_i(\mathbf{x}), \tag{8.7}$$

requiring, at each time step, the solution of a linear system of reduced size $M_{\mathbf{u}} \times M_{\mathbf{u}}$.

8.3.2 Reduced order blood flow simulation on individual patients

To obtain the POD basis functions for pressure and velocity on the reference geometry we performed a full CFD simulation. The key idea of our method is to map these *reference* basis functions onto individual patient meshes, in order to obtain reduced bases without the need of full individual simulations.

The procedure is summarized in Algorithm 6. Firstly, we use the atlas geometry as a *reference* domain, introducing geometrical mappings from each 3D-patient mesh onto the atlas geometry (*3D-shape registration*, section 8.3.2). Next, we use these mappings to transport the template POD basis onto each individual domain (section 8.3.2). Finally, this allows us to perform the POD reduction of the FE formulation for the patient-specific problem (section 8.3.2).

3D-shape registration

The first step towards the construction of individual POD bases is the computation of a map between the reference and each individual mesh. In particular, let $\hat{\Omega}$ and Ω denote the spatial domain of the reference and patient geometries, respectively, and let us consider the discretized representations of $\hat{\Omega}$ and Ω, defined by two tetrahedral meshes $\hat{\mathcal{T}}_h$ and $\mathcal{T}_h$. We aim to compute a map

$$\mathcal{A} : \hat{\Omega} \to \Omega \tag{8.8}$$

which maps $\hat{\mathcal{T}}_h$ onto $\mathcal{T}_h$ preserving the mesh topology. In particular, $\mathcal{A}$ defines a one-to-one correspondence between the nodes of the two meshes. In the following, $\mathcal{A}$ will be called a *3D-shape registration*.

To construct $\mathcal{A}$, we start from the *surface diffeomorphism* (introduced in section 8.2.2)

$$\phi : \widehat{S} \to S$$

which maps the atlas surface $\hat{S}$, i.e. the boundary of the reference domain, onto an approximation of the patient surface S. Since, in the discrete formulation, $\hat{S}$ and S are represented by triangular surface meshes, the diffeomorphism ϕ is a piecewise linear deformation defined on the whole surface. Let us denote this deformation as a displacement field $\mathbf{d}_s : \partial\widehat{\Omega} \to \mathbb{R}^3$ such that

$$\partial\Omega = \partial\widehat{\Omega} + \mathbf{d}_s(\partial\widehat{\Omega})\,.$$

The 3D registration $\mathcal{A}$ will be defined as an extension of the field $\mathbf{d}_s$ onto the three-dimensional domain with a suitable *volume* deformation field

$$\mathbf{d}_v : \hat{\Omega} \to \mathbb{R}^3\,, \tag{8.9}$$

compatible with the surface displacement $\mathbf{d}_s$ on the boundary. In particular, once $\mathbf{d}_v$ is computed, we can define the deformation as

$$\mathcal{A}(\hat{\mathbf{x}}) = \hat{\mathbf{x}} + \mathbf{d}_v(\hat{\mathbf{x}})\,, \text{for } \hat{\mathbf{x}} \in \hat{\Omega}. \tag{8.10}$$

There are different choices available for the computation of the extension $\mathbf{d}_v$. For instance, one could take the harmonic extension of $\mathbf{d}_s$ into $\widehat{\Omega}$. However, since the displacement field $\mathbf{d}_v$ will be used to deform the computational mesh, this simple extension could yield poor quality meshes, especially if the surface deformation is large.

Instead, we decomposed the boundary deformation $\mathbf{d}_s$ in K sub-steps and computed the extension $\mathbf{d}_v$, by solving a sequence of harmonic problems, for $k = 0, \ldots, K-1$

$$\begin{aligned} \Delta \mathbf{d}_v^{k+1} &= 0, \quad \text{in } \widehat{\Omega}^k \\ \mathbf{d}_v^{k+1} &= \frac{k+1}{K}\mathbf{d}_s, \text{ on } \partial\widehat{\Omega}^k \,, \end{aligned} \tag{8.11}$$

considering at each step a new computational domain, defined by $\widehat{\Omega}^{k+1} = \widehat{\Omega}^k + \mathbf{d}^k$.

This procedure corresponds to a non-linear extension of the surface displacement, obtained by solving a sequence of linear problems (8.11). In particular, it allows the size of the boundary deformation imposed at each sub-step to be controlled by the value of K. This iterative approach could be replaced by other non-linear extensions of the surface displacement, e.g. considering the volume mesh as a hyperelastic material, which might be more robust in the case of very large deformations (see a stricking example in Cairncross et al. [2000], p. 382). Notice that each solution of (8.11) on the reference mesh $\hat{\mathcal{T}}_h$ automatically yields a deformation which preserves the topology of the reference mesh, i.e. such that the nodes of the $\hat{\mathcal{T}}_h$ are mapped onto the nodes of the individual volume mesh $\mathcal{T}_h$.

Transporting the reference POD basis

The map constructed in section 8.3.2 provides a coordinate change between reference and individual domains. This will now be used to compute *individual POD bases* for pressure and velocity on the patient geometries, starting from the reference reduced basis.

An individual POD basis for the pressure Ψ can be obtained from the reference POD basis $\hat{\Psi}_i$ through a coordinate change, namely,

$$\psi_i(\mathbf{x}) \stackrel{\text{def}}{=} \hat{\psi}_i(\hat{\mathbf{x}}), \quad \hat{\mathbf{x}} = \mathcal{A}^{-1}(\mathbf{x}) \tag{8.12}$$

for all $i = 1, \ldots, M_p$.

To construct an individual POD basis for the velocity field on a given patient, one has to explicitly take into account the deformation of the domain, in order to preserve the properties of the vector field. To do this, we consider the *inverse Piola transform* of the basis elements of $\hat{\mathbf{\Phi}}$, given by

$$\boldsymbol{\varphi}_i(\mathbf{x}) = \boldsymbol{P}(\hat{\boldsymbol{\varphi}}_i)(\mathbf{x}) \stackrel{\text{def}}{=} \frac{1}{J(\hat{\mathbf{x}})}\mathbf{F}(\hat{\mathbf{x}})\hat{\boldsymbol{\varphi}}_i(\hat{\mathbf{x}}), \quad \hat{\mathbf{x}} = \mathcal{A}^{-1}(\mathbf{x}) \tag{8.13}$$

for $i = 1, \ldots, M_{\mathbf{u}}$. Here, $\mathbf{F}(\hat{\mathbf{x}})$ stands for the deformation gradient, i.e., $\mathbf{F}(\hat{\mathbf{x}}) \stackrel{\text{def}}{=} \nabla\mathcal{A}(\hat{\mathbf{x}})$, and $J(\hat{\mathbf{x}}) = \det \mathbf{F}(\hat{\mathbf{x}})$ is the jacobian of $\mathbf{F}$. From the properties of the Piola transform (see, e.g., [Ciarlet, 1988]), we can infer that

$$J(\hat{\mathbf{x}})\text{div}_{\mathbf{x}}\boldsymbol{\varphi}_i(\mathbf{x}) = \text{div}_{\hat{\mathbf{x}}}\hat{\boldsymbol{\varphi}}_i(\hat{\mathbf{x}}). \tag{8.14}$$

Hence, if the POD basis is divergence free in the reference geometry then the transformed basis has the same property in the individual geometry. Note that a similar transform was used in Løvgren et al. [2007] in a different context.

Considering the shape registration in the form (8.10), we approximate the gradient

$$F(\hat{\mathbf{x}}) = \mathbf{I} + \nabla\mathbf{d}_v(\hat{\mathbf{x}}) \,, \tag{8.15}$$

by its L^2-projection on the piecewise linear finite element space. In practice, this is done by solving a linear system associated with the *mass matrix*, whose entries are given by $\hat{M}_{ij} = \int_{\widehat{\Omega}} \hat{\mathbf{v}}_i\hat{\mathbf{v}}_j \, d\widehat{\Omega}$, $\hat{\mathbf{v}}_i$ and $\hat{\mathbf{v}}_j$ being basis functions of the finite element space in $\hat{\Omega}$.

Reduced simulation

With a little abuse of notation, let us denote with $\Phi = (\boldsymbol{\varphi}_1|\ldots|\boldsymbol{\varphi}_{M_{\mathbf{u}}})$ an individual POD basis in matrix form, where each column contains a basis element, obtained with the procedure described in Sections 8.3.2-8.3.2.

At each time step t_n, let us call A^n and $\mathbf{f}^n$ the matrix and the right-hand side of the linear system associated to the finite element approximation of problem (8.5) in the patient geometry. The reduced model is given by

$$(\Phi^T A^n \Phi)\,\widetilde{\mathbf{U}} = \Phi^T \mathbf{f}^n, \tag{8.16}$$

where $\widetilde{\mathbf{U}} = \{\alpha_1 \dots \alpha_{M_\mathbf{u}}\}^T$ defines the reduced numerical solution (8.7). Analogously, the reduced system for the pressure-problem (8.6) is built by considering the transported pressure basis $\Psi = (\psi_1 | \dots | \psi_{M_p})$.

Algorithm 6 Individual reduced order simulations

1: **Given:** Individual surface S_i and reference POD bases ($\hat{\mathbf{\Phi}}$, $\hat{\Psi}$)
2: Compute volume deformation $\mathcal{A}_i$ from the surface diffeomorphism ϕ_i
3: Compute patient-specific deformation gradient $\mathbf{F}_i$
4: Compute POD bases (from (8.13) and (8.12))
5: Assemble FE formulations and reduce the linear systems (e.g., (8.16) for the velocity)
6: **return** Reduced order solution

8.4 Numerical experiments on the pulmonary artery of repaired ToF patients

8.4.1 Data Collection

Subjects and Image Preparation A data-set of 17 adults with repaired tetralogy of Fallot was used in this study. MRI angiography of the heart was acquired with a $1.5\,T$ scanner (Signa excite, GE Medical Systems) with isotropic in-plane resolution $0.703\,mm \times 0.703\,mm$ and $1\,mm$ thick slices.

Image segmentation of the pulmonary artery In order to extract the surfaces of the pulmonary artery, a user-guided 3D image segmentation tool was applied to delineate the boundaries of the artery. Using this tool, a small number of control points (less than 100) are added by the user to define the inside, outside, and border of the region. With these control points as a guide, a 3D mesh is constructed by an implicit variational surfaces approach. The tool is included within the CardioViz3D software package available for download[1], see [Mansi, 2010] for further details. This tool was applied to each of the patient images to define the artery for at least $3cm$ of the inflow before the bifurcation and at least $2cm$ of each outflow branch after the bifurcation (see Fig. 8.3). The variable branch length in the final geometries resulted from the variability of the images used, so in the case when it was possible to include more than $2cm$ of the outflow, this was included. In particular, images with little image information at the outflow branches resulted in a shorter segmentation.

8.4.2 Statistical shape model of the pulmonary arteries

The obtained meshes were used to compute a centered atlas as a reference for the population (see Fig. 8.4 and 8.5). The atlas construction pipeline described in Sec. 8.2 requires two parameters to be set to control the 'stiffness' of the non-linear deformations. First, σ_V, the standard deviation of the LDDMM Gaussian kernel K_V, which can be seen as the typical distance of coherence of the deformation (higher values give more global transformations, such as rigid body transformations). Second, a parameter σ_W (the standard deviation of the currents Gaussian kernel K_W), that characterizes the resolution of the currents representation, to control how finer deformations are treated as either noise or shape features. Since we were mainly interested in the regional ToF alterations related to dilation, valve enlargement, and regional bulging, these parameters were set to $\sigma_W = 30\,mm$, $\sigma_V = 5\,mm$ for the atlas. With the algorithm described in Sec. 8.2, an atlas was constructed by 4

[1] *http://www-sop.inria.fr/asclepios/software/CardioViz3D/*

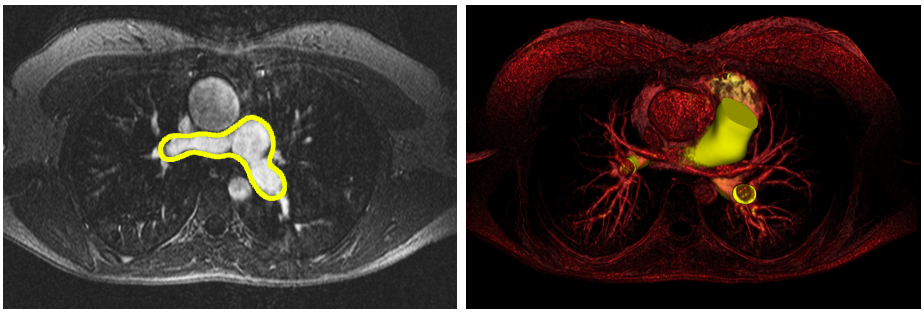

Figure 8.3: Left: 2D slice of one patient with the segmented outline in yellow. Right: 3D rendering of the same patient with the 3D mesh overlaid (in yellow).

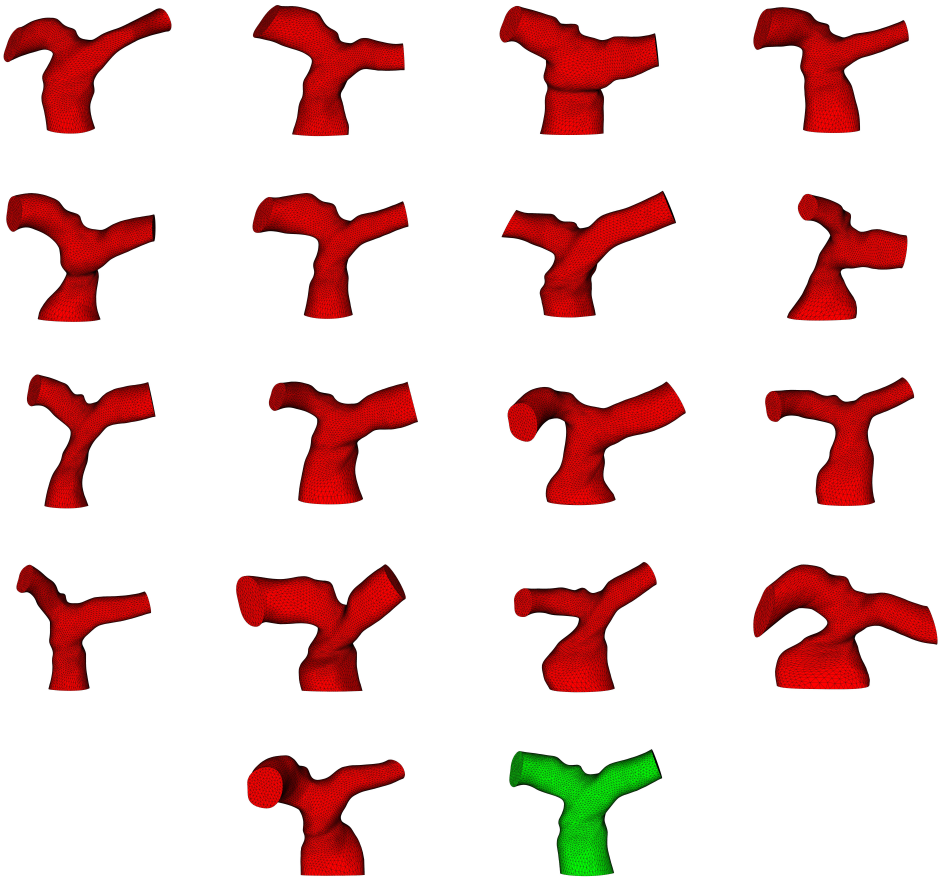

Figure 8.4: The 17 patient meshes (red) and associated atlas mesh (green).

iterations of the alternate minimization (the number of iterations needed to reach the convergence criteria). This was sufficient to give a well-centered geometry in which to apply the atlas refinement pipeline described in algorithm 8.2.4.

Un-biased validation of the atlas To test how biased the atlas is to the population used to create it, we performed a *leave-one-out* validation by creating 17 atlases using 16 patients each. The resulting atlases are shown overlaid on one another in Fig. 8.6. Though there is a large shape variability observed in the population, there is little difference between each of the computed atlases.

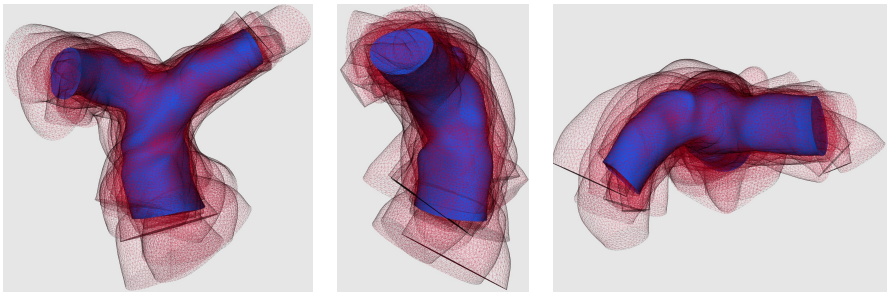

Figure 8.5: Front view (left), side view (center) and top view (right) of the atlas (blue) and the 17 meshes used to create the atlas (wire-frame red). Though there is a wide shape variability in the population, the atlas is well-centered.

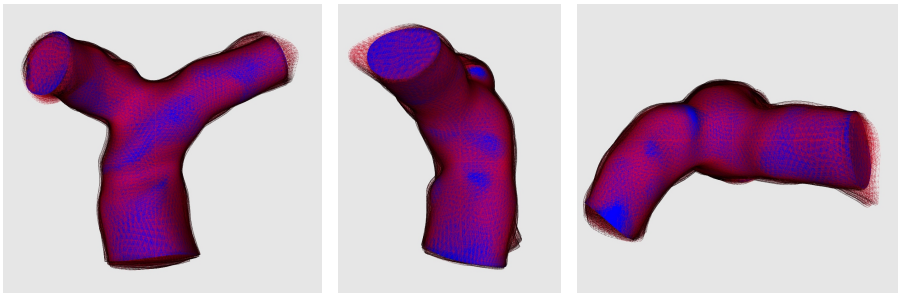

Figure 8.6: Front view (left), side view (center) and top view (right) of the atlas created on all the patients (blue) and the 17 atlases created on 16 patients (wire-frame red). There is little difference between the atlases, even given the high variability of shape in the population, which displays the un-biased property of the atlas construction step.

8.4.3 Patient-specific full and reduced order CFD simulations

For the full CFD simulations on the individual geometries, rather than the original patient meshes, we used the geometries obtained by mapping the atlas to each patient via the deformation computed in the 3D-shape registration step (described in Sec. 8.3.2). Note that this results in a discrepancy between the original meshes and the atlas-to-patient deformed meshes, since we allow for some noise in the atlas construction step. However, due to the fact that the atlas is well-centered, these differences are small. The simulation approach described in Sec. 8.3 was applied for normal (functioning valve case) and pathological (regurgitant or absent valve) regimes. The aim was to investigate how such a reduced approach performs for both hemodynamic conditions. For each regime, a full simulation was performed on the atlas, extracting a POD basis containing 30 modes. Then, for each of the individuals, a reduced order simulation was performed with this transported POD and the hemodynamic boundary conditions of that regime. Subsequently, for both regimes, the PODs built under *rest* conditions were tested under *exercise* conditions. Furthermore, the robustness of the method was assessed by investigating if the POD constructed for the reference pathological condition was able to capture other pathological conditions.

To assess the reduced order method, we simulated the flow in the different geometries both with a full FE model and with the reduced POD basis as described in Sec. 8.3. For each simulation, we monitored four different errors in time indicating the global errors in velocity, pressure, outlet flows through the two branches and the pressure drop between the right ventricle and the two outlets. The last two are particularly interesting from the clinical point of view, while the first two aid in assessing the accuracy of the reduced flow simulation:

- Instantaneous L^2-norm difference in velocity and pressure, adimensionalized by the maximum

L^2-norm in time:

$$E_{\mathbf{u}} = \frac{\|\mathbf{u}_{\text{reduced}} - \mathbf{u}_{\text{full}}\|_{L^2}}{\max\left(\|\mathbf{u}_{\text{full}}\|_{L^2}\right)} \quad \text{and} \quad E_p = \frac{\|p_{\text{reduced}} - p_{\text{full}}\|_{L^2}}{\max\left(\|p_{\text{full}}\|_{L^2}\right)} \tag{8.17}$$

- Instantaneous pressure drop (difference between averaged over the surface inlet and outlet pressures), adimensionalized by the maximum value in time:

$$E_{\Delta p} = \max_{i=1,2}\left(\frac{\| \left(p_{\text{in}} - p^i_{\text{out}}\right)_{\text{reduced}} - \left(p_{\text{in}} - p^i_{\text{out}}\right)_{\text{full}} \|}{\max\left(p_{\text{in}} - p^i_{\text{out}}\right)_{\text{full}}}\right) \tag{8.18}$$

- Instantaneous outlet flow error, adimensionalized by the maximum value in time:

$$E_q = \max_{i=1,2}\left(\frac{\|q^i_{\text{out reduced}} - q^i_{\text{out full}}\|}{\max \|q^i_{\text{out full}}\|}\right), \text{ with } q^i_{\text{out}} = \int_{\Gamma_i} \mathbf{u}\cdot\mathbf{n}\,. \tag{8.19}$$

Renormalizing the error w.r.t. the instantaneous norm actually leads to large and less informative relative errors when the norms of velocity and pressure are close to zero. It is more relevant from a practical point of view to have an idea of the error with respect to a fixed meaningful quantity. Thus the absolute errors are normalized w.r.t a constant factor which allows e.g. to compare the situation on different patients and with different boundary conditions, when peak flows and pressures might differ.

POD validation: simulations on the reference geometry

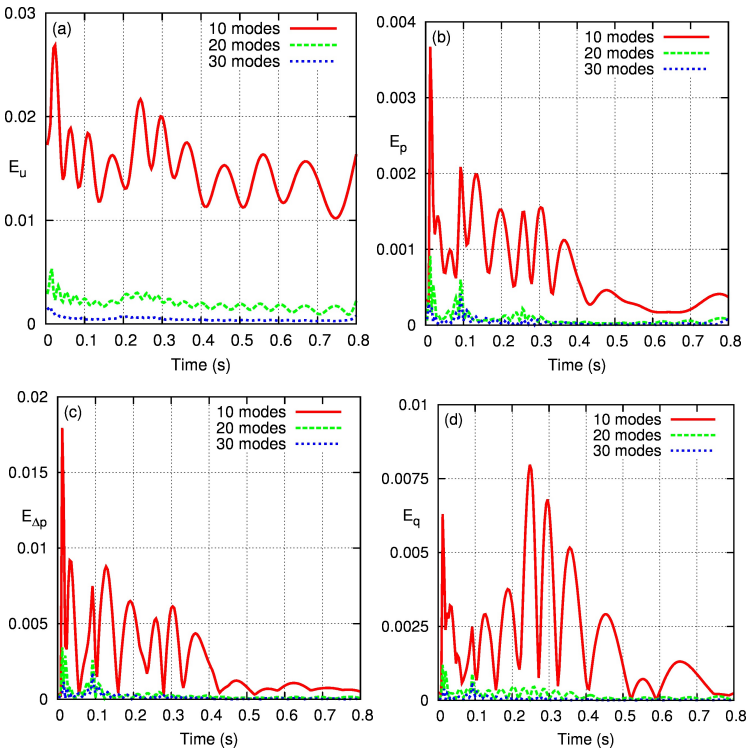

Figure 8.7: Comparison between full and reduced simulations on the reference geometry for (a) velocity, (b) pressure, (c) presure drop and (d) outlet flow, following (8.17)-(8.19) and variying the numbers of POD modes retained for reduced simulations.

As a preliminary validation, we tested the capability of the POD basis to solve the problem on the reference geometry only (*e.g.* without transporting the basis), using the inlet flow conditions depicted in figure 8.8 and the 0D-Windkessel model defined in table 8.1. Figure 8.7 shows the errors

in time (defined in (8.17)-(8.19)) using POD bases with increasing numbers of modes for the reduced simulation. We obtained a very satisfactory accuracy with the POD basis (all errors below 1%) using around 20 - 30 POD modes. In view of these results, all the simulations of this study were performed with 30 POD modes. Enriching the POD basis might yield a better approximation of the solution on the reference geometry. However, in our numerical tests, it did not reduce the errors between the full and reduced individual patient simulations, since in those cases, errors due to the transport on patient geometries were dominant.

Flow simulations in normal and pathological regimes

First, we used the pre-computed reduced models to simulate the flow in the individual geometries with different flow conditions. In particular, we distinguished between a *normal cardiac flow condition*, i.e. with very little backflow as it is the case in the pulmonary artery of a healthy pulmonary valve, and a *pathological flow condition* with 30% of backflow during diastole, the average amount of expected backflow for patients without pulmonary valves [Schwartz et al., 2011].

Note that flow curves were not available for all patients, thus the pathological flow curve corresponds to a single patient measurement, typical of such ToF physiology. The same 0D-Windkessel model was applied at both outlets, but the parameters were chosen in the simulations to obtain pressure waveforms typical of a normal pulmonary artery and right ventricle (pathological pressure in the pulmonary artery due to the absence of a valve) respectively (see table 8.1). The inlet flow profiles and the resulting outlet pressures for the atlas simulations for these two cases are depicted in Fig. 8.8 and 8.9. In particular, one can see the characteristic pressure bump at the end of diastole that is observed in the pulmonary artery, as in the right ventricle, for the pathological case. Furthermore, we investigated different degrees of pathological conditions, with 15% and 40% of backflow during diastole (see Fig. 8.9).

Remark 8.4.1 *A POD basis transported as in* (8.13) *and* (8.12) *is associated to a single patient mesh, and can be employed to reduce a simulation for this specific geometry. It should be noted that even though the solution snapshots depend on particular essential boundary conditions, the POD basis is built from the corresponding set of snapshots with homogeneous essential boundary data, which are the genuine degrees of freedom of the system. Hence it is possible to run the reduced model with different boundary conditions, such as the inlet velocity in* (8.5)*. It is also possible to vary other physical parameters, e.g. in* (8.4)*. It is therefore technically possible to use the same basis for different physiological regimes. The accuracy of the reduced model has nevertheless to be tested in those cases, which is the aim of various tests presented in this paper.*

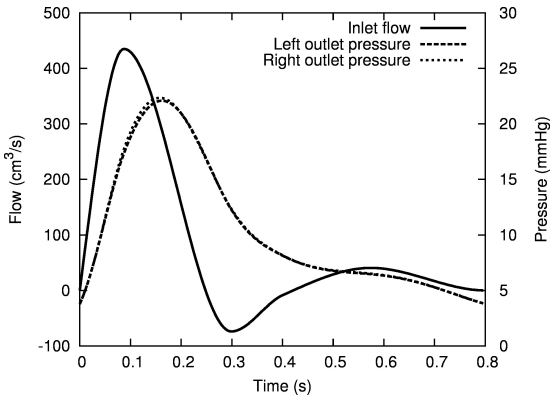

Figure 8.8: Normal boundary conditions: flow rate is prescribed at the inlet (with a mean value of $4.9\,\mathrm{L}\cdot\mathrm{min}^{-1}$) and outlet pressure for the atlas obtained the Winkessel model in Table 8.1. These outlet pressures change slightly from one geometry to another.

The errors (8.17)-(8.18) for normal flow conditions for the different patients are shown in Fig. 8.10. To provide a better picture of the error variability among patients, mean errors and standard deviations

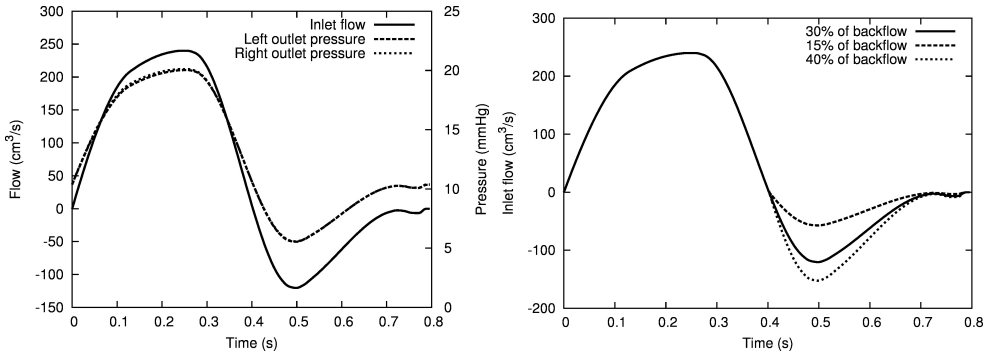

Figure 8.9: **Left.** Inlet flow (mean inlet flow rate of $3.5\,\mathrm{L}\cdot\mathrm{min}^{-1}$) and outlet pressure for the atlas under pathological boundary conditions. **Right** pathological inlet flows with different backflows. The prescribed inlet flows with 15% and 40% of backflow respectively present a mean value of 4.3 and $3.1\,\mathrm{L}\cdot\mathrm{min}^{-1}$.

$\mathrm{R_p}$ $(\mathrm{dyn}\cdot\mathrm{s}\cdot\mathrm{cm}^{-5})$	40
C $(\mathrm{cm}^5\cdot\mathrm{dyn}^{-1})$	10^{-3}
$\mathrm{R_d}$ $(\mathrm{dyn}\cdot\mathrm{s}\cdot\mathrm{cm}^{-5})$	300

$\mathrm{R_p}$ $(\mathrm{dyn}\cdot\mathrm{s}\cdot\mathrm{cm}^{-5})$	107
C $(\mathrm{cm}^5\cdot\mathrm{dyn}^{-1})$	0.32
$\mathrm{R_d}$ $(\mathrm{dyn}\cdot\mathrm{s}\cdot\mathrm{cm}^{-5})$	308

Table 8.1: RCR Windkessel model values imposed at each outlet for normal (left) and pathological inlet flow conditions (right).

are reported in Fig. 8.11. The error in velocity varies over time and among patients between 3% and 42%, with an average curve rising from 7% to 27% and then decreasing slowly down back to 7% (mean over time being 15%). Pressure errors vary over time and among patients from negligible values to 14%, typically rising quickly to its peak value and decreasing equally fast to very low values and remaining low for the rest of the cycle. The mean over time is thus 1%. Pressure loss errors follow similar pattern as the pressure, with a peak over time and among patients at 45%, and an average among patients and over time of 5%.

Fig. 8.12 shows the errors (8.17)-(8.18) for the different patients under pathological flow conditions. The corresponding mean errors and standard deviations are further reported in Fig. 8.13. We obtained an error in velocity that varies over time and among patients between 10% and 47%, with an average curve going from 18% to 30% with a double-bump waveform (mean in time being 23%). Conversely, the errors in pressure vary over time and among patients from negligible values to below 5%, also with a double-bump waveform but with a much lower second peak. The mean over time is 1%. Pressure loss errors follow a four-bump pattern, with a negligible minimum value and a peak of 40% over time and amongst patients, and an average over patients and time of 11%.

Figure 8.14 shows mean errors and standard deviations for the outlet flows (equation (8.19)) for normal and pathological inlet boundary conditions. In both cases, the mean error over all patients and over time is close to 2.5%. Notice that as the imposed inlet flows are identical for full and reduced simulations, evaluating the amount of outlet flows allows to measure indirectly the accuracy of the reduced calculations regarding the flow split between the two branches.

To better visualize the underlying differences of the 3D fields, velocity magnitude 3D-cuts of the full and the reduced simulations are presented for two representative patients under normal and pathological conditions respectively, at different times in the cardiac cycle. In Fig. 8.15, one can see that the main features of velocity magnitude are well captured in the reduced simulation with respect to the full simulation for patient 7 under normal conditions. There are larger differences during deceleration (2nd row), in coherence with the profile of the L^2-error (Fig. 8.10). Fig. 8.16 shows that the main features of velocity magnitude are also well captured in the reduced simulation with respect to the full simulation for patient 13 under pathological conditions. In accordance with the L^2-errors (Fig. 8.12), that do not vary much in time but peak at the beginning of deceleration, we

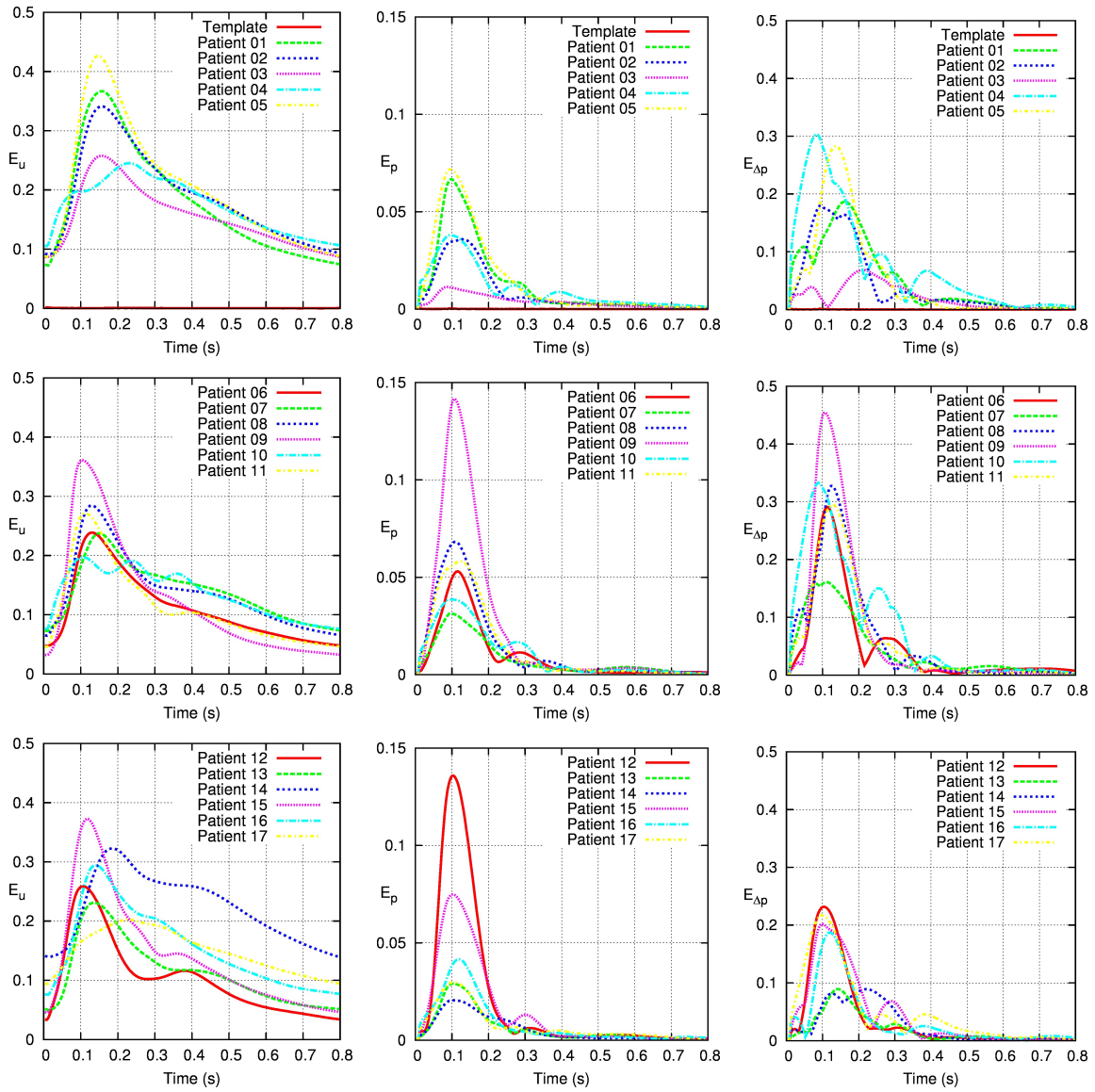

Figure 8.10: Velocity (left), pressure (center) and pressure drop (right) errors (computed according to equations (8.17)-(8.18)), between the full and the reduced order solutions for the same normal boundary conditions.

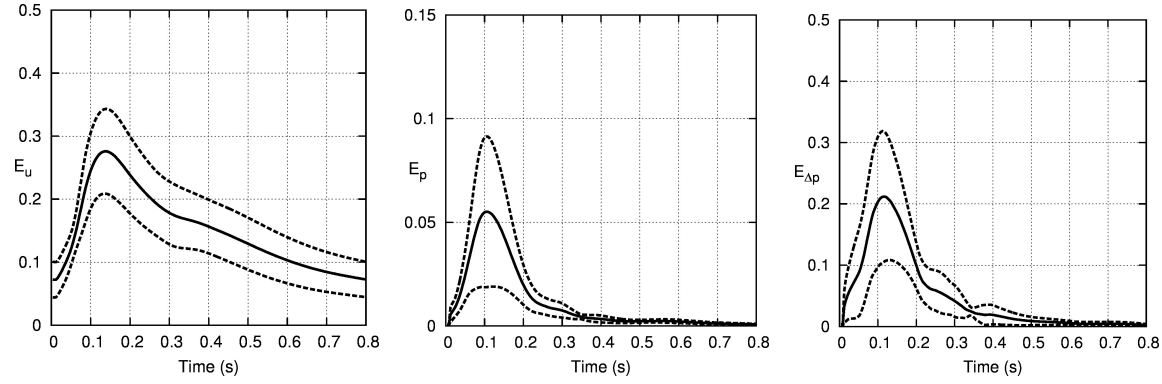

Figure 8.11: Mean (solid line) and standard deviation (dashed line) for velocity (left), pressure (center) and pressure drop (right) errors (computed according to equations (8.17)-(8.18)) between the full and the reduced order solutions with the same normal boundary conditions.

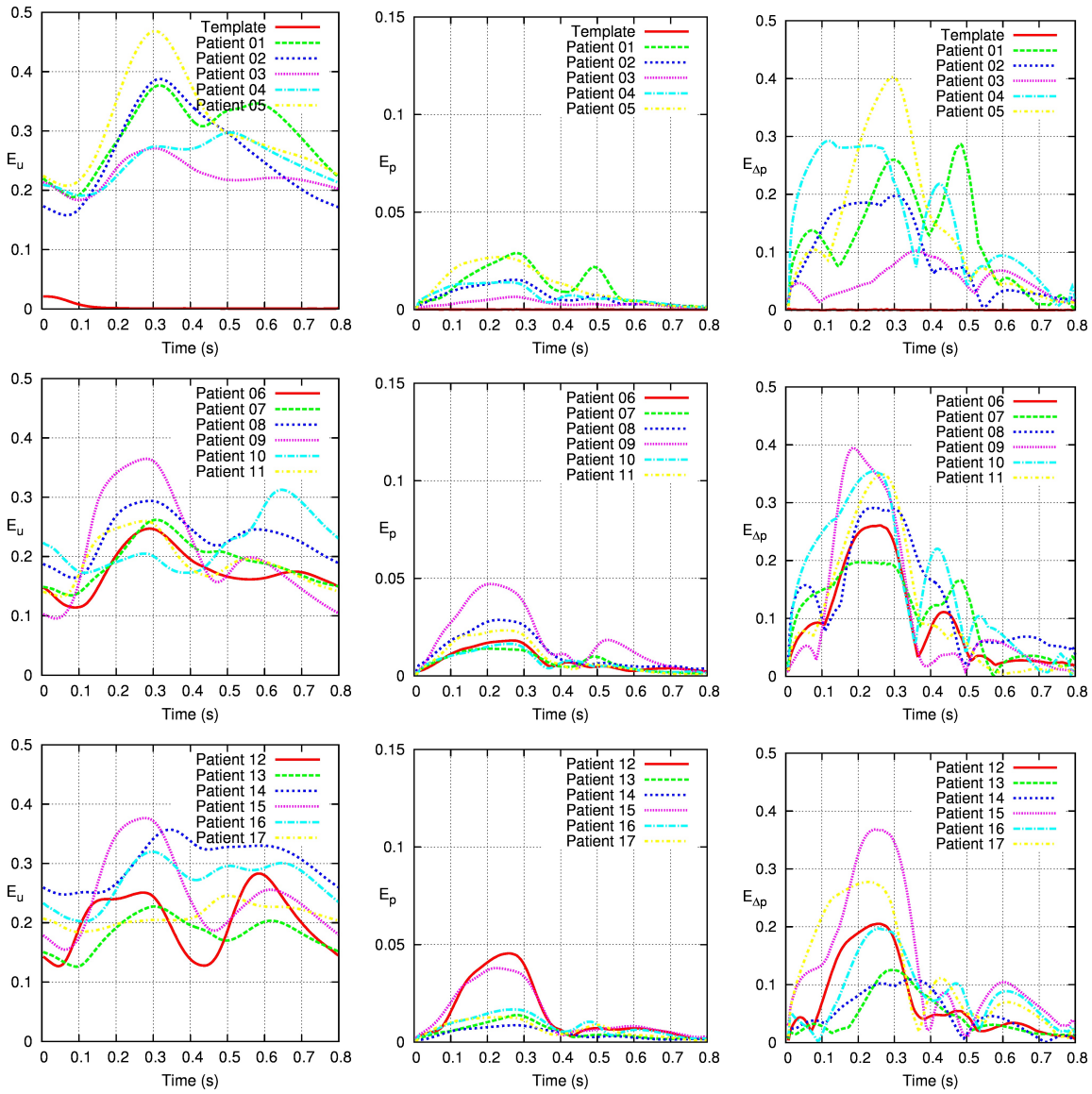

Figure 8.12: Velocity (left), pressure (center) and pressure drop (right) errors (computed according to equations (8.17)-(8.18)) between the full and the reduced order solutions for the same pathological boundary conditions.

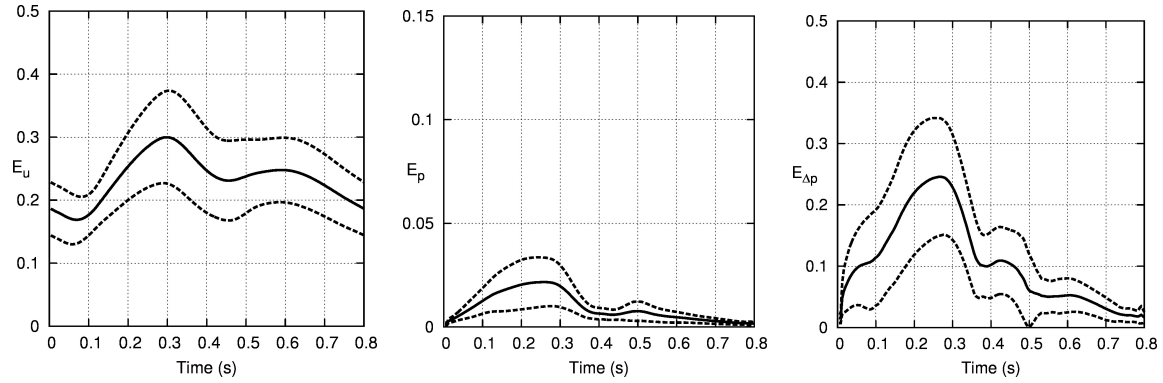

Figure 8.13: Mean (solid line) and standard deviation (dashed line) for velocity (left), pressure (center) and pressure drop (right) errors (computed according to equations (8.17)-(8.18)) between the full and the reduced order solutions for the same pathological boundary conditions.

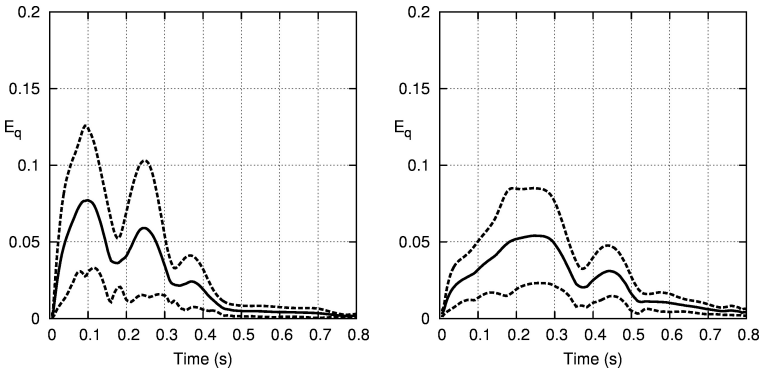

Figure 8.14: Mean (solid line) and standard deviation (dashed line) for outlet flow (computed according to equation (8.19)) between the full and the reduced order solutions under (left) normal and (right) pathological boundary conditions.

observe the highest difference during the beginning of the deceleration (2nd row), although the four snapshots all show differences. For both normal and pathological flows, flow jets through the main pulmonary artery during peak systole, and presents complex structures in the pulmonary arteries at peak backflow and subsequent diastole.

Simulations during exercise based on the resting conditions POD

The inlet boundary conditions for the reduced simulations (step 5 of Algorithm 6) were modified to simulate normal and pathological conditions under exercise regimes, increasing heart rate and systolic flows (Fig. 8.17).

The resulting average flow rates are $7.5\,\mathrm{L}\cdot\mathrm{min}^{-1}$ in the normal case and $6.2\,\mathrm{L}\cdot\mathrm{min}^{-1}$ with 20% backflow in the pathological case. For the reduced simulations, we used the reference POD basis computed in normal conditions, thus without performing an additional full computation on the reference geometry with the new boundary conditions. Fig. 8.18 summarizes the results for the different patients. The error in velocity on average rises from 7% to 30% and then decreases slowly back to 7%. Pressure errors vary over time on average from negligible values to 7.5%, typically rising rapidly to its peak value and decreasing equally quickly to very low values and remaining low for around 60% of the cycle. Pressure loss errors follow similar pattern as the pressure, with a peak at 25%. Overall, the mean and standard deviation time variations and average are very similar to the resting conditions. Figure 8.19 displays the results of the exercise reduced simulations for pathological conditions. As in the normal case, we used the POD basis computed on the atlas under rest conditions (see Remark 8.4.1). In this case, the error in velocity on average rises from 14% to 32%, then decreasing with a small second bump back to 14%. Pressure errors vary over time from negligible values to 3%, remaining very low for around 60% of the cycle. Pressure loss errors follow a four-bump evolution, with a peak at 28%. Overall the mean and standard deviation time variations are similar to resting conditions, but with less pronounced secondary bumps.

Simulations of different pathological conditions based on the reference pathological POD

To further test the robustness of the POD approach, the atlas POD basis computed with 30% backflow was used as reduced basis for the flow in the different patients under other pathological conditions, considering 15% and 40% of backflow. Mean errors and standard deviation results for these pathological conditions are respectively shown in Fig. 8.20 and Fig. 8.21. During systole, the flow conditions are the same for all the pathological conditions, and there is no increase of error during that period. In fact, pressure losses even decrease for the 40% backflow case. During diastole, the 15% flow reversal case has a decrease in all errors compared to the 30% flow reversal case on which the POD was constructed. The velocity error decays at the same rate as for normal flow conditions. The averages over patients and time are 21% for velocity, 1% for pressure and 9% for pressure loss.

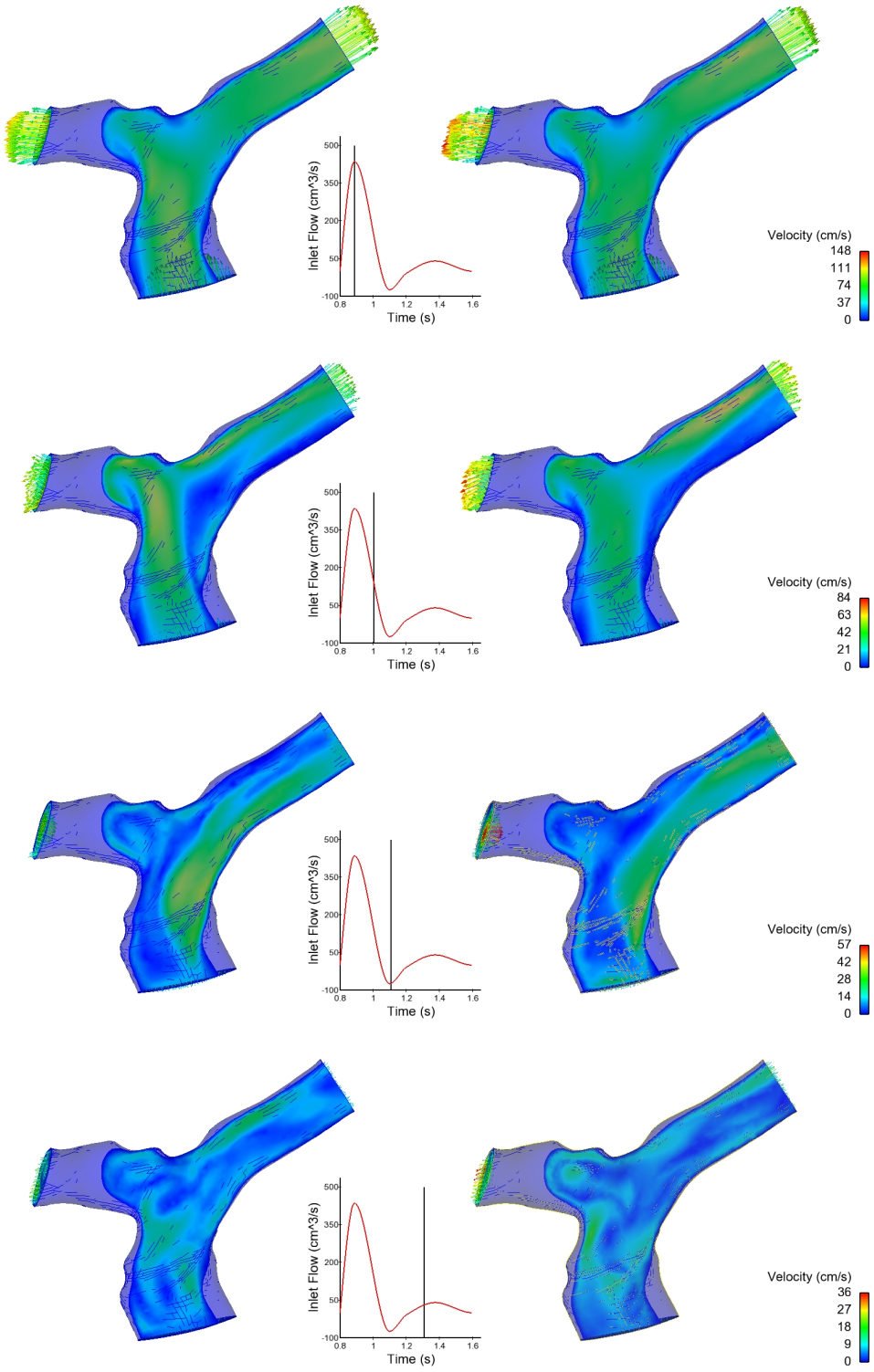

Figure 8.15: Full (left) and reduced (right) velocity fields for patient 07 under normal conditions shown at four instances along the cardiac cycle.

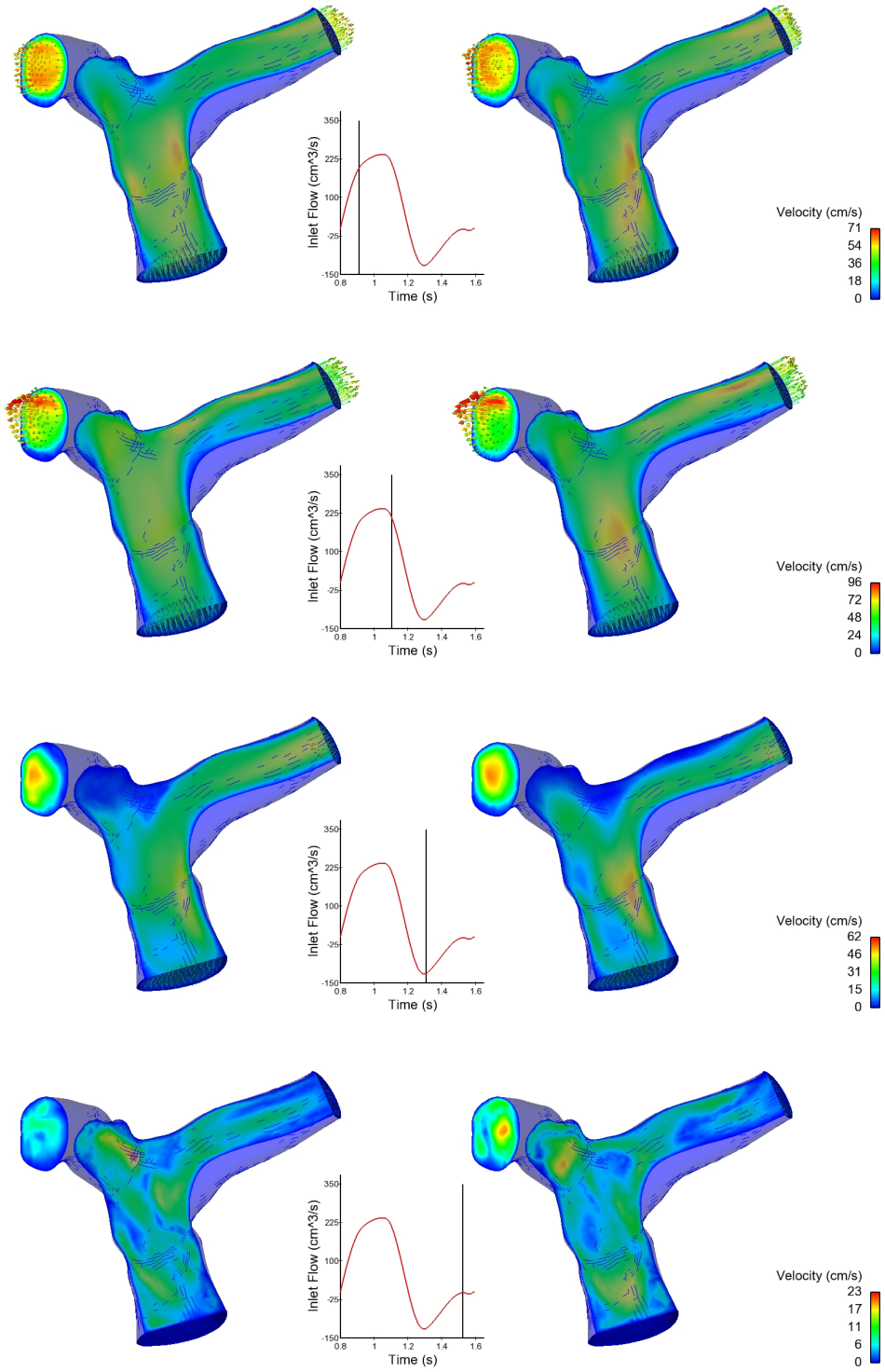

Figure 8.16: Full (left) and reduced (right) velocity fields for patient 13 under pathological conditions shown at four instances along the cardiac cycle.

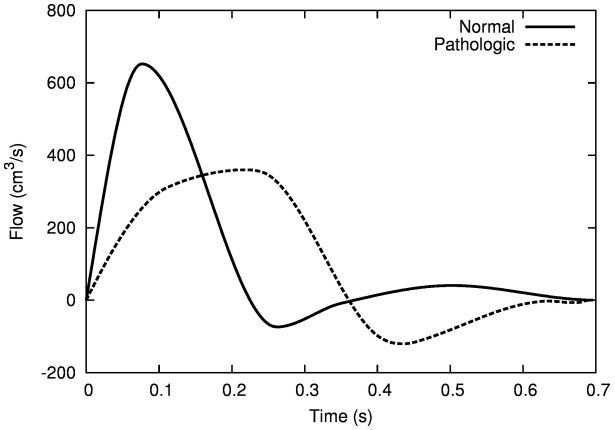

Figure 8.17: Normal and pathological inlet flows under exercise. Average flow rates are $7.5\,\mathrm{L}\cdot\mathrm{min}^{-1}$ in the normal case and $6.2\,\mathrm{L}\cdot\mathrm{min}^{-1}$ with 20% backflow in the pathological case.

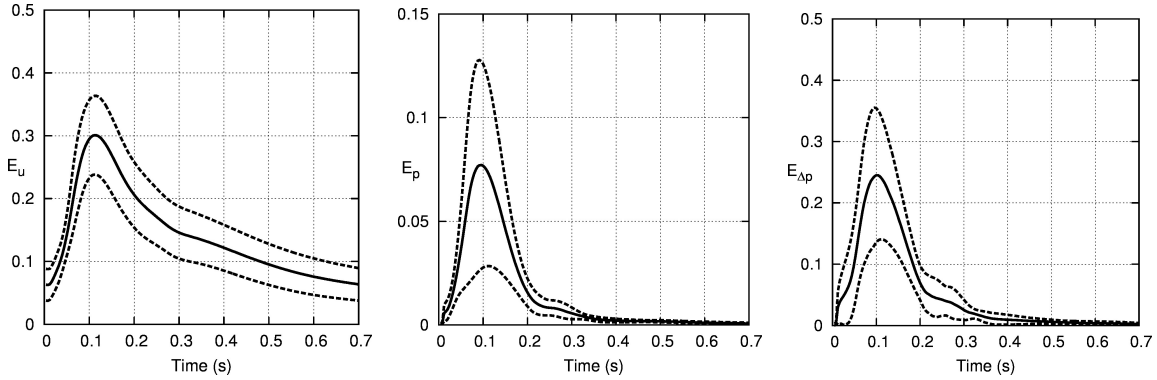

Figure 8.18: Mean (solid line) and standard deviation (dashed line) for velocity (left), pressure (center) and pressure drop (right) errors (computed according to equations (8.17)-(8.18)) between the full and the reduced order solutions under normal exercise boundary conditions (computed with the resting condition POD basis).

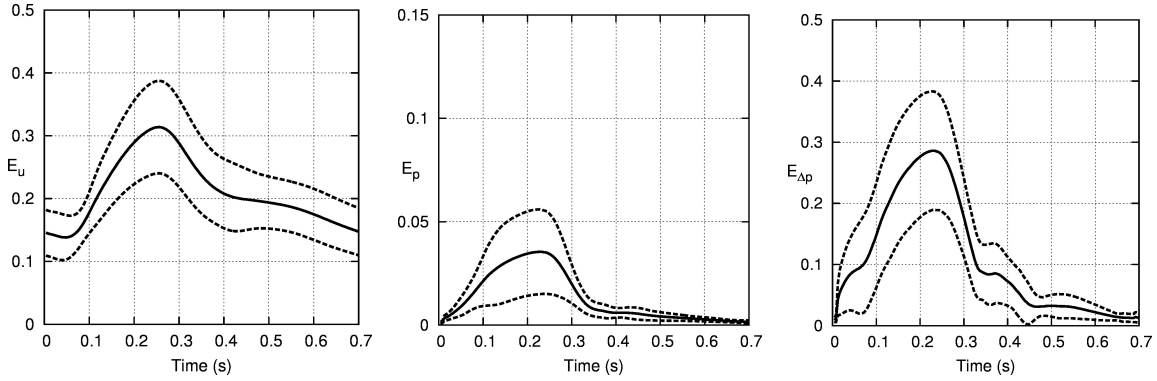

Figure 8.19: Mean (solid line) and standard deviation (dashed line) for velocity (left), pressure (center) and pressure drop (right) errors between the full and the reduced order solutions under pathological exercise boundary conditions (computed with the pathological resting conditions POD basis).

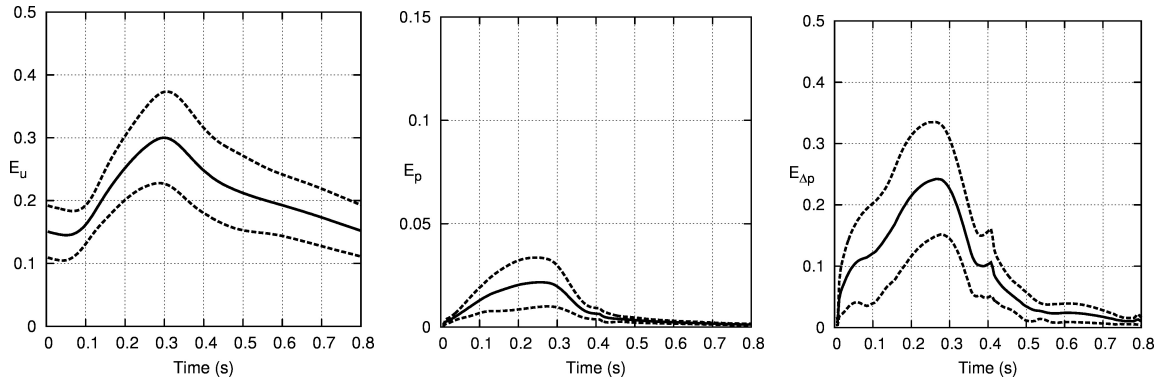

Figure 8.20: Mean (solid line) and standard deviation (dashed line) for velocity (left), pressure (center) and pressure drop (right) errors between the full and the reduced order solutions using pathological boundary conditions with 15% of backflow (using original pathological POD bases obtained with 30% of backflow).

For the higher flow reversal case (40%), there is an increase in errors (especially in velocity) after peak flow reversal. The velocity error has a second bump as high as the first one, even though in absolute value peak backflow is not as high as peak forward flow, and similarly for its derivative (re-acceleration versus deceleration). Pressure errors are, on the other hand, only slightly higher. The averages over patients and time are 26% for velocity, 1% for pressure and 10% for pressure loss.

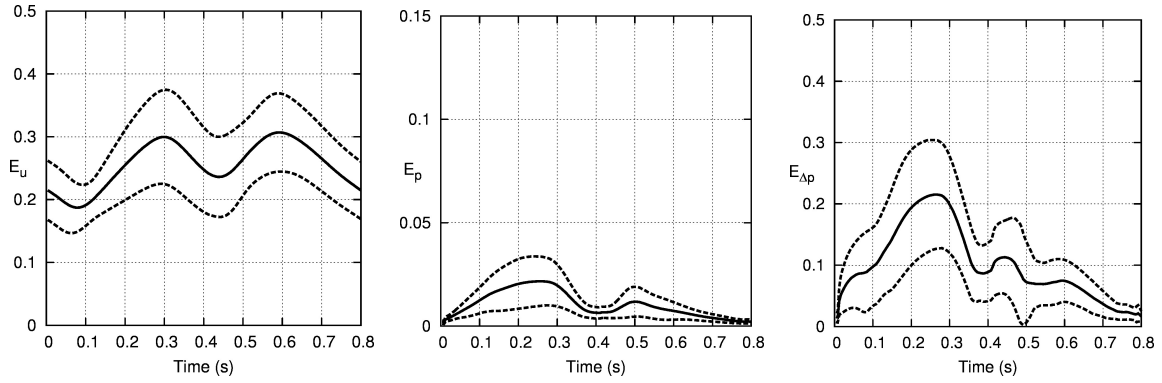

Figure 8.21: Mean (solid line) and standard deviation (dashed line) for velocity (left), pressure (center) and pressure drop (right) errors between the full and the reduced order solutions using pathological boundary conditions with 40% of backflow (using original pathological POD bases obtained with 30% of backflow).

Simulations of the flow on the original patient meshes

Since there are no experimental data to compare the reduced model results with, the simulations on the original patient meshes can be considered as the "ground truth". It is then natural to wonder what additional error is introduced by this small geometrical change between the original patient mesh and the atlas-to-patient deformed mesh (the registered patient mesh), and how it compares to the overall error, i.e. the difference between the reduced order solution computed in the sections above, and the solution on the original patient mesh. Studying these errors in detail would require to interpolate between 3D meshes of different topologies, resulting in a much harder procedure in practice, that can introduce an artificial additional error. Thus, for a restricted set of patients under normal conditions, additional simulations were run on the original patient meshes. Integrated quantities such as the pressure drop and the outflow distribution errors were computed; for such quantities a point-to-point

mesh correspondence is not needed. These preliminary results (Table 8.2) show that the error due to the change of geometry is of the same order of magnitude as the overall error and the reduced order modeling error extensively studied in the sections above.

Pressure drop	Error original *vs.* full	Error original *vs.* reduced
Patient 7	0.055	0.043
Patient 13	0.051	0.061
Outlet flow	Error original *vs.* full	Error original *vs.* reduced
Patient 7	0.032	0.040
Patient 13	0.020	0.023

Table 8.2: Average errors (instantaneous errors computed according to equations (8.18)-(8.19), averaged over one cardiac cycle) for the pressure drop and the outflow errors of two patients under normal conditions. *Original* corresponds to the full solution on the original patient mesh, *full* to the solution on the registered patient mesh, and *reduced* to the reduced order solution on the registered patient mesh.

8.5 Discussion

8.5.1 Results of reduced flow simulations

The reduced model framework has been tested with 17 tetralogy of Fallot patients to create the atlas as a centered reference geometry. Although the pipeline has been designed to simulate reduced-order blood flow on new patients, in this work we tested the method on the same patients the atlas was created from. This is justified by the fact that the atlas was shown to be unbiased (see the *leave-one-out* validation step of Fig. 8.6), and since the POD basis is computed solely on the atlas geometry, this should have a minor effect on the conclusions of the study. From a qualitative point of view, the numerical tests show that the flow dynamics can be well captured by the reduced model in both normal and pathological conditions. However, when looking at velocity magnitude maps at specific times and with their own scales, Fig. 8.15 and 8.16, differences can be more easily seen.

Normal flow conditions

Let us consider the case of blood flow simulations under normal conditions (Fig. 8.11). In this situation, the error is lowest for pressure with maximum in general below 10% (Fig. 8.10), and an average over patients and time of 1%. Higher errors were in general obtained for pressure drop. The peaks of these errors are located at the beginning of flow deceleration, where flow patterns appear to be more dependent on the geometry. However, the average over time of the mean error in pressure drop (Fig. 8.11) is 5% only. Concerning the velocity field, the error norm in time resulted between 3% and 42%, with relatively high variability among subjects (Fig. 8.10). Despite the high peaks, velocity errors stay limited for most of the cycle, and the average over time of the mean curve (Fig. 8.11) is only 15%. In general, note that the error is not proportional to flow, and, as for the pressure and pressure drop, the maximum error occurs during early deceleration. Moreover, the error does not decrease to zero when flow does, but it rather decreases when the flow approaches a steady state, and velocity is lower in the whole domain.

Pathological flow conditions

Next, we studied the performance of the reduced order model for pathological boundary conditions, employing for individual simulations a mapped POD basis computed with the same conditions on the reference geometry. In this case, the peak pressure error is twice lower than in the normal case, with a lower variability between the subjects (lower standard deviation in Fig. 8.13). But the time average

remains at 1%. Unlike the case of normal conditions, in this situation the average error follows closely the absolute flow time variation, with the highest bump occurring during high flow (or high pressure, which in this case is almost in phase with flow, see Fig. 8.9). At the same time, the error decrease is less evident than in the normal case, and the error increases again in correspondence to peak flow reversal, which is higher in this pathological condition. In contrast with the pressure field, the velocity and pressure loss errors under pathological flow conditions are larger (increase on average from 15% to 23%, and from 5% to 10% respectively), with more variability among subjects on the magnitude and timing of the error extrema (Fig. 8.10). This suggests that the multiple changes of direction in the flow accentuate geometrical differences and lead to more complex velocity patterns, more sensitive to the individual geometries.

Exercise boundary conditions

Finally, reduced simulation under exercise conditions were performed with the POD generated under rest conditions. The velocity errors are very comparable on average, with similar time variation and standard deviation as under rest, for both the normal and pathological conditions. This is quite remarkable, since flow peak increases by 50% in the normal case and even by 100% in the pathological case. Concerning pressure, peak errors in normal conditions generally increase, but remain on the order of 10%, while errors in pressure drop increase slightly. These trends are more pronounced for the pathological regime, with less effect of flow reversal compared to the rest condition, coherent with the fact that there is less backflow under the exercise condition. On average over time however, pressure and pressure drop errors do not change and thus remain low for both conditions.

8.5.2 Limitations and perspectives

The present study shows that the atlas-based reduced order model is able to capture the main hemodynamic features of the flow for a reasonable range of boundary conditions (e.g., rest versus exercise conditions, different degrees of pathologies).

In particular, results point out the capability of the reduced order method to approximate the pressure fields in different geometries (the time average errors are 1% for pressure and 5-10% for pressure losses). In fact, since pressure represents the main component of the fluid force, this feature could be applied to perform efficient numerical studies of medical device design and stability under varying flow conditions, considering different configurations as deformations of a reference domain.

POD for different flow regimes

Nevertheless, the study of different inlet boundary conditions underlines the sensitivity of the errors to the flow regime (average errors, timings of peak errors), suggesting the importance of using a reference POD basis computed under the same regime (normal or pathological conditions respectively). Within a regime however, the POD generated for rest boundary conditions yielded satisfactory results also in the case of exercise conditions. Similarly, a POD generated in a pathological case successfully simulated other degrees of pathology. The importance of the POD basis flow regime has been confirmed by further numerical studies (results not shown), which demonstrated that the POD basis computed with normal boundary conditions does not approximate well the fluid dynamics under pathological conditions. Moreover, we observed that a POD basis combining snapshots of both normal and pathological simulations did not yield any gain (nor loss) in the accuracy (results not shown) of the simulation in the pathological regime.

Relevance of geometry variability

Another important observation concerns the increase of the error among patients for velocity compared to pressure, especially under complex flow conditions. This for now precludes the use of the method if detailed hemodynamics quantities are sought, such as wall shear stress. In addition, since complex flow patterns are more sensitive to the domain shape, this suggests that the main contribution to the error comes from the mismatch between the atlas and individual geometries. The

influence of the variability of the geometry on the approximation properties of the POD basis remains an open issue. In particular, identifying the geometric parameters at the core of the highest errors would allow a great advance in the understanding of the flow characteristics and in the construction of better POD bases. However, identifying those that robustly describe flow disturbances is not an easy task [Bijari et al., 2012].

A key point is that the reduced order method has been tested with blood flow solutions, for different regimes, always computed on a single geometry. This surely limits the information contained in the reference POD basis, reducing the ability of the transported POD to capture the full flow dynamics on different geometries. In order to decrease the error, a possible extension of the method could consider the use of multiple atlas geometries (from different populations) and the computation of different POD bases, which could be combined when building the reduced models for the flow simulations on new patients. Ultimately, we would like to better understand the impact of the geometric features on the flow. However, to this aim, a larger number of patients is needed in order to obtain statistically significant results.

Reduced vs. full simulations

As noted earlier, the full CFD simulations on the individual geometries, used for benchmarking the POD reduced models, were based on the geometries obtained by registering the atlas to each patient (3D-shape registration, described in Section 8.3.2), i.e. the same geometries used for the reduced simulations. This results in a discrepancy between the original meshes and the atlas-to-patient deformed meshes, since we allowed for some noise in the atlas construction step. However, due to the fact that the atlas is well-centered, these differences are geometrically small. We kept separated the error due to the noise in the atlas computation procedure from the error introduced by the transported model reduction. Addressing the first error in detail would require an additional interpolation between meshes with different topologies. For a restricted set of patients, we have monitored the pressure drop and flow split errors with respect to the original geometries. These quantities can be easily compared, even on different meshes. The results have shown that the errors due to the noise in the atlas construction step are of the same order of magnitude as the errors due to the transported model reduction. Future work should confirm these results on a larger set of patients and conditions.

In fact, this question raises the more general question of validation. It would be interesting to compare the error between the reduced and full simulations, and the error between in vivo data and these CFD simulations [Arzani et al., 2012]. However, with the current measurement technologies, this remains a very challenging task (this would necessitate e.g. real-time MRI velocity information or flow rate in different locations, pressure measurements recorded at the same time with precision of 1 mmHg or less). Such comparison might be more easily done with in-vitro data [Kung et al., 2011a; Pekkan et al., 2009].

As a final remark, we observe that the main focus of the paper was to assess the proposed atlas-based reduced order modeling in terms of capability to reproduce different scenarios (e.g., from different geometries, boundary conditions), without directly discussing the issue of computational time. It is important to remind that, even when the number of degrees of freedom is drastically reduced (from about 10^5 to a few dozen in our case), the nonlinearities may compromise the reduction of computational time if they are not correctly handled. A number of works have addressed this issue, see, e.g., [Carlberg et al., 2011; Grepl et al., 2007; Baiges et al., 2012; Wang et al., 2012; Yano et al., 2012; Grinberg et al., 2009; Grinberg, 2012]. With the current implementation of our method, we observed a reduction of 20% to 30% of the CPU time with respect to the full order model. There is therefore still room for improvement, and this will be the topic of future work.

8.6 Conclusion

We presented a model order reduction approach, which combines statistical shape analysis for the computation of a reference geometry and proper orthogonal decomposition (POD). The reduced

model framework has been tested with 17 tetralogy of Fallot patients to create the atlas as a centered reference geometry. Reduced simulations were computed on these same patients. In order to apply the procedure for the reduced simulation on new patients, the framework requires simply the surface mapping between the atlas and the new geometry, in order to compute the specific reduced basis.

Numerical experiments show that the algorithm yields errors that are acceptable for applications that need to capture pressure and the main velocity features, as, e.g., in the study of medical devices. However, if velocity field or pressure loss are required with higher precision, more accurate approaches may be necessary, which take into account the geometric variability at a smaller scale. This is especially true under pathological conditions. Furthermore, our numerical simulations demonstrate that the reduced model is robust with respect to changes in boundary conditions, in particular to simulate exercise conditions from rest simulations, or different degrees of pathology.

8.A Currents representation of surfaces

The basic principle of the currents approach is to probe a surface by a set of vector fields in a space W, subset of the square integrable three-dimensional vector fields. In this way, a surface S is represented by a current, which maps any vector field ω in W to the flux of the vector through the surface:

$$C_S(\omega) = \int_S \omega(x)^t \mathbf{n}(x) d\lambda(x). \tag{8.20}$$

In (8.20), $\mathbf{n}(x)$ is the unit normal of the surface at a point x, and $d\lambda$ is the Lebesgue measure on the surface. The space W, called the *test space*, is chosen as the set of convolutions between any square integrable vector field and a smoothing kernel. Hence, W is a Reproducing Kernel Hilbert Space (RKHS). In this work we use a Gaussian kernel, which can be defined, for any points (x, y), as

$$K_W(x, y) = \exp^{\frac{-\|x-y\|^2}{\lambda_W^2}}, \tag{8.21}$$

where λ_W is the standard deviation. With this choice for the reproducing kernel, we can then control a metric in the space of currents that allows the distance between two surfaces to be efficiently computed, though other choices of kernels are possible. This space also has the important property that it is the dense span of basis vector fields of the form $\omega(x) = K_W(x, y)\beta$, for any fixed point y and fixed vector β. As a consequence, any vector field ω can be written as an infinite linear combination of the basis elements $K_W(x, y)\beta$. We can also define an inner product in W using the kernel K_W with these basis vectors as

$$\langle K_W(., x)\alpha, K_W(., y)\beta\rangle_W = \alpha^t K_W(x, y)\beta. \tag{8.22}$$

This inner product holds for any vector field $\omega(x) = K_W(x, y)\beta$ in W.

The space of currents is defined as the *dual* space of W, denoted W^*, representing the vector space of linear mappings from W to $\mathbb{R}$. Since W is a Reproducing Kernel Hilbert Space, the evaluation functionals are bounded. From the properties of W (the fact that W is densely spanned by the vector fields $\omega(x)$, and has an associated inner product) its dual space W^* is densely spanned by the dual representations of the basis vectors $\omega(x)$, called the Dirac delta currents, defined as:

$$\langle \delta_x^\alpha, \omega\rangle_W = \langle K_W(x, .)\alpha, \omega\rangle_W = \alpha^t \omega(x). \tag{8.23}$$

Given that W^* is a vector space, we can define the sum of two surfaces (represented by currents) C_{S_1} and C_{S_2} (obtained from equation (8.20)) as $(C_{S_1} + C_{S_2})(\omega) = C_{S_1}(\omega) + C_{S_2}(\omega)$. In terms of the flux, this means that the flux through the sum of two surfaces is the sum of the flux through each surface. The vector space property of scalar multiplication in this case means that we can scale a current by simply scaling the Dirac delta currents. We can also define an inner product in W^* as:

$$\left\langle \delta_x^\alpha(\omega), \delta_y^\beta(\omega)\right\rangle_{W^*} = \langle K_W(x, .)\alpha, K_W(y, .)\beta\rangle_W = \alpha^t K_W(x, y)\beta. \tag{8.24}$$

A key advantage of the currents representation is that a metric can be defined which does not assume point correspondences between surfaces. Rather than measuring the distances between points on the surface, surfaces are compared at an anatomical level. The distance between two surfaces can then be expressed as the norm of the difference between the surfaces, which is the distance between their currents:

$$\| C_{S_1} - C_{S_2} \|_{W^*} . \tag{8.25}$$

8.B LDDMM framework for inter-patient surface registration

The LDDMM framework uses a group of diffeomorphisms constructed through the integration of time-varying velocity fields, determined by the initial velocity at time $t = 0$ parameterized by moment vectors, that belong to a RKHS. This yields a diffeomorphism ϕ as well as a differentiable flow of the diffeomorphism ϕ_k for a continuous parameter k within the interval $[0, t]$. At time $k = 0$, we have the identity mapping ϕ_0. The mapping at time t gives the desired transformation ϕ_t which we require for the atlas estimation. We can then define the path at any point x as $\phi_k(x)$ that leads to the final position $\phi_t(x)$. By following the path that passes through the point x, we can compute easily operations on diffeomorphisms, such as the inverse path from point t to 0. Using this framework, we can minimize the difference between a deformed surface $\phi_t(S_1)$ and another surface S_2, therefore finding the geodesic path from $\phi_t(S_1)$ to S_2. The deformation ϕ_t is estimated by the minimisation of a weighted sum of two terms: $\varepsilon(\phi) = d^2(\phi_t(S_1, S_2)) + \lambda \int \| v_t \|^2$, the first term is the distance between surfaces (measured in the space of currents), and the second is the energy of the trajectory in the space of deformations, with $\partial\phi_t(x)/\partial t = v_t(x)$, $\phi_0(x) = x$. The $v_t(x)$ are time-varying velocity fields parameterised by the initial velocity field $v_0(x)$, which belongs to a RKHS generated by a Gaussian kernel $K_V(x, y)$.

Chapter 9

Combined Learning and Modelling Approach for Ablation

– This chapter is based on [Cabrera Lozoya, 2015]: Cabrera Lozoya, R. Radiofrequency ablation planning for cardiac arrhythmia treatment using modeling and machine learning approaches. PhD thesis, *Université Nice Sophia Antipolis*, Sept. 2015.

9.1 Introduction

Radio-frequency ablation (RFA) target identification for the treatment of life-threatening cardiac arrhythmias remains an open challenge. The complete elimination through ablation of Local Abnormal Ventricular Activities (LAVA) has been associated with a superior clinical outcome [Jaïs et al., 2012]. The generation of this abnormal electrical activities have been related to regions with the presence of surviving myocardial fibres within scar tissue.

Scar topology and tissue heterogeneity can be assessed using non-invasive imaging measures such as delayed-enhanced magnetic resonance imaging (DE-MRI). In previous works [Cabrera-Lozoya et al., 2014], we demonstrated the feasibility in the identification of RFA targets using solely DE-MR image-based features in a machine learning framework while integrating the influence of the inherent error sources of the complex multi-modal data in the training set. Furthermore, we presented previously the simulation from DE-MR images of distinguishable healthy and LAVA-like intracardiac electrograms [Cabrera-Lozoya et al., 2016].

The aim of this work is to develop an enhanced learning scheme using imaging and simulation data to guide RFA therapy by improving the identification of ablation targets, which are defined by the presence of LAVA. First, the performance of the classification is assessed when using solely imaging or simulation data. Then, three different approaches merging both data sources are evaluated. The highest performance was obtained when using a fused-learning algorithm. The results derived from this study open up possibilities for non-invasive cardiac arrhythmia ablation planning.

9.2 Clinical Data

Five patients referred for cardiac ablation for post-infarction in ventricular tachycardia were included in this study. The patients underwent cardiac MRI prior to high-density EP contact mapping of the endocardium.

Electrophysiological Data. The CARTO mapping system (Biosense Webster) enables the 3D localization of the catheter tip and provides the distribution of EP signals on cardiac surfaces. Contact mapping was achieved in sinus rhythm on the endocardium (trans-septal approach) with a multi-spline catheter (PentaRay, Biosense Webster). Signals were categorised as normal or LAVA by an experienced electrophysiologist.

Imaging Data. The scar tissue was imaged on a 1.5 Tesla clinical device (Avanto, Siemens Medical Systems) 15 minutes after the injection of a gadolinium contrast agent. A whole heart image was acquired using an inversion-recovery prepared, ECG-gated, respiratory-navigated, 3D gradient-echo pulse sequence with fat-saturation ($1.25\times1.25\times2.5mm^3$). The myocardium was manually segmented on reformatted images of isotropic voxel size ($0.625mm^3$). Abnormal myocardium (dense scar and grey zone areas) was segmented using adaptive thresholding of the histogram, with a cut-off at 35% of maximal signal intensity. Segmentations were reviewed by an experienced radiologist, with the option of manual correction.

9.3 Methods

9.3.1 Learning from Image Features

Image based features included intensity and texture features. Intensity features included minimal, maximal, mean and standard deviation intensity values of voxels contained within the catheter's sensing range. Myocardium thickness, scar transmurality and standard deviation over the average intensity in the region were also considered. Haralick features [Tesar et al., 2007] of the myocardial tissue neighboring the site of the electro-anatomical point (EAP) projection onto the endocardium were used to describe the tissue texture within the region of interest. Concatenation of the intensity and texture features yielded a final image-based feature vector of 475 dimensions which was used for classification.

We used a random forest [Criminisi et al., 2011] classification framework with a nested cross-validation scheme [Ruschhaupt et al., 2004] and optimized the classifier for precision performance using the scikit-learn library [Pedregosa et al., 2011]. Furthermore, we assigned a confidence weighting value to the samples during the training phase based on their temporal displacement during EGM recording. This way, image features from EAPs which were less affected by movement were considered more reliable for the forest construction.

9.3.2 Learning from Simulated Intracardiac EGM

Imaging data was used to construct a personalized bi-ventricular model, including distributions of scarred and grey zone regions. The GPU implementation of the Mitchell-Schaeffer model in the SOFA public framework was used along with tissue-specific characteristics to simulate cardiac electrophysiology.

A dipole approach was used for unipolar electrogram simulation at locations where clinical recordings were performed, these spatial coordinates were obtained from the CARTO system. Bipolar electrograms were later computed as the difference between the unipolar measurements of two consecutively placed electrodes.

Feature extraction was performed on the distal-most bipolar simulated EGMs. The feature vector was composed of eight elements: signal range, number of inflection points, signal energy, dominant frequency, mean slope, fractionation index and minimum and maximum signal values.

The same random forests classification framework with a nested cross-validation scheme as the one described for image-based learning was used. Similarly, the classifier was optimized for precision performance. Nonetheless, no sample weighting due to temporal displacement was included as the precise locations of the catheter electrodes are known during simulation.

9.3.3 Fused-Learning Schemes

Three fusion schemes were proposed to combine the MR image-based and simulated EGM-based learning frameworks:

- **Maximum Confidence Fusion.** Classification results were obtained independently using image-based or simulated EGM-based features and the confidence in their predictions were analyzed. The final label assigned to the EAP was that of the learning scheme with the highest prediction confidence.

- **Image-based, Simulation-Enhanced Fusion.** This learning fusion scheme gives greater importance to the classifications performed through image-based learning with temporal displacement weighting. Classification results obtained through simulated EGM-based learning were used solely in the instances where the image prediction had a confidence level below 0.75. In this case, the simulated EGM-based prediction was analyzed. If it was in disagreement with that of the image-based classification and had a higher confidence label, the prediction was modified to that given by the simulated EGM-based classifier. Else, the image-base classification was left intact.

- **Feature Set Fusion.** A new feature set was created using both the image-based and the simulated EGM-based features that have been described in the previous section. This combined feature set was fed to the random forest classification framework using temporal displacement weighting.

9.4 Evaluation Metrics

The results of the classification algorithms were projected onto an endocardial surface mesh to create confidence maps for potential RF ablation targets. The study in [Ilg et al., 2010] reports an average endocardial area of 3.5cm^2 for RFA lesions. Therefore, the endocardial surface was divided into regions of area 1.7cm^2, two times smaller than the average RFA lesions. Figure 9.1 shows a sample endocardial surface mesh partition.

EAP were projected to their closest endocardial surface region along with their prediction and confidence results. Also, a region was considered LAVA if at least one of the EAP projected onto it was labeled as such. The justification behind this is given by the physical constraints of RFA: the ablation of a LAVA site will affect neighboring tissue within the extension of the RFA lesion size, even if they are considered non-LAVA inducing.

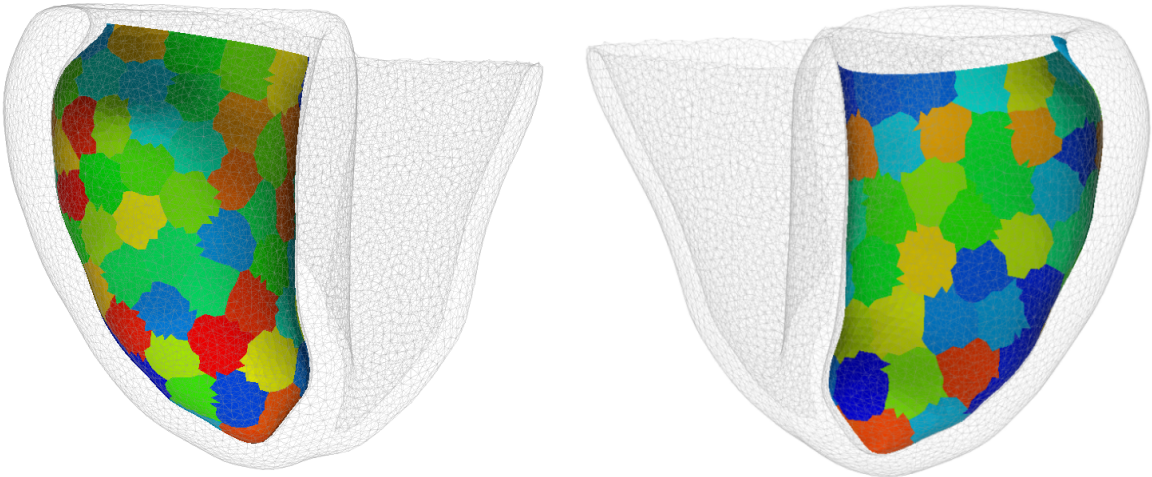

Figure 9.1: (Left) Anterior and (Right) posterior resulting regions for classification result display after endocardial surface division.

After projection of the classification results onto the regions in the surface mesh and its comparison with the ground truth, a confusion matrix was generated and the following statistics were computed:

- **Accuracy** represents the fraction of correct predictions. Its formulation is given by $ACC = (TP + TN)/(TP + FP + TN + FN)$

- **Sensitivity**, also known as true positive rate, measures the proportion of positives which are correctly identified as such. $TPR = TP/P = TP/(TP + FN)$

- **Specificity**, or true negative rate, measures the proportion of negatives which are correctly identified as such. $TNR = TN/N = TN/(FP + TN)$

- **Precision**, or positive predictive value, is intuitively the ability of the classifier not to label as positive a sample that is negative and is computed as $PPV = TP/(TP + FP)$

where TP, TN, FP, FN correspond to the true positive, true negative, false positive and false negative values of the confusion matrix, respectively.

9.5 Results and Discussion

This section presents the results from the previously described learning schemes and ablation target maps from Patient 1 are used to illustrate the algorithm's performance. Further statistics on the classification results are shown in Table 9.1 and Figure 9.7.

9.5.1 Results from Image-based Learning

Classification maps for Patient 1 with their respective confidence values for the LAVA region predictions obtained through MR image-based features are shown in Figure 9.2 for illustrative purposes. As can be seen from Table 9.1, the algorithm has an overall accuracy of 92.9% across the five patients, with a LAVA-specificity of 99.4% and a LAVA-precision of 96.4%. This means that when a region is classified as LAVA, in general, the algorithm is quite confident. Nonetheless, there is a severe compromise on the LAVA-sensitivity, which has an overall score of 33.2%.

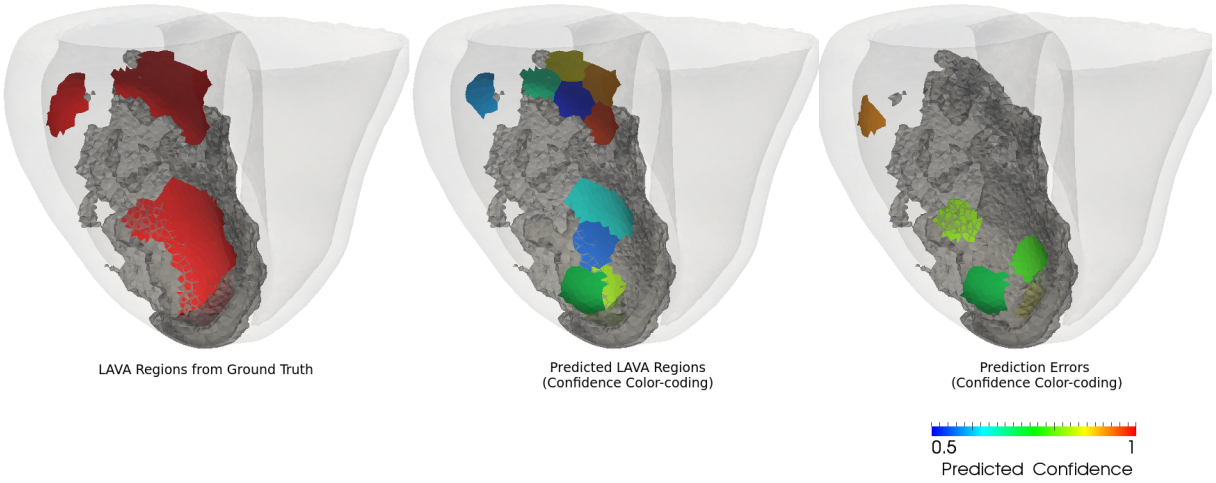

Figure 9.2: **Image-based Learning.** (Left) LAVA regions from ground truth. (Center) Predicted LAVA regions with confidence level color-coding. (Right) Prediction errors with confidence level color-coding.

9.5.2 Results from Simulated EGM-based Learning

Classification maps for Patient 1 with their respective confidence values for the LAVA region predictions obtained through the classification of simulated intracardiac electrograms are shown in Figure 9.3. Although the results for this prediction scheme are slightly lower in terms of LAVA-specificity (97.8%) and LAVA-precision (89.4%) than those obtained through MR image-based features, they remain high. The overall accuracy of the algorithm across the five patients is of 94.4%, but more importantly, the LAVA-sensitivity presents a considerable increase, with a value of 73.2%.

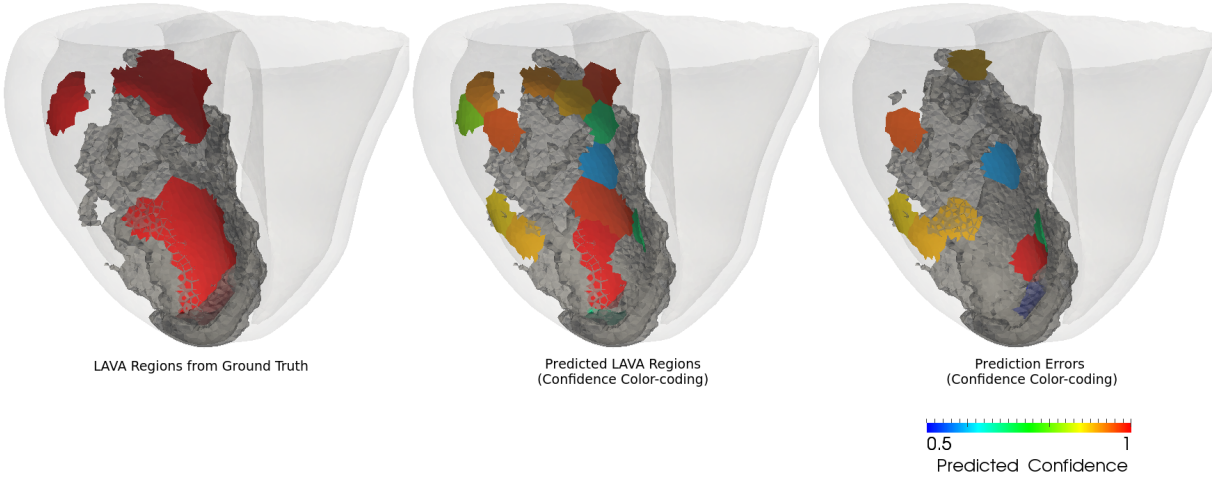

Figure 9.3: **Simulation-based Learning.** (Left) LAVA regions from ground truth. (Center) Predicted LAVA regions with confidence level color-coding. (Right) Prediction errors with confidence level color-coding.

9.5.3 Results from Maximum Confidence Fusion

Figure 9.4 show the merged results for image and simulation features by selecting the predictions with the highest confidence for Patient 1. The *maximum confidence fusion* scheme had overall high scores across patients. A slight increase in the classification accuracy (95.0%), LAVA-specificity (99.2%) and LAVA-precision (95.4%) is obtained with respect to the results yielded by the simulation-based classification. This happens at the expense of LAVA-sensitivity (63.0%). Nevertheless, the value is still considerably higher than that obtained by image-based classification alone.

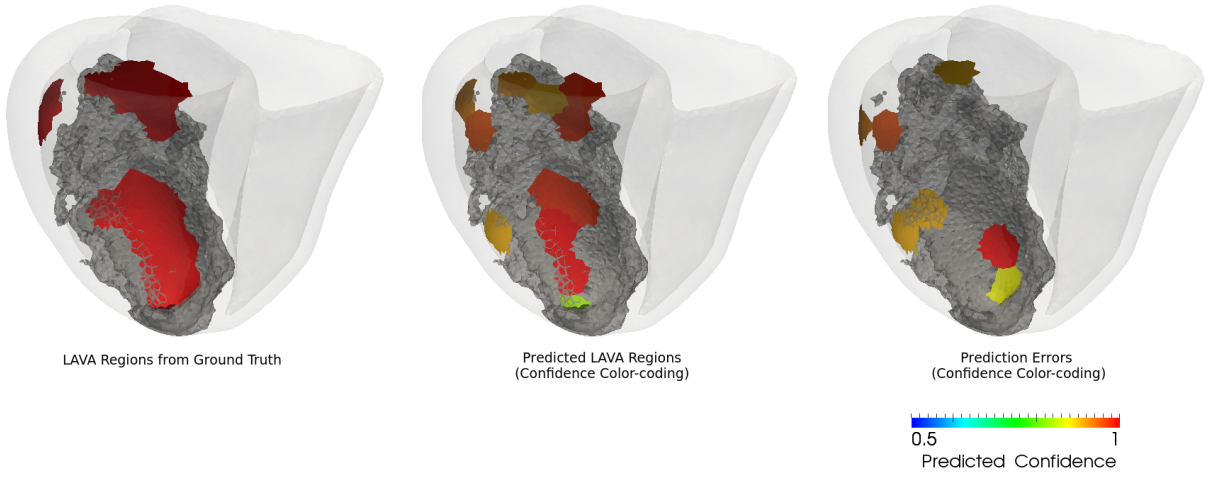

Figure 9.4: **Maximum Confidence Fusion.** (Left) LAVA regions from ground truth. (Center) Predicted LAVA regions with confidence level color-coding. (Right) Prediction errors with confidence level color-coding.

9.5.4 Results from Image-based, Simulation-Enhanced Fusion

Results for the confidence maps of Patient 1 are presented in Figure 9.5. Although the accuracy achieved is the same as with the *maximum confidence fusion* scheme and there are slightly higher scores for LAVA-specificity (99.8%) and LAVA-precision (98.8%), there is a drop in LAVA-sensitivity (57.4%).

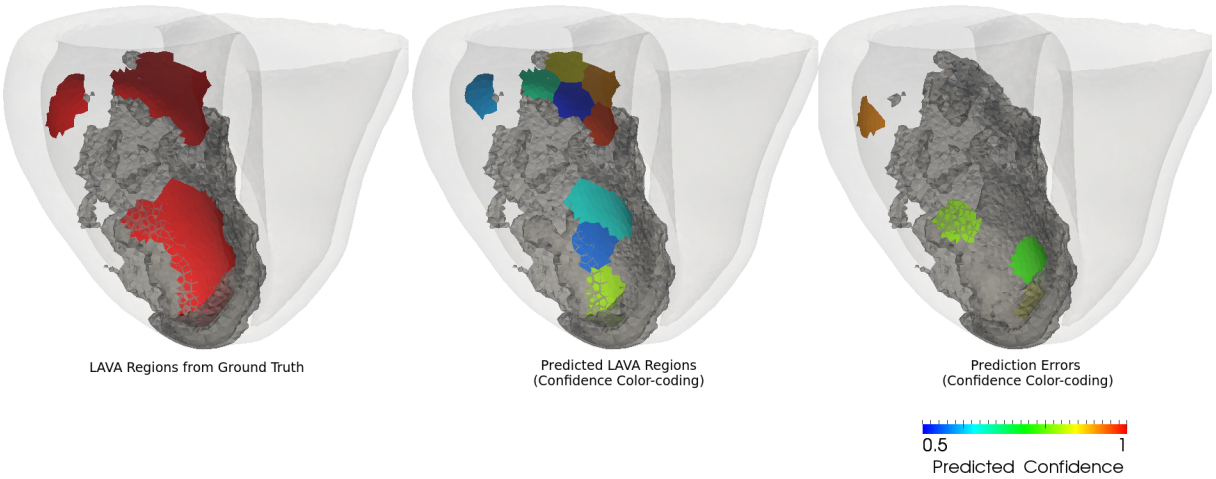

Figure 9.5: **Image-based, Simulation-Enhanced.** (Left) LAVA regions from ground truth. (Center) Predicted LAVA regions with confidence level color-coding. (Right) Prediction errors with confidence level color-coding.

9.5.5 Results from Feature Set Fusion

The graphical results for this fusion scheme on Patient 1 are shown in Figure 9.6. This method obtained both the top accuracy (97.2%) and LAVA-sensitivity (82.4%) scores while yielding high values for LAVA-specificity (99.2%) and LAVA-precision (95.0%) across the five patients. Therefore, it can be said that this scheme outperformed the classification frameworks when using solely image-based or simulation-based features and the two other fusion methodologies.

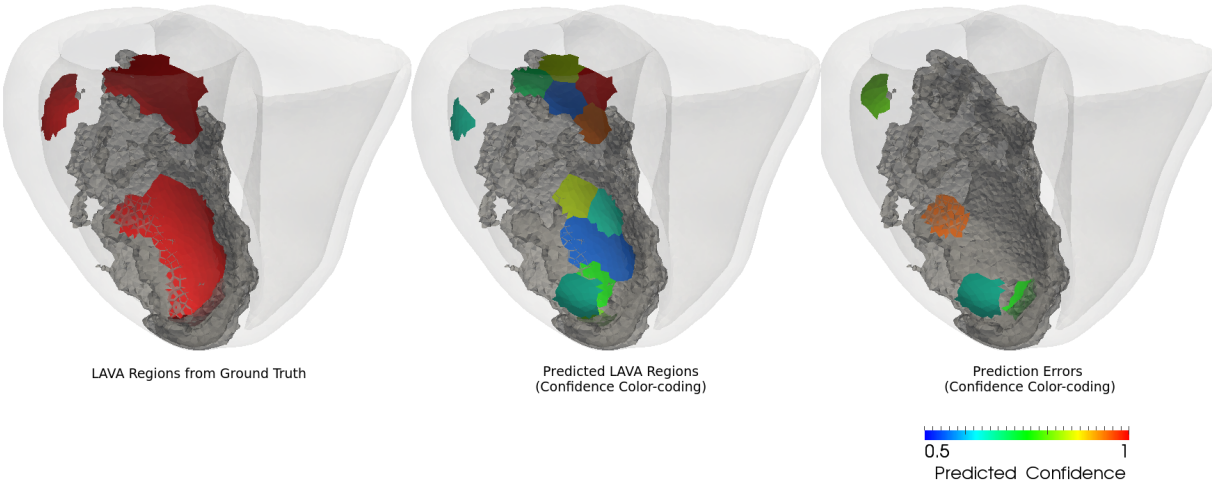

Figure 9.6: **Feature Set Fusion.** (Left) LAVA regions from ground truth. (Center) Predicted LAVA regions with confidence level color-coding. (Right) Prediction errors with confidence level color-coding.

9.5.6 Classification Results Summary

Table 9.1 and Figure 9.7 summarize the statistics on the results of the different classification schemes across the five patients. Forest construction parameters are detailed in Table 9.2.

Table 9.1: Classification Statistics On Five Patients

		Accuracy	Sensitivity	Specificity	Precision
Image-based	P1	94.0	73.3	98.5	91.6
	P2	92.6	33.3	100	100
	P3	91.8	39.0	99.0	90.0
	P4	93.7	11.0	100	100
	P5	92.5	10.0	100	100
	Mean	**92.9**	**33.2**	**99.4**	**96.4**
Simulated EGM-based	P1	89.2	73.3	92.7	68.7
	P2	95.4	66.6	98.0	88.0
	P3	92.6	78.0	98.0	90.0
	P4	99.2	89.0	100	100
	P5	95.7	60.0	100	100
	Mean	**94.4**	**73.2**	**97.8**	**89.4**
Maximum Confidence Fusion	P1	91.6	66.7	97.1	83.3
	P2	92.6	33.0	100	100
	P3	96.7	78.0	99.0	94.0
	P4	97.6	67.0	100	100
	P5	96.8	70.0	100	100
	Mean	**95.0**	**63.0**	**99.2**	**95.4**
Image-based, Simulation-Enhanced	P1	95.2	73.3	100	100
	P2	92.6	33.3	100	100
	P3	96.2	74.0	99.0	94.0
	P4	97.6	67.0	100	100
	P5	93.6	40.0	100	100
	Mean	**95.0**	**57.4**	**99.8**	**98.8**
Feature Set Fusion	P1	95.2	80.0	98.5	92.3
	P2	96.3	66.6	100	100
	P3	96.2	87.0	98.0	83.0
	P4	99.2	89.0	100	100
	P5	98.9	90.0	100	100
	Mean	**97.2**	**82.4**	**99.2**	**95.0**

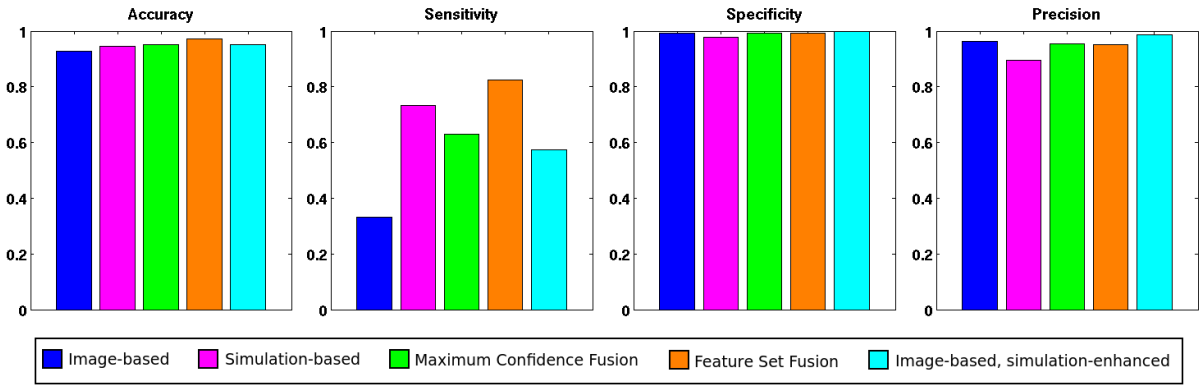

Figure 9.7: Classification Statistics Summary On Five Patients.

9.5.7 Ground Truth Re-evaluation

For illustrative purposes, misclassified regions in Patient 1 after the fused-learning schemes were further analyzed. Because most of them correspond to false negatives areas (true LAVA which were

Table 9.2: Forest Construction Parameters

Method	Patient	# Trees	# Features	# Inner Folds
Image-based	P1	60	80	5
	P2	80	50	5
	P3	60	10	5
	P4	20	30	5
	P5	20	50	5
Simulation-based	P1	45	2	5
	P2	45	2	5
	P3	20	2	5
	P4	15	2	5
	P5	50	4	5
Feature Set Fusion	P1	20	70	5
	P2	140	200	5
	P3	50	3	5
	P4	140	125	5
	P5	20	9	5

classified as non-LAVA), we first assess the *LAVAness* of the CARTO clinical signals in these regions which were categorized as LAVA by an experienced electrophysiologist. The characteristics these electrograms were compared to the patient's feature distributions of LAVA and non-LAVA clinical signals.

Figure 9.8 shows the mean slope value for these signals. They lie between the 25^{th} and 75^{th} percentiles values expected for a LAVA signal, dissipating the suspicions of these signals having non-typical or outlier LAVA signatures.

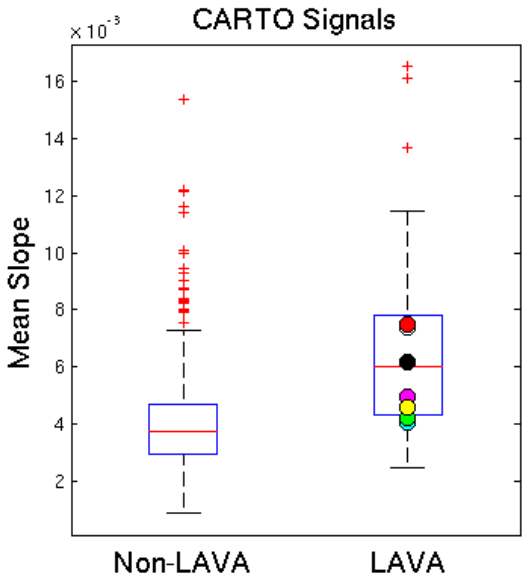

Figure 9.8: Verifying ground truth

9.5.8 False Positives Evaluation

In Patient 1, from Figure 9.6 it can be seen that one endocardial region was initially misclassified by the classification algorithm as a false positive and presented a low confidence level (0.65).By

analyzing the characteristics of the electroanatomical point, it was found that the considered sample was one where the catheter presented a high degree of temporal displacement. Its normalized weight was of 0.54, where the weights range from 0.5 for the EAP with the highest degree of movement and 1 for those with most stable positions. So far, sample weighting has been incorporated into our learning scheme in the training phase, but not during the testing phase. This exemplifies the need to consider sample weighting during testing phases of our classification algorithm.

9.6 Conclusion

We presented the use of a machine learning framework using real and synthetic data towards the prediction of RFA target identification, defined by the presence of LAVA. The real data was obtained from delayed-enhanced MR imaging while the synthetic was produced using a personalized image-based model for the simulation of intracardiac electrograms. First, the performance of image-based versus simulation-based learning algorithms was compared. Next, several fused-learning frameworks were assessed. The highest performance scores were obtained when both feature sets were merged into a single dataset, the *feature set fusion* scheme, yielding a mean 97.2% accuracy and 82.4% LAVA-sensitivity scores across five patients. Error regions were characterized by containing EAP with high temporal displacement values. The results derived from this study open up possibilities for non-invasive cardiac arrhythmia ablation planning.

Bibliography

Aggarwal, N. R., Martinez, M. W., Gersh, B. J., and Chareonthaitawee, P. Role of cardiac mri and nuclear imaging in cardiac resynchronization therapy. *Nature Reviews Cardiology*, 6(12):759–770, Dec 2009. URL http://www.hubmed.org/display.cgi?uids=19884903. 51

Akaike, H. A new look at the statistical model identification. *IEEE transactions on automatic control*, 19(6):716–723, 1974. 83

Aliot, E. M., Stevenson, W. G., Almendral-Garrote, J. M., Bogun, F., Calkins, C. H., Delacretaz, E., Della Bella, P., Hindricks, G., Jaïs, P., and Josephson, M. E. Ehra/hrs expert consensus on catheter ablation of ventricular arrhythmias developed in a partnership with the european heart rhythm association (ehra), a registered branch of the european society of cardiology (esc), and the heart rhythm society (hrs); in collaboration with the american college of cardiology (acc) and the american heart association (aha). *Europace*, 11(6):771–817, 2009. 37

Anderson, R. H., Smerup, M., Sanchez-Quintana, D., Loukas, M., and Lunckenheimer, P. P. The Three-Dimensional Arrangement of the Myocytes in the Ventricular Walls. *Clinical Anatomy*, 22: 64–76, 2008. 19, 32

Arevalo, H., Plank, G., Helm, P., Halperin, H., and Trayanova, N. Tachycardia in post-infarction hearts: insights from 3d image-based ventricular models. *PloS one*, 8(7):e68872, 2013. 48

Arevalo, H., Rodriguez, B., and Trayanova, N. Arrhythmogenesis in the heart: Multiscale modeling of the effects of defibrillation shocks and the role of electrophysiological heterogeneity. *Chaos: An Interdisciplinary Journal of Nonlinear Science*, 17(1):–, 2007. URL http://scitation.aip.org/content/aip/journal/chaos/17/1/10.1063/1.2430637. 37

Arridge, S. R., Kaipio, J. P., Kolehmainen, V., Schweiger, M., Somersalo, E., Tarvainen, T., and Vauhkonen, M. Approximation errors and model reduction with an application in optical diffusion tomography. *Inverse Problems*, 22(1):175, 2006. 143

Arsigny, V., Commowick, O., Ayache, N., and Pennec, X. A fast and log-euclidean polyaffine framework for locally linear registration. *Journal of Mathematical Imaging and Vision*, 33(2): 222–238, 2009. 90, 92

Arsigny, V., Fillard, P., Pennec, X., and Ayache, N. Log-euclidean metrics for fast and simple calculus on diffusion tensors. *Magn Reson Med*, 56(2):411–421, Aug 2006. ISSN 0740-3194. 25, 29

Arzani, A., Dyverfeldt, P., Ebbers, T., and Shadden, S. C. In vivo validation of numerical prediction for turbulence intensity in an aortic coarctation. *Ann Biomed Eng*, 40:860–870, 2012. 171

Ashikaga, H., Arevalo, H., Vadakkumpadan, F., Blake, R. C., Bayer, J. D., Nazarian, S., Zviman, M. M., Tandri, H., Berger, R. D., and Calkins, H. Feasibility of image-based simulation to estimate ablation target in human ventricular arrhythmia. *Heart Rhythm*, 10(8):1109–1116, 2013. 37, 48

Bader, B. W., Kolda, T. G., et al. Matlab tensor toolbox version 2.5. Available online, January 2012. URL http://www.sandia.gov/~tgkolda/TensorToolbox/. 103

Baiges, J., Codina, R., and Idelsohn, S. Explicit reduced order models for the stabilized finite element approximation of the incompressible Navier-Stokes equations. Submitted preprint., 2012. 171

Banville, I. and Gray, R. A. Effect of action potential duration and conduction velocity restitution and their spatial dispersion on alternans and the stability of arrhythmias. *Journal of Cardiovascular Electrophysiology*, 13(11):1141–1149, 2002. 37

Basser, P., Mattiello, J., and LeBihan, D. Mr diffusion tensor spectroscopy and imaging. *Biophysical journal*, 66(1):259–267, 1994. 21

Basser, P., Pajevic, S., Pierpaoli, C., Duda, J., and Aldroubi, A. In vivo fiber tractography using DT-MRI data. *Magnetic Resonance in Medicine*, 44:625–632, 2000. 19

Bazilevs, Y., Hsu, M.-C., Benson, D. J., Sankaran, S., and Marsden, A. L. Computational fluid-structure interaction: methods and application to a total cavopulmonary connection. *Comp. Mech.*, 45(1):77–89, 2009. 153

Beeler, G. W. and Reuter, H. Reconstruction of the action potential of ventricular myocardial fibers. *Journal of Physiology*, 268:177–210, 1977. 57

Beg, M., Helm, P., McVeigh, E., Miller, M., and Winslow, R. Computational cardiac anatomy using MRI. *Magn. Reson. Medicine*, 52(5):1167–1174, 2004. 150

Beg, M., Miller, M., Trouvé, A., and Younes, L. Computing large deformation metric mappings via geodesic flows of diffeomorphisms. *Int. Journal of Computer Vision*, 61(2):139–157, 2005. 79

Berger, T., Fischer, G., Pfeifer, B., Modre, R., Hanser, F., Trieb, T., Roithinger, F., Stuehlinger, M., Pachinger, O., Tilg, B., and Hintringer, F. Single-beat noninvasive imaging of cardiac electrophysiology of ventricular pre-excitation. *Journal of the American College of Cardiology*, 48(10): 2045–52, 2006. 113

Bergmann, M., Bruneau, C., and Iollo, A. Enablers for robust POD models. *J. Comp. Phys.*, 228 (2):516–538, 2009. 148, 153

Bertoglio, C., Caiazzo, A., and Fernández, M. Fractional-step schemes for the coupling of distributed and lumped models in hemodynamics. *SIAM J. Sci. Comp.*, 35(3):B551–B575, 2013. 153

Beshai, J. F., Grimm, R. A., Nagueh, S. F., Baker, J. H., Beau, S. L., Greenberg, S. M., Pires, L. A., and Tchou, P. J. Cardiac-resynchronization therapy in heart failure with narrow QRS complexes. *N Engl J Med*, 357(24):2461–2471, Dec 2007. 51

Bestel, J., Clément, F., and Sorine, M. A biomechanical model of muscle contraction. In Niessen, W. and Viergever, M., editors, *Medical Image Computing and Computer-Assisted intervention (MICCAI'01)*, volume 2208 of *Lecture Notes in Computer Science (LNCS)*, pages 1159–1161. Springer-Verlag, Berlin, Germany, 2001. 58, 62

Bijari, P. B., Antiga, L., Gallo, D., Wasserman, B. A., and Steinman, D. A. Improved prediction of disturbed flow via hemodynamically-inspired geometric variables. *J. Biomech.*, 45(9):1632–1637, 2012. URL http://www.sciencedirect.com/science/article/pii/S0021929012002059. 171

Billet, F., Sermesant, M., Delingette, H., and Ayache, N. Cardiac motion recovery by coupling an electromechanical model and Cine-MRI data: First steps. In *Workshop Computational Biomechanics for Medicine III (MICCAI'08)*, 2008. 60

Billet, F., Sermesant, M., Delingette, H., and Ayache, N. Cardiac motion recovery and boundary conditions estimation by coupling an electromechanical model and cine-MRI data. In *Proceedings of Functional Imaging and Modeling of the Heart 2009 (FIMH'09)*, volume 5528 of *LNCS*, pages 376–385, 3-5 June 2009. 60

Bistoquet, A., Oshinski, J., and Skrinjar, O. Left ventricular deformation recovery from cine MRI using an incompressible model. *IEEE Trans. Med. Imaging*, 26(9):1136–1153, 2007. 92

Biswas, R., editor. *Parallel Computational Fluid Dynamics: Recent Advances and Future Directions*. DEStech Publications, 2010. 148

Blanco, P. J., Pivello, M. R., Urquiza, S. A., and Feijoo, R. A. On the potentialities of 3d-1d coupled models in hemodynamics simulations. *J. Biomech.*, 42:919–930, 2009. URL <GotoISI>://WOS:000266299300019. 148

Bookstein, F. *The Measurement of Biological Shape and Shape Change*, volume 24 of *Lecture Notes in Biomathematics*. Springer-Verlag, 1978. 75

Bookstein, F. Size and shape spaces for landmark data in two dimensions (with discussion). *Statistical Science*, 1:181–242, 1986. 75

Bovendeerd, P., Arts, T., Huyghe, J., van Campen, D., and Reneman, R. Dependence of local left ventricular wall mechanics on myocardial fiber orientation: A model study. *Journal of Biomechanics*, 25(10):1129 – 1140, 1992. ISSN 0021-9290. 19

Cabrera Lozoya, R. *Radiofrequency ablation planning for cardiac arrhythmia treatment using modeling and machine learning approaches*. Phd thesis, Université Nice Sophia Antipolis, Sept. 2015. 15, 175

Cabrera-Lozoya, R., Berte, B., Cochet, H., Jaïs, P., Ayache, N., and Sermesant, M. Image-based biophysical simulation of intracardiac abnormal ventricular electrograms. *IEEE Transactions on Biomedical Engineering*, 2016. (accepted). 175

Cabrera-Lozoya, R., Margeta, J., Le Folgoc, L., Komatsu, Y., Benjamin, B., Relan, J., Cochet, H., Haissaguerre, M., Jais, P., Ayache, N., and Sermesant, M. Confidence-based training for clinical data uncertainty in image-based prediction of cardiac ablation targets. In *bigMCV Workshop on the Medical Image Computing and Computer Assisted Intervention Conference – MICCAI 2014*, 2014. 175

Caillerie, D., Mourad, A., and Raoult, A. Cell-to-muscle homogenization. Application to a constitutive law for the myocardium. *Math. Mod. Numer. Anal.*, 37(4):681–698, July 2003. 62

Cairncross, R., Schunk, P., Baer, T., Rao, R., and Sackinger, P. A finite element method for free surface flows of incompressible fluids in three dimensions. Part I: Boundary fitted mesh motion. *Int. Jour. Num. Meth. Fluids*, 33:375–403, 2000. 155

Caldwell, B. J., Trew, M. L., Sands, G. B., Hooks, D. A., LeGrice, I. J., and Smaill, B. H. Three distinct directions of intramural activation reveal nonuniform side-to-side electrical coupling of ventricular myocytes. *Circ Arrhythm Electrophysiol*, 2(4):433–440, Aug 2009. URL http://www.hubmed.org/display.cgi?uids=19808500. 56, 68

Camara, O., Pashaei, A., Sebastián, R., and Frangi, A. F. Personalization of fast conduction purkinje system in eikonal-based electrophysiological models with optical mapping data. In *STACOM/CESC*, volume 6364 of *Lecture Notes in Computer Science*, pages 281–290. Springer, 2010. 132

Carlberg, K., Bou-Mosleh, C., and Farhat, C. Efficient non-linear model reduction via a least-squares Petrov-Galerkin projection and compressive tensor approximations. *International Journal for Numerical Methods in Engineering*, 86(2):155–181, 2011. ISSN 1097-0207. URL http://dx.doi.org/10.1002/nme.3050. 171

Carroll, J. D. and Chang, J.-J. Analysis of individual differences in multidimensional scaling via an n-way generalization of "eckart-young" decomposition. *Psychometrika*, 35(3):283–319, 1970. 97

Cates, J., Fletcher, P., and Whitaker, R. A hypothesis testing framework for high-dimensional shape models. In *In MICCAI Workshop on Mathematical Foundations of Computational Anatomy*, page 170, 2008. 82

Cawley, G. C. Leave-one-out cross-validation based model selection criteria for weighted LS-SVMs. In *IJCNN'06*, pages 1661–1668, Vancouver, 2006. IEEE. 121

Cazeau, S., Leclercq, C., Lavergne, T., Walker, S., Varma, C., Linde, C., Garrigue, S., Kappenberger, L., Haywood, G. A., Santini, M., Bailleul, C., Daubert, J. C., and Multisite Stimulation in Cardiomyopathies (MUSTIC) Study Investigators. Effects of multisite biventricular pacing in patients with heart failure and intraventricular conduction delay. *N Engl J Med*, 344(12):873–880, Mar 2001. URL http://www.hubmed.org/display.cgi?uids=11259720. 51

Chabiniok, R., Chapelle, D., Lesault, P., Rahmouni, A., and Deux, J. Validation of a biomechanical heart model using animal data with acute myocardial infarction. In *CI2BM09 - MICCAI Workshop on Cardiovascular Interventional Imaging and Biophysical Modelling*, London, UK, 2009. URL http://hal.inria.fr/inria-00418373/en/. 63

Chai, L., Ding, J., and Liu, Y. *Hemodynamics Simulation of Patient-Specific Surgical Planning For Tetralogy of Fallot*. 2010 3rd International Conference on Biomedical Engineering and Informatics. Yu, W. Zhang M. Wang L. Song Y., 2010. URL <GotoISI>://WOS:000293143500066. 148

Chandrashekara, R., Mohiaddin, R., and Rueckert, D. Cardiac motion tracking in tagged MR images using a 4D B-spline motion model and nonrigid image registration. In *IEEE Int. Symp. on Biomed. Imaging: Nano to Macro*, pages 468–471, 2004. 90

Chandrashekara, R., Rao, A., Sanchez-Ortiz, G., Mohiaddin, R., and Rueckert, D. Construction of a statistical model for cardiac motion analysis using nonrigid image registration. In *Information Processing in Medical Imaging*, pages 599–610. Springer, 2003. 91

Chapelle, D., Clément, F., Génot, F., Tallec, P. L., Sorine, M., and Urquiza, J. A physiologically-based model for the active cardiac muscle contraction. In Katila, T., Magnin, I., Clarysse, P., Montagnat, J., and Nenonen, J., editors, *Functional Imaging and Modeling of the Heart (FIMH'01)*, number 2230 in Lecture Notes in Computer Science (LNCS), pages 128–133. Springer, 2001. 62

Chapelle, D., Le Tallec, P., Moireau, P., and Sorine, M. An energy-preserving muscle tissue model: formulation and compatible discretizations. *International Journal for Multiscale Computational Engineering*, 10(2):189–211, 2012. 117

Chen, Z., Cabrera-lozoya, R., Relan, J., Sohal, M., Shetty, A., Karim, R., Delingette, H., Gill, J., Rhode, K., Ayache, N., Taggart, P., Rinaldi, C., Sermesant, M., and Razavi, R. Biophysical modelling predicts ventricular tachycardia inducibility and circuit morphology: A combined clinical validation and computer modelling approach. *Journal of Cardiovascular Electrophysiology*, 2016. in press. 7, 37

Chern, M.-J., Wu, M.-T., and Wang, H.-L. Numerical investigation of regurgitation phenomena in pulmonary arteries of Tetralogy of Fallot patients after repair. *J. Biomech.*, 41(14):3002–3009, 2008. URL <GotoISI>://WOS:000260985700016. 148

Cherry, E. M. and Fenton, F. H. Suppression of alternans and conduction blocks despite steep apd restitution: electrotonic, memory, and conduction velocity restitution effects. *American Journal of Physiology-Heart and Circulatory Physiology*, 286(6):H2332–H2341, 2004. 37

Chinchapatnam, P., Rhode, K., Ginks, M., Rinaldi, C., Lambiase, P., Razavi, R., Arridge, S., and Sermesant, M. Model-based imaging of cardiac apparent conductivity and local conduction velocity for diagnosis and planning of therapy. *IEEE Transactions on Medical Imaging*, 27(11):1631–1642, 2008. 41, 57, 58, 131, 132

Chorin, A. Numerical solution of the Navier-Stokes equations. *Math. Comp.*, 22:745–762, 1968. 153

Chung, E. S., Leon, A. R., Tavazzi, L., Sun, J. P., Nihoyannopoulos, P., Merlino, J., Abraham, W. T., Ghio, S., Leclercq, C., Bax, J. J., Yu, C. M., Gorcsan, J., St John Sutton, M., De Sutter,

J., and Murillo, J. Results of the predictors of response to crt (PROSPECT) trial. *Circulation*, 117(20):2608–2616, May 2008. 51

Ciarlet, P. *Mathematical elasticity. Vol. I*, volume 20 of *Studies in Mathematics and its Applications*. North-Holland Publishing Co., 1988. 155

Clayton, R., Bernus, O., Cherry, E., Dierckx, H., Fenton, F., Mirabella, L., Panfilov, A., Sachse, F., Seemann, G., and Zhang, H. Models of cardiac tissue electrophysiology: progress, challenges and open questions. *Progress in Biophysics and Molecular Biology*, 104(1):22–48, 2011a. 37

Clayton, R., Bernus, O., Cherry, E., Dierckx, H., Fenton, F., Mirabella, L., Panfilov, A., Sachse, F., Seemann, G., and Zhang, H. Models of cardiac tissue electrophysiology: Progress, challenges and open questions. *Prog Biophys Mol Biol*, 104(1–3):22–48, 2011b. 131

Cleland, J. G., Daubert, J. C., Erdmann, E., Freemantle, N., Gras, D., Kappenberger, L., Tavazzi, L., and Cardiac Resynchronization-Heart Failure (CARE-HF) Study Investigators. The effect of cardiac resynchronization on morbidity and mortality in heart failure. *N Engl J Med*, 352(15): 1539–1549, Apr 2005. URL http://www.hubmed.org/display.cgi?uids=15753115. 51

Colli Franzone, P., Guerri, L., and Rovida, S. Wavefront propagation in activation model of the anisotropic cardiac tissue. *J. Math. Biol.*, 28(2):121–176, 1990. 57, 131

Commowick, O., Arsigny, V., Isambert, A., Costa, J., Dhermain, F., Bidault, F., Bondiau, P.-Y., Ayache, N., and Malandain, G. An efficient locally affine framework for the smooth registration of anatomical structures. *Med. Image Anal.*, 12(4), 2008. 90

Coronel, R., Wilms-Schopan, F. J., Groot, J. R., Janse, M. J., Capelle, F. J., and Bakker, J. M. Laplacian electrograms and the interpretation of complex ventricular activation patterns during ventricular fibrillation. *Journal of Cardiovascular Electrophysiology*, 11(10):1119–1128, 2000. 39

Costa, K. D., Hunter, P. J., Wayne, J. S., Waldman, L. K., Guccione, J. M., and McCulloch, A. D. A Three-Dimensional Finite Element Method for Large Elastic Deformations of Ventricular Myocardium: II - Prolate Spheroidal Coordinates. *J Biomech Eng*, 118(4):464–472, Nov 1996. 22

Courtemanche, M. and Winfree, A. T. Re-entrant rotating waves in a beeler-reuter based model of two-dimensional cardiac electrical activity. *International Journal of Bifurcation and Chaos*, 01(02):431–444, 1991. URL http://www.worldscientific.com/doi/abs/10.1142/S0218127491000336. 37

Crampin, E. J., Halstead, M., Hunter, P., Nielsen, P., Noble, D., Smith, N., and Tawhai, M. Computational physiology and the physiome project. *Experimental Physiology*, 89(1):1–26, Jan 2004. 52

Criminisi, A., Shotton, J., and Konukoglu, E. Decision forests for classification, regression, density estimation, manifold learning and semi-supervised learning. *Microsoft Research Cambridge, Tech. Rep. MSRTR-2011-114*, 5(6):12, 2011. 176

D'Arcy Thompson, W. *On Growth and Form*. Cambridge University Press, England., 1917. 76

Das, A., Gottliebson, W. M., Karve, M., and Banerjee, R. Comparison of hemodynamic endpoints between normal subject and tetralogy patient using Womersley velocity profile and MR based flow measurements. *Mol. & Cell. Biomech.*, 8(1):21–42, 2011. URL <GotoISI>://MEDLINE:21391326. 148

De-Craene, M., Tobon-Gomez, C., Butakoff, C., Duchateau, N., Piella, G., Rhode, K., and Frangi, A. Temporal diffeomorphic free form deformation (TDFFD) applied to motion and deformation quantification of tagged MRI sequences. In *Proc. STACOM MICCAI Workshop*, LNCS. Springer, 2011. 90, 99

Decker, K. F. and Rudy, Y. Ionic mechanisms of electrophysiological heterogeneity and conduction block in the infarct border zone. *American Journal of Physiology-Heart and Circulatory Physiology*, 299(5):H1588–H1597, 2010. 43

Dong, J., Calkins, H., Solomon, S., Lai, S., Dalal, D., Lardo, A., Brem, E., Preiss, A., Berger, R., Halperin, H., et al. Integrated electroanatomic mapping with three-dimensional computed tomographic images for real-time guided ablations. *Circulation*, 113(2):186, 2006. 135

Donoho, D. Compressed sensing. *IEEE Transactions on Information Theory*, 52(4):1289–1306, 2006. 145

Doostan, A., Owhadi, H., Lashgari, A., and Iaccarino, G. Non-adapted sparse approximation of PDEs with stochastic inputs. Center for Turbulence Research, Annual Research Briefs, 2009. 131, 134, 145

Dou, J., Tseng, W.-Y. I., Reese, T. G., and Wedeen, V. J. Combined Diffusion and Strain MRI Reveals Structure and Function of Human Myocardial Laminar Sheets In-Vivo. *Magnetic Resonance in Medicine*, 50:107–113, 2003. 19, 21

Dru, F. and Vercauteren, T. An ITK Implementation of the Symmetric Log-Domain Diffeomorphic Demons Algorithm. Insight Journal – 2009 January - June, May 2009. 22, 31, 106

Dryden, I. and Mardia, K. Theoretical and distributional aspects of shape analysis. In *Probability Measures on Groups, X (Oberwolfach, 1990)*, pages 95–116, New York, 1991. Plenum. 76

DuBois, D. and DuBois, E. The measurement of the surface area of man. *Archives of Internal Medicine*, 15(5), 1915. 84

Durrleman, S. *Statistical models of currents for measuring the variability of anatomical curves, surfaces and their evolution*. Thèse de sciences (phd thesis), Université de Nice-Sophia Antipolis, 2010. 73

Durrleman, S., Pennec, X., Trouvé, A., and Ayache, N. A forward model to build unbiased atlases from curves and surfaces. In Pennec, X. and Joshi, S., editors, *Proc. of the International Workshop on the Mathematical Foundations of Computational Anatomy (MFCA-2008)*, September 2008a. 151

Durrleman, S., Pennec, X., Trouvé, A., and Ayache, N. Statistical Models of Sets of Curves and Surfaces based on Currents. *Med. Im. Anal.*, 13(5):793–808, 2009a. 149, 150, 151

Durrleman, S., Pennec, X., Trouvé, A., and Ayache, N. Statistical models on sets of curves and surfaces based on currents. *Medical Image Analysis*, 13(5):793–808, 2009b. 73, 78, 80, 151

Durrleman, S., Pennec, X., Trouvé, A., Gerig, G., and Ayache, N. Spatiotemporal atlas estimation for developmental delay detection in longitudinal datasets. In *Medical Image Computing and Computer-Assisted Intervention (MICCAI'09), Part I*, volume 5761 of *Lecture Notes in Computer Science*, pages 297–304, London, UK, 2009c. Springer. 73

Durrleman, S., Pennec, X., Trouvé, A., Thompson, P., and Ayache, N. Inferring brain variability from diffeomorphic deformations of currents: an integrative approach. *Medical Image Analysis*, 12(5):626–637, 2008b. URL http://dx.doi.org/10.1016/j.media.2008.06.010. PMID: 18658005. 73, 76

Ecabert, O., Peters, J., Schramm, H., Lorenz, C., von Berg, J., Walker, M. J., Vembar, M., Olszewski, M. E., Subramanyan, K., Lavi, G., and Weese, J. Automatic model-based segmentation of the heart in ct images. *IEEE Trans. Med. Imaging*, 27(9):1189–1201, 2008. 55, 68

Elen, A., Choi, H. F., Loeckx, D., Gao, H., Claus, P., Suetens, P., Maes, F., and D'hooge, J. Three-dimensional cardiac strain estimation using spatio-temporal elastic registration of ultrasound images: A feasibility study. *Medical Imaging, IEEE Transactions on*, 27:1580–1591, 2008. 114

Faure, F., Duriez, C., Delingette, H., Allard, J., Gilles, B., Marchesseau, S., Talbot, H., Courtecuisse, H., Bousquet, G., Peterlik, I., and Cotin, S. Sofa: A multi-model framework for interactive physical simulation. In Payan, Y., editor, *Soft Tissue Biomechanical Modeling for Computer Assisted Surgery*, volume 11 of *Studies in Mechanobiology, Tissue Engineering and Biomaterials*, pages 283–321. Springer Heidelberg, 2012. 117

Fenton, F. and Karma, A. Erratum: "vortex dynamics in three-dimensional continuous myocardium with fiber rotation: Filament instability and fibrillation" [chaos 8, 20-47 (1998)]. *Chaos*, 8(4):879, Dec. 1998. URL http://dx.doi.org/10.1063/1.166374. 40

Fillard, P., Arsigny, V., Pennec, X., and Ayache, N. Clinical DT-MRI estimation, smoothing and fiber tracking with log-Euclidean metrics. *IEEE Transactions on Medical Imaging*, 26(11):1472–1482, 2007. 25, 31

Fillard, P., Arsigny, V., Pennec, X., Thompson, P., and Ayache, N. Extrapolation of sparse tensor fields: Application to the modeling of brain variability. In Christensen, G. and Sonka, M., editors, *Information Processing in Medical Imaging*, volume 3565 of *Lecture Notes in Computer Science*, pages 357–376. Springer Berlin / Heidelberg, 2005. ISBN 978-3-540-26545-0. 25

Fillard, P. and Gerig, G. Analysis tool for diffusion tensor MR. In *MICCAI'03*, volume 2 of *LNCS*, pages 979–980. Springer, November 2003. 30

Formaggia, L., Quarteroni, A., and Vergara, C. On the physical consistency between three-dimensional and one-dimensional models in haemodynamics. *J. Comp. Phys.*, 2012. 148

Frangi, A. F., Niessen, W. J., and Viergever, M. A. Three-dimensional modeling for functional analysis of cardiac images, a review. *Medical Imaging, IEEE Transactions on*, 20(1):2–5, 2001. 90

Frank, O. Die Grundform Des Arteriellen Pulses. *Zeitung für Biologie*, 37:483–586, 1899. 152

Frindel, C., Robini, M., Croisille, P., and Zhu, Y.-M. Comparison of Regularization Methods for Human Cardiac Diffusion Tensor MRI. *Medical Image Analysis*, 13(3):405 – 418, 2009. ISSN 1361-8415. 25

Gamper, U., Boesiger, P., and Kozerke, S. Diffusion Imaging of The In Vivo Heart Using Spin Echoes - Considerations on Bulk Motion Sensitivity. *Magnetic Resonance in Medicine*, 57:331–337, 2007. 19, 21

Geneser, S. E., Kirby, R. M., and MacLeod, R. S. Application of stochastic finite element methods to study the sensitivity of ECG forward modeling to organ conductivity. *IEEE Trans Biomed Eng*, 55(1):31–40, Jan 2008. 134

Ghai, A., Silversides, C., Harris, L., Webb, G. D., Siu, S. C., and Therrien, J. Left ventricular dysfunction is a risk factor for sudden cardiac death in adults late after repair of tetralogy of fallot. *Journal of the American College of Cardiology*, 40(9):1675–1680, 2002. 106

Ghanem, R. and Doostan, A. On the construction and analysis of stochastic models: Characterization and propagation of the errors associated with limited data. *J. Comp. Physics*, 217:63–81, 2006. 130, 133, 144, 145

Ghanem, R. N., Jia, P., Ramanathan, C., Ryu, K., Markowitz, A., and Rudy, Y. Noninvasive electrocardiographic imaging (ECGI): comparison to intraoperative mapping in patients. *Heart Rhythm*, 2:339–354, Apr 2005. 113

Girolami, M. and Calderhead, B. Riemann manifold Langevin and Hamiltonian Monte Carlo methods. *J.R. Statist. Soc. B*, 2011. 136

Glaunès, J. *Transport par difféomorphismes de points, de mesures et de courants pour la comparaison de formes et l'anatomie numérique*. Thèse de sciences, Université Paris 13, Nov. 2005. 77, 80

Grenander, U. *General Pattern Theory: A Mathematical Study of Regular Structures*. Oxford University Press Inc., New York, NY., 1993. 76

Grepl, M. A., Maday, Y., Nguyen, N. C., and Patera, A. T. Efficient reduced-basis treatment of non affine and nonlinear partial differential equations. *M2AN Math. Model. Numer. Anal.*, 41(3): 575–605, 2007. 171

Grinberg, L. Proper orthogonal decomposition of atomistic flow simulations. *Journal of Computational Physics*, 231(16):5542 – 5556, 2012. ISSN 0021-9991. 171

Grinberg, L., Cheever, E., Anor, T., Madsen, J. R., and Karniadakis, G. E. Modeling blood flow circulation in intracranial arterial networks: A comparative 3d/1d simulation study. *Ann Biomed Eng*, 39:297–309, 2011. URL <GotoISI>://WOS:000287213100026. 148

Grinberg, L., Yakhot, A., and Karniadakis, G. E. Analyzing transient turbulence in a stenosed carotid artery by proper orthogonal decomposition. *Annals of biomedical engineering*, 37(11):2200–2217, 2009. 171

Gudbjartsson, H. and Patz, S. The rician distribution of noisy mri data. *Magnetic Resonance in Medicine*, 34(6):910–914, 2005. 29

Guermond, J.-L., Minev, P., and Shen, J. An Overview of Projection methods for incompressible flows. *Comput. Methods Appl. Mech. Engrg.*, 195:6011–6045, 2006. 153

Guibert, R., Mcleod, K., Caiazzo, A., Mansi, T., Fernández, M. Á., Sermesant, M., Pennec, X., Vignon-Clementel, I., Boudjemline, Y., and Gerbeau, J.-F. Group-wise construction of reduced models for understanding and characterization of pulmonary blood flows from medical images. *Medical Image Analysis*, 18(1):63–82, Oct. 2013. 14, 147

Han, C., Pogwizd, S. M., Killingsworth, C. R., and He, B. Noninvasive imaging of three-dimensional cardiac activation sequence during pacing and ventricular tachycardia. *Heart Rhythm*, 8(8):1266–72, 2011. 113

Han, C., Pogwizd, S. M., Killingsworth, C. R., and He, B. Noninvasive reconstruction of the three-dimensional ventricular activation sequence during pacing and ventricular tachycardia in the canine heart. *American Journal of Physiology Heart and Circulatory Physiology*, 302(1):H244–52, 2012. 113

Hansen, M. S., Thorup, S. S., and Warfield, S. K. Polyaffine parametrization of image registration based on geodesic flows. In *Proc. MMBIA Workshop*, pages 289–295. IEEE, 2012. 90

Hansen, P. C. Analysis of Discrete Ill-posed Problems by Means of the L-Curve. *SIAM Review*, 34 (4):561, 1992. 29

Härdle, W. K. and Marron, J. S. Optimal Bandwidth Selection in Nonparametric Regression Function Estimation. *Annals of Statistics*, 13(4):1465–1481, 1985. 26

Hargreaves, B. A., Cunningham, C. H., Nishimura, D. G., and Conolly, S. M. Variable-Rate Selective Excitation for Rapid MRI Sequences. *Magnetic Resonance in Medicine*, 52:590–597, 2004. 21

Harshman, R. A. Foundations of the parafac procedure: models and conditions for an" explanatory" multimodal factor analysis. 1970. 97

He, Y. and Keyes, D. Reconstructing parameters of the FitzHugh-Nagumo system from boundary potential measurements. *J. Comput. Neurosci.*, 23:251–264, 2007. 129

Heiberg, E., Sjögren, J., Ugander, M., Carlsson, M., Engblom, H., and Arheden, H. Design and validation of segment-freely available software for cardiovascular image analysis. *BMC medical imaging*, 10(1):1, 2010. 104

Helm, P. A., Tseng, H. J., Younes, L., McVeigh, E. R., and Winslow, R. L. Ex-Vivo 3D Diffusion Tensor Imaging and Quantification of Cardiac Laminar Structure. *Magnetic Resonance in Medecine*, 54(4):850–859, 2005. 19, 27

Helm, P. A., Younes, L., Beg, M. F., Ennis, D. B., Leclercq, C., Faris, O. P., McVeigh, E., Kass, D., Miller, M. I., and Winslow, R. L. Evidence of structural remodeling in the dyssynchronous failing heart. *Circulation Research*, 98(1):125–132, 2006. 19

Helm, R. H., Byrne, M., Helm, P. A., Daya, S. K., Osman, N. F., Tunin, R., Halperin, H. R., Berger, R. D., Kass, D. A., and Lardo, A. C. Three-dimensional mapping of optimal left ventricular pacing site for cardiac resynchronization. *Circulation*, 115:953–961, February 2007. 114

Heyde, B., Barbosa, D., Claus, P., Maes, F., and D'hooge, J. Three-dimensional cardiac motion estimation based on non-rigid image registration using a novel transformation model adapted to the heart. In *Proc. STACOM MICCAI Workshop*, LNCS, 2012. 90, 92

Hodgkin, A. and Huxley, A. A quantitative description of membrane current and its application to conduction and excitation in nerve. *Journal of Physiology*, 177:500–544, 1952. 57

Hoffman, J. and Kaplan, S. The incidence of congenital heart disease. *Journal of the American College of Cardiology*, 39(12):1890–1900, 2002. 74

Holmes, A. A., Scollan, D., and Winslow, R. L. Direct histological validation of diffusion tensor mri in formaldehyde-fixed myocardium. *Magnetic Resonance in Medicine*, 44(1):157–161, 2000. ISSN 1522-2594. 19

Hsia, T. Y., Cosentino, D., Corsini, C., Pennati, G., Dubini, G., Migliavacca, F., and Investigators, M. o. C. H. A. M. Use of mathematical modeling to compare and predict hemodynamic effects between hybrid and surgical norwood palliations for hypoplastic left heart syndrome. *Circulation*, 124(11 Suppl):S204–10, 2011. URL http://www.ncbi.nlm.nih.gov/pubmed/21911814. 147

Hsu, E. W., Muzikant, A. L., Matulevicius, S. A., Penland, R. C., and Henriquez, C. S. Magnetic Resonance Myocardial Fiber-Orientation Mapping With Direct Histological Correlation. *Am J Physiol Heart Circ Physiol*, 274:1627–1634, 1998. 19

Hu, Z., Metaxas, D., and Axel, L. In vivo strain and stress estimation of the heart left and right ventricles from mri images. *Med Image Anal*, 7(4):435–444, Dec 2003. URL http://www.hubmed.org/display.cgi?uids=14561549. 52

Hufnagel, H. *A probabilistic framework for point-based shape modeling in medical image analysis*. Phd thesis, University of Lübeck, 2010. 73

Hui, W., Slorach, C., Dragulescu, A., Mertens, L., Bijnens, B., and Friedberg, M. K. Mechanisms of right ventricular electromechanical dyssynchrony and mechanical inefficiency in children after repair of tetralogy of fallot. *Circulation: Cardiovascular Imaging*, pages CIRCIMAGING–113, 2014. 100

Humphrey, J. *Cardiovascular Solid Mechanics*. Springer, 2002. 62

Humphrey, J., Strumpf, R., and Yin, F. Determination of a constitutive relation for passive myocardium: I. A new functional form. *ASME Journal of Biomechanical Engineering*, 112:333–339, 1990. 62

Hunter, P., McCulloch, A., and ter Keurs, H. Modelling the mechanical properties of cardiac muscle. *Progr. Biophys. Mol. Biol.*, 69:289–331, 1998. 62

Hunter, P., Nash, M., and Sands, G. *Computational Biology of the Heart*, chapter 12: Computational Electromechanics of the Heart, pages 345–407. John Wiley & Sons Ltd, West Sussex UK, 1997. 62

Hunter, P. and Nielsen, P. A strategy for integrative computational physiology. *Physiology (Bethesda)*, 20:316–325, Oct 2005. 52

Ilg, K., Baman, T. S., Gupta, S. K., Swanson, S., Good, E., Chugh, A., Jongnarangsin, K., Pelosi, F., Crawford, T., and Oral, H. Assessment of radiofrequency ablation lesions by cmr imaging after ablation of idiopathic ventricular arrhythmias. *Journal of the American College of Cardiology: Cardiovascular Imaging*, 3(3):278–285, 2010. 177

Ismail, H. and Makaryus, A. N. Predictors of response to cardiac resynchronization therapy: the holy grail of electrophysiology. *Int J Cardiovasc Imaging*, 26(2):197–198, Feb 2010. URL http://www.hubmed.org/display.cgi?uids=20041306. 51

Jaïs, P., Maury, P., Khairy, P., Sacher, F., Nault, I., Komatsu, Y., Hocini, M., Forclaz, A., Jadidi, A. S., and Weerasooryia, R. Elimination of local abnormal ventricular activities a new end point for substrate modification in patients with scar-related ventricular tachycardia. *Circulation*, 125 (18):2184–2196, 2012. 175

Jalife, J. and Gray, R. Drifting vortices of electrical waves underlie ventricular fibrillation in the rabbit heart. *Acta Physiologica Scandinavica*, 157(2):123–132, 1996. 37

Jing, L., Haggerty, C. M., Suever, J. D., Alhadad, S., Prakash, A., Cecchin, F., Skrinjar, O., Geva, T., Powell, A. J., and Fornwalt, B. K. Patients with repaired tetralogy of fallot suffer from intra- and inter-ventricular cardiac dyssynchrony: a cardiac magnetic resonance study. *European Heart Journal-Cardiovascular Imaging*, 15(12):1333–1343, 2014. 100

Johnson, S. G. The NLopt nonlinear-optimization package, 2012. URL http://ab-initio.mit.edu/nlopt. 121

Joshi, S., Davis, B., Jomier, M., and Gerig, G. Unbiased diffeomorphic atlas construction for computational anatomy. *NeuroImage*, 23(Supplement 1):S151 – S160, 2004. Mathematics in Brain Imaging. 76

Joshi, S., Kaziska, D., Srivastava, A., and Mio, W. Riemannian structures on shape spaces: A framework for statistical inferences. In Krim, H. and Yezzi, A., editors, *Statistics and Analysis of Shapes*, Modeling and Simulation in Science, Engineering and Technology, pages 313–333. Birkhäuser Boston, 2006. ISBN 978-0-8176-4481-9. URL http://dx.doi.org/10.1007/0-8176-4481-4_13. 76

Joshi, S., Klassen, E., Srivastava, A., and Jermyn, I. A novel representation for riemannian analysis of elastic curves in rn. *Computer Vision and Pattern Recognition, IEEE Computer Society Conference on*, 0:1–7, 2007a. 76

Joshi, S., Klassen, E., Srivastava, A., and Jermyn, I. Removing shape-preserving transformations in square-root elastic (sre) framework for shape analysis of curves. In *EMMCVPR'07*, pages 387–398, 2007b. 76

Julier, S. and Uhlmann, J. A new extension of the Kalman filter to nonlinear systems. In *International Symposium on Aerospace/Defense Sensing, Simulation and Controls*, volume 3, page 26, 1997. 117

Kaipio, J. and Somersalo, E. *Statistical and Computational Inverse Problems*. Springer, first edition, 2005. 130, 132, 133

Kanai, A. and Salama, G. Optical Mapping Reveals That Repolarization Spreads Anisotropically and Is Guided by Fiber Orientation in Guinea Pig Hearts. *Circulation Research*, 77:784–802, 1995. 19

Keener, J. and Sneyd, J. *Mathematical Physiology*. Springer, 1998. 41, 57

Kendall, D. A survey of the statistical theory of shape (with discussion). *Statistical Science*, 4: 87–120, 1989. 76

Kerckhoffs, R. C., Lumens, J., Vernooy, K., Omens, J. H., Mulligan, L. J., Delhaas, T., Arts, T., McCulloch, A. D., and Prinzen, F. W. Cardiac resynchronization: Insight from experimental and computational models. *Prog Biophys Mol Biol*, 97(2-3):543–561, Jun-Jul 2008a. 52

Kerckhoffs, R. C., McCulloch, A. D., Omens, J. H., and Mulligan, L. J. Effects of biventricular pacing and scar size in a computational model of the failing heart with left bundle branch block. *Med Image Anal*, Jul 2008b. 52

Kerckhoffs, R. C., Narayan, S. M., Omens, J. H., Mulligan, L. J., and McCulloch, A. D. Computational modeling for bedside application. *Heart Failure Clinics*, 4(3):371–378, Jul 2008c. URL http://www.hubmed.org/display.cgi?uids=18598988. 52

Kerckhoffs, R. C., Omens, J. H., McCulloch, A. D., and Mulligan, L. J. Ventricular dilation and electrical dyssynchrony synergistically increase regional mechanical nonuniformity but not mechanical dyssynchrony: a computational model. *Circulation Heart Failure*, 3(4):528–536, Jul 2010. URL http://www.hubmed.org/display.cgi?uids=20466849. 52

Killeen, M. J., Sabir, I. N., Grace, A. A., and Huang, C. L.-H. Dispersions of repolarization and ventricular arrhythmogenesis: Lessons from animal models. *Progress in Biophysics and Molecular Biology*, 98(2–3):219 – 229, 2008. ISSN 0079-6107. URL http://www.sciencedirect.com/science/article/pii/S0079610708000746. Focussed Issue: Translational models for cardiac arrhythmogenesis. 37

Kilner, P. J., Balossino, R., Dubini, G., Babu-Narayan, S. V., Taylor, A. M., Pennati, G., and Migliavacca, F. Pulmonary regurgitation: The effects of varying pulmonary artery compliance, and of increased resistance proximal or distal to the compliance. *Int. J. Cardiology*, 133(2):157–166, 2009. URL <GotoISI>://WOS:000264284500004. 148

Kim, H. W., Farzaneh-Far, A., and Kim, R. J. Cardiovascular magnetic resonance in patients with myocardial infarction: current and emerging applications. *Journal of the American College of Cardiology*, 55(1):1–16, 2009. 39

Kirn, B., Jansen, A., Bracke, F., van Gelder, B., Arts, T., and Prinzen, F. W. Mechanical discoordination rather than dyssynchrony predicts reverse remodeling upon cardiac resynchronization. *Am J Physiol Heart Circ Physiol*, 295(2):640–646, Aug 2008. URL http://www.hubmed.org/display.cgi?uids=18515652. 51

Knauth, A. L., Gauvreau, K., Powell, A. J., Landzberg, M. J., Walsh, E. P., Lock, J. E., del Nido, P. J., and Geva, T. Ventricular size and function assessed by cardiac mri predict major adverse clinical outcomes late after tetralogy of fallot repair. *Heart*, 94(2):211–216, 2008. 100

Kolda, T. G. and Bader, B. W. Tensor decompositions and applications. *SIAM review*, 51(3): 455–500, 2009. 97, 106, 108

Konofagou, E. E. and Provost, J. Electromechanical wave imaging for noninvasive mapping of the 3D electrical activation sequence in canines and humans in vivo. *Journal of Biomechanics*, 45(5): 856 – 864, 2012. Special Issue on Cardiovascular Solid Mechanics. 114

Konukoglu, E., Relan, J., Cilingir, U., Menze, B., Chinchapatnam, P., Jadidi, A., Cochet, H., Hocini, M., Delingette, H., Jaïs, P., Haïssaguerre, M., Ayache, N., and Sermesant, M. Efficient probabilistic model personalization integrating uncertainty on data and parameters: Application to eikonal-diffusion models in cardiac electrophysiology. *Progress in Biophysics and Molecular Biology*, 107 (1):134–146, 2011. 13, 49, 129

Konukoglu, E., Sermesant, M., Clatz, O., Peyrat, J. M., Delingette, H., and Ayache, N. A recursive anisotropic fast marching approach to reaction diffusion equation: application to tumor growth modeling. *Inf Process Med Imaging*, 20:687–699, 2007. 131

Koo, B.-K., Erglis, A., Doh, J.-H., Daniels, D. V., Jegere, S., Kim, H.-S., Dunning, A., DeFrance, T., Lansky, A., Leipsic, J., and Min, J. K. Diagnosis of ischemia-causing coronary stenoses by noninvasive fractional flow reserve computed from coronary computed tomographic angiograms. Results from the prospective multicenter DISCOVER-FLOW (Diagnosis of Ischemia-Causing Stenoses Obtained Via Noninvasive Fractional Flow Reserve) study. *J. Am. Coll. Cardiol.*, 58(19): 1989–1997, Nov 2011. URL http://dx.doi.org/10.1016/j.jacc.2011.06.066. 147

Kung, E. O., Les, A. S., Figueroa, C. A., Medina, F., Arcaute, K., Wicker, R. B., McConnell, M. V., and Taylor, C. A. In vitro validation of finite element analysis of blood flow in deformable models. *Ann. Biomed. Eng.*, 39:1947–1960, 2011a. 171

Kung, G. L., Nguyen, T. C., Itoh, A., Skare, S., Ingels, N. B., Miller, D. C., and Ennis, D. B. The presence of two local myocardial sheet populations confirmed by diffusion tensor mri and histological validation. *Journal of Magnetic Resonance Imaging*, 34(5):1080–1091, 2011b. ISSN 1522-2586. URL http://dx.doi.org/10.1002/jmri.22725. 27

LaDisa, J. F., Dholakia, R. J., Figueroa, C. A., Vignon-Clementel, I. E., Chan, F. P., Samyn, M. M., Cava, J. R., Taylor, C. A., and Feinstein, J. A. Computational simulations demonstrate altered wall shear stress in aortic coarctation patients treated by resection with end-to-end anastomosis. *Congenit. Heart Dis.*, 6(5):432–43, 2011. URL http://www.ncbi.nlm.nih.gov/pubmed/21801315. 147

Larrabide, I., Omedas, P., Martelli, Y., Planes, X., Nieber, M., Moya, J. A., Butakoff, C., Sebastián, R., Camara, O., and De Craene, M. Gimias: an open source framework for efficient development of research tools and clinical prototypes. In *Functional Imaging and Modeling of the Heart (FIMH)*, pages 417–426. Springer, 2009. 39

Le, H. and Kendall, D. The Riemannian structure of Euclidean shape space: a novel environment for statistics. *Annals of Statistics*, 21:1225–1271, 1993. 76

Le Folgoc, L., Delingette, H., Criminisi, A., and Ayache, N. Sparse bayesian registration. In *Medical Image Computing and Computer-Assisted Intervention–MICCAI 2014*. Springer, 2014. 93

Le Tallec, P. Numerical methods for nonlinear three-dimensional elasticity. In Ciarlet, P. and Lions, J.-L., editors, *Handbook of Numerical Analysis*, volume 3. Elsevier, 1994. 63

LeGrice, I. J., Takayama, Y., and Covell, J. W. The Architecture of the Heart: a Data-based Model. *Philosophical Transactions: Mathematical, Physical and Engineering Sciences*, 359:1217–1232, 2001. 22

Liang, Z., Li, Y., and Shi, P. A note on two-dimensional linear discriminant analysis. *Pattern Recognition Letters*, 29(16):2122–2128, 2008. 103

Liu, C., Skadsberg, N., Ahlberg, S., Swingen, C., Iaizzo, P., and He, B. Estimation of global ventricular activation sequences by noninvasive three-dimensional electrical imaging: validation studies in a swine model during pacing. *Journal of Cardiovascular Electrophysiolgy*, 19(5):535–40, 2008. 113

Liu, H. and Shi, P. State-space analysis of cardiac motion with biomechanical constraints. *IEEE Transactions on Image Processing*, 16(4):901–917, 2007. 52

Lombaert, H., Peyrat, J.-M., Croisille, P., Rapacchi, S., Fanton, L., Clarysse, P., Delingette, H., and Ayache, N. Statistical analysis of the human cardiac fiber architecture from dt-mri. In Axel, L. and Metaxas, D., editors, *Proceedings of FIMH Conference 2011*, volume 6666 of *LNCS*, pages 171–179. Springer, May 2011a. Best Paper Award. 27, 33

Lombaert, H., Peyrat, J.-M., Fanton, L., Cheriet, F., Delingette, H., Ayache, N., Clarysse, P., Magnin, I., and Croisille, P. Variability of the human cardiac laminar structure. In *Proceedings of STACOM Workshop at MICCAI 2011*. Springer, September 2011b. 19, 33

Løvgren, A., Maday, Y., and Rønquist, E. The reduced basis element method for fluid flows. In *Analysis and simulation of fluid dynamics*, Adv. Math. Fluid Mech., pages 129–154. Birkhäuser, 2007. 155

Luo, C. and Rudy, Y. A model of the ventricular cardiac action potential: depolarization, repolarization, and their interaction. *Circulation Research*, 68:1501–1526, 1991. 57

Lustig, M., Donoho, D., Santos, J. M., and Pauly, J. M. Compressed sensing in MRI. *IEEE Signal Processing Magazine*, 72, March 2008. 145

Ma, X. and Zabaras, N. An efficient Bayesian inference approach to inverse problems based on an adaptive sparse grid collocation. *Inverse Problems*, 25, 2009. 131, 145

Mansi, T. *Image-Based Physiological and Statistical Models of the Heart, Application to Tetralogy of Fallot*. Thèse de sciences (phd thesis), Ecole Nationale Supérieure des Mines de Paris, 2010. 73, 156

Mansi, T., Durrleman, S., Bernhardt, B., Sermesant, M., Delingette, H., Voigt, I., Lurz, P., A. M. Taylor, J. B., Boudjemline, Y., Pennec, X., and Ayache, N. A statistical model of right ventricle in tetralogy of fallot for prediction of remodelling and therapy planning. In *Proc. Medical Image Computing and Computer Assisted Intervention (MICCAI'09)*, volume 5761 of *Lecture Notes in Computer Science*, pages 214–221. Springer, 2009. 73

Mansi, T., Pennec, X., Sermesant, M., Delingette, H., and Ayache, N. iLogDemons: A Demons-Based Registration Algorithm for Tracking Incompressible Elastic Biological Tissues. *Int. J. of Computer Vision*, 92(1):92 – 111, 2011a. 23, 27, 31, 90, 99, 114

Mansi, T., Voigt, I., Leonardi, B., X. Pennec, S. D., Sermesant, M., H. Delingette, A. M. T., Boudjemline, Y., Pongiglione, G., and Ayache, N. A statistical model for quantification and prediction of cardiac remodelling: Application to tetralogy of fallot. *IEEE Transactions on Medical Images*, 2011b. 73, 83

Manzoni, A., Quarteroni, A., and Rozza, G. Model reduction techniques for fast blood flow simulation in parametrized geometries. *Int. J. Num. Meth. Biomed. Engnr.*, 2011. 148

Marchesseau, S., Delingette, H., Sermesant, M., and Ayache, N. Fast parameter calibration of a cardiac electromechanical model from medical images based on the unscented transform. *Biomechanics and Modeling in Mechanobiology*, 2012a. 116, 117

Marchesseau, S., Delingette, H., Sermesant, M., and Ayache, N. Fast parameter calibration of a cardiac electromechanical model from medical images based on the unscented transform. *Biomechanics and modeling in mechanobiology*, 12(4):815–831, 2013. 8

Marchesseau, S., Delingette, H., Sermesant, M., Rhode, K., Duckett, S., Rinaldi, C., Razavi, R., and Ayache, N. Cardiac mechanical parameter calibration based on the unscented transform. In Ayache, N., Delingette, H., Golland, P., and Mori, K., editors, *Medical Image Computing and Computer-Assisted Intervention - MICCAI 2012*, volume 7511 of *LNCS*, pages 41–48. Springer, Heidelberg, October 2012b. 117

Markl, M., Geiger, J., Jung, B., Hirtler, D., and Arnold, R. Noninvasive Evaluation of 3D Hemodynamics in a Complex Case of Single Ventricle Physiology. *J. Magn. Reson. Imaging*, 35:933–937, 2012. 147

Marzouk, Y., Najm, H., and Rahn, L. Stochastic spectral methods for efficient Bayesian solution of inverse problems. *Journal of Computational Physics*, 224:560–586, 2007. 131

Marzouk, Y. and Xiu, D. A stochastic collocation approach to Bayesian inference in inverse problems. *Communications in computational physics*, 6(7):826–847, 2009. 131, 132

Marzouk, Y. M. and Najm, H. N. Dimensionality reduction and polynomial chaos acceleration of Bayesian inference in inverse problems. *Journal of Computational Physics*, 228:1862–1902, 2009. 131, 132, 133

McGregor, R., Szczerba, D., Muralidhar, K., and Székely, G. A fast alternative to computational fluid dynamics for high quality imaging of blood flow. *Medical Image Computing and Computer-Assisted Intervention–MICCAI 2009*, pages 124–131, 2009. 148

Mcgregor, R., Szczerba, D., von Siebenthal, M., Muralidhar, K., and Székely, G. Exploring the use of proper orthogonal decomposition for enhancing blood flow images via computational fluid dynamics. *Medical Image Computing and Computer-Assisted Intervention–MICCAI 2008*, pages 782–789, 2008. 148

McInerney, T. and Terzopoulos, D. Deformable models in medical images analysis: a survey. *Medical Image Analysis*, 1(2):91–108, 1996. 60

McLeod, K., Caiazzo, A., Fernández, M. A., Mansi, T., Vignon-Clementel, I. E., Sermesant, M., Pennec, X., Boudjemline, Y., and Gerbeau, J.-F. Atlas-Based Reduced Models of Blood Flows for Fast Patient-Specific Simulations. In *Proc. MICCAI Workshop on Statistical Atlases and Computational Models of the Heart: Mapping Structure and Function + a Cardiac Electrophysiological Simulation Challenge (STACOM+CESC'10)*, volume 6364 of *LNCS*, pages 95–104, Beijing, September 2010. Springer. 148

McLeod, K., Mansi, T., Sermesant, M., Pongiglione, G., and Pennec, X. Statistical shape analysis of surfaces in medical images applied to the tetralogy of fallot heart. In *Modeling in Computational Biology and Biomedicine*, Lectures Notes in Mathematical and Computational Biology, pages 165–191. Springer, 2013. ISBN 978-3-642-31207-6. URL http://www-sop.inria.fr/asclepios/Publications/Xavier.Pennec/McLeod_Pennec_CBB.pdf. 10, 73

McLeod, K., Prakosa, A., Mansi, T., Sermesant, M., and Pennec, X. An incompressible log-domain demons algorithm for tracking heart tissue. In *Proc. STACOM MICCAI Workshop*, LNCS. Springer, 2011. 92, 99, 114

McLeod, K., Seiler, C., Sermesant, M., and Pennec, X. A near-incompressible poly-affine motion model for cardiac function analysis. In *Proc. STACOM MICCAI Workshop*, LNCS. Springer, 2012. 90, 91, 92, 99

Mcleod, K., Seiler, C., Sermesant, M., and Pennec, X. Spatio-temporal dimension reduction of cardiac motion for group-wise analysis and statistical testing. In *MICCAI - Medical Image Computing and Computer Assisted Intervention - 2013*, Lecture Notes in Computer Science. Springer, Heidelberg, 2013a. 91, 95, 97, 107

Mcleod, K., Seiler, C., Toussaint, N., Sermesant, M., and Pennec, X. Regional analysis of left ventricle function using a cardiac-specific polyaffine motion model. In *Proc. FIMH'13*, 2013b. 90, 91, 92, 99, 106

McLeod, K., Sermesant, M., Beerbaum, P., and Pennec, X. Spatio-temporal tensor decomposition of a polyaffine motion model for a better analysis of pathological left ventricular dynamics. *IEEE Transactions on Medical Imaging*, 34(7):1562–1575, July 2015. ISSN 0278-0062. 11, 89

McVeigh, E. R., Prinzen, F. W., Wyman, B. T., Tsitlik, J. E., Halperin, H. R., and Hunter, W. C. Imaging asynchronous mechanical activation of the paced heart with tagged MRI. *Magnetic Resonance in Medicine*, 39:507–513, April 1998. 114

Miller, M., Trouvé, A., and Younes, L. On the metrics and Euler-Lagrange equations of computational anatomy. *Annual Re-view of Biomedical Engineering*, pages 375–405, 2003. 79

Miller, M. and Younes, L. Group actions, homeomorphisms, and matching: A general framework. *International Journal of Computer Vision*, 41(1/2):61–84, 2001. 76

Miller, M. I. and Qiu, A. The emerging discipline of computational functional anatomy. *NeuroImage*, 45(1, Supplement 1):S16 – S39, 2009. ISSN 1053-8119. URL http://www.sciencedirect.com/science/article/pii/S1053811908011622. Mathematics in Brain Imaging. 9

Mio, W., Srivastava, A., and Joshi, S. H. On shape of plane elastic curves. *International Journal of Computer Vision*, pages 307–324, 2007. 76

Mitchell, C. C. and Schaeffer, D. G. A two current model for the dynamics of cardiac membrane. *Bulletin of Mathematical Biology*, 65(5):767–793, 2003. 40, 117

Moireau, P., Chapelle, D., and Le Tallec, P. Joint state and parameter estimation for distributed mechanical systems. *Computer Methods in Applied Mechanics and Engineering*, 197:659–677, 2008. 60, 68

Moireau, P., Chapelle, D., and Le Tallec, P. Filtering for distributed mechanical systems using position measurements: Perspectives in medical imaging. *Inverse Problems*, 25(3):10–35, 2009. 68

Montagnat, J. and Delingette, H. 4D deformable models with temporal constraints: application to 4D cardiac image segmentation. *Medical Image Analysis*, 9(1):87–100, February 2005. 60

Moore, S. M., Moorhead, K. T., Chase, J. G., David, T., and Fink, J. One-dimensional and three-dimensional models of cerebrovascular flow. *J. Biomech. Engnr.-Trans. Asme*, 127:440–449, 2005. 148

Morales, H. G., Kim, M., Vivas, E. E., Villa-Uriol, M. C., Larrabide, I., Sola, T., Guimaraens, L., and Frangi, A. F. How do coil configuration and packing density influence intra-aneurysmal hemodynamics? *Am. J. Neuroradiol.*, 32(10):1935–1941, Nov-Dec 2011. 148

Moreau-Villéger, V., Delingette, H., Sermesant, M., Ashikaga, H., McVeigh, E., and Ayache, N. Building maps of local apparent conductivity of the epicardium with a 2D electrophysiological model of the heart. *IEEE Transactions on Biomedical Engineering*, 53(8):1457–1466, August 2006. 57

Moss, A. J., Hall, W. J., Cannom, D. S., Daubert, J. P., Higgins, S. L., Klein, H., Levine, J. H., Saksena, S., Waldo, A. L., Wilber, D., Brown, M. W., and Heo, M. Improved survival with an implanted defibrillator in patients with coronary disease at high risk for ventricular arrhythmia. *New England Journal of Medicine*, 335(26):1933–1940, 1996. URL http://dx.doi.org/10.1056/NEJM199612263352601. PMID: 8960472. 37

Murray, J. *Mathematical Biology*. Springer-Verlag, second edition, 2002. 129, 130

Nash, M. *Mechanics and Material Properties of the Heart using an Anatomically Accurate Mathematical Model*. PhD thesis, University of Auckland, 1998. 62

Nash, M. P., Bradley, C. P., Sutton, P. M., Clayton, R. H., Kallis, P., Hayward, M. P., Paterson, D. J., and Taggart, P. Whole heart action potential duration restitution properties in cardiac patients: a combined clinical and modelling study. *Experimental Physiology*, 91(2):339–354, 2006. 37

TA095: arrhythmia—implantable cardioverter defibrillators (ICDs) (review). National Institute for Health and Clinical Excellence, London, 2006. URL www.nice.org.uk/TA95. 37, 39

Nielles-Vallespin, S., Mekkaoui, C., Reese, T. G., Gatehouse, P., Feiweier, T., Speier, P., Sosnovik, D. E., , and Firmin, D. Fiber Tracking of the Human Heart in Vivo. In *Proc. of the the annual meeting of International Society of Magnetic Resonance in Medicine (ISMRM'11)*, 2011. Abstract 3372. 19

Nielsen, P. M., Grice, I. J. L., Smaill, B. H., and Hunter, P. J. Mathematical Model of Geometry and Fibrous Structure of the Heart. *Am J Physiol Heart Circ Physiol*, 260:1365–1378, 1991. 22

Nobile, F., Tempone, R., and Webster, C. A sparse grid stochastic collocation method for partial differential equations with random input data. *SIAM J. Numer. Anal.*, 46(5):2309–2345, 2008. 131, 145

Noble, D. A modification of the Hodgkin–Huxley equations applicable to purkinje fibre action and pace-maker potentials. *J Physiol*, 160:317–352, 1962. 57

Noble, D., Varghese, A., Kohl, P., and Noble, P. Improved guinea-pig ventricular cell model incorporating a diadic space, I_{Kr} and I_{Ks}, and length and tension dependent processes. *Canadian Journal of Cardiology*, 14:123–134, 1998. 57

Otani, N., Luther, S., Singh, R., and Gilmour, R. Transmural ultrasound-based visualization of patterns of action potential wave propagation in cardiac tissue. *Annals of Biomedical Engineering*, 38:3112–3123, 2010. 114, 115

Oubel, E., Koob, M., Studholme, C., Dietemann, J.-L., and Rousseau, F. Reconstruction of scattered data in fetal diffusion mri. *Medical Image Analysis*, 16(1):28 – 37, 2012. ISSN 1361-8415. 21

Ourselin, S., Roche, A., Prima, S., and Ayache, N. Block matching: A general framework to improve robustness of rigid registration of medical images. In DiGioia, A. and Delp, S., editors, *Third International Conference on Medical Robotics, Imaging And Computer Assisted Surgery (MICCAI 2000)*, volume 1935 of *Lectures Notes in Computer Science*, pages 557–566, Pittsburgh, Penn, USA, octobre 11-14 2000. Springer. 60

Panfilov, A. and Keener, J. Re-entry in an anatomical model of the heart. *Chaos, Solitons and Fractals*, 5(3–4):681–689, 1995. ISSN 0960-0779. URL http://www.sciencedirect.com/science/article/pii/0960077993E0050L. Nonlinear Phenomena in Excitable Physiological Systems. 37

Pant, S., Limbert, G., Curzen, N. P., and Bressloff, N. W. Multiobjective design optimisation of coronary stents. *Biomaterials*, 32(31):7755–7773, 2011. URL <GotoISI>://WOS:000295072600002. 147

Park, J., Metaxas, D., and Axel, L. Analysis of left ventricular wall motion based on volumetric deformable models and MRI-SPAMM. *Medical Image Analysis*, pages 53–71, 1996. 60

Pedregosa, F., Varoquaux, G., Gramfort, A., Michel, V., Thirion, B., Grisel, O., Blondel, M., Prettenhofer, P., Weiss, R., and Dubourg, V. Scikit-learn: Machine learning in python. *The Journal of Machine Learning Research*, 12:2825–2830, 2011. 176

Pekkan, K., Dasi, L. P., de Zélicourt, D., Sundareswaran, K. S., Fogel, M. A., Kanter, K. R., and Yoganathan, A. P. Hemodynamic performance of stage-2 univentricular reconstruction: Glenn vs. hemi-Fontan templates. *Ann Biomed Eng*, 37(1):50–63, Jan 2009. 171

Pennec, X. Intrinsic statistics on riemannian manifolds: Basic tools for geometric measurements. *Journal of Mathematical Imaging and Vision*, 25(1):127–154, July 2006. A preliminary appeared as INRIA RR-5093, January 2004. 76

Pennec, X. Statistical computing on manifolds: from riemannian geometry to computational anatomy. In *Emerging Trends in Visual Computing*, volume 5416 of *LNCS*, pages 347–386. Springer, 2008. 76

Pernod, E., Sermesant, M., Konukoglu, E., Relan, J., Delingette, H., and Ayache, N. A multi-front Eikonal model of cardiac electrophysiology for interactive simulation of radio-frequence ablation. *Computers and Graphics*, 35:431–40, 2011. 131

Perperidis, D., Lorenzo-Valdes, M., Chandrashekara, R., Rao, A., Mohiaddin, R., Sanchez-Ortiz, G., and Rueckert, D. Building a 4D atlas of the cardiac anatomy and motion using MR imaging. In *Biomedical Imaging: Nano to Macro, 2004. IEEE International Symposium on*, pages 412–415. IEEE, 2004. 90

Perperidis, D., Mohiaddin, R. H., and Rueckert, D. Spatio-temporal free-form registration of cardiac mr image sequences. *Medical image analysis*, 9(5):441–456, 2005. 107

Perperidis, D., Rao, A., Lorenzo-Valdés, M., Mohiaddin, R., and Rueckert, D. Spatio-temporal alignment of 4D cardiac MR images. In *Functional Imaging and Modeling of the Heart*, pages 205–214. Springer, 2003. 90

Peters, J., Ecabert, O., Meyer, C., Kneser, R., and Weese, J. Optimizing boundary detection via simulated search with applications to multi-modal heart segmentation. *Medical Image Analysis*, 14 (1):70 – 84, 2010. ISSN 1361-8415. URL http://www.sciencedirect.com/science/article/B6W6Y-4XHCJ4V-1/2/d321a70669d2012651ee5a342d1c3d7c. 55, 68

Peters, J., Ecabert, O., Meyer, C., Schramm, H., Kneser, R., Groth, A., and Weese, J. Automatic whole heart segmentation in static magnetic resonance image volumes. In *Medical Image Computing and Computer-Assisted Intervention–MICCAI 2007*, pages 402–410. Springer, 2007. 39

Peyrat, J.-M., Sermesant, M., Pennec, X., Delingette, H., Xu, C., McVeigh, E. R., and Ayache, N. A computational framework for the statistical analysis of cardiac diffusion tensors: Application to a small database of canine hearts. *IEEE Transactions on Medical Imaging*, 26(11):1500–1514, November 2007. 19, 24, 33, 56

Pfeifer, B., Hanser, F., Seger, M., Fischer, G., Modre-Osprian, R., and Tilg, B. Patient-specific volume conductor modeling for non-invasive imaging of cardiac electrophysiology. *Open Med Inform J*, 2:32–41, 2008. URL http://www.hubmed.org/display.cgi?uids=19415133. 68

Powell, M. The NEWUOA software for unconstrained optimization without derivatives. In Pillo, G. D. and Roma, M., editors, *Large-Scale Nonlinear Optimization*, pages 255–297. Springer, 2006. 57

Powell, M. J. D. Developments of NEWUOA for Minimization Without Derivatives. *Journal of Numerical Analysis*, pages 1–16, February 2008. 29

Powell, M. J. D. The BOBYQA algorithm for bound constrained optimization without derivatives. *DAMTP 2009/NA06*, August 2009. 121

Prakosa, A., Sermesant, M., Allain, P., Villain, N., Rinaldi, C. A., Rhode, K. S., Razavi, R., Delingette, H., and Ayache, N. Cardiac electrophysiological activation pattern estimation from images using a patient-specific database of synthetic image sequences. *IEEE Trans. Biomed. Engineering*, 61(2):235–245, 2014. URL http://dx.doi.org/10.1109/TBME.2013.2281619. 12, 113

Prakosa, A., Sermesant, M., Delingette, H., Marchesseau, S., Saloux, E., Allain, P., Villain, N., and Ayache, N. Generation of synthetic but visually realistic time series of cardiac images combining a biophysical model and clinical images. *Medical Imaging, IEEE Transactions on*, 32(1):99–109, 2013. 114, 117, 118, 127

Prakosa, A., Sermesant, M., Delingette, H., Saloux, E., Allain, P., Cathier, P., Etyngier, P., Villain, N., and Ayache, N. Non-invasive activation times estimation using 3D echocardiography. In Camara, O., Pop, M., Rhode, K., Sermesant, M., Smith, N., and Young, A., editors, *Statistical Atlases and Computational Models of the Heart*, volume 6364 of *LNCS*, pages 212–221, Beijing, China, 2010. Springer, Heidelberg. 114, 115

Prakosa, A., Sermesant, M., Delingette, H., Saloux, E., Allain, P., Cathier, P., Etyngier, P., Villain, N., and Ayache, N. Synthetic echocardiographic image sequences for cardiac inverse electro-kinematic learning. In Fichtinger, G., Martel, A., and Peters, T., editors, *Medical Image Computing and Computer-Assisted Intervention - MICCAI 2011*, volume 6891 of *LNCS*, pages 500–507, Toronto, Canada, September 2011. Springer, Heidelberg. 114, 119

Prasad, A., To, L. K., Gorrepati, M. L., Zarins, C. K., and Figueroa, C. A. Computational analysis of stresses acting on intermodular junctions in thoracic aortic endografts. *J. Endovasc. Ther.*, 18 (4):559–68, 2011. URL http://www.ncbi.nlm.nih.gov/pubmed/21861748. 147

Provost, J., Gurev, V., Trayanova, N., and Konofagou, E. E. Mapping of cardiac electrical activation with electromechanical wave imaging: An in silico–in vivo reciprocity study. *Heart Rhythm*, 8(5): 752 – 759, 2011. 114

Provost, J., Lee, W., Fujikura, K., and Konofagou, E. Electromechanical wave imaging of normal and ischemic hearts in vivo. *Medical Imaging, IEEE Transactions on*, 29:625–635, March 2010. 114

Pueyo, E., Corrias, A., Virág, L., Jost, N., Szél, T., Varró, A., Szentandrássy, N., Nánási, P. P., Burrage, K., and Rodríguez, B. A multiscale investigation of repolarization variability and its role in cardiac arrhythmogenesis. *Biophysical Journal*, 101(12):2892 – 2902, 2011. ISSN 0006-3495. URL http://www.sciencedirect.com/science/article/pii/S0006349511012410. 37

Puranik, R., Muthurangu, V., Celermajer, D. S., and Taylor, A. M. Congenital Heart Disease and Multi-modality Imaging. *Heart Lung and Circulation*, 19(3):133–144, 2010. 147

Qian, Z., Liu, Q., Metaxas, D. N., and Axel, L. Identifying regional cardiac abnormalities from myocardial strains using nontracking-based strain estimation and spatio-temporal tensor analysis. *Medical Imaging, IEEE Transactions on*, 30(12):2017–2029, 2011. 90, 91, 103

Ramanathan, C., Ghanem, R. N., Jia, P., Ryu, K., and Rudy, Y. Noninvasive electrocardiographic imaging for cardiac electrophysiology and arrhythmia. *Nature Medicine*, 10(4):422–8, 2004. 113, 135

Rao, A., Sanchez-Ortiz, G. I., Chandrashekara, R., Lorenzo-Valdés, M., Mohiaddin, R., and Rueckert, D. Comparison of cardiac motion across subjects using non-rigid registration. In *Medical Image Computing and Computer-Assisted Intervention—MICCAI 2002*, pages 722–729. Springer, 2002. 90

Rao, A., Sanchez-Ortiz, G. I., Chandrashekara, R., Lorenzo-Valdés, M., Mohiaddin, R., and Rueckert, D. Construction of a cardiac motion atlas from mr using non-rigid registration. In *Functional Imaging and Modeling of the Heart*, pages 141–150. Springer, 2003. 90

Rathinam, M. and Petzold, L. A new look at proper orthogonal decomposition. *SIAM J Num. An.*, 41(5):1893–1925, 2004. 148, 153

Reese, T. G., Weisskoff, R. M., Smith, R. N., Rosen, B. R., Dinsmore, R. E., and Wedeen, V. J. Imaging Myocardial Fiber Architecture In-Vivo With Magnetic Resonance. *Magnetic Resonance in Medicine*, 34:786–791, 1995. 19

Relan, J., Chinchapatnam, P., Sermesant, M., Rhode, K., Ginks, M., Delingette, H., Rinaldi, C. A., Razavi, R., and Ayache, N. Coupled personalization of cardiac electrophysiology models for prediction of ischaemic ventricular tachycardia. *Journal of the Royal Society Interface Focus*, 1(3): 396–407, 2011a. 7, 37, 40, 42, 132

Relan, J., Pop, M., Delingette, H., Wright, G., Ayache, N., and Sermesant, M. Personalisation of a cardiac electrophysiology model using optical mapping and mri for prediction of changes with pacing. *Bio-Medical Engineering, IEEE Transactions on*, 58(12):3339–3349, 2011b. 7, 40, 41, 125

Reymond, P., Perren, F., Lazeyras, F., and Stergiopulos, N. Patient-specific mean pressure drop in the systemic arterial tree, a comparison between 1-d and 3-d models. *J. Biomech.*, 45:2499–2505, 2012. 148

Rhode, K., Sermesant, M., Brogan, D., Hegde, S., Hipwell, J., Lambiase, P., Rosenthal, E., Bucknall, C., Qureshi, S., Gill, J., Razavi, R., and Hill, D. A system for real-time XMR guided cardiovascular intervention. *IEEE Transactions on Medical Imaging*, 24(11):1428–1440, 2005. 54

Richardson, P., McKenna, W., Bristow, M., Maisch, B., Mautner, B., O'Connell, J., Olsen, E., Thiene, G., Goodwin, J., and Gyarfas, I. Report of the 1995 who/isfc task force on the definition and classification of cardiomyopathies. *Circulation*, 93(5):841–842, 1996. 38

Richmond, L., Rajappan, K., Voth, E., Rangavajhala, V., Earley, M., Thomas, G., Harris, S., Sporton, S., and Schilling, R. Validation of computed tomography image integration into the EnSite NavX mapping system to perform catheter ablation of atrial fibrillation. *Journal of Cardiovascular Electrophysiology*, 19(8):821–827, 2008. ISSN 1540-8167. 135

Rineau, L., Tayeb, S., and Yvinec, M. 3D mesh generation. In CGAL Editorial Board, editor, *CGAL User and Reference Manual*. 3.5 edition, 2009. 116

Rohmer, D. and Gullberg, G. T. A Bloch-Torrey Equation for Diffusion in a Deforming Media. Technical report, University of California, 2006. Technical report Paper LBNL-61295. 22

Rougon, N. F., Petitjean, C., and Preteux, F. J. Building and using a statistical 3D motion atlas for analyzing myocardial contraction in MRI. In *Medical Imaging 2004*, pages 253–264. International Society for Optics and Photonics, 2004. 90

Rudy, Y. Noninvasive electrocardiographic imaging of arrhythmogenic substrates in humans. *Circulation Research*, 112(5):863–874, 2013. 49

Ruschhaupt, M., Huber, W., Poustka, A., and Mansmann, U. A compendium to ensure computational reproducibility in high-dimensional classification tasks. *Statistical Applications in Genetics and Molecular Biology*, 3(1), 2004. 176

Sacher, F., Roberts-Thomson, K., Maury, P., Tedrow, U., Nault, I., Steven, D., Hocini, M., Koplan, B., Leroux, L., Derval, N., Seiler, J., Wright, M., Epstein, L., Haissaguerre, M., Jais, P., and Stevenson, W. Epicardial ventricular tachycardia ablation: A multicenter safety study. *Journal of the American College of Cardiology*, 55(21):2366 – 2372, 2010. ISSN 0735-1097. 135

Sachse, F. B. *Computational Cardiology, Modeling of Anatomy, Electrophysiology, and Mechanics*, volume 2966 of *Lecture Notes in Computer Science*. Springer, 2004. 62

Sainte-Marie, J., Chapelle, D., Cimrman, R., and Sorine, M. Modeling and estimation of the cardiac electromechanical activity. *Computers & Structures*, 84:1743–1759, 2006. 62, 63

Sanchez-Ortiz, G., Sermesant, M., Chandrashekara, R., Rhode, K., Razavi, R., Hill, D., and Rueckert, D. Detecting the onset of myocardial contraction for establishing inverse electro-mechanical coupling in XMR guided RF ablation. In *Proceedings of International Symposium on Biomedical Imaging*, pages 1055–1058, Arlington, 2004. IEEE. 114

Schär, M., Kozerke, S., Fischer, S. E., and Boesiger, P. Cardiac ssfp imaging at 3 tesla. *Magnetic Resonance in Medicine*, 51(4):799–806, 2004. ISSN 1522-2594. 20

Schilling, R. J., Peters, N. S., and Davies, D. W. Simultaneous endocardial mapping in the human left ventricle using a noncontact catheter comparison of contact and reconstructed electrograms during sinus rhythm. *Circulation*, 98(9):887–898, 1998. 39, 48

Schwartz, M., Rome, J., Gillespie, M., Whitehead, K., Harris, M., Fogel, M., and Glatz, A. Relation of Left Ventricular End Diastolic Pressure to Right Ventricular End Diastolic Volume After Operative Treatment of Tetralogy of Fallot. *Am. J. Card.*, 2011. 160

Scollan, D. F., Holmes, A., Zhang, J., and Winslow, R. L. Reconstruction of Cardiac Ventricular Geometry and Fiber Orientation Using Magnetic Resonance Imaging. *Annals of Biomedical Engineering*, 28:934–944, 2000. 19, 27, 32, 33

Seiler, C., Pennec, X., and Reyes, M. Capturing the multiscale anatomical shape variability with polyaffine transformation trees. *Med. Image Anal.*, 2012. 92

Sermesant, M., Chabiniok, R., Chinchapatnam, P., Mansi, T., Billet, F., Moireau, P., Peyrat, J., Wong, K., Relan, J., Rhode, K., Ginks, M., Lambiase, P., Delingette, H., Sorine, M., Rinaldi, C., Chapelle, D., Razavi, R., and Ayache, N. Patient-specific electromechanical models of the heart for the prediction of pacing acute effects in CRT: A preliminary clinical validation. *Medical Image Analysis*, 16(1):201–215, 2012. 8, 51, 126

Sermesant, M., Coudière, Y., Moreau-Villéger, V., Rhode, K. S., Hill, D. L., and Razavi, R. A fast-marching approach to cardiac electrophysiology simulation for xmr interventional imaging. In *Medical Image Computing and Computer-Assisted Intervention–MICCAI 2005*, pages 607–615. Springer, 2005. 40

Sermesant, M., Delingette, H., and Ayache, N. An electromechanical model of the heart for image analysis and simulation. *IEEE Transactions in Medical Imaging*, 25(5):612–625, 2006a. 58, 60

Sermesant, M., Konukoglu, E., Delingette, H., Coudiere, Y., Chinchaptanam, P., Rhode, K., Razavi, R., and Ayache, N. An anisotropic multi-front fast marching method for real-time simulation of cardiac electrophysiology. In *Proceedings of Functional Imaging and Modeling of the Heart 2007 (FIMH'07)*, volume 4466 of *LNCS*, pages 160–169, 7-9 June 2007. 57, 117

Sermesant, M., Moireau, P., Camara, O., Sainte-Marie, J., Andriantsimiavona, R., Cimrman, R., Hill, D. L., Chapelle, D., and Razavi, R. Cardiac Function Estimation from MRI Using a Heart Model and Data Assimilation: Advances and Difficulties. *Medical Image Analysis*, 10(4):642–656, 2006b. 68

Shi, W., Zhuang, X., Wang, H., Duckett, S., Luong, D. V., Tobon-Gomez, C., Tung, K., Edwards, P. J., Rhode, K. S., Razavi, R. S., et al. A comprehensive cardiac motion estimation framework using both untagged and 3D tagged MR images based on nonrigid registration. *IEEE Trans. Med. Imaging*, 31(6):1263–1275, 2012. 90

Small, C. *The Statistical Theory of Shapes*. Springer series in statistics. Springer, 1996. 76

Smith, N., Nickerson, D., Crampin, E., and Hunter, P. Computational mechanics of the heart. from tissue structure to ventricular function. *J. of Elasticity*, 61(1):113–141, 2000. 62

Sohal, M., Shetty, A., Duckett, S., Chen, Z., Sammut, E., Amraoui, S., Carr-White, G., Razavi, R., and Rinaldi, C. A. Non-invasive assessment of left ventricular contraction patterns using cardiac magnetic resonance imaging to identify responders to cardiac resynchronization therapy. *Journal of the American College of Cardiology: Cardiovascular Imaging*, 2013. In press, available online. 114

Sosnovik, D. E., Wang, R., Dai, G., Reese, T. G., and Wedeen, V. J. Diffusion MR Tractography of the Heart. *Journal of Cardiovascular MR*, 11:1–47, 2009. 19

Spilker, R., Feinstein, J., Parker, D., Reddy, V., and Taylor, C. Morphometry-Based Impedance Boundary Conditions for Patient-Specific Modeling of Blood Flow in Pulmonary Arteries. *Ann. Biomed. Engnr.*, 35(4):546, 2007. URL http://dx.doi.org/10.1007/s10439-006-9240-3. 148

Steinhaus, B. Estimating cardiac transmembrane activation and recovery times from unipolar and bipolar extracellular electrograms: a simulation study. *Circulation Research*, 64(3), 1989. 132, 137

Stejskal, E. and Tanner, J. Spin Diffusion Measurements: Spin Echoes in the Presence of a Time-Dependant Field Gradient. *Journal Of Chemical Physics*, 42:288–292, 1965. 21

Stergiopulos, N., Westerhof, B., and Westerhof, N. Total arterial inertance as the fourth element of the windkessel model. *American Journal of Physiology*, 276:H81–8, 1999. 60

Stoeck, C. T., Toussaint, N., and Kozerke, S. Adaptative trigger delay for cardiac diffusion weighted mr. In *Book of Abstracts, International Society in Magnetic Resonance in Medicine, Sockholm, June 2010 (ISMRM'10)*, 2011. 20

Streeter, D. *Handbook of Physiology*, chapter The Cardiovascular System: Gross Morphology and Fiber Geometry of the Heart. Williams & Wilkins, 1979. 55

Streeter, D. D. and Hanna, W. T. Engineering mechanics for successive states in canine left ventricular myocardium (II. fiber angle and sarcomere length). *Circulation Research*, 33:656–664, 1973. 32

Sutton, M. G. S. J. and Sharpe, N. Left Ventricular Remodeling After Myocardial Infarction. *Circulation: Cardiovascular Imaging*, 101:2981–2988, 2000. 19

Sutton, M. S. and Keane, M. G. Reverse remodelling in heart failure with cardiac resynchronisation therapy. *Heart*, 93(2):167–171, Feb 2007. 52

Tarantola, A. *Inverse Problem Theory*. SIAM, 2005. 130

Tautz, L., Hennemuth, A., and Peitgen, H.-O. Motion analysis with quadrature filter based registration of tagged MRI sequences. In *Proc. STACOM MICCAI Workshop*, LNCS. Springer, 2011. 90

Team, R. D. C. R: A language and environment for statistical computing. *R Foundation for Statistical Computing, Vienna, Austria*, 2009. 83

Temam, R. Une méthode d'approximation de la solution des équations de Navier-Stokes. *Bull. Soc. Math. France*, 96:115–152, 1968. 153

Ten Tusscher, K., Noble, D., Noble, P., and Panfilov, A. A model for human ventricular tissue. *American Journal of Physiology*, 286:H1573–H1589, 2004. 57, 117

Tesar, L., Smutek, D., Shimizu, A., and Kobatake, H. 3d extension of haralick texture features for medical image analysis. In *Signal Processing, Pattern Recognition and Applications (SPPRA) 2007 proceedings of the fourth conference on International Association of Science and Technology for Development (IASTED) international conference*, pages 350–355, 2007. 176

Thompson, P. M., Miller, M. I., Ratnanather, J. T., Poldrack, R. A., and Nichols, T. E. Preface to the special issue mathematics in brain imaging. *NeuroImage*, 23, Supplement 1(0):S1 –, 2004. 75

Tobon-Gomez, C., Butakoff, C., Aguade, S., Sukno, F., Moragas, G., and Frangi, A. Automatic construction of 3D-ASM intensity models by simulating image acquisition: Application to myocardial gated SPECT studies. *Medical Imaging, IEEE Transactions on*, 27(11):1655 –1667, November 2008. 114

Tobon-Gomez, C., Craene, M. D., Dahl, A., Kapetanakis, S., Carr-White, G., Lutz, A., Rasche, V., Etyngier, P., Kozerke, S., Schaeffter, T., Riccobene, C., Martelli, Y., Camara, O., Frangi, A. F., and Rhode, K. S. A multimodal database for the 1 st cardiac motion analysis challenge. In Camara, O., Konukoglu, E., Pop, M., Rhode, K., Sermesant, M., and Young, A., editors, *Statistical Atlases and Computational Models of the Heart: Imaging and Modelling Challenges*, volume 7085 of *LNCS*, pages 33–44, Toronto, Canada, 2012. Springer, Heidelberg. 114

Tobon-Gomez, C., De-Craene, M., McLeod, K., Lautz, T., Shi, W., Hennemuth, A., Prakosa, A., Wang, H., Carr-White, G., Kapetanakis, S., Lutz, A., Rasche, V., Schaeffter, T., Butakoff, C., Friman, O., Mansi, T., Sermesant, M., Zhuang, X., Ourselin, S., Peitgen, H.-O., Pennec, X., Razavi, R., Reuckert, D., Frangi, A., and Rhode, K. Benchmarking framework for myocardial tracking and deformation algorithms: An open access database. *Med. Image Anal.*, 2013. 99

Tomasian, A., Krishnam, M. S., Lohan, D. G., Moghaddam, A. N., and Finn, J. P. Adult Tetralogy of Fallot Quantitative Assessment of Pulmonary Perfusion With Time-Resolved Three Dimensional Magnetic Resonance Angiography. *Investigative Radiology*, 44(1):31–37, 2009. URL <GotoISI>://WOS:000262021800005. 147

Tomioka, R. and Sugiyama, M. Dual augmented Lagrangian method for efficient sparse reconstruction. *IEEE Signal Processing Letters*, 16(12):1067–70, 2009. 145

Tomlinson, K. *Finite element solution of an eikonal equation for excitation wavefront propagation in ventricular myocardium*. PhD thesis, University of Auckland, 2000. 57

Tomlinson, K., Hunter, P., and Pullan, A. A finite element method for an eikonal equation model of myocardial excitation wavefront propagation. *SIAM J. Appl. Math.*, 2002. 131

Toussaint, N., Mansi, T., Delingette, H., Ayache, N., and Sermesant, M. An integrated platform for dynamic cardiac simulation and image processing: Application to personalised tetralogy of fallot simulation. In *Proc. Eurographics Workshop on Visual Computing for Biomedicine (VCBM)*, Delft, The Netherlands, 2008. 31, 55, 116

Toussaint, N., Sermesant, M., and Fillard, P. vtkinria3d: A vtk extension for spatiotemporal data synchronization, visualization and management. In *Proc. of Workshop on Open Source and Open Data for MICCAI*, Brisbane, Australia, 2007. 31

Toussaint, N., Stoeck, C., Sermesant, M., Kozerke, S., and Batchelor, P. Three-dimensional prolate spheroidal extrapolation for sparse DTI of the in-vivo heart. In *International Society for Magnetic Resonance in Medicine (ISMRM) Scientific Meeting*, 2010. 68

Toussaint, N., Stoeck, C. T., Schaeffter, T., Kozerke, S., Sermesant, M., and Batchelor, P. G. In vivo human cardiac fibre architecture estimation using shape-based diffusion tensor processing. *Medical Image Analysis*, 17(8):1243 – 1255, 2013. ISSN 1361-8415. 6, 19, 92, 96

Trayanova, N. A. and Tice, B. M. Integrative computational models of cardiac arrhythmias–simulating the structurally realistic heart. *Drug Discovery Today: Disease Models*, 6(3):85–91, 2009. 37

Troianowski, G., Taylor, C. A., Feinstein, J. A., and Vignon-Clementel, I. E. Three-Dimensional Simulations in Glenn Patients: Clinically Based Boundary Conditions, Hemodynamic Results and Sensitivity to Input Data. *J. Biomech. Engnr.-Trans. Asme*, 133(11), 2011. URL <GotoISI>://WOS:000298009500006. 147

Trouvé, A. Diffeomorphisms groups and pattern matching in image analysis. *International Journal of Computer Vision*, 28(3):213–221, 1998. ISSN 0920-5691. 76

Tseng, W.-Y. I., Reese, T. G., Weisskoff, R. M., and Wedeen, V. J. Cardiac Diffusion Tensor MRI In Vivo without Strain Correction. *Magnetic Resonance in Medicine*, 42(2):393–403, 1999. 19

Tucker, L. R. Implications of factor analysis of three-way matrices for measurement of change. *Problems in measuring change*, pages 122–137, 1963. 97

Tucker, L. R. Some mathematical notes on three-mode factor analysis. *Psychometrika*, 31(3): 279–311, 1966. 97

Turk, G. and O'Brien, J. Variational implicit surfaces. Technical report, Georgia Institute of Technology, 1999. 55

Vaillant, M. and Glaunes, J. Surface matching via currents. In *Proc. of IPMI'05*, pages 381–392, 2005. 80, 150

Vaillant, M., Miller, M., Younes, L., and Trouvé, A. Statistics on diffeomorphisms via tangent space representations. *NeuroImage*, 23(Supp. 1):S161–S169, 2004. 76

Valverde, I., Parish, V., Tzifa, A., Head, C., Sarikouch, S., Greil, G., Schaeffter, T., Razavi, R., and Beerbaum, P. Cardiovascular MR Dobutamine Stress in Adult Tetralogy of Fallot: Disparity Between CMR Volumetry and Flow for Cardiovascular Function. *J. Magn. Res. Im.*, 33(6):1341–1350, 2011. 147

Vercauteren, T., Pennec, X., Perchant, A., and Ayache, N. Symmetric log-domain diffeomorphic registration: A demons-based approach. In Metaxas, D., Axel, L., Fichtinger, G., and Székely, G., editors, *Medical Image Computing and Computer-Assisted Intervention - MICCAI 2008*, volume 5241 of *LNCS*, pages 754–761, New York, USA, September 2008. Springer, Heidelberg. 116, 118

Vignon-Clementel, I., Figueroa, C., Jansen, K., and Taylor, C. Outflow boundary conditions for 3D simulations of non-periodic blood flow and pressure fields in deformable arteries. *Comp. Meth. Biomech. Biomed. Engnr.*, 111(3):502–513, 2010a. 152

Vignon-Clementel, I. E., Marsden, A. L., and Feinstein, J. A. A primer on computational simulation in congenital heart disease for the clinician. *Progr. Ped. Card.*, 30(1-2):3–13, 2010b. URL http://www.sciencedirect.com/science/article/B6TBS-51D895W-1/2/4b2e9379dbf920c8e2188092574c8d81. 147

Volkwein, S. Proper orthogonal decomposition and singular value decomposition. Technical report, Karl-Franzens-Univ. Graz & Techn. Univ. Graz, 1999. http://www.uni-graz.at/imawww/volkwein/POD.pdf. 148

Voss, H. and Timmer, J. Nonlinear dynamical system identification from uncertain and indirect measurements. *Int. J. Bifurcation and Chaos*, 14(6):1905–33, 2004. 130

Wang, H. and Amini, A. Cardiac motion and deformation recovery from MRI: a review. *IEEE Trans. Med. Imaging*, 31(2), 2012. 90, 99

Wang, L., Wong, K. C., Zhang, H., Liu, H., and Shi, P. Noninvasive computational imaging of cardiac electrophysiology for 3-D infarct. *IEEE Trans Biomed Eng*, 58(4):1033–1043, Apr 2011a. 132

Wang, V. Y., Lam, H. I., Ennis, D. B., Cowan, B. R., Young, A. A., and Nash, M. P. Modelling passive diastolic mechanics with quantitative MRI of cardiac structure and function. *Med Image Anal*, 13(5):773–784, Oct 2009. URL http://www.hubmed.org/display.cgi?uids=19664952. 68

Wang, Y., Cuculich, P., Zhang, J., Desouza, K., Vijayakumar, R., Chen, J., Faddis, M., Lindsay, B., Smith, T., and Rudy, Y. Noninvasive electroanatomic mapping of human ventricular arrhythmias with electrocardiographic imaging. *Science Translational Medicine*, 3(98):98ra84, 2011b. 113

Wang, Z., Akhtar, I., Borggaard, J., and Iliescu, T. Proper orthogonal decomposition closure models for turbulent flows: a numerical comparison. *Computer Methods in Applied Mechanics and Engineering*, 2012. 171

Watanabe, M. A., Fenton, F. H., Evans, S. J., Hastings, H. M., and Karma, A. Mechanisms for discordant alternans. *Journal of Cardiovascular Electrophysiology*, 12(2):196–206, 2001. 37

Weinstein, D., Kindlmann, G., and Lundberg, E. Tensorlines: advection-diffusion based propagation through diffusion tensor fields. In *Proceedings of the conference on Visualization '99: celebrating ten years*, VIS '99, pages 249–253, Los Alamitos, CA, USA, 1999. IEEE Computer Society Press. ISBN 0-7803-5897-X. 30

Wellens, H. J., Brugada, P., and Stevenson, W. G. Programmed electrical stimulation of the heart in patients with life-threatening ventricular arrhythmias: what is the significance of induced arrhythmias and what is the correct stimulaton protocol? *Circulation*, 72(1):1–7, 1985. 39

Wong, K., Billet, F., Mansi, T., Chabiniok, R., Sermesant, M., Delingette, H., and Ayache, N. Cardiac motion estimation using a proactive deformable model: Evaluation and sensitivity analysis. In Camara, O., Pop, M., Rhode, K., Sermesant, M., Smith, N., and Young, A., editors, *Statistical Atlases and Computational Models of the Heart*, volume 6364 of *Lecture Notes in Computer Science*, pages 154–163. Springer Berlin / Heidelberg, 2010. 62

Wu, M.-T., Su, M.-Y. M., Huang, Y.-L., Chiou, K.-R., Yang, P., Pan, H.-B., Reese, T. G., Wedeen, V. J., and Tseng, W.-Y. I. Sequential Changes of Myocardial Microstructure in Patients Postmyocardial Infarction by Diffusion-Tensor Cardiac MR. *Circulation: Cardiovascular Imaging*, 2: 32–40, 2009. 19, 68

Xiu, D. Efficient collocational approach for parametric uncertainty analysis. *Communications in Computational Physics*, 2(2):293–309, 2007. 131

Xiu, D. Fast numerical methods for stochastic computations: A review. *Communications in Computational Physics*, 5(2-4):242–272, 2009. 131, 133, 144

Xiu, D. and Karniadakis, G. Modeling uncertainty in steady state diffusion problems via generalized polynomial chaos. *Computer Methods in applied Mechanics and Engineering*, 191:4927–4948, 2002. 130, 131, 144, 145

Xue, Z., Shen, D., and Davatzikos, C. Statistical representation of high-dimensional deformation fields with application to statistically constrained 3D warping. *Medical Image Analysis*, 10(5): 740–751, 2006. 91

Yan, P., Sinusas, A., and Duncan, J. S. Boundary element method-based regularization for recovering of LV deformation. *Medical Image Analysis*, 11(6):540–554, Dec 2007. URL http://www.hubmed.org/display.cgi?uids=17584521. 52

Yang, F., Zhu, Y.-M., Magnin, I. E., Luo, J.-H., Croisille, P., and Kingsley, P. B. Feature-based interpolation of diffusion tensor fields and application to human cardiac dt-mri. *Medical Image Analysis*, 16(2):459 – 481, 2012. ISSN 1361-8415. 25, 34

Yang, W., Vignon-Clementel, I. E., Troianowski, G., Reddy, V. M., Feinstein, J. A., and Marsden, A. L. Hepatic blood flow distribution and performance in conventional and novel Y-graft Fontan geometries: A case series computational fluid dynamics study. *J. Thorac. Cardiovasc. Surg.*, 2011. URL http://www.ncbi.nlm.nih.gov/pubmed/21962841. 147

Yano, M., PATERA, A. T., and URBAN, K. A space-time certified reduced basis method for burgers' equation. *Math. Mod. Meth. Appl. S.,(submitted)*, 2012. 171

Yao, J.-A., Hussain, W., Patel, P., Peters, N. S., Boyden, P. A., and Wit, A. L. Remodeling of gap junctional channel function in epicardial border zone of healing canine infarcts. *Circulation Research*, 92(4):437–443, 2003. 43

Yeung, J. J., Kim, H. J., Abbruzzese, T. A., Vignon-Clementel, I. E., Draney-Blomme, M. T., Yeung, K. K., Perkash, I., Herfkens, R. J., Taylor, C. A., and Dalman, R. L. Aortoiliac hemodynamic and morphologic adaptation to chronic spinal cord injury. *J. Vasc. Surg.*, 44(6):1254–1265, Dec 2006. URL http://dx.doi.org/10.1016/j.jvs.2006.08.026. 147

Yue, A. M., Franz, M. R., Roberts, P. R., and Morgan, J. M. Global endocardial electrical restitution in human right and left ventricles determined by noncontact mapping. *Journal of the American College of Cardiology*, 46(6):1067 – 1075, 2005. ISSN 0735-1097. URL http://www.sciencedirect.com/science/article/pii/S0735109705014087. 37

Yue, A. M., Paisey, J. R., Robinson, S., Betts, T. R., Roberts, P. R., and Morgan, J. M. Determination of human ventricular repolarization by noncontact mapping validation with monophasic action potential recordings. *Circulation*, 110(11):1343–1350, 2004. 39

Zettinig, O., Mansi, T., Neumann, D., Georgescu, B., Rapaka, S., Seegerer, P., Kayvanpour, E., Sedaghat-Hamedani, F., Amr, A., and Haas, J. Data-driven estimation of cardiac electrical diffusivity from 12-lead ecg signals. *Medical Image Analysis*, 18(8):1361–1376, 2014. 49

Zhang, W., Noble, J., and Brady, J. Spatio-temporal registration of real time 3D ultrasound to cardiovascular MR sequences. *Medical Image Computing and Computer-Assisted Intervention–MICCAI 2007*, pages 343–350, 2007. 90

Zhang, X., Ramachandra, I., Liu, Z., Muneer, B., Pogwizd, S. M., and He, B. Noninvasive three-dimensional electrocardiographic imaging of ventricular activation sequence. *American Journal of Physiology Heart and Circulatory Physiology*, 289(6):H2724–H2732, Dec. 2005. 113

Zheng, Y., Barbu, A., Georgescu, B., Scheuering, M., and Comaniciu, D. Four-chamber heart modeling and automatic segmentation for 3-D cardiac CT volumes using marginal space learning and steerable features. *IEEE Trans Med Imaging*, 27(11):1668–1681, Nov 2008a. URL http://www.hubmed.org/display.cgi?uids=18955181. 55, 68

Zheng, Y., Barbu, A., Georgescu, B., Scheuering, M., and Comaniciu, D. Four-chamber heart modeling and automatic segmentation for 3-d cardiac CT volumes using marginal space learning and steerable features. *IEEE Trans. Med. Imaging*, 27(11):1668–1681, 2008b. URL http://dx.doi.org/10.1109/TMI.2008.2004421. 81

Zimmerman, S. D., Karlon, W. J., Holmes, J. W., Omens, J. H., and Covell, J. W. Structural and mechanical factors influencing infarct scar collagen organization. *Am J Physiol Heart Circ Physiol*, 278(1):194–200, Jan 2000. URL http://www.hubmed.org/display.cgi?uids=10644599. 68